INNOVATIONS SUSTAINABILITY MODERNITY OPENNESS

SERIES OF MONOGRAPHS

TOM 44

MODERN SOLUTIONS IN ENGINEERING

Edited by
Dorota Anna Krawczyk
Ewa Szatyłowicz
Anna Justyna Werner-Juszczuk
Dorota Gawryluk

Politechnika Białostocka

FACULTY OF CIVIL ENGINEERING
AND ENVIRONMENTAL SCIENCES
BIALYSTOK UNIVERSITY
OF TECHNOLOGY

ASSOCIATION
OF SANITARY ENGINEERS
AND TECHNICIANS

INNOVATIONS – SUSTAINABILITY – MODERNITY – OPENNESS
MODERN SOLUTIONS IN ENGINEERING

Editied by
Dorota Anna Krawczyk
Ewa Szatyłowicz
Anna Justyna Werner-Juszczuk
Dorota Gawryluk

SERIES OF MONOGRAPHS
VOLUME 44

Bialystok 2022

Patronage

Bialystok Univeristy of Technology

Silesian University of Technology

Faculty of Civil Engineering and Environmental Sciences Bialystok University of Technology

Student's Branch of the Polish Association of Sanitary Engineers and Technicians

Association of Sanitary Engineers and Technicians

EN	This project has been funded with support from European Commission. This publication [communication] reflects the views only of the author, and the European Commission and Erasmus+ Programme National Agency cannot be held responsible for any use which may be made of the information contained therein.
PL	Ten projekt został sfinansowany przy wsparciu Komisji Europejskiej. Niniejsza publikacja [komunikat] odzwierciedla wyłącznie poglądy autora, a Komisja Europejska oraz Narodowa Agencja Programu Erasmus+ nie ponosi odpowiedzialności za jakiekolwiek wykorzystanie informacji w niej zawartych.
LT	Šis projektas finansuotas remiant Europos Komisijai. Šis leidinys [pranešimas] atspindi tik autoriaus požiūrį, todėl Europos Komisija ir Erasmus+ programos nacionalinė agentūra negali būti laikoma atsakinga už bet kokį jame esančios informacijos naudojimą.
ES	Este proyecto ha sido financiado con el apoyo de la Comisión Europea. Esta publicación [comunicación] es responsabilidad exclusive de su autor, y la Comisión Europea y la Agencia nacional del Programa Erasmus+ no es responsable del uso que pueda hacerse de la información contenida en el mismo.

INNOVATIONS – SUSTAINABILITY – MODERNITY – OPENNESS
MODERN SOLUTIONS IN ENGINEERING

Editied by
Dorota Anna Krawczyk
Ewa Szatyłowicz
Anna Justyna Werner-Juszczuk
Dorota Gawryluk

SERIES OF MONOGRAPHS
VOLUME 44

Printing House of Bialystok University of Technology
Bialystok 2022

Reviewers:
Prof. Antonio Rodero Serrano, UCO
Assoc. Prof. Edyta Dudkiewicz, PhD, DSc, Eng, PWr

Science editor in the discipline of environmental engineering, mining and energy:
Assoc. Prof. Izabela Anna Tałałaj, DSc, PhD

Copy editor:
mgr Aniela Staszewska

DTP & cover of a book:
Marcin Dominów

Photo on the cover: ilyessuti
https://pixabay.com/pl/photos/bonsai-drewno-amber-flora-makro-4634224/

ISBN 978-83-67185-50-9 (eBook)
DOI: 10.24427/978-83-67185-50-9

Faculty of Civil Engineering and Environmental Sciences
Bialystok University of Technology
45E, Wiejska Street
15-351 Bialystok
www.wb.pb.edu.pl

Association of Sanitary Engineers
and Technicians in Bialystok
2, M. C. Skłodowskiej Street
15-950 Bialystok
www.pzits.bialystok.pl

Table of contents

Authors

Agata Ołtarzewska – Bialystok University of Technology, Faculty of Civil Engineering and Environmental Sciences, Department of HVAC Engineering

Ciacci Cecilia – University of Florence, Faculty of Engineering, Department of Civil and Environ-mental Engineering (DICEA)

Dorota Anna Krawczyk – Bialystok University of Technology, Faculty of Civil Engineering and Environmental Sciences, Department of HVAC Engineering

Dorota Gawryluk – Bialystok University of Technology, Faculty of Civil and Environmental Engineering, Department of Building Structures

Egle Klumbyte – Faculty of Civil Engineering and Architecture, Kaunas University of Technology

Ebru Çokay – Dokuz Eylul University, Engineering Faculty, Dept of Environmental Engineering

Ecrin Ekici – Izmir Institute of Technology, Faculty of Engineering, Department of Energy Systems Engineering

Ewelina Gołębiewska – Bialystok University of Technology, Faculty of Civil Engineering and Environmental Science, Department of Chemistry, Biology and Biotechnology

Fatma Defne Çalık – Izmir Institute of Technology, Faculty of Engineering, Department of Energy Systems Engineering

Francisco Comino – University of Cordoba, Escuela Politécnica Superior de Córdoba, Department of Mechanics

Frida Bazzocchi – University of Florence, Faculty of Engineering, Department of Civil and Environmental Engineering (DICEA)

Grzegorz Świderski – Bialystok University of Technology, Faculty of Civil and Environmental Engineering, Department of Chemistry, Biology and Biotechnology

Gülsün Gizem Taylan – Izmir Institute of Technology, Faculty of Engineering, Department of Energy Systems Engineering

Güray Yildiz – Izmir Institute of Technology, Faculty of Engineering, Department of Energy Systems Engineeringy

Jolanta Šadauskienė – Faculty of Civil Engineering and Architecture, Kaunas University of Technology

Juozas Ramanauskas – Building Physics Laboratory of Institute of Architecture and Construction, Kaunas University of Technology

Kamila Gryko – Izmir Institute of Technology, Engineering Faculty

Kamila Koronkiewicz – Białystok University of Technology, Faculty of Civil Engineering and Environmental Sciences, Department of Chemistry, Biology and Biotechnology

Magdalena Osial – University of Warsaw, Faculty of Chemistry, Polish Academy of Sciences, Institute of Fundamental Technological Research

Manuel Ruiz de Adana – University of Cordoba, Escuela Politécnica Superior de Córdoba, Department of Physical Chemistry and Applied Thermodynamics

María Aurora Flórez de la Colina – Universidad Politécnica de Madrid. Building Construction School, Department of Building Construction Technology

María Jesús Romero-Lara – University of Cordoba, Escuela Politécnica Superior de Córdoba, Department of Physical Chemistry and Applied Thermodynamics

Monika Borkowska – Bialystok University of Technology, Faculty of Civil and Environmental Engineering, Department of Chemistry, Biology and Biotechnology

Monika Kalinowska – Bialystok University of Technology, Faculty of Civil and Environmental Engineering, Department of Chemistry, Biology and Biotechnology

Monika Parcheta – Maria Curie-Sklodowska University in Lublin, Institute of Chemical Sciences, Department of Polymer Chemistry

Natalia Kowalczyk – Bialystok University of Technology, Faculty of Civil Engineering and Environmental Sciences, Department of Chemistry, Biology and Biotechnology

Neri Banti – University of Florence, Faculty of Engineering, Department of Civil and Environmental Engineering (DICEA)

Paris A. Fokaides – School of Engineering, Frederick University

Renata Świsłocka – Bialystok University of Technology, Faculty of Civil Engineering and Environmental Sciences, Department of Chemistry, Biology and Biotechnology

Serkan Eker – Dokuz Eylül University, Engineering Faculty, Department of Environmental Engineering

Sławomir Wilczewski – Bydgoszcz University of Science and Technology, Faculty of Chemical Technology and Engineering

Vincenzo Di Naso – University of Florence, Faculty of Engineering Department of Civil and Environmental Engineering (DICEA)

Weronika Urbańska – Wrocław University of Science and Technology, Faculty of Environmental Engineering

Investigation of thermal bridges of a new high-performance windows installation using 2D and 3D methodology

Keywords: thermal bridges, thermal conductivity, thermal insulation, window, passive house

Abstract: The investigation of energy saving building elements is a paramount issue at this moment when EU Directives focus on achieving new goals regarding energy performance of buildings and energy efficiency. This work is focused on the investigation of thermal bridges of a new high-performance windows installation. This work aims to investigate in detail the thermal properties of the window installed in the thermal insulation layer and to compare different installation methods and thermal bridge evaluation methodologies from the point of view of thermal physics. The results show that, comparing the obtained values of the thermal bridge according to 2D and 3D calculation methods, the values show a difference of 68%. Furthermore, the arrangement of the values of the thermal bridge according to the distance from the load-bearing wall took the opposite trend. Therefore, when designing energy-efficient buildings, it is risky to evaluate thermal bridges only with the 2D methodology.

Introduction

The investigation of energy saving building elements is a paramount issue at this moment when EU Directives focus on achieving new goals regarding energy performance of buildings and energy efficiency. [1]. Correct window installation is still one of the most difficult hurdles that must be overcome in order to achieve a higher energy efficiency in buildings [2]. The thermal imaging made by professionals clearly

shows the thermal bridges at window openings [3]. Thermal bridges are caused by full or partial penetration of the building envelope by materials with different thermal conductivities, and/or a change in fabric thickness, and/or a difference between internal and external areas, such as those found at wall/floor/ceiling junctions) [4]. According to a literature review, the total impact of thermal bridges on heating energy demand is significant in general, ranging from 5% to 39**%** [5–8]**.** The factors mentioned above are determined by weather conditions, insulation level, thermal bridge constructive solutions, building type (use and geometry), and methods used to implement its effects within the calculation of the building energy demand [9]. Thermal bridges can impact a single point, a linear area, or an entire spatial configuration. Typically, the linear thermal bridges (LTB) that occur at the junction of two or more building envelope elements are evaluated in the calculations of the building energy demand. Several scientific studies have been conducted in which LTB was investigated using various calculations and simulation methodologies, such as static/dynamic and 1D/2D/3D [10–13]. The majority of these studies present empirical LTB dependences, which determine the linear thermal transmittance value of a specific construction element [14]. On these foundations, numerical calculation software and catalogues are developed. The European Standard EN ISO 14683 [15] is one of the most widely used atlases and contains seventy-six cases referring to eight thermal bridge typologies, (roofs, corners, intermediate floors, internal walls, slab-on-ground floors, suspended ground floors, pillars, window and door openings). On the other hand, these atlases provide thermal bridge values calculated using the 2D method. These calculations exclude PTB, which is formed by thermally conductive fasteners such as waxes, varnishes, etc.

The national document stated that the thermal transmittance of a linear thermal bridge of the Nero Zero Energy Buildings (NZEB) must be a maximum 0.05 W/(mK) [16]. However, the attainment of such a value has become difficult among project designers and builders. They are looking for new ways to reduce the impact of point thermal bridges on a building's energy costs [17]. A new method of installing windows in a thermal insulation layer is currently being applied in practice. A prefabricated frame, made of higher density stone wool boards and auxiliary elements, for installation of window frames is being used (Fig. 1). Practice shows that such window installations are not complicated due to the lightness of the thermal insulation board and the simplicity of the fastening elements. Moreover, it is suitable for installing on any type of retaining wall and the thermal conductivity of the frame made of thermal insulation material is low. In fact, since the metal fasteners do not connect to each other, it is unlikely to create a point thermal bridge effect. The static properties of such a frame are sufficient enough to install a high-performance window up to 350 mm away from the retaining wall layer. However, the method of installing windows in this way is little studied, compared to the general thermal research context. Therefore, the aim of this work is to investigate in detail the thermal properties of the windows installed in the thermal insulation layer and to compare different installation methods and thermal bridge evaluation methodologies from the point of view of thermal physics.

Methods

In terms of this study, the physics for the calculation of the heat transfer from point thermal bridges, followed the requirements of the ISO 10211:2017 standard [4].

Particularly the linear thermal transmittance with calculated with the use of Equation (1).

$$\psi = L_{2D} - \sum U_j l_j \tag{1}$$

where: L_{2D} – is the linear thermal coefficient obtained by calculating the 2D component for the two environments considered, W/m·K; U_j – is the thermal transmittance of the 1D component *j* separating the two environments being considered, W/m²K; l_j – is the length within the 2D model which the value of U_j applies, m.

The point thermal transmittance is calculated as in Eq. 2:

$$\chi = L_{3D} - \sum\nolimits_{i=1}^{N_i} U_i A_i - \sum_{j=1}^{N_j} \Psi_j \tag{2}$$

where: L_{3D} – is the linear thermal coefficient obtained by calculating the 3D component for the two environments considered, W/m·K; U_j – is the thermal transmittance of the 1D component *I* separating the two environments considered, W/m²K; A_i – is the area which the value U_i applies, m²; Ψ_j – are linear thermal transmittance, W/(m · K); l_j – is the length which the value of Ψ_j applies, m; N_j – is the number of 2D components; N_i – is the number of 1D components.

The average point thermal transmittance $\overline{\chi}$, was calculating using Eq. 3:

$$\overline{\chi} = \frac{\int_a^b \chi \, dl}{b - a} \tag{3}$$

where: *a* – starting position; *b* – end position; χ – point thermal transmittance as a function of length from the masonry layer, W/(m · K).

The longitudinal thermal transmittance $\Delta\psi_S$ was defined as the sum of the point thermal transmittance of the individual components, calculated according to Equation 4

$$\Delta\psi_S = (n\chi)_a + (n\chi)_\beta + \ldots + (n\chi)_\gamma \tag{4}$$

where: *n* – average number of fasteners per meter of opening, *i, j, ..., m* – different types of metal fasteners.

The total linear thermal transmittance was also calculated analytically with the use of the HEAT3 application, referred to in this study as the calculation procedure of the complex structure, denoted with the indicator C.

The total linear thermal transmittance of the thermal bridges was calculated based on the sum-up of the linear thermal transmittance of the individual components, and the thermal transmittance of the stone wool construction, in accordance with Eq. 5

$$\psi_{TS} = \psi_{SWB} + \Delta\psi_S \tag{5}$$

or by considering the linear thermal transmittance of the complex structure, in accordance with Eq. 6

$$\psi_{TC} = \psi_{SWB} + \Delta\psi_C \tag{6}$$

where: ψ_{TS} – total linear thermal transmittance of the thermal bridges was calculated based on the sum-up, W/(m · K); ψ_{SWB} – linear thermal transmittance of the thermal bridges of the window opening with stone wool boards (SWB), W/(m · K); $\Delta\psi_S$ – longitudinal thermal transmittance, W/(m · K); ψ_{TC} – linear thermal transmittance of the complex structure, W/(m · K); $\Delta\psi_C$ – linear thermal transmittance calculated analytically with the use of the HEAT3 application, W/(m · K).

The parameters of the wall construction selected for the study were as follows: 250 mm masonry with thermal conductivity λ = 0.5 W/(m · K); 250 mm thermal insulation material with λ = 0.035 W/(m · K); 10 mm layer of external plaster with thermal conductivity λ = 1.0 W/(m · K). Accordingly, the heat transfer coefficient of the wall structure was U = 0.12 W/(m^2 · K). The window frame was 6 chambers and its thickness was 100 mm with a heat transfer coefficient value of U_f = 1.06 W/(m^2 · K). In this case, the area of the window is evaluated up to the surface of the opening plaster.

The installation of a window on the opening edge of the building using stone wool boards was chosen for the study (Fig. 1). The thermal conductivity coefficient of a special rigid stone wool board (Fig. 1 or Fig. 3) was λ = 0.059 W/(m · K). The length of the window frame fastener W was 192 mm; width – 50 mm; wall thickness – 2 mm; thermal insulation thickness – 48 mm. The length of the corner fastener CL of the thermal insulation panels (when the thickness of the thermal insulation layer was > 200 mm) was 192 mm; width – 192 mm (respectively 96 mm on one side of the corner); wall thickness – 2 mm. One wall mounting piece measuring 80 × 100 mm was estimated in the calculations. The length of the thermal insulation board interconnects EL was 192 mm; width – 192 mm; wall thickness – 2 mm. Two wall mounting parts measuring 80 × 100 mm were evaluated in the calculations.

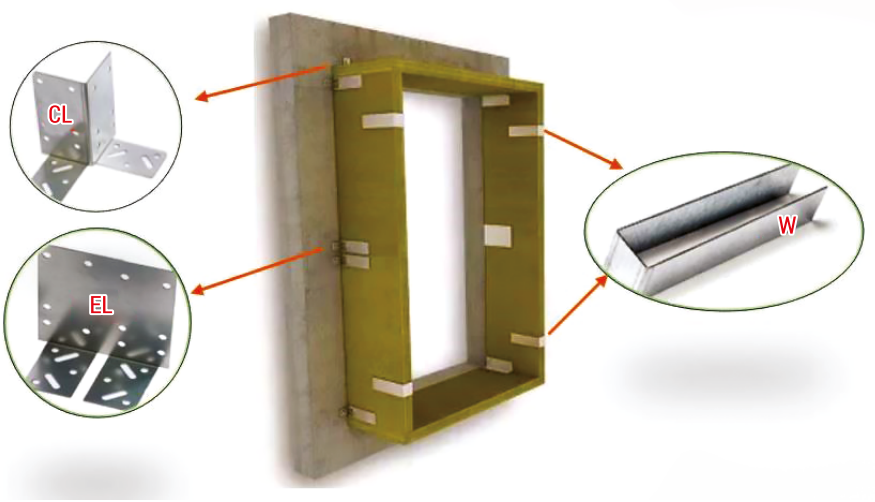

FIG. 1. System of window installation in the insulation layer using the stone wool boards REDAir TM LINK

SOURCE: own elaboration based on [18]

This study was guided by two methodologies of the standard EN ISO 14683 [15]: 1) numerical calculation of the coefficient values (3D), where HEAT software was used and 2) calculation by means of THERM computer software, working under steady state conditions (2D). The calculation scheme is given in Figure 2.

In order to evaluate the influence of fasteners on heat loss through the window opening edge, the computer program HEAT3 with a 3D temperature field calculation was used in the study. At this stage of the calculation, two cases of window frame installation in stone wool boards were analyzed (Fig. 2):

1) A 1 m high wall fragment with three fasteners installed: corner piece CL, middle piece EL and window fastener W (Fig. 1). Point thermal bridges χ_{CL}, χ_{EL}, χ_{W4} are determined;
2) A 1 m long window opening with two corner elements CL and two window fasteners W48 (Fig. 1). Point thermal bridges χ_{2xCL}, χ_{2xW} are determined.

In this study we analyzed how the value of point thermal bridges Ψ_T will be distributed by changing the window installation location in the thermal insulation layer. The values in the thermal insulation layer of the longitudinal thermal bridge were calculated from a value of 0 by adding 10 mm towards the outer side of the barrier, *i.* from $0 + 10i + 10j\ldots + 10n = 150$ mm (Fig. 3).

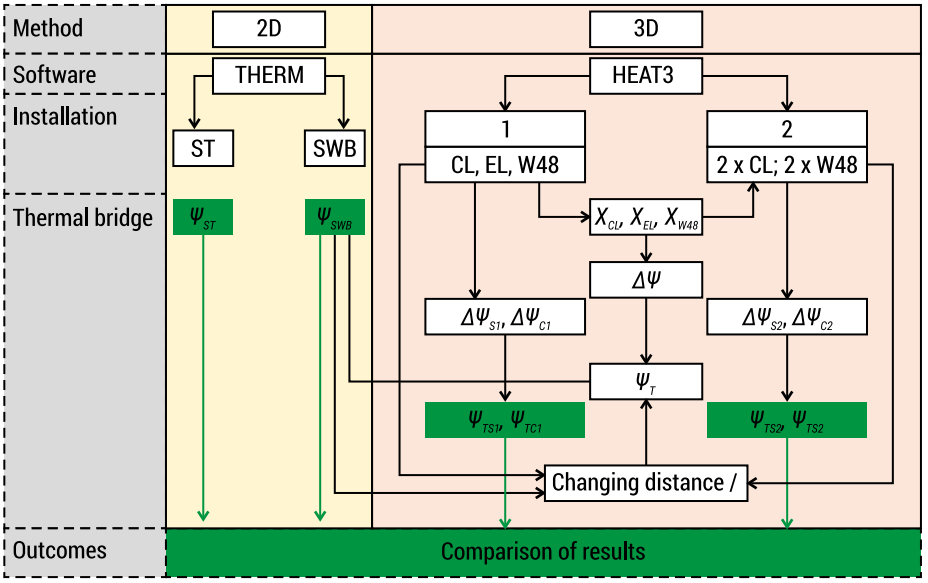

FIG. 2. Thermal bridge estimation algorithm

SOURCE: own elaboration

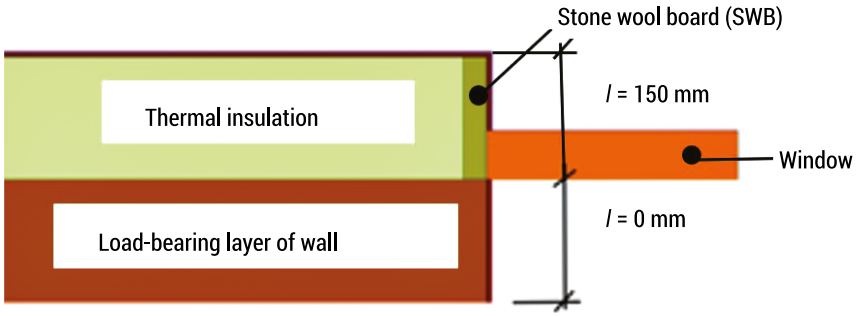

FIG. 3. Schema of basic positions of the window frame in the section of the thermal insulation layer using SWB

SOURCE: own elaboration

Also, an investigation using different calculations methods for determining the additional thermal bridge values: complex $\Delta\Psi_C$ (calculation option (2)) and summed $\Delta\Psi_S$ (calculation option (1)), was done (Eq. 5 and 6.). At this stage, we evaluated the opening edge of a 1 m long window with two corner elements CL and two window fasteners W.

Results and discussion

A comparison of the values of all linear thermal bridges analyzed in this study is presented in Figure 4.

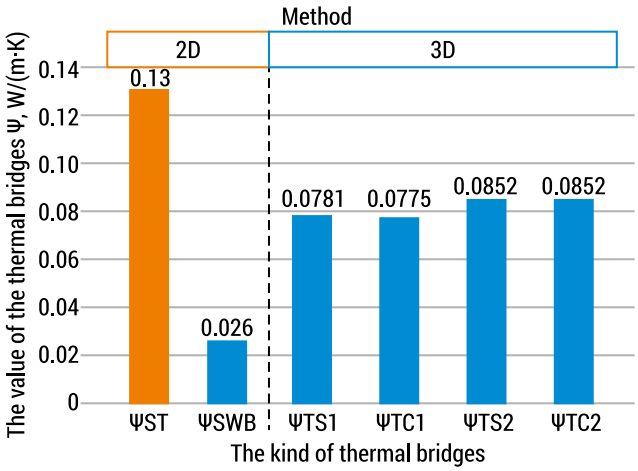

FIG. 4. Comparison of the values of thermal bridges analyzed by different calculation methods
SOURCE: own elaboration

The results of the study show that the thermal bridge through the standard installation site (old building, without insulating the window frame with stone wool boards) will give a transmittance of Ψ_{ST} = 0.13 W/(m · K), while using stone wool boards for window frame insulation, the value of the thermal bridge transmittance is Ψ_{SWB} = 0.026 W/(m · K). The difference between these values is 80%. However, after estimating the metal fasteners, the difference is on average 37%.

If we compare the calculation results according to different methodologies, we will see that when the window is installed right next to the edge of the masonry (l = 0 mm), the results of the total thermal bridge (Ψ_{TS1} = 0.0781 W/(m · K); Ψ_{TS2} = 0.0852 W/(m · K)) is almost the same (difference 0.8% and 0%) as for the complex thermal bridge (Ψ_{TC1} = 0.0775 W/(m · K); Ψ_{TC2}= 0.0852 W/(m · K)), therefore, the results of the calculation according to the methodology specified in EN ISO 10211 [4]: 2008 differ insignificantly from the results provided by the HEAT3 program.

However, when assessing the change in the installation location of the window frame in relation to the thermal insulation layer, there is a discrepancy between the results of the different methodologies used. The results (Fig. 5) show that the values obtained by estimating the sum of the point thermal bridge values ($\Delta\Psi_{S2}$) of individual metal fasteners may differ from 26% to 41% compared to the complex values $\Delta\Psi_{C2}$ used in the same calculations that were made by HEAT3 program. As the installation

distance *l* of the window frame from the load-bearing wall increases, the difference between the values of the thermal bridge obtained by different methods increases (Fig. 5).

This deviation is due to the thermal interaction of the individual fasteners, even though they are separated by a sufficiently large layer of thermal insulation material. Thus, the necessity for employing 3D thermal numerical simulations to accurately estimate the influence of metal fasteners on heat loss is revealed. This conclusion is also reached when comparing the obtained values of the linear thermal transmittance using the 2D and the 3D calculation tool. Particularly, a deviation of close to 70% on the calculation of the linear thermal transmittance was found (Ψ_{SWB} = 0.026 [W/mK] versus Ψ_{T} = 0.0815 [W/mK]). This finding underlines the significance of the use of 3D models and the consideration of the impact of point thermal bridges, a conclusion which is in agreement with previous relevant studies [19].

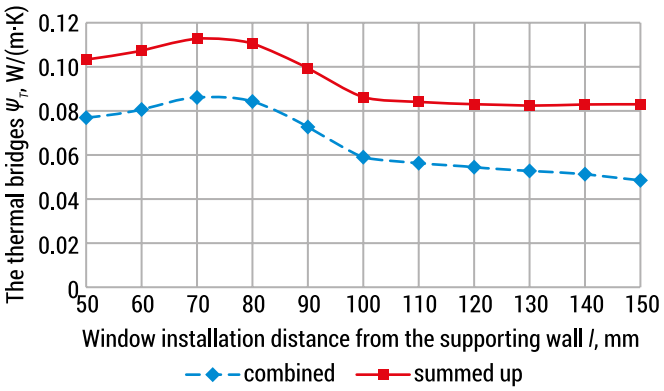

FIG. 5. Linear thermal transmittance ψ [W/mK] versus linear installation distance from supporting wall l [mm] for complex (C) and summed-up (S) methods

SOURCE: own elaboration

The results show that in the calculations, applying the sum of thermal bridge values ($\Delta\Psi_{S2}$) and installing a window at a distance of 50–100 mm from the masonry layer, the value of thermal bridges increases by 28% compared to the values of thermal bridges at a distance of 100–150 mm from the load-bearing wall. The highest value of the thermal bridge (Ψ_{TS2} = 0.1122, W/(m · K)) was at a distance of 70 mm from the masonry layer, and the lowest value of Ψ_{TS2} (0.0820, W/(m · K)) was at a distance of 130 mm from the masonry layer. As a general conclusion, it can be stated that by applying $\Delta\psi_{C2}$ and installing the window in the thermal insulation layer at a distance of 50–100 mm from the masonry layer, increased values of linear thermal transmittance by 30% are observed, compared to the values of linear thermal transmittance at a distance of 100–150 mm from the retaining wall.

Another interesting finding of this study, related to the calculation methods employed is presented in Figure 6. Particularly in this figure, the linear thermal transmittance ψ [W/m·K] versus linear installation distance from supporting wall l [mm] for 2D and 3D calculation domains is presented. As it can be deduced from this figure, the linear thermal transmittance values decrease when increasing the installation distance for the case of the 3D domain, whereas for the 2D the trend is the opposite. This performance can be attributed to the fact that in the 3D domain calculations, the thermal interaction of the individual point thermal bridges is considered. Similar results were obtained by other researchers [6; 20].

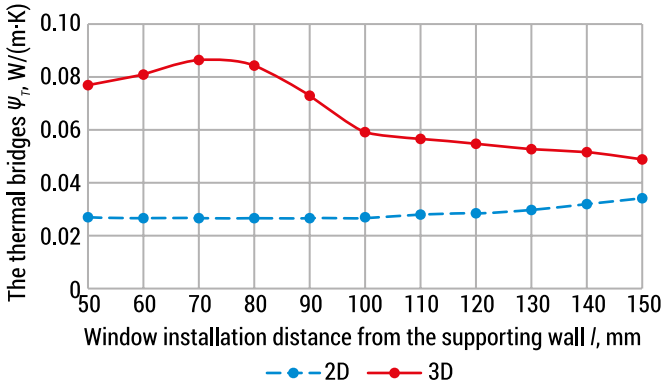

FIG. 6. Linear thermal transmittance ψ [W/mK] versus linear installation distance from supporting wall l [mm] for 2D and 3D calculation domains

SOURCE: own elaboration

In addition, looking at the results from Figure 6, an interpolation of the curves can be done from which a crossing point of both graphs can be deduced. The functional dependence for the 2D graph was (7):

$$y(2D) = \left(1.41 \cdot 10^{-6}\right) - 6 \cdot l^2 - \left(2.17 \cdot 10^{-4}\right) \cdot l + 0.0342 \tag{7}$$

The functional dependence for the 3D graph was (8):

$$y(3D) = \left(2 \cdot 10^{-4}\right) \cdot l + 0.0787 \tag{8}$$

Figure 7 summarizes some of the major findings of this study. This figure is tailored based on the minimum requirements of an EU member state, the legislative provisions of which are similar for many other members states of the central and northern European continent [1, 5, 21]. The results reveal that minimum legislative requirements should be fulfilled, then the installation of the window structure from the supporting

wall, in cases where they are directly mounted to the thermal insulating material, should not be less than 100 mm. Apparently this assessment is based on the assumptions made in this study, which are thought typical for other similar structures.

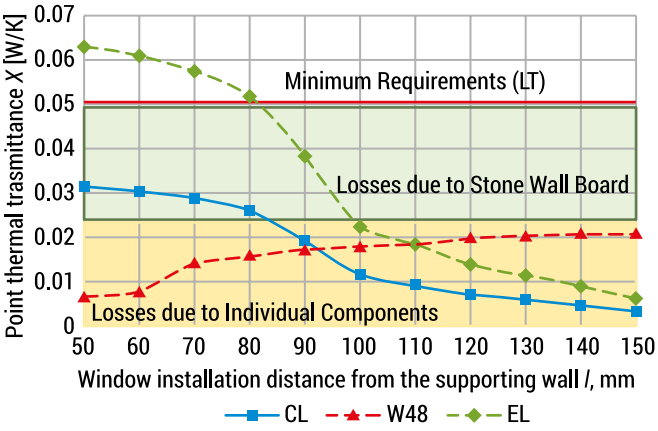

FIG. 7. Point thermal transmittance χ [W/K] of individual fasteners versus linear installation distance from supporting wall l [mm] in accordance to minimum legislative requirements

SOURCE: own elaboration

Conclusions

The investigation has shown that by insulating the window frame with stone wool boards and not evaluating the metal fasteners, we can reduce the value of the thermal bridge at the junction of the wall and the window frame by 80%. However, the evaluation of metal fasteners reduce the value of the thermal bridge by up to 37% compared to the standard option without insulation.

Comparing the obtained values of the thermal bridge according to 2D and 3D calculation methods, the values show a difference of 68%.

Furthermore, comparing the results of the 2D and 3D calculation methodologies, the arrangement of the values of the thermal bridge according to the distance l from the load-bearing wall took the opposite trend. Therefore, when designing energy efficient buildings, it is risky to evaluate thermal bridges using only the 2D methodology.

Literature

[1] Fokaides P.A., Apanaviciene R., Černeckiene J., Jurelionis A., Klumbyte E., Kriauciunaite-Neklejonoviene V., Pupeikis D., Rekus D., Sadauskiene J., Seduikyte L., Stasiuliene L., Vaiciunas J., Valancius, R., Ždankus T., *Research Challenges and Advancements in the field of Sustainable Energy Technologies in the Built Environment,* Sustainability 2020, 12.

[2] Bergero S., Cavalletti P., Chiari A., *Energy refurbishment in existing buildings: thermal bridge correction according to DM* 26/06/2015 *limit values*, Energy Procedia 2017, 140, p.127–140.

[3] O'Grady M., Lechowska A.A., Harte A.M., *Application of infrared thermography technique to the thermal assessment of multiple thermal bridges and window,.* Energy and Buildings 2018, 168, p.347–362.

[4] EN ISO 10211:2017 *Thermal bridges in building construction – Heat flows and surface temperatures – Detailed calculations*. CEN committee ISO/TC 163/SC, 2017.

[5] Theodosiou T., Tsikaloudaki K., Bikas D., Aravantinos D., Kontoleon K.N. *Assessing the use of simplilied and analytical methods for approaching thermal bridges with regard to their impact on the thermal performance of the building envelope*, World SB 14 Conference on the Sustainable Building: Result 2014, October 28–30th, Barcelona, Span. Available from internet: http://wsb14barcelona.org/programme/pdf_poster/P-059.pdf

[6] Theodosiou T.G., Papadopoulos A.M., *The impact of thermal bridges on the energy demand of buildings with double brick wall construction*, Energy and Buildings 2008, 40. https://doi.org/10.1016/j.enbuild.2008.06.006

[7] Citterio M., Cocco M., Erhorn-Klutting H. 2008. *Thermal bridges in the EPBD context: overview on MS apptoaches in regulations*, in: ASIEPI Information Paper.

[8] Evola G., Margani G., Marletta L., *Energy and cost evaluation of thermal bridge correction in Mediterranean climate*, Energy and Buildings 2011, 43, p. 2385–2393.

[9] Martin K., Escudero C., Erkoreka A., Flores I., Sala J.M., *Equivalent wall method for dynamic characterization of thermal bridges,* Energy and Building 2012, 55, p. 704–714.

[10] Gao Y., Roux J.J., Zhao L.H., Jiang Y. *Dinamical building simulation: a low order model for thermal bridges losses,* Energy and Buildings 2008, 40 p. 2236–2243.

[11] Tadeu A., Simoes I., Simoes N., Prata J., *Simulation of dynamic liner thermal bridges using a boundary element method model in the frequency domain*, Energy and Building 2011, 43, p. 3685–3695.

[12] Berggren B., Wall M., *Calculation of thermal bridges in* (*Nordic*) *building envelopes – Risk of performance failure due to inconsistent use of methodology*, Energy Build 2013, 65, p. 331–339.

[13] Ascione F., Bianco N., de Rossi F., Turni G., Vanoli G.P., *Different metchods for the modeling of thermal bridges into energy simulation programs: comparisons of accuracy for flat heterogeneous roofs in Italian climates*. Applied Energy 2012, 97, p. 405–418.

[14] Capozzoli A., Gorrino A., Corrado V., *A building thermal bridges sensitivity analysis.* Applied Energy 2013, 107, p. 229–243.

[15] EN ISO 14683:2017 *Thermal bridges in building construction – Linear thermal transmittance – Simplified methods and default values.*

[16] Cerneckiene J., Zdankus T., Valancius R., Fokaides P. A., *Numerical Investigation of the impact of longitudinal thermal bridging on energy efficient buildings under humid continental climate conditions: The Case of Lithuania,* In IOP Conference Series: Earth and Environmental Science 2020, 410, 1, 012105.

[17] Hallik J., Kalamees T., *A new method to estimate point thermal transmittance based on combined two-dimensional heat flow calculation,* 12TH NORDIC SYMPOSIUM ON BUILDING PHYSICS (NSB 2020), E3SWeb of Conferences 2020, 172, 8005 0. Available online: https://doi.org/10.1051/e3sconf/202017208005

[18] Rockwool. Available online: https://docplayer.me/3412936-Redair-tm-link-montering sanvisning.html

[19] Ascione F., Bianco N., De Masi R.F., Mauro G.M., Musto M., Vanoli G.P., *Experimental validation of a numerical code by thin film heat flux sensors for the resolution of thermal bridges in dynamic condition,* Applied Energy 2014, 124.

[20] Sadauskiene J., Ramanauskas J., Vasylius A., *Impact of point thermal bridges on thermal properties of building envelopes*, Thermal Science 2020, 24.

[21] Construction Technical Regulation STR 2.01.02: 2016, Design and certification of energy performance of buildings, Ministry of Environment of the Republic of Lithuania, 2020.

Catalytic pyrolysis of low density polyethylene

Keywords: Silica-alumina catalyst, ZSM-5, acidity, in-situ catalytic pyrolysis, waste plastics

Abstract: Scientists are searching for innovative and sustainable energy production by meeting the eco-friendly solutions needed. Increasing plastic use and depletion of fossil fuels brought the energy need and waste management to a common denominator. Many of the developed thermochemical (pyrolysis, gasification, etc.) and biochemical, recycling, and recovery methods achieve promising results for the environment. It has been observed that polyolefins (low density polyethylene, high density polyethylene, polypropylene) are suitable for producing valuable chemicals and fuels by the pyrolysis method. Low density polyethylene produces quite a lot of wax when pyrolyzed. With the help of different acidic catalysts, these waxes can produce hydrocarbons in the gasoline-diesel range in in-situ or ex-situ mode. In this work, we investigated the liquid yield and contents of the products formed by the in-situ mode and semi-continuous operation. A commercial ZSM-5 and a silica-alumina catalyst produced by the sol-gel method were used for catalyst screening with four different catalyst-to-plastic ratios. At a catalyst-to-plastic ratio of 1/250, ZSM-5 produced 38.83 wt.% of liquid, while silica-alumina produced 84.18 wt.%. They showed molecular distribution with 92.08 wt.% and 58.34 wt.% in the range of C_5-C_{15}, respectively.

Introduction

The increasing population in the world brings with it the need for energy. The depletion of fossil resources draws attention to renewable energy. Many strategies have been developed to eliminate the large amounts of existing waste (agricultural waste, urban waste, disposable products, paper, plastic, construction waste, etc.) that arise every day. Various thermochemical methods are used for resource recovery from these waste management strategies. Various types of plastic appear in different fields (food

and cleaning industry, disposable products, healthcare, etc.). Polyolefins (low density polyethylene (LDPE), high density polyethylene (HDPE), polypropylene (PP)), PET, and PVC are plastic types that are frequently used in daily life. As determined, polyethylenes have the largest share of global annual consumption as 102.9 MMT/yr. [1].

Examples of thermochemical methods are pyrolysis, gasification, and hydrocracking [2, 3]. Pyrolysis is the chemical cracking that takes place in an oxygen-free environment at atmospheric pressure and medium-high temperatures (400-600°C). Polyethylenes' chemical (non-catalytic) pyrolysis generally results in heavy wax (C_{21}–C_{40}) products. To address the production of lighter hydrocarbons from waste plastics, catalytic pyrolysis (CP) is considered to be an effective technique. When using the in-situ mode of the CP, the raw material and catalyst are in direct contact in the reactor. A secondary reactor or catalytic bed is used where the pyrolysis vapors form in the first reactor and meet with the catalyst for ex-situ mode. In addition, there are three different operation modes: batch, semi-continuous, and continuous. There are no inlet and/or outlet streams for the batch operation to and from the reactor. In semi-continuous systems, the raw material is inside the reactor. There is no continuous feeding, but a continuous output is observed. Finally, there is continuous feeding and product output in continuous mode [4]. In addition, parameters such as feedstock type, temperature, reactor type and operation mode, catalyst type, and catalyst-to-plastic ratio for the pyrolysis process determine the quality and quantity of the products.

In order to obtain gasoline-diesel range fuels from the pyrolysis of plastics, various acidic catalysts (silica-alumina, FCC catalysts, activated Carbon, clays, metal oxides, carbonates, zeolites (Zeolyte Y, ZSM-5, β-zeolyte, natural zeolytes) are used (Mark, 2020). Low density polyethylene can be converted to benzene, toluene, xylene, di and trimethyl benzene, indane, indene, naphthalene, fluorene, and acenaphthene hydrocarbons by pyrolysis [5]. The reason why acidic catalysts are specially chosen is to provide thermochemical cracking successfully. The aim is to obtain target products (i.e. aromatic hydrocarbons) with high selectivity, and the most essential catalyst types that achieve this are zeolites [6]. New and competitive catalysts can be developed using various catalyst production and modification methods (such as precipitation, co-precipitation, impregnation, and sol-gel) [7].

In this study, the optimization of a bench-scale pyrolysis setup was performed by using the LDPE as feedstock. For a selected condition, thermal and in-situ catalytic pyrolysis products were analyzed. A silica-alumina (Si/Al=30) catalyst was produced by the sol-gel method to crack LDPE, considering the ability of the ZSM-5 catalyst to crack polyolefins into light alkenes and aromatics. In-situ CP of LDPE plastics was semi-continuously performed. The aim is to perform catalyst screening using different catalyst-to-plastic ratios and to produce hydrocarbons in the C_5–C_{15} range while achieving maximum liquid yields.

Characterization of waste LDPE

For this study, household plastic wastes were collected and separated according to their types in a certain time period. Generally, food and cleaning packaging and single-use products were collected. Among these products, LDPEs were selected, and various characterization methods were applied. First of all, proximate and ultimate analyzes were performed to understand whether this raw material, which will be pyrolyzed, would be suitable for producing innovative and sustainable hydrocarbons (Table 1). Proximate analysis was performed using the related ASTM standards.

TAB. 1. Proximate and ultimate analysis of waste plastics

Moisture (wt%)	Volatile Matter (wt%)	Ash (wt%)	Fixed Carbon* (wt%)	C (wt%)	H (wt%)	O* (wt%)	N (wt%)	S (wt%)
1,33±1,39	93,27±1,49	1,74±0,05	3,65±0,17	81.61	13.22	5.17	0	0

*By difference

SOURCE: own elaboration

Also, ICP-MS was used to detect the elements in LDPE that could not be observed with ultimate analyses. High amounts of Al, Na, K, Ca, Mg, Fe, and some Cu, Zn, Ba, Cr, Sr, and Pb were also detected in waste LDPE. The presence of these ingredients can be caused by the additives, dyes, etc. that are used during the production of the packaging.

In addition to these analyses, TGA analysis was used to predict the behavior of LDPE as a feedstock in the pyrolysis reactions. With a heating rate of 10°C/min, the plastics were heated from 25°C to 800°C. At this time, there is a N_2 flowrate at a rate of 40 mL/min. As can be detected from the TGA and DTG curves, 310°C stands for cracking onset, and 481°C represents the temperature with the highest mass loss. Thus, using 480–500°C for the pyrolysis temperature may be an ideal choice for maximum cracking of LDPE.

Non-catalytic pyrolysis of LDPE

In order to examine the thermal and catalytic pyrolysis of low density polyethylene, pure LDPE was purchased. Prior to performing the experiments, four different control factors (N_2 flowrate, feeding period, plastic amount per feeding, and condensation temperature) and three different levels (0.9, 1, 1.1 L/min N_2 flowrates; 10, 15, 20 min; 10, 20, 30 g; 0, –5, –10°C) were determined. If experiments were to be carried out under all these conditions, 81 experiments, and to minimize the error, repetitions of these experiments would be needed. For this reason, an optimization scheme was

created using the basic Taguchi L9 (3 4) orthogonal array method, and the number of experiments was reduced to nine. Thus, both parameter changes could be interpreted, and a preliminary experiment plan was obtained. Table 2 shows the product yields according to the related control factor and levels.

The flowrate of N_2 gas in the system used for thermal pyrolysis experiments was determined by a mass flow controller (MFC). When the oxygen-free environment was provided in the experimental set-up with gas flow, the system was started to be heated. When the target temperature was reached, feedstocks were continuously fed to the reactor at regular intervals. With the help of a single condenser, the condensed liquids at various condensation temperatures were collected, and the noncondensable gases were exhausted. All experiments were kept constant at a 450°C pyrolysis temperature, and the process duration was about 80 minutes for all. No solid product was obtained in these nine experiments.

TAB. 2. Optimization experiments for thermal pyrolysis of pure LDPE

Run	N_2 flow rate, L/min	Feeding period, min	Plastic amount per feeding, g	Condensation temperature, °C	Liquid yield, wt%	Gas yield, wt%	Conversion, wt%
1	**0.9**	**10**	**10**	**0**	**95.07**	**4.93**	**100**
2	0.9	15	20	−5	91.51	8.49	100
3	0.9	20	30	−10	64.38	25.18	89.57
4	1	10	20	−10	55.01	23.60	78.61
5	**1**	**15**	**30**	**0**	**79.45**	**20.55**	**100**
6	1	20	10	−5	64.90	35.10	100
7	**1.1**	**10**	**30**	**−5**	**83.87**	**16.13**	**100**
8	1.1	15	10	−10	64.67	35.33	100
9	1.1	20	20	0	74.22	25.78	100

SOURCE: own elaboration

As can be seen in Table 2, for 0.9 L/min N_2 flow rate, 10 grams of plastic feeding in 10 minutes and condensation temperature of 0°C provided the highest liquid yield with 95.07 wt.% and 100% conversion. The resulting liquid was completely nonviscous pyrolysis oil. In run 2, where 20 grams of LDPE was fed in 15 minutes, 100% conversion was reached, but its liquid yield was lower than in run 1. Due to experimental errors, run 3 and run 4 could not provide total conversions. When the experiments with 1 L/min were examined, the most successful test was run 5 with 100% conversion and 79.45% liquid yield. However, all the liquid obtained consists of wax. The reason for this is residence time which decreases with the increase of N_2 flowrate, and pyrolysis vapors leave the reactor before cracking sufficiently. In addition, the increase in feeding rate is also a factor. While the N_2 flowrate was 1.1 L/min,

all three experiments have reached 100% conversion; run 7 was the most efficient experiment with 83.87 wt.% of liquid yield and fluid state.

Run 1 and 9 were compared with the same feeding rate (1 g/min) and cooling temperature (0°C); run 1 produced more liquid than run 9. While 0.9 L/min N_2 flowrate provides 95.07% liquid obtainment, it was observed that 74.22 wt.% liquid was produced with a 1.1 L/min nitrogen flowrate. Here again, the reason is the residence time, which is shortened by the increased gas flow. Because if the pyrolysis vapors were broken in enough time and left the reactor, the liquid would increase, but with short residence times, it quickly reached the condenser without cracking and could not condense. Thus, the amount of noncondensable gases was increased.

As a result of all these experiments and comparisons, run 5 was chosen as the most suitable experiment to be tested in in-situ catalytic pyrolysis. One of the reasons is its high liquid yield of 79.45%. The most important reason was that it produced full wax and observed in what intervals the catalysts could break LDPE from wax to light hydrocarbons.

Catalytic pyrolysis of LDPE

ZSM-5 zeolite was purchased from Zeolyst International to investigate the catalytic pyrolysis of plastics. In this research, a silica-alumina catalyst was produced by the sol-gel method based on the Si/Al = 30 ratio of the acidic ZSM-5 catalyst. The sol-gel method basically consists of hydrolysis and condensation reactions. Hydrolysis reactions took place, and metal hydroxide and alcohols were revealed. Then metal hydroxides came together with metal hydroxides/alkoxides to produce long chains [8]. First, the alumina precursor, aluminum isopropoxide (AIP), was mixed with an excess amount of distilled water at 85°C, 900 rpm, and stirred for 1 hour. Afterward, HNO_3 was added, and the solution continued to stir for 1 hour under the same conditions. Meanwhile, a silica solution was prepared. Tetraethyl orthosilicate (TEOS), ethanol, distilled water, and HCl were mixed at 75°C, 150°C/min heating rate, and 900 rpm for 1 hour. The solutions obtained were added to each other and mixed for an hour at 900 rpm & 85°C, and the sol was obtained. After that, the gel was formed by decreasing the temperature to 70°C and turning on the system. The transparent gel was then dried at 120°C overnight. After drying, catalysts were calcined at 500°C for 6 hours. The obtained catalyst particles were ground and sieved to 250 μm (60 mesh) as a final step.

In this study, catalytic pyrolysis experiments were semi-continuously operated. Different from the thermal pyrolysis experiments, LDPE and catalysts were preplaced inside the reactor. It was then heated from room temperature to pyrolysis temperature. The gas flow was again determined with the help of the mass flow controller. While the pyrolysis oil and waxes produced were collected at the condenser outlet, noncondensable gases were exhausted. Spent catalysts remaining in the reactor were

also collected separately. Catalytic pyrolysis was applied in-situ mode with commercial ZSM-5 & silica-alumina catalysts. Plastic type, pyrolysis temperature, N_2 flowrate, condensation temperature, and process duration were kept constant for each experiment as pure LDPE, 450°C, 1 L/min, 0°C, and 1 hour, respectively. In each run, 120 grams of LDPE was fed into the reactor and started to be heated. Catalyst screening was performed by simply changing the catalyst-to-plastic ratio, and the liquid yield was observed. Four different experiments were performed for catalyst-to-plastic ratio as 1/100, 1/250, 1/500, and 1/1000 for the ZSM-5. Before each experiment, ZSM-5 catalysts were calcined for 4 hours at 550°C. 1/250 was determined as the optimum ratio, and in-situ CP was performed with silica-alumina catalyst under the same conditions. Experiments were repeated in duplicates for each catalyst type. Table 3 represents the yields of the pyrolysis products & coke formation according to catalyst type and catalyst-to-plastic ratio.

TAB. 3. Experimental results of thermal pyrolysis and catalyst screening of LDPE

Run	Catalyst type	Cat./plastic ratio	Liquid yield, wt.%	Gas yield, wt.%	Solid* yield, wt.%
5	Thermal	–	79.45	20.55	0
5.1	ZSM-5 (Si/Al = 30)	1/100	32.21	67.79	0
5.2	ZSM-5 (Si/Al = 30)	1/250	38.83	61.17	1.06
5.3	ZSM-5 (Si/Al = 30)	1/500	43.12	56.88	0.96
5.5	ZSM-5 (Si/Al = 30)	1/1000	45.80	54.20	2.79
5.6	Silica-alumina (Si/Al = 30)	1/250	84.18	15.82	0

*Coke

SOURCE: own elaboration

By thermal pyrolysis of LDPE, approximately 80% liquid yield and 20% gas yield was obtained. The liquid was made of full wax. There was not any solid product observed. With a catalyst-to-plastic ratio of 1/100 for ZSM-5, the liquid yield was decreased to 32 wt.%, and the gas yield was increased up to 68 wt.%. No wax was observed in the liquid. The ratios of 1/250, 1/500, and 1/1000 were also tested with ZSM-5, and 38.83 wt.%, 43.12 wt.%, and 45.8 wt.% liquid yields were obtained, respectively. Coke formation was observed in all three ratios. In addition, although by decreasing the ratios of 1/500 and 1/1000, the liquid yield was increased but wax formation started to be observed and increased. Thus, the optimum ratio of 1/250 was chosen with a liquid yield of 38.83 wt.%. Afterward, the silica-alumina catalyst was tested at a 1/250 ratio, and it was observed that the amount of liquid was more (84.18 wt.%) than that produced in thermal pyrolysis. However, 17.35 wt.% of the amount of liquid produced was brown-colored heavy wax. While this amount was 2.2 wt.% in thermal pyrolysis, it was not observed in other catalyst-to-plastic ratios.

The liquid samples obtained from the non-catalytic and catalytic pyrolysis of two catalysts under the same conditions were examined by GC-MS. Liquids were dissolved by tetrahydrofuran (THF) to prepare for GC-MS analysis. Fig. 1 is the illustration of the carbon number distribution for runs 1, 3, and 6.

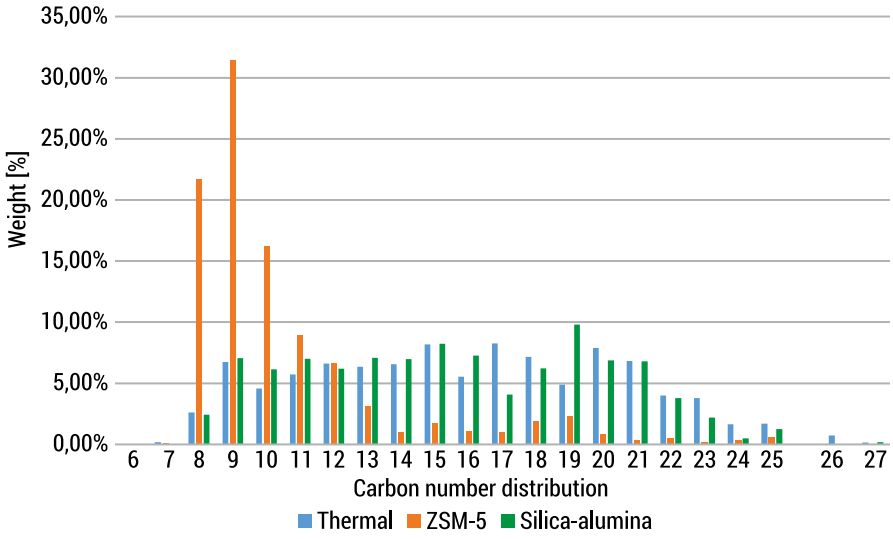

FIG. 1. Carbon number distribution of liquid hydrocarbons according to thermal and catalytic pyrolysis

SOURCE: own elaboration

The content of the liquid obtained from thermal pyrolysis ranged from C_6 to C_{27}. 53.01 wt.% of this distribution included C_6–C_{15} hydrocarbons that were initially targeted. In addition, aromatic hydrocarbons such as benzene, toluene, and xylene were not detected in the liquid content. After in-situ pyrolysis with ZSM-5, the distribution narrowed in the C_6–C_{24} range. 92.08 wt.% of this hydrocarbon distribution was in the C_6–C_{15} range. It has been observed that important aromatics such as benzene derivatives, ethylbenzene, toluene, p-xylene, and o-xylene can be produced. On the other hand, silica-alumina gave peaks in the range of C_7–C_{27}. No hydrocarbons were found in the range of C_{25} and C_{26}. 58.34% of this distribution comprised the C_7–C_{15} section. Also, essential aromatics, benzene derivatives, and toluene were determined in the pyrolysis oil.

Conclusions

The study clearly demonstrated the importance of arranging parameters to succeed in optimization experiments. Continuously operated thermal pyrolysis of LDPE was investigated. Also, it was essential to keep significant parameters constant in order

to examine the effect of process parameters. Preliminary results were obtained using different catalyst-to-plastic ratios. Semi-continuously operated in-situ CP was examined. In thermal pyrolysis, pyrolysis vapors were exhausted within 80 minutes, whereas in catalytic pyrolysis, 1 hour was sufficient as a process duration.

In conclusion, according to the results of the catalyst screening, silica-alumina catalysts can be produced with higher acidity (i.e. higher Si/Al ratio) or can be supported by zeolites or metal oxides. Optimization experiments for catalytic pyrolysis should be performed by changing process duration, temperature, and N_2 flowrate parameters, and the results should be improved. In addition, cracking of intermediate liquid products (wax) or ex-situ CP can be tried to prevent waxes that occur as the catalyst/plastic ratio decreases. Moreover, a second condenser with a different temperature (i.e. the first condenser is at 0°C and the second is at –25°C) can be added to the set-up so that oil and wax products can be collected separately. For future studies, waste LDPE tests should be performed to compare with pure plastics. In addition, mixtures can be formed with different plastic types, and their effects on each other can be observed. Waste polyethylene blends and polyolefin blends are the studies that are aimed to be carried out in the continuation of this research.

Acknowledgments: This work is supported and funded by the UK Department for Business, Energy and Industrial Strategy together with the Scientific and Technological Research Council of Turkey (TÜBİTAK; Project No. 119N302) and delivered by the British Council.

Literature

[1] Ellis L.D. et al., *Chemical and biological catalysis for plastics recycling and upcycling,* Nature Catalysis 2021, 4, p. 39–556.

[2] Zhang F. et al., *Current technologies for plastic waste treatment: A review*, Journal of Cleaner Production 2021, 282, 124523.

[3] Solis M., Silveira S., *Technologies for chemical recycling of household plastics – A technical review and TRL assessment*, Waste Management 2020, 105, 128–138.

[4] Yildiz G., Ronsse F,, Prins W., *Chapter* 10 *Catalytic Fast Pyrolysis Over Zeolites,* Fast Pyrolysis of Biomass: Advances in Science and Technology 2017, p. 200–230. Royal Society of Chemistry, London.

[5] Miandad R. et al., *Effect of plastic waste types on pyrolysis liquid oil,* International Biodeterioration & Biodegradation 2017, 119, p. 239–252.

[6] Mark L.O, Cendejas M.C., Hermans I., *The Use of Heterogeneous Catalysis in the Chemical Valorization of Plastic Waste,* ChemSusChem 2020, 13, p. 5808–5836.

[7] Farrauto R.J., Bartholomew C.H., *Chapter* 2 *Catalyst Materials, Properties and Preparation*, Fundamentals of Industrial Catalytic Processes 2006, John Wiley & Sons, New York.

[8] de Jong K.P., *Sol-Gel Processing*, Synthesis of Solid Catalysts, 2009, p. 83–109, WILEY-VCH Verlag GmbH & Co. KGaA, Weinheim.

Derivatives of tannic acid as effective antioxidants

Keywords: bioactive substances, tannic acid, spectroscopic methods, biological activity

Abstract: There is a growing interest in the use of natural antioxidants as food preservatives, food supplements, drugs or other special purpose materials instead of synthetic antioxidants because of their possible adverse effects including skin allergies, gastrointestinal tract problems or even risk of cancer. Tannic acid (TA) is a plant polyphenol that possesses strong antioxidant, antibacterial and antiviral properties against Sars-CoV-2 virus. TA is a biocompatible and biodegradable material. It has been affirmed as a safe food-product additive by the US FDA. The paper reviews the recent knowledge about the antioxidant properties of TA and its application in different industry sectors as new tannic acid – hybrid materials or supramolecular self-assembled molecules.

Introduction

Tannic acid (TA) formally contains 10 galloyl(3,4,5-trihydroxyphenyl) units surrounding a glucose center (Figure 1) [1–4]. The polyphenolic moieties are responsible for the outstanding biological properties of TA. The presence of catechol or galloyl groups allows the formation of tannic acid-metal complexes. It can be extracted from cocoa, green or black tea, pomegranate peel (*Punica granatum*), sorghum, grapes, pears, bananas, black-eyed peas or lentils [5,6].

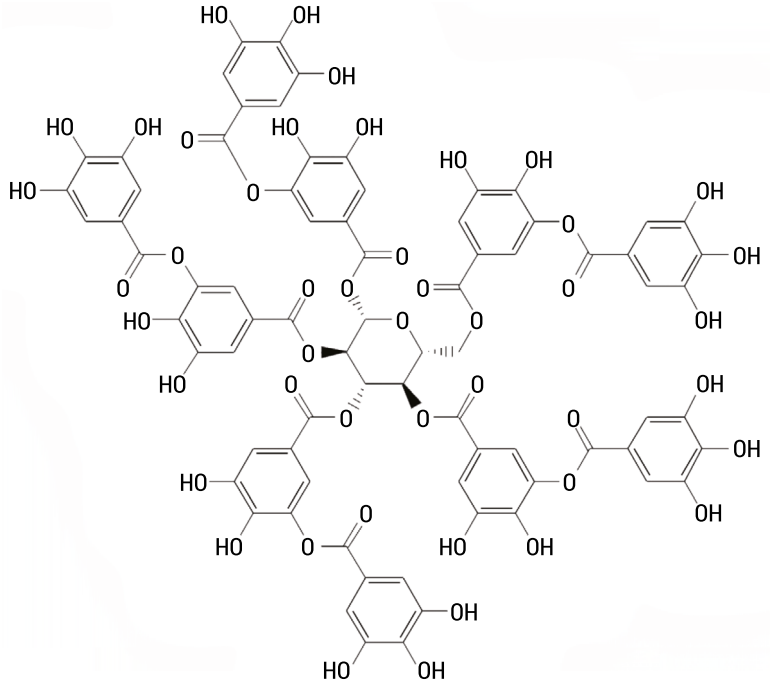

FIG. 1. Structure of tannic acid
SOURCE: own elaboration

Many studies have proved that tannic acid has numerous positive biological properties, such as being: antioxidant, antimutagenic, antitumor, antibacterial (in relation to *Staphylococcus aureus, Escherichia coli, Streptococcus pyogenes, Enterococcus faecalis, Pseudomonas aeruginosa, Yersinia enterocolitica, Listeria innocua, Bacillus cereus*) [7], homeostatic, antiparasitic, antiviral (in relation to Inflilloma Noroviruses, Herpes simplex virus type 1 and 2, HIV) [7]. In addition, recent studies claim that TA can prevent SARS-CoV-2 infectivity by inhibiting extracellular RBD (receptor-binding domain)/ACE2 (angiotensin converting enzyme 2) interactions and the activity of TMPRSS2 (transmembrane serine protease 2) and 3CLpro (3-chymotrypsin like protease) [2]. Tannic acid is involved in the prevention of diseases related to oxidative stress, such as cardiovascular disease, cancer and osteoporosis [8]. TA has the ability to neutralize free radicals that are responsible for the development of various diseases, such as allergies, diabetes, Parkinson's disease and Alzheimer's disease [7]. It is believed that the number of hydroxyl groups and the degree of polymerization of the tannic acid correlate with their free radical scavenging ability. The tannins with the highest number of hydroxyl groups are most easily oxidized and therefore have the highest antioxidant activity. The effectiveness of tannic acid as a natural antioxidant has been shown to be due to its complex combination of reducing and redox effects, which also contribute to its radical scavenging capacity [8]. Moreover, it is believed that

the antioxidant capacity is the greatest, the easiest and fastest radical scavenging activity [9]. Interestingly, some researchers argue that the structural features of tannic acid, which are important in antioxidant mechanisms, could be better exploited in pro-oxidative activities [10]. The antioxidant properties of TA against different radicals, described as reducing potential or chelating properties are shown in Table 1.

The aim of the work was the synthesis of the manganese(II) complex of tannic acid and the study of the structure and antioxidant properties of this compound by means of spectroscopic (FT-IR, UV) and thermogravimetric (TGA/DSC) methods. Mn(II)-TA can serve as a new material with enhanced antioxidant activity compared to TA.

TAB. 1. Antioxidant activity of tannic acid

Method	Results	References
DPPH radical scavenging activity [%]	95.1 (C_{TA} = 45 μg/cm^3; C_{DPPH} = 0.1 mmol/L; t = 30 min)	[5]
	82.82±0,57 (C_{TA} = 50 μg/cm^3; C_{DPPH} = 500 μmol/dm^3; t = 40 min)	[11]
DPPH, IC_{50}*, [μmol/dm^3]	7.8±2.3 (Cp_{DPPH} = 0.004%; t = 30 min)	[12]
	4.87 μg/cm^3 (C_{DPPH} = 2x10^{-4} mol/dm^3; t = 30 min)	[13]
ABTS radical scavenging activity [%]	96.9 (C_{TA} = 45 μg/cm^3; C_{ABTS} = 2 mmol/dm^3; t = 30 min)	[5]
ABTS, IC_{50}*, [μmol/dm^3]	0.3±0.0 (C_{ABTS} = 60 μmol/dm^3; t = 15 min)	[12]
	18.68 μg/cm^3 (t = 10 min)	[13]
FRAP, IC_{50}*, [μmol/dm^3]	160±10 (t = 4 min)	[14]
	66±14 (t = 30 min)	[14]
Superoxide anion radical scavenging activity [%]	69.1±4.2 (C_{TA} = 15 μg/cm^3; $C_{riboflavin}$ = 1.33x10^{-5} mol/dm^3; $C_{methionine}$ = 4.46x10^{-5} mol/dm^3; C_{NBT} = 8.15x10^{-8} mol/dm^3; t = 40 min)	[5]
$^{\bullet}O_2^-$, IC_{50}*, [μmol/dm^3]	704.6±106.8 (C_{EDTA} = 0.1 mmol/dm^3)	[12]
FTC (peroxidation inhibition of linoleic acid – the effect of different TA concentration) [%]	97.7 (C_{TA} = 15 μg/cm^3); 98 (C_{TA} = 30 μg/cm^3); 98.4 (C_{TA} = 45 μg/cm^3); (Cp_{FeCl2} = 3.5%; Cp_{SCN} = 30%; t = 30 h)	[5]
Ferrous ions (Fe^{2+}) chelating activity [%]	66.8±6.2 (C_{TA} = 15 μg/cm^3; C_{FeCl2} = 2 mmol/dm^3; t = 10 min)	[5]
H_2O_2 scavenging activity [%]	52.8±5.4 (C_{TA} = 15 μg/cm^3; C_{H2O2} = 43 mmol/dm^3)	[5]
H_2O_2, IC_{50}*, [μmol/dm^3]	21.9±4.6 (C_{H2O2} = 10 mmol/dm^3; t = 30 min)	[12]
$^{\bullet}OH^-$, IC_{50}*, [μmol/dm^3]	89.4±18.1 ($C_{deoxyribose}$ = 2.8 mmol/dm^3; C_{FeCl3} = 20 μmol/dm^3; C_{EDTA} = 100 μmol/dm^3; C_{AscA} = 50 μmol/dm^3; C_{H2O2} = 1.42 mmol/dm^3; t = 60 min)	[12]

*IC_{50}– the concentration of TA, which reduces the initial concentration of a given compound by 50%

SOURCE: own elaboration

Materials and methods

In order to synthesize solid Mn(II) complex with tannic acid, 10 cm^3 of TA (C = 0.1 mol/dm^3, in Tris-HCl solution, pH = 7.4), 10 cm^3 of NaOH (C = 0.1 mol/dm^3, aqueous solution) and 10 cm^3 of $MnCl_2$ (C = 0.1 mol/dm^3) were mixed, so that the molar ratio of tannic acid: NaOH : metal chloride was 1:1:1. The pH of the final mixture was 6.6. After a few minutes a brown precipitate was obtained, which was then filtered with a filter paper and allowed to dry for 3 days. The resulting precipitate was carefully collected from the filter and transferred to an Eppendorf tube for further study (thermal and spectroscopic analysis).

Thermal TA/DSC analysis of Mn(II)-TA was performed with a STA 6000 thermal analyzer (Perkin Elmer, Waltham, MA, USA). Acid and complex samples (tannic acid: 4.67 mg; complex: 5.24 mg) were heated in ceramic crucibles at 30–995°C under air atmosphere at 10°C/min. The results were processed in the Pyris program.

The infrared spectra (FT-IR) of TA and Mn(II)-TA were recorded using FT-IR Alfa Bruker spectrophotometer, using two methods: KBr pellet pressing and ATR (Attenuated Total Reflectance) accessory equipped with a diamond crystal. The spectra were recorded in the range of 4000–600 cm^{-1} with resolution 2 cm^{-1}, using the OPUS software. The spectra analysis was performed with the SpecViewer program distributed by ACD/Labs.

To determine the Mn(II):TA molar ratio in aqueous solution the spectrophotometric mole-ratio method was applied. 1 cm^3 of TA solution with a concentration of 10^{-4} mol/dm^3, prepared in Tris-HCl buffer (pH = 7.4; 0.01 mol/dm^3) was transferred to 18 volumetric flasks with a capacity of 10 cm^3. Next, appropriate volume of $MnCl_2$ (C = 10^{-3} mol/dm^3, in Tris-HCl solution pH = 7.4, C = 0.01 mol/dm^3), and then made up to 10 cm^3 with Tris-HCl buffer. Finally, the concentration of $MnCl_2$ was in the range of 0.001 mol/dm^3. The flask was mixed and after 1h the absorbance of successive series of solutions was measured (at a wavelength of 276 nm). All experiments were done in five repetitions in three independent experiments.

In order to test the antioxidant properties of the Mn(II)-TA the spectrophotometric DPPH (2,2-diphenyl-1-picrylhydrazyl radical) assay was employed. A working solution of $DPPH^{\bullet}$ (2,2-diphenyl-1-picrylhydrazyl radical) with a concentration of C = 60 μmol/dm^3 was prepared. In a series of test tubes, 2 cm^3 of the DPPH solution and 1 cm^3 of tested substance (in appropriate concentrations; the initial C = 10 μmol/dm^3) were mixed and incubated in the dark for 1h at room temperature. Then, the absorbance of the solutions was measured at the wavelength λ = 516 nm against a blank. The control sample was the mixture of 2 cm^3 DPPH solution and 1 cm^3 of Tris-HCl (pH = 7.4; C = 0.01 mol/dm^3). The antioxidant activity of the substances was presented as the percentage of inhibition of the $DPPH^{\bullet}$ radical (% Inh) based on formula 1:

$$\%Inh = \left(\frac{A_{control} - A_{sample}}{A_{control}} \right) \cdot 100\% \quad (1)$$

where: *%Inh* – the percentage of inhibition of the DPPH$^{\bullet}$ radical, $A_{control}$ – absorbance of the control sample, A_{sample} – absorbance of the test sample.

The statistical analysis of the obtained results was developed in an Excel spreadsheet based on five absorbance measurements in three independent experiments. Statistical analysis was performed by Student's t-test at 5% probability.

Results

The registered spectra of TA and Mn(II)-TA proved the formation of manganese complexes with tannic acid in solid state. Based on data from the literature [10; 11] the bands present in the FT-IR spectra of TA and Mn(II)-TA were assigned (Figure 2, Table 2).

TAB. 2. The values of the wavenumbers [cm^{-1}], the intensities and the assignment of bands from the FT-IR spectra of tannic acid (TA) and its complex with manganese(II) (Mn(II)-TA)

TA		Mn(II)-TA		Assignment
IR_{KBr}	IR_{ATR}	IR_{KBr}	IR_{ATR}	
3418 vs	3387 w	3419 vs	3337 w	ν(OH)
3302 s	–	–	–	ν(OH)
3231 s	–	–	–	ν(OH)
2972 m	–	2959 m	–	ν(OH))
2926 m	–	2925 m	2935 w	ν(OH)
2854 m	–	2854 m	2872 w	ν(C–H)
–	2363 vw	–	–	ν(C–H)
–	2336 vw	–	2341 w	ν(C–H)
1722 s	1708 m	1714 m	–	ν(C = O)
1660 m		–	1654 w	ν(C = O)
1613 s	1610 m	1616 m	1606 w	ν(C = C)
1547 w	1534 w	–	–	β(OH)
1537 m	1516 w	1535 w	1508 w	β(OH)
1448 s	1448 m	1449 m	1455 w	β(C–C)
1382 s	–	1381 m	1375 w	β(OH)
1346 s	–	1348 m	–	β(OH)
1324 s	1316 s	1327 m	1296 w	β(OH)
1201 VS	1197 vs	1201 s	1171 m	β(C–H)
1031 S	1027 s	1033 m	–	β(C–H)
971 W	952 w	968 w	942 vw	β(C–H)
870 W	873 w	871 vw	–	γ(OH)

TA		Mn(II)-TA		Assignment
IR_{KBr}	IR_{ATR}	IR_{KBr}	IR_{ATR}	
824 VW	814 w	–	836 w	γ(OH)
758 M	756 m	758 w	754 w	γ(OH)
739 W	–	–	–	γ(OH)
667 W	686 m	–	–	γ(OH)
652 W	640 m	–	646 m	γ(OH)
589 W	613 m	595 w	–	γ(OH)

*symbols denote: ν – stretching vibrations, β – deforming in-plane vibrations, γ – out-of-plane deformation vibrations; intensity: m – medium, s – strong, vs – very strong.

SOURCE: own elaboration

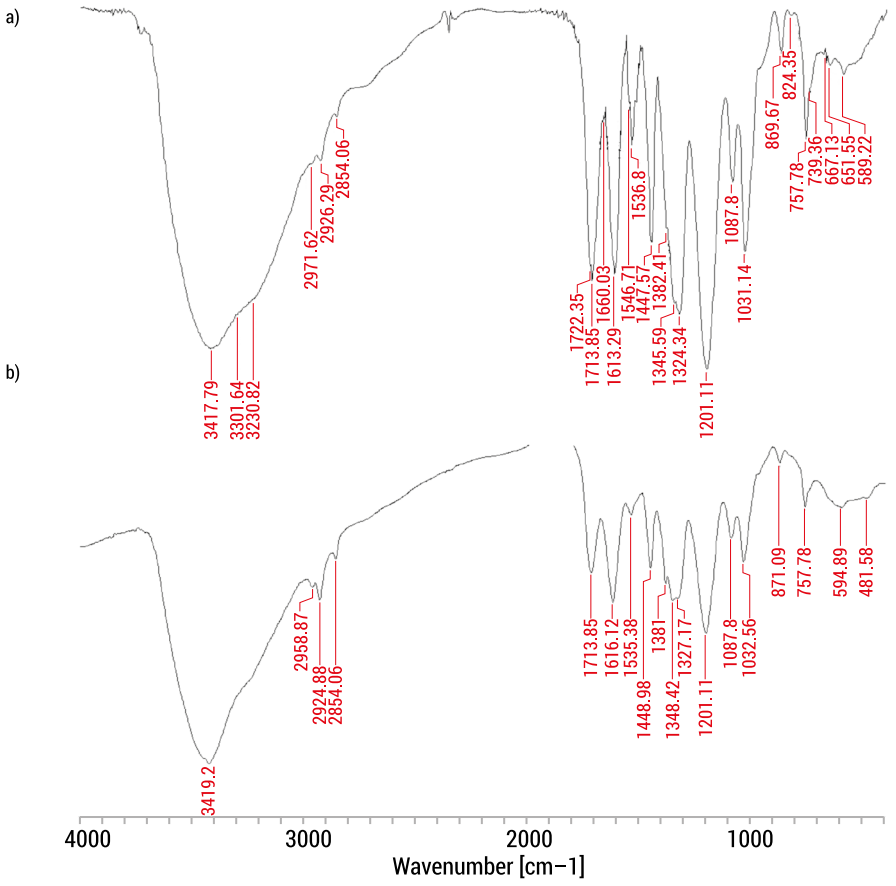

FIG. 2. Infrared spectra recorded by pressing a KBr pellet in the range of 400–4000 cm^{-1} for: (a) tannic acid, (b) manganese (II) complex with tannic acid

SOURCE: own elaboration

In the FT-IR spectra of the complex (compared to the spectra of TA) the following changes were noticed: (a) disappearance of the bands derived from the stretching vibrations of the hydroxyl groups ν(OH) at 3302 and 3231 cm^{-1}, (b) shift towards lower or higher wavenumbers of the bands assigned to the stretching vibrations of the carbonyl groups ν(C = O) at ~1722, 1660 and 1613 cm^{-1}, (c) disappearance of the band assigned to deformations in the plane of the β(OH) hydroxyl groups at ~1547 cm^{-1}, (d) shift towards lower wavenumbers among bands assigned to the in plane deformations of β(OH) at ~1537, ~1324 cm^{-1}, and out of plane deformations of the hydroxyl groups γ(OH) in the range: 739–589 cm^{-1}. The above-mentioned changes in the spectra of Mn(II)-TA compared to the spectra of TA suggest that the formation of metal complexes takes place with the participation of hydroxyl groups of the aromatic ring and carbonyl groups of gallic acid subunits.

The curves below show the results of the thermal analysis of tannic acid (Figure 3) and its complex with manganese (II) (Figure 4).

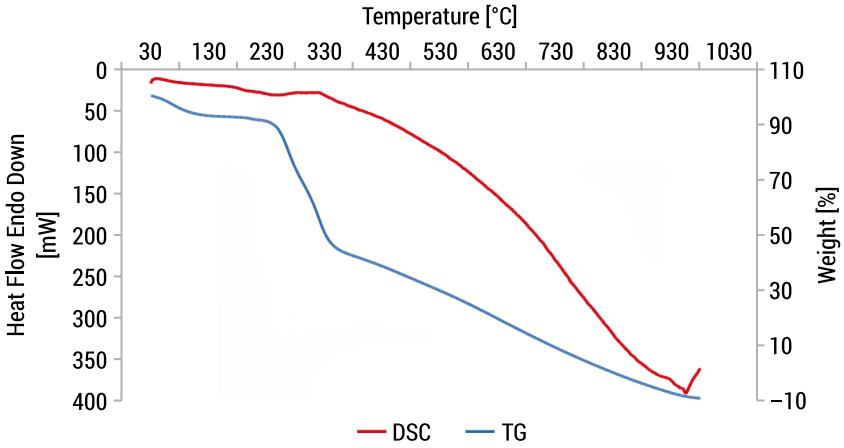

FIG. 3. TGA/DSC curves for thermal decomposition of TA (in air atmosphere)
SOURCE: own elaboration

Table 3 summarizes the characteristic steps of thermal decomposition (TGA curves) of TA and Mn(II)-TA. In the first stage of decomposition, the weight loss was observed, which for all analyzed compounds was similar (approx. 10%). This is attributed to the removal of small molecules such as H_2O, CO, CO_2, and phenol [15]. In the second stage, the greatest weight loss was observed in the case of TA rather than Mn(II)-TA. This can be attributed to the depolymerization, hydrolysis or partial degradation of the compounds [11;15]. However, the differences between the complex and the acid may result from the greater thermal stability of the complex [11]. The last stage was carried out in extremely high temperature ranges. As in the previous stage, the weight loss of TA was greater compared to Mn(II)-TA. This was due

to further decomposition of the samples. In the final step, a greater solid residue was observed for the complex rather than for the acid itself. This could be due to the presence of metal or its oxides [11;16].

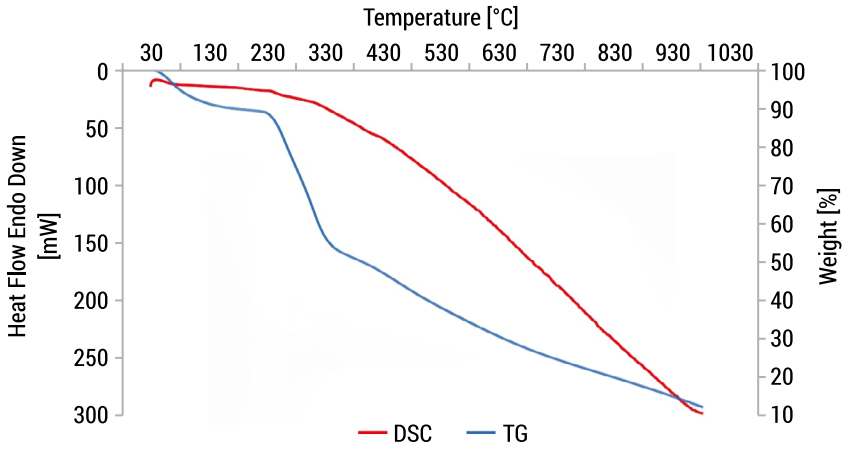

FIG. 4. TGA/DSC curves for thermal decomposition of Mn(II)-TA(II) (in air atmosphere)
SOURCE: own elaboration

TAB. 3. Summary of characteristic steps of thermal analysis (TGA/DSC curves) of tannic acid and its complex with manganese (II)

		Stage I	Stage II	Stage III
TA	Temperature range °C	0–183.33	183.33–400.60	400.60–829.07
	% by weight*	92.056	40.751	0.226
Mn(II)-TA	Temperature range °C	0–183.33	183.33–382.25	382.25–981.15
	% by weight*	89.315	50.549	11.895

*percentage of the compound, compared to the initial content (100%)

SOURCE: own elaboration

The composition of the complex Mn(II)-TA in aqueous solution was determined by the use of the spectrophotometric mole-ratio method. The result of the measurement is depicted in Figure 5.

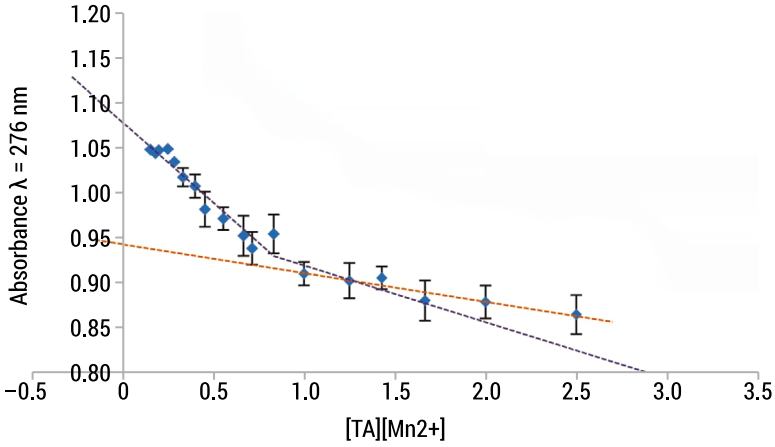

FIG. 5. Determination of composition of the Mn(II)-TA complex by a mole-ratio method (standard deviation were shown)

SOURCE: own elaboration

The above diagram shows that at pH = 7.4, the molar ratio of ligand (tannic acid) to metal (manganese (II)) is 1:1, which is confirmed in the literature [17].

Metal complexes of tannic acid can be present in various molar ratios. According to some authors, it depends on the pH of the reaction. For example, Iffat and colleagues studied complexes of tannic acid with iron (III). They found that at pH 3, 4 and 5, the metal : ligand molar ratio was 2:1, while at the higher pH (8 and 10), the ratio was 4:1 [18]. Erdem found that at pH 2.4 the molar ratio was 1:1, at pH 4.4 and 6.4–2:1, while at pH 8.4 the ratio was 4:1 [11]. In another work, the molar ratio of TA : iron ion (in the second and third oxidation stages) at different pH was investigated. It was found that at pH 9, the molar ratio of metal to ligand was 1:1 (for Fe (III) and 3:1 (for Fe (II)), while at pH 2.2 the ratio was 1:1 for both metals [4].

The antioxidant properties of studied compounds were established by the use of spectrophotometric DPPH assay. The relationship between the % inhibition of the DPPH$^{\bullet}$ radical and the concentration of Mn(II)-TA was shown in Figure 6. The IC_{50} parameter was determined (IC_{50} = 0.394 ± 0.027 μmol/dm^3), i.e. the concentration of Mn(II)-TA at which 50% of DPPH$^{\bullet}$ radical inhibition was obtained. The IC_{50} value for TA was determined in the same way [19] (Table 4). The results showed that uncomplexed tannic acid showed lower antioxidant activity against the DPPH$^{\bullet}$ radical than its complex with manganese(II).

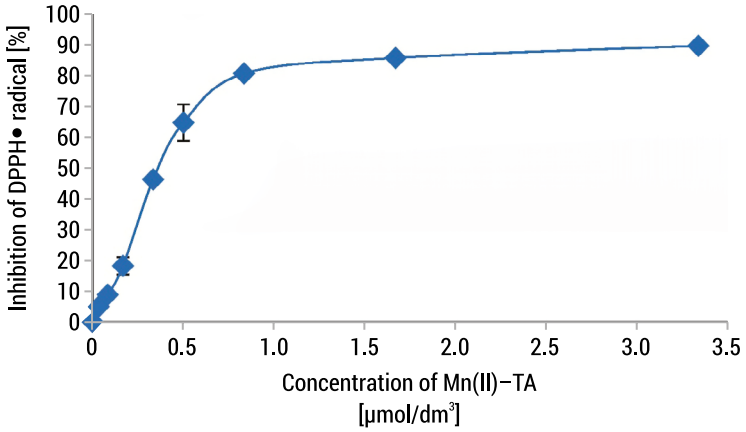

FIG. 6. The relationship between the % inhibition of the DPPH$^{\bullet}$ radical and the concentration of Mn(II)-TA (standard deviations were shown)

SOURCE: own elaboration

TAB. 4. Comparison of the IC_{50} parameter of tannic acid and its complex with manganese (II) (along with standard deviations)

Compound	IC_{50} [μmol/dm^3]
TA	0.533±0.042 [19]
Mn(II)-TA	0.394±0.027

SOURCE: own elaboration

Erdem investigated the activity of tannic acid and its complex with iron (III) using the DPPH method as well. He found that at the concentration of 50 μg/mL, tannic acid was active at the level of 82.82%. On the other hand, its iron complex showed a slightly lower activity, the value being 73.53% [11].

In the study of Costa [10], the antioxidant properties of tannic acid with zinc (II) and copper (II) were investigated. The reduced antioxidant activity of the complex comparing with TA molecule was observed. It was found that this is due to the coordination of metal ions with the hydroxyl groups of ligand. This type of coordination reduces the number of available hydrogen donors and reduces the antioxidant activity of metal complex compared to the uncomplexed molecule of TA [10].

Summary

The manganese(II) complex with tannic acid was successfully synthetized in the solid state and confirmed by FT-IR and thermal analysis. Hydroxyl groups of the aromatic ring and carbonyl groups of gallic acid moieties participate in the formation of the metal

complex. The TGA/DSC analysis showed higher thermal stability of Mn(II)-TA compared to TA. The Mn(II)-TA complex was stable in an aqueous solution at pH = 7.4. The ratio of ligand (TA) : metal ion (Mn^{2+}) (pH = 7.4) in the solution was 1:1. Mn(II)-TA showed high antioxidant activity in DPPH assay. The antioxidant activity of the complex was higher than the ligand (TA) alone (IC_{50} = 0.394±0.027 μmol/dm^3 for Mn(II)-TA and IC_{50} = 0.533±0.042 μmol/dm^3 for TA). Mn(II)-TA is a potential new material with enhanced antioxidant activity compared to TA.

Funding: This work was financially supported by the National Science Centre, Poland, underthe research project number 2018/31/B/NZ7/03083.

Literature

[1] Lourenço S.C., Moldão-Martins M., Alves V.D., *Antioxidants of Natural Plant Origins: From Sources to Food Industry Applications.* Molecules 2019, 24(22), p. 4132.

[2] Haddad M., Roger G., Sasseville G., Nguyen P.T., Wiebe H., Van De Ven T., Bourgault S., Mousseau N., Ramassamy C., *Molecular Interactions of Tannic Acid with Proteins Associated with SARS-CoV-2 Infectivity.* International Journal of Molecular Sciences 2022, 23(5), p. 2643.

[3] Rahim M.A., Ejima H., Cho K.L., Kempe K., Müllner M., Best J.P., Caruso F., *Coordination-Driven Multistep Assembly of Metal–Polyphenol Films and Capsules.* Chem. Mater 2014, 26, p. 1645–1653.

[4] Fu Z., Chen R, Study *of Complexes of Tannic Acid with Fe(III) and Fe(II).* Hindawi Journal of Analytical Methods in Chemistry 2019, p. 1–6.

[5] Gülçin İ., Huyut Z., Elmastaş M., Aboul-Enein H.Y, *Radical scavenging and antioxidant activity of tannic acid*. Arabian Journal of Chemistry 2010, 3, p. 43–53.

[6] Koopmann A.K., Schuster C., Torres-Rodríguez J., Kain S., Pertl-Obermeyer H., Petutschnigg A., Hüsing N., *Tannin-Based Hybrid Materials and Their Applications: A Review.* Molecules 2020, 25(21), p. 4910.

[7] Kaczmarek B., *Tannic Acid with Antiviral and Antibacterial Activity as A Promising Component of Biomaterials—A Minireview. Materials* 2020, 13(14), p. 3224.

[8] Huang Q., Liu X., Zhao G., Hu T., Wang Y. *Potential and challenges of tannins as an alternative to in-feed antibiotics for farm animal production.* Anim. Nutr. 2018, 4, p. 137–150.

[9] Pizzi A., *Tannins: Prospectives and Actual Industrial Applications.* Biomolecules 2019, 9(344).

[10] Costa G.G., Brito C.S.M., Terezo A.J., Cardoso A.P., Ionashiro E.Y., de Siqueira A.B., *Preparation, Characterization and Antioxidant Evaluation of Cu(II) and Zn(II) Tannates.* Open Chemistry Journal 2018, 5, p. 158–171.

[11] Erdem P., *Synthesis, characterization and applications of polyphenol-Fe(III) complexes and tannic acid resin.* Dokuz Eylul University, Graduate School of Natural and Applied Sciences, 2013, Izmir.

[12] Choi J.M., Han J., Yoon B.S., Chung J.H., Shin D.B., Lee S.K., Hwang J.K, Ryang R., *Antioxidant Properties of Tannic Acid and its Inhibitory Effects on Paraquat-Induced Oxidative Stress in Mice*. Food Sci. Biotechnol. 2006, 15(5), p. 728–734.

[13] Lou, W., Chen, Y., Ma, H., Liang G., Liu B., *Antioxidant and α-amylase inhibitory activities of tannic acid*. J. Food Sci. Technol. 2018, 55, p. 3640–3646.

[14] Pulido R., Bravo L., Saura-Calixto F., *Antioxidant Activity of Dietary Polyphenols As Determined by a Modified Ferric Reducing/Antioxidant Power Assay*. J. Agric. Food Chem. 2000, 48, p. 3396–3402.

[15] Ahmad N., Alam M., Naushad M., Ansari A.A., Alrayes B.F., Alotaibe M.A., *Thermal decomposition and kinetic studies of tannic acid using model free-methods*. J. Chil. Chem. Soc. 2018, 63(1).

[16] Bielański A., *Podstawy chemii nieorganicznej* 2. Wydawnictwo naukowe PWN 2013, Warszawa.

[17] Hem J. D., *Reduction and Complexing of Manganese by Gallic Acids*. Geological survey water-supply paper 1965, p.1667.

[18] Iffat K., Fatima N., Maqsood Z., *Study of Complex Formation of Fe*(*III*) *with Tannic Acid*. Journal – Chemical Society of Pakistan 2005, 27(2), p. 174–177.

[19] Pawluczuk N., *Zastosowanie metod spektroskopowych w badaniach właściwości antyrodnikowych kwasu taninowego*. Praca dyplomowa magisterska 2021, Białystok.

Identification and prioritization of specific pollutants in Marmara Basin

Keywords: risk assessment, specific pollutants, water framework directive

Abstract: Long-term water management is at the core of the European Union's Water Framework Directive (WFD). "Good ecological and chemical status" is desired for surface, coastal, and transitional waters to protect human health, water resources, ecosystems, and biodiversity. Physically and chemically untainted water sources are essential for chemical quality. In contrast, each basin has its own specific pollution spectrum resulting from agricultural, industrial, and human factors. Determining the compounds that pose a risk to human health is crucial for later monitoring and risk assessment studies. 104 pollutants that could have originated from the industrial sectors in the Marmara basin in Turkey were found as part of this study. Due to the increasing number of chemicals, obtaining accurate monitoring data can be both difficult and costly. As a result, additional evaluation studies were conducted in the river basin to define the prioritization of substances with risk in the short, medium, and long term for the substances found in the basin. As a consequence of the prioritizing evaluation using the TSH/TIS/COMPS model for 104 pollutants on the specific pollutant list, chemicals with a significant impact on the aquatic environment have been identified. The highlighted substances are among the contaminants that must be monitored in the basin and for which immediate action must be taken.

Introduction

River Basin Management Plan concepts are covered under the Water Framework Directive of the European Union, which also establishes a time frame and program for EU member states to create management plans. The Water Framework Regulation

is an organizational directive regarding water. In terms of bringing together the legislation especially with regard to water directives, it is hoped that this legislation will serve as a single source of information for all of these different water directives and specific substances and pollution sources. Members of the European Union and candidate countries like Turkey are concerned about the implementation of the WFD in their country. The WFD is also seen as a significant tool for developing countries' water management strategies. However, a country's economic or environmental conditions may affect the approach utilized to implement the WFD [1–3].

The priority pollutant list specified in the "Surface Water Quality Management Regulation" was published by the Minister of Forestry and Water Management, Turkey on November 30, 2012. According to the EU directive published in 2013, additional pollutants have been added and monitoring is recommended. Priority pollutant monitoring occurs 13 times a year, or every four weeks. It is also recommended to monitor additional pollutants determined by taking into account the country's needs, and method development studies are carried out in this regard. The frequency of WFD monitoring of specific pollutants has been established to be once every three months and four times per year. In this context, it is important to monitor the compounds in this class in surface waters at the prescribed frequency, to give the EQS values produced at the national or river basin scale for these substances, and to put into effect the steps to be taken. Every six years, member states are required by the WFD to look at specific pollutants and EQS levels. This is also the time when river basin management plans are updated.

Turkey's Ministry of Agriculture and Forestry conducted a number of projects to detect specific contaminants, which were all financed by the European Union. Potential contaminants were compiled based on the results of field investigations, surveys, and literature reviews, among many other sources. Using point sources, primarily industrial activities, capacity reports of substances, which are produced or imported at a rate of up to 1 ton per year, and non-point sources, such as pesticides that have been detected in the river basin or are widely used in Turkey, a list of specific pollutants was created [3–5]. As a result of multiple evaluations, thousands of different pollutants have been included in the list of possible specific pollutants that may exist in the river basins. Therefore, prioritization is needed to evaluate specific pollutants among the candidate chemicals.

Specific pollutants in Turkey

Despite the lack of a generally accepted method for the substances' list, Member States prioritize specific contaminants using a two-tiered system [3]. In Turkey, the first stage was to create a professional and legally specific pollutant list after the assessment of the candidate pollutants. The elimination approach is used in the second step to evaluate specific pollutants among the candidate chemicals.

The selection of the most hazardous pollutants to monitor in Turkey's river basins was carried out using the combined monitoring-based and modelling-based priority setting scheme (COMMPS) [6] and Total Hazard Scoring (THS) methods [7], as well as risk code, expert assessment, and bioaccumulation characteristics of substances, and a national specific pollutant list. Due to the evaluations, the final specific contaminant list decreased from 3762 to 250 pollutants [4,5].

Methods for categorization of specific pollutants

A database has been created for prioritization along with the determination of priority methodologies. An evaluation should be made of the list formed. This evaluation can be made according to the short, medium, and long terms. A risk assessment has also been conducted for each individual chemical. In the short-term evaluation, chemicals that require immediate action are included. Medium and long-term plans can be considered for four and eight years, respectively. Besides, pollutants can be categorized according to their detection (category A) and non-detection (category B) at monitoring points or detection in the receiving environment (category C). Another category C is made according to the risk group of the pollutant. If a manufacturing capacity report of the substance has information about the amount of use, the "Combined Monitoring-Based and Modeling-Based Priority Setting" (COMMPS) method can be applied. If this information is not available, elimination is possible using the Total Hazard Score (THS) and Total Impact Score (TIS) methods [6,7]. If the chemical is in the low-risk group, it is evaluated in the other category D. According to expert opinion, chemicals in these categories can be given more importance [4–7].

Prioritization for monitoring of specific pollutants

An additional assessment within the river basin is required for the prioritization of substances. It is suggested that point pollution sources operating in the basin be examined in the short, medium, and long term based on industrial capacity reports, since each basin contains a significant number of pollutants. This allows professionals to detect contaminants that require quick attention in order to continue monitoring program activities. Chemical properties of substances (molecular weight, water resolution, Henry constant), toxicity data (Risk Codes, LC50, EC50, NOEC, PNEC) for risk assessment, Resistance/permanence data (semi-life, degradation/hydraulics), and bioaccumulation features (logKow, BCF) are needed.

Total Hazard Score (THS) is the evaluation of the chemical (pollutant) in terms of dangerousness. The total dangerousness score of the pollutant is determined

according to the pollutant's resistance score (P), bioaccumulation score (B), toxicity score (T) and endocrine disrupting property score (ED). The score is calculated according to the specified formula. Total Hazards Score = P + T + B + ED. After entering all of the information into the appropriate fields, the stated formula is used to get the final score. One point is added to the overall danger score if the chemical is both highly resistant and bioaccumulating. As a result, the pollutant's score is calculated. An environmental pollutant's Total Hazard Value indicates whether or not it is likely to cause harm. The scale ranges from zero to four and assigns each pollutant a value between zero (low impact) and four (high impact).

As part of the chemical hazard evaluation, an exposure assessment is done using the Total Impact Score (TIS). To compute the overall effect value, the environmental impact of the chemical and the potential for exposure must be taken into account. The toxicity (LC50/EC50) and bioaccumulation concentration (BCF) data are used to estimate the environmental impact of the chemical. Henry's coefficients and half-life data are used to determine the chemical's potential for exposure. Exposure potential multiplied by Environmental Impact is known as Total Impact Score. There are three categories of pollutants: low effect (1–20), medium impact (21–60), and high impact (61–100) based on the Total Impact Score. Risk scoring is done using the THS and TIS, and chemicals with a high-risk score are added to the pollutant list. The model, the chemical substance, and a pollutant list must all be considered in risk scoring.

When using the COMMPS approach, chemicals are prioritized according to their danger, exposure risk, and annual quantity. The COMMPS approach may be used to prioritize or remove compounds with an annual production volume more than 1 tons/year, and risk assessments are also available. The COMMPS model expresses the capability of risk rating for substances via capacity reports.

The chemical characteristics of the parameters, toxicity data, Resistivity/Persistence data, bioaccumulation properties are required for risk assessment. The contaminants' exposure and effect scores are calculated based on this information. Emission, dispersion, and degradation characteristics are all taken into account when calculating an exposure score. Toxicity, logKow, and BCF are all factors in determining the impact score, as is the human effect (Risk Codes). The exposure and impact scores are multiplied to arrive at the COMMPS score. Once the COMMPS score is calculated, the pollutant status of the substance is determined. As a results, The COMMPS Score is derived from the multiplication of exposure score and impact score [4–7].

These results represent potential hazards to human health and the environment, particularly loss of life and property. In addition, substances are registered under the Registration, Evaluation, Authorization, and Restriction of Chemicals System (REACH), which is currently used in Europe to regulate chemicals, notably those categorized as R50-R53, R51-R53, etc. REACH is the European Union's principal legislation for evaluating chemical risk while safeguarding human health and the environment.

It is recommended to evaluate pollutants in terms of risk codes. Pollutants with a risk code of R50-53 are extremely harmful to the water environment and will have long-term adverse effects.

Study area: Marmara Basin in Turkey

The Marmara Basin covers a total area of 2,308,464 hectares, which includes artificial areas, agricultural areas, forest and semi-natural regions, wet areas, and water surfaces. There are heavily industrial areas in the basin. Industrial facilities in the basin area produce plastic, textiles, fibers and marble as well as chemicals, frozen food, paper, packaging and automobile spare parts. Another important pollutant source in the basin is agriculture. The number of companies by sectors is provided in Table 1.

TAB. 1. Number of sectors in the basin

Sectors	Total	Sectors	Total
Textile	267	Construction	4
Automotive	184	Marble, Mine, Ceramic	10
Food	225	Non-Ferrous Metal Industry	141
Wine And Olive Industry	180	Paint And Varnish	93
Leather	170	Iron And Steel	114
Chemical	251	Medicine	122
Energy	1	Metal Production	65
Paper	2	Agrochemical	38
Plastic	13		

SOURCE: own elaboration

Industrial sector codes (The standard European nomenclature of productive economic activities – NACE) that are the most active and pressure on the Marmara basin water masses are 15.11, 13.30, 29.10, 20.30, 17.21, 20.13, 24.10, 24.54, 24.45, 22.21, 22.22, and 22.29. The sector codes in the basin according to the industrial sector groups are given in Table 2.

TAB. 2. Industrial sector codes and group name in the basin

NACE	Professional Group Name
15.11	Leather Clothing and Leather Accessories
13.30	Ready-Made Garment Materials and Machines

NACE	Professional Group Name
29.10	The Manufacture Wholesale and Retail Sales of The Spare Parts of Automobiles and Other Transportation Vehicles
20.30	Construction Materials
17.21	Paper And Packaging
20.13	Chemicals, Agricultural Pesticide and Fertilisers
24.10; 24.45;24.54	Iron, Steel, Aluminum and Smelting
22.21;22.22;22.29	Plastics

SOURCE: own elaboration

After the studies, the number of possible contaminants present in the basin were evaluated as 104 (Table 3).

TAB. 3. Specific pollutants in the basin

Chemical name	CAS no	Chemical name	CAS no
Perchloroethylene (PER) (=Tetrachloroethylene)	127–18–4	Triphenyltin; Fentin	668–34–8
Biphenyl	92–52–4	Propetamphos	31218–83–4
Benzyl benzoate	120–51–4	1,1,2,2-Tetrachloroethane	79–34–5
Styrene; Vinylbenzene	100–42–5	3,4-dichloroaniline	95–76–1
Bis(2-ethylhexyl) terephthalate; Dioctyl terephthalate (DOTP)	6422–86–2	Benzo(a)fluoren	238–84–6
n-hexane	110–54–3	4-Chlorotoluene	106–43–4
2-[2-[2-[2-(4-nonylphenoxy) ethoxy]ethoxy]ethoxy]ethanol	7311–27–5	4-Chlorophenol	106–48–9
Chlorothalonil	1897–45–6	1,2-Dichlorobenzene	95–50–1
Dibutyltin oxide	818–08–6	m-xylene	108–38–3
Diphenylamine	122–39–4	Arsenic	7440–38–2
Triclosan; 2,4,4'-trichloro-2'-hydroxy-diphenyl-ether; 5-chloro-2-(2,4-dichlorophenoxy)phenol	3380–34–5	Zinc	7440–66–6
Diazinon	333–41–5	Copper	7440–50–8
Benzothiazole-2-thiol; 2-Mercaptobenzothiazole (MBT)	149–30–4	Chromium	7440–47–3
Dioctyl phthalate; DnOP	117–84–0	Antimony	7440–36–0
Imidazolidine-2-thione; Ethylenethiourea (ETU)	96–45–7	Kalay	7440–31–5
1,2,4-trimethylbenzene	95–63–6	Boron	7440–42–8

Chemical name	CAS no	Chemical name	CAS no
Mesitylene; 1,3,5-trimethylbenzene	108–67–8	Cobalt	7440–48–4
Diphenyl ether; Diphenyl oxide	101–84–8	Silver	7440–22–4
Benzododecinium chloride	139–07–1	Iron	7439–89–6
BBP; Benzylbutylphthalate	85–68–7	Aluminium	7429–90–5
Ethylenediamine Tetra Acetic Acid (EDTA)	60–00–4	Crom+6	18540–29–9
1,1'-isopropylidenebis(p-phenyleneoxy)dipropan-2-ol	116–37–0	Titanium	7440–32–6
2,2-dibromo-2-cyanoacetamide	10222–01–2	Barium	7440–39–3
4,5-dichloro-2-octyl-2H-isothiazol-3-on; DCOIT	64359–81–5	Vanadium	7440–62–2
Tributyl phosphate	126–73–8	Ammonia	n.a
1-Methylnaphthalene	90–12–0	Total petroleum hydrocarbons (TPH)	n.a.
Dibutylphthalate (DBP)	84–74–2	Kjeldahl nitrogen	n.a.
2,6-xylenol; 2,6-dimethylphenol	576–26–1	Free Cyanide	57–12–5
Tris(nonylphenyl) phosphite; TNPP	26523–78–4	Oil-grease	n.a.
4-Chloro-3-methylphenol; Parachlorometacresol	59–50–7	Total Phosphorus	n.a.
Propylbenzene	103–65–1	Suspended solid matter (SS)	n.a.
1,4-Dichlorobenzene	106–46–7	Chemical Oxygen Demand (COD)	n.a.
Tetrabromobisphenol A (TBBP-A)	79–94–7	Total cyanide	n.a.
o-xylene	95–47–6	Ammonium Nitrogen	n.a.
p-(1,1-dimethylpropyl)phenol; p-(tert-amyl)phenol	80–46–6	Polychlorinated biphenyls (PCBs) (PCB 28, PCB 31, PCB 52, PCB 101, PCB 118, PCB 138, PCB 153, PCB 180)	1336–36–3
Permethrin	52645–53–1	Polyaromatic Hydrocarbons (PAHs) (Acenaphthene; Acenaphthylene; Benzo(a) anthracene; Chrysene; Dibenzo(a,h)anthracene; Fluorene; Phenantherene; Pyrene)	n.a.
Propanenitrile, 3-[(2-acetoxyethyl) [4-[(2-chloro-4-nitrophenyl)azo] phenyl]amino]-	6021–61–0	2-kloro-N-(etoksimetil)-N-(2-etil-6-metilfenil)asetamid; Acetachlor	34256–82–1
2,4,6-tri-tert-butylphenol	732–26–3	Bromide	7726–95–6
Isopropylbenzene; cumene	98–82–8	1.2-Diklor-4-nitrobenzen	99–54–7

Chemical name	CAS no	Chemical name	CAS no
Chlorobenzene	108–90–7	Carbon tetrachloride	56–23–5
4,4'-DDD	72–54–8	Trichloroethylene	79–01–6
Perylene	198–55–0	Silicon	7440–21–3
DDT	50–29–3	2,4-Dichlorophenol	120–83–2
Dieldrin	60–57–1	2,2'-dimethyl-4,4'-methylenebis(cyclohexylamine)	6864–37–5
2-Amino-4-chlorophenol	95–85–2	2(3)-Tert-butyl-4-methoxyphenol	25013–16–5
Endrin	72–20–8	2,2'-dichloro-4,4'-methylenedianiline	101–14–4
N,N,N',N'-tetramethyl-4,4'-methylenedianiline	101–61–1	Benzo(e)pyrene	192–97–2
2-Chloronaphthalene	91–58–7	1,3-Dichlorobenzene	541–73–1
Aldrin	309–00–2	Monobromodifenil eter; 4-bromodifenil eter	101–55–3
4-Chloroaniline	106–47–8	Diizobütil adipat	141–04–8
1-Chloro-2,4-dinitrobenzene	97–00–7	4,4'-Dibromodifenil eter	2050–47–7
4-Aminoazobenzene Aniline yellow	60–09–3	Tribromodiphenyl ether	49690–94–0

SOURCE: own elaboration

In total, the number of specific pollutants that may have an impact on the basin is considered to be 104 and the necessary elimination models have been applied. The prioritization study results showed the pollutants may be widely observed and it is recommended that they should be monitored in Marmara basin, according to a short-term assessment.

According to the prioritization evaluation using the THS/TIS/COMMPS model for 104 pollutants in the specific pollutant list, Perchloroethylene, Parachlorometacresol, Benzo(a)fluoren, Zinc, Copper, Chromium, Tin, Cobalt, Iron, Aluminum, Titanium, Total petroleum hydrocarbons, Polychlorinated biphenyls (PCBs) (PCB 28, PCB 31, PCB 52, PCB 101, PCB 118, PCB 138, PCB 153, PCB 180), Polyaromatic Hydrocarbons (PAHs) (Acenaphthene; Acenaphthylene; Benzo(a)anthracene; Chrysene; Dibenzo(a,h) anthracene; Fluorene; Phenantherene; Pyrene) substances have a very harmful effect on the aquatic environment. Therefore, they are among the pollutants that need to be monitored in the basin and this requires immediate action in the short term.

Summary

The WFD 2000/60/EC of the European Union establishes the strategic approach for dealing with chemically contaminated rivers. It aims at both the monitoring and detection of 45 priority pollutants and specific pollutants in surface waters. Increasing the number of chemicals to be monitored will prevent the process from being carried out properly. Since there is a very high concentration of pollutants in the basin, it is important to classify the pollutants that require urgent action in the short, medium, and long term, according to industry capacity reports. As a result, prioritization studies on the basin gain importance in terms of planning the monitoring of chemicals that require urgent action and reducing monitoring costs. It was determined that the COMMPS approach, THS and TIS were the best ways to prioritize and eliminate particular pollutants, respectively, in order to detect specific pollutants. The number of pollutants in the basin and a list of potential contaminants were both established using the prioritizing methods.

Literature

[1] European Commission, *Directive* 2000/60/*EC of the European Parliament and of the Council establishing a framework for Community action in the field of water policy*, available online: https://www.eea.europa.eu/policy-documents/directive-2000-60-ec-of (accessed on 06 December 2022).

[2] European Commission, *Strategies Against Chemical Pollution of Surface Waters,* available online: https://ec.europa.eu/environment/water/water-dangersub/candidate_list_1.htm (accessed on 06 December 2022).

[3] Cokay E., Eker S., Karapınar İ., Karaman Ş., *Implementation of Water Framework Directive in Turkey*, Turkish Journal of Scientific Reviews 2016, 9 (2), p. 6–10.

[4] Karahan Ozgun O., Basak B., Eropak C., Abat S., Kirim G., Girgin E., Hanedar A., Gunes E., Citil E., Görgün E., Gomec C.Y., Babuna F. G., Ovez S., Tanik A., Ozturk I., Kinaci C., Karaaslan Y., Gucver S. M., Siltu E., Orhon A. K., *Prioritization methodology of dangerous substances for water quality monitoring with scarce data*, In Clean Technologies and Environmental Policy 2016, 19(1), p. 105–122.

[5] Orhon A.K., *Methodology for the Development of Environmental Quality Standards for Hazardous Substances in Surface Waters*, T.R. Ministry of Forestry and Water Affairs, July 2015 (in Turkish).

[6] Klein W., Denzer S., Herrchen M., Lepper P., Müller M., Sehrt R., Strom A., Volmer, J., *Revised proposal for a list of priority substances in the context of the Water Framework Directive* (*COMMPS procedure*), Fraunhofer-Institut Umweltchemie und Ökotoxikologie, Schmallenberg, 1999.

[7] Daginnus K., Gottardo S., Payá-Pérez A., Whitehouse P., Wilkinson H., Zaldívar J., *A model-base prioritization exercise for the European Water Framework Directive*, Int. J. Environ. Res. Public Health 2011,8, p. 435–455.

Evaluating buildings and urban external layout green retrofitting to improve micro-climate conditions at district level

Keywords: sustainable retrofitting; ENVI-met; environmental redevelopment; residential buildings; green urban district

Abstract: In the context of sustainable cities and communities, to meet the European aim of a carbon-free economy by 2050 and to tackle current climate change, the retrofitting of Italian residential building stock as well as the green regeneration of urban districts is essential. The research aims at assessing the influence of some cooling strategies applied in a defined hypothetic but realistic urban grid located in 3 different Italian cities (Milan, Florence and Palermo) evaluating multistorey, tower and courtyard building types respectively. Using ENVI-met software several micro-climate parameters are evaluated. The most significant outcomes are related to the substitution of the current dark asphalt (reference case) with cool pavements as cool improvement strategy. This measure results in a reduction of external air temperature (~ 1.2°C). Additionally, the application of green façade technology on buildings noticeably impacts both the wall surface temperature (Milan, Florence and Palermo: reduction of around 10°C–12°C) and the wall energy balance with respect to traditional external wall configurations. For the city of Palermo the cool redevelopment measures results in a slight improvement in terms of microclimate parameters compared to other cities.

Introduction

According to the Enerdata report [1] in Europe buildings are responsible of 43% of final energy consumption and only 15% is satisfied by renewables [2]. Households account for 2/3 of this need for energy, equaling to about 240 Mtoe in 2019 [1]. At the Italian

level, residential building stock is nowadays aged and obsolete. This is because 25% of Italian houses were built before 1950 [3] without meeting any standards concerning energy saving or emissions reduction. According to the ENEA report of 2020 in Italy a total of 40% of primary energy demand is needed in fact for civilian use [3] and the households' energy consumption accounts for about 31 Mtoe (data from 2019) [4]. Twenty six percent of Italian residential building stock is classified as energy efficiency class lower than C (1.2 $EP_{gl,nren,rif,standard(2019/21)}$ reference building global energy performance index for non-renewable < global energy performance index for non-renewables $EP_{gl,nren}$ < 1.50 $EP_{gl,nren,rif,standard(2019/21)}$) [5]. Moreover, natural gas is always the main source (50%) for energy production while electricity accounts only for about 18% [4]. In fact, Carpino et al. [6] demonstrate through a survey of about 80 Italian families that 60% of heating systems of their apartments is characterized by a traditional gas boiler.

Lack of use of renewables for heating and cooling is not only an Italian issue. Due to climate change, Tootkaboni et al. [7] affirm that a significant increase of about 255.1% for cooling demand will occur in the near future for densely built existing residential districts. Zinzi et al. [8] mention a monitoring campaign in Rome (Italy), in line with previous cited research, which demonstrates that the urban environment and heat island effect noticeably influence the cooling demand of existing residential buildings. In this context, retrofitting of Italian residential building stock is essential to meet the European aim of a carbon-free economy by 2050, as well as increasing energy efficiency up to 32.50%, as called for by the European 2030 climate and energy framework.

Urban environment design and especially the use of effective cooling strategies (such as implementation of flowerbeds or cool pavements for the external neighborhood environment or introduction of trees etc.) can tackle climate change and the rise in external air temperature, avoiding an increase in energy needs during the summer season and overheating effects inside buildings. Moreover, some efficient cooling strategies to reduce the heat island effect can be applied also on buildings, on both green façades and roofs. In the literature, many studies demonstrate that a properly designed urban environment and appropriate micro-climate condition positively affect human comfort and wellbeing. For instance, Yldiz et al. [9] developed a model to demonstrate the relationship between the built urban environment (for instance in terms of providing open spaces, landscaping, sustainable pedestrian routes, layout of buildings and streets etc.) and social sustainability, highlighting that accessibility and quality of social life have the most weight (33%). Abdallah et al. [10] observed that cooling strategies applied in both deep and shallow canyons can improve the outdoor thermal comfort for people in terms of PET (Physiological Equivalent Temperature) for urban districts located in hot humid climates.

The research discussed in the chapter aims at assessing the influence of implementing both green roofs and façades (as retrofitting measures for existing residential buildings in urban districts) and some single external cooling strategies, as well

as a combination of them on micro-climate conditions at both building and urban level using ENVI-met software [11]. The main goal is providing useful indications for the designers to choose the most suitable and effective retrofitting strategy for green urban redevelopment interventions in the context of the European SDGs (Sustainable Development Goals) concerned with sustainable cities and communities.

State of the art

In the literature there are many studies concerning a systematic review on ENVI-met software to validate its use in the evaluation of some micro-climate parameters typical of the urban environment and affecting both users' external thermal comfort and building energy performance. For instance, Ouyang et al. [12] validate the performance of ENVI-MET software using full forcing meteorology and considering several thermal-radiative parameters (such as air temperature and mean radiant temperature). For validating the model, they perform in situ measurements for different kinds of scenarios. Crank et al. [13] tried to test the effectiveness of the software to calculate external air temperature in presence of urban mitigation strategies such as high albedo materials and trees. According to this study, Tsoka et al. [14] performed a systematic review to estimate the suitability of the ENVI-MET model to calculate changes in external air, surface and mean radiant temperature due to the use of urban greenery and cool materials for pavements. As regard to ENVI-MET validation, Perini et al. [15] performed a comparison between ENVI-MET and TRANSYS to evaluate the mean radiant temperature in a typical canyon between 2 row buildings, considering the insertion of trees. A reduction in mean radiant temperature equal to 20°C occurs as a result of the insertion of trees and the ENVI-MET software allows for the evaluation of the design of trees and their influence on humans' external comfort and wellbeing.

The air temperature parameter is one of the most evaluated to measure the possible reduction of the heat island effect. Liu et al. [16] with a detailed literature review affirm that the external air temperature is the most used and suitable parameter to evaluate human external wellbeing. They also advise to consider a parameter related to solar radiation and one concerning ventilation. Faragallah et al. [17] proposed the use of external cool pavements to reduce outdoor temperature and consequently the heat island effect during the summer season. They point out that this improvement is the most effective and a decrease in external air temperature by 3.5°C occurs. In line with previous researchers, to tackle climate change, Cortes et al. [18] propose a combination of three green retrofitted measures (increase in the number of trees, grass-covered areas and green roofs in buildings) that results in a reduction in external air temperature in a range between 0.5°C and 0.8°C for a zone characterized by warm summer.

In general, 52% of researchers considered the PET parameter to evaluate the level of humans' external comfort [19] but also the evaluation of the mean radiant temperature is frequently performed as well. In regard to PET, Karimimoshaver et al. [19] point out that for an urban context both the buildings height (H) and the distance between buildings in the urban district (W) affect external micro-climate parameters. An increase in the ratio H/W results in a decrease in PET. For instance, they conclude that if the H/W parameter varies in a range between 1 and 1.5 the PET drops by about 2°C. In line with that, Wai et al. [20] highlight that a decrease in heat-stress at pedestrian level can be obtained by the reduction of buildings length and minor density.

Finally, in regard to the integration of active strategies to produce energy from renewable sources, Vassiliades et al. [21] perform studies dealing with the influence on urban thermal comfort with the possible installation of photovoltaic (PV) systems on urban factories. They compare the solution with and without the active strategy in terms of PET. They point out that in the spring season with the installation of a PV system there is a reduction of the thermal stresses and so an improvement in pedestrians' comfort.

Methodology

The methodology to assess the possible configuration for a green redeveloped urban district or a new one is the following:

- Identification of a possible typical scheme of an Italian urban district. An urban grid of 80 m X 80 m was outlined in ENVI-met spaces and located in Milan, Florence and Palermo that belongs to 3 different Italian climate zones. Milan is located in northern Italy; it is characterized by subcontinental climate and 2404 Heating Degree Days (HDD). Florence is sited in central Italy and the climate is a temperate and sub-coastal climate with 1415 HDD. Finally, Palermo, located in southern Italy, has 751 HDD with a Mediterranean climate characterized by hot and arid summers. For each location, the maximum outdoor air temperature registered for the simulation day selected (14th of July) was assumed at 31°C, 36°C and 37°C respectively. The district configuration is assumed as invariant.
- Definition of 3 different residential building types to be introduced into the delineated urban grid: multistorey, tower and courtyard buildings. (Figure 1). For the multistorey buildings a configuration characterized by lower density (Figure 1) is considered to evaluate the influence of distance between buildings on the external micro-climate parameters.

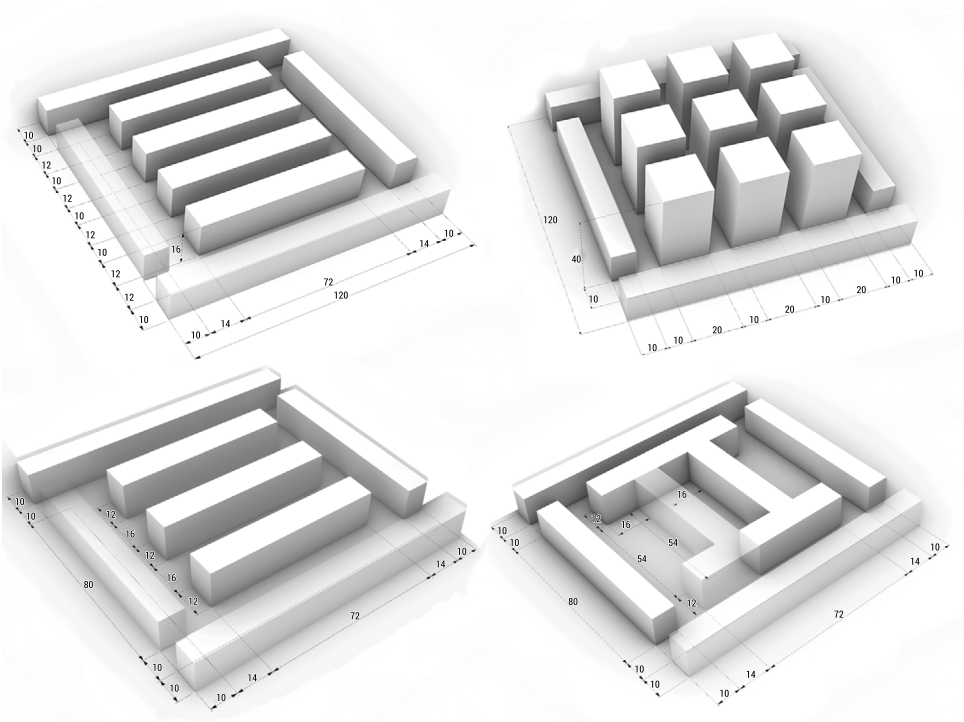

FIG. 1. Sketch of the 4 considered urban layouts for simulation tasks
SOURCE: own elaboration

- Outlining of different cooling strategies at both buildings and urban level. For the former, the use of vertical greenery for South oriented walls combined with green roof technological solutions is proposed. Green façades for buildings are used in different configurations with changing degrees of greening: for multistorey buildings 20%, 30% and 50% of greenery with respect to the total southern wall surface are investigated while for tower buildings only 50% of greenery is considered characterized by a height of 10 m and 30 m.

Various green urban strategies are evaluated in the different configurations of the outlined typical urban district considering the 3 residential building types (Table 1). In the initial solution, asphalt pavement for the whole urban grid surface is considered.

TAB. 1. Characteristics of Green Strategies considered the different residential building types. In the table below the percentages refer to the whole surface of the considered urban grid without buildings. The low-density configuration obviously permits more trees to be included in the urban grid

Green Strategy	Residential building type			
	High density Multistorey	Low density Multistorey	Tower*	Courtyard**
Flowerbeds [%]: grass 25 cm thick	46.7%	47%	31.5%	57%
Flowerbeds and trees [number of trees]: rancho trees 8.63 m height	56	150	58	120
Cool pavements [%]: concrete pavement light	100%	100%	100%	100%

*For tower buildings due to the high density of the built environment the same number of trees are provided but the flowerbeds are lower.

**For courtyard buildings the number of trees is higher because of the shape of the building and to overcome the decrease in flowerbeds.

SOURCE: own elaboration

In Table 2 the main characteristics of the different kind of pavement for both the base solution and the cool one is defined.

TAB. 2. Main characteristics of reference case pavement (asphalt road) and cool pavement (concrete pavement light)

Pavement	Albedo	Emissivity
Asphalt road	0.20	0.90
Concrete pavement light	0.80	0.90

SOURCE: own elaboration

- Evaluation of different micro-climate parameters with respect to the different strategies modeled: external air temperature, relative humidity (RH), wall surface temperature, external temperature outside the wall and energy balance (last 3 only for greenery strategy).

For ENVI-met set up, the climate files created by Italian CTI (Italian Thermotechnical Committee) referencing the different cities are used. In addition to the nesting grids already set up by the software (5 grids), 3 empty grid rows (6 m) are added on each side of the model area to avoid errors related to uncertainties in boundary conditions. The buildings are modeled according to typological features widely spread in the Italian context, in terms of geometry and envelope characteristics (Table 3).

TAB. 3. Main characteristics of the materials used for the different technological solutions

Exiting external wall					
Material	**Thickness [m]**	**Conductivity [W/mK]**	**Specific Heat [J/kgK]**	**Absorption [%]**	**Reflection [%]**
Bricks – plaster	0.12	0.84	829.84	42	45
Air	0.08	0.03	1006.00	–	–
Aerated bricks	0.08	0.30	840.00	–	–
Green façade					
Material	**Thickness [m]**	**Emissivity**	**Conductivity [W/mK]**	**Transmittance [W/m^{2}K]**	**Albedo**
Greening	0.10	–	–	0.30	0.20
Substrate – Sandy loam	0.05	0.98	–	–	0.20
Styrofoam	0.01	–	0.10 W/mK	–	–
Air gap	0.08	–	–	–	–
Existing roof					
Material	**Thickness [m]**	**Conductivity [W/mK]**	**Specific Heat [J/kgK]**	**Absorption [%]**	**Reflection [%]**
Roofing tiles	0.02	0.84	800.00	50	50
Insulation	0.08	0.07	1500.00	–	–
Reinforced bricks	0.24	1.10	840	–	–
Green roof					
Material	**Thickness [m]**	**Emissivity**	**Conductivity [W/mK]**	**Transmittance [W/m^{2}K]**	**Albedo**
Greening	0.10	–	–	0.30	0.20
Substrate – Sandy loam	0.15	0.98	–	–	0.20
Styrofoam	0.08	–	0.10	–	–

SOURCE: own elaboration

Results and discussion

ENVI-met performed the analysis for over 2400 points in the meshed analysis grid considering 4 hours (10:00 – 14:00) of 14th of July. The results reported in this section refer to noon. The graph in Figure 2 relates to the number of points [%]

and the corresponding value of external air temperature for the city of Florence and multistorey building types (high density). The results highlight that for the reference case, distinguished by the presence of dark asphalt for the whole external pavement, about 8% of points (highest and so representative value) are characterized by a temperature equal to 27.86°C. In this case the higher value of the external air temperature is calculated for the external points in the nesting grid where there are no shadows cast by buildings. This happens for all considered cooling strategies.

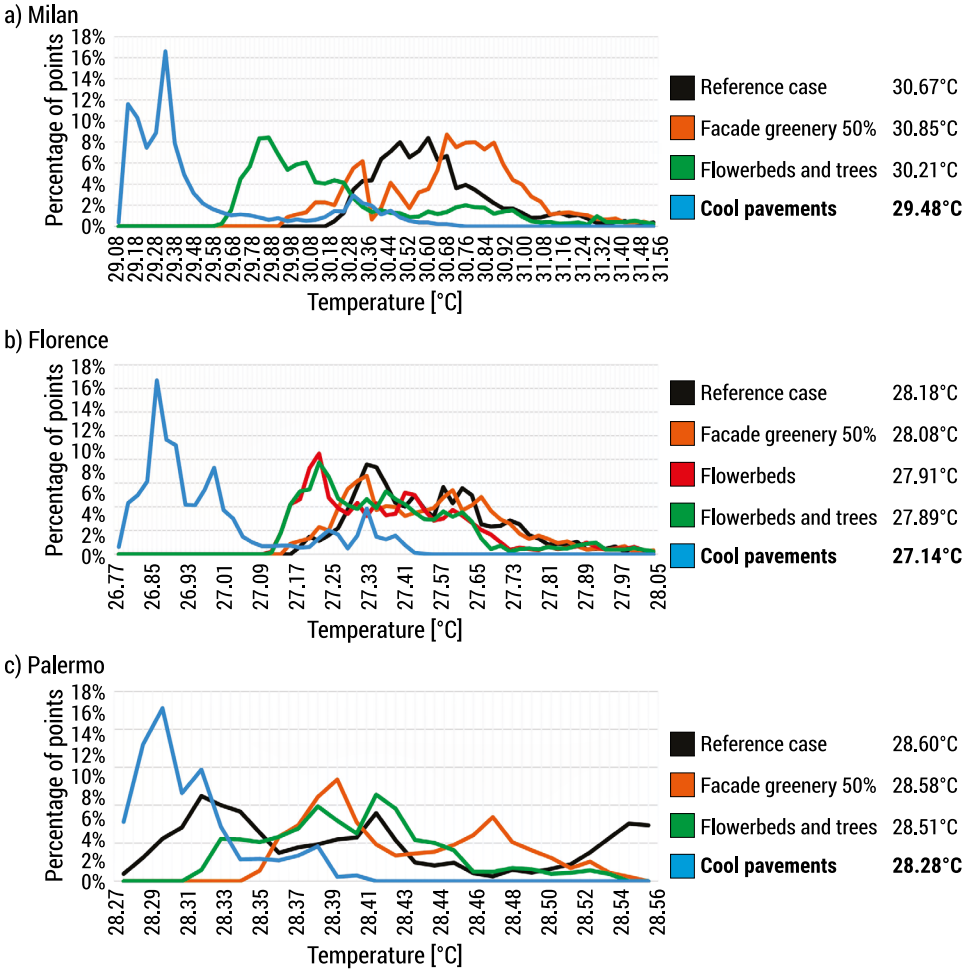

FIG. 2. Percentage of points with respect to the external air temperature considering different cities and different intervention scenario. On the right the average of the external air temperature for each analysed cooling strategy

SOURCE: own elaboration

The configurations with the presence of flowerbeds and the latter combined with trees do not result in a significant decrease in the average of external air temperature. In fact, about 8% of points are characterized by a temperature equal to 27.61°C with a slight reduction of 0.6°C with respect to the reference case. This is probably related to the evaluation point of the external air temperature fixed at 1.5 m (man-height to evaluate urban external comfort) while trees are about 9 m tall.

It is worth highlighting that the most significant result is related to the layout characterized by cool pavements. This solution is the most advantageous considering the external air temperature parameter. The decrease in the average external air temperature is equal to about 1°C and as previous graph shows (Figure 2) 15% of points (representative amount) have a temperature equal to 26.93°C. Consequently, a significant reduction of about 1.5°C occurs. Even according to literature [22] the use of cool pavements is the most advantageous cool strategy also with respect to the introduction of green flowerbeds. This should be analyzed and verified also in terms of CO_2 emissions.

As for the city of Florence and the city of Milan, the introduction of cool pavements is the most effective green strategies to reduce the average external air temperature by about 1°C. In this case, 16.6% of points is at a temperature equal to 29.3°C while in the reference case 8% of points is at 30.5°C. Furthermore, the cool pavements result in an increase in relative humidity by about 4%. Otherwise for the city of Florence there is a slight increase in RH (~ 0.6%) with cool pavement improvement strategy. It is worth to notice that in the case of Milan the use of the combination of flowerbeds and trees causes a higher reduction in external air temperature compared to Florence. The decrease in air temperature is about 0.6°C. In regard to the green façade the most significant result is related to the relative humidity that increased by about 1%.

Regarding the city of Palermo, it is worth to notice that green improvements only slightly influence the micro-climate parameters compared to the other 2 cities. For instance, the decrease in external air temperature with cool pavements is lower by 0.4°C even if most of the points (about 23%) are at 28.3°C. The same occurs for the relative humidity: the introduction of the green façade for southern orientated walls results in a low decrease of RH of about 0.4%.

In regards to the results concerning the variation of the relative humidity for the different cooling strategies adopted for the analysed urban grid, it is proved that the vertical greenery (50%) on the façade is the most influential (Figure 3). In fact, an increase in relative humidity of around 1.6% occurs with respect to the reference case (65.50% average of RH). This is probably due to the evapotranspiration of the green façade. The other cooling strategies are comparable in terms of the relative humidity parameter.

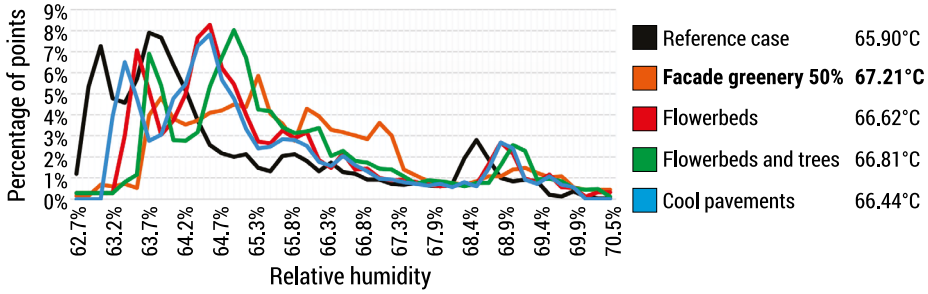

FIG. 3. Percentage of points included in the urban grid with respect to relative humidity considering the city of Florence and the high-density multistorey building types. On the right, the average relative humidity for each analysed cooling strategy is shown

SOURCE: own elaboration

Finally, as for low density multistorey buildings included in the grid, the results show that the increase in distance between buildings and the reduction in covered area significantly influences the value of relative humidity rather than external temperature. In fact, even if the temperature is lower than the high-density configuration, only a slight decrease occurs. In this configuration, relative humidity rises by 4% compared to the high-density grid. Compared to the other models, in this one the most advisable configuration for both temperature decrease and relative humidity increase is the redevelopment of the area with cool pavements.

Figure 4 shows the variation of the external air temperature in the outlined urban grid considering the different analyzed cooling strategies (on top of the figure) applied for the high density multistorey grids located in 3 cities (Florence, Milan and Palermo). For instance, regarding the city of Florence, this result confirms the previous results. In fact, in the last grid (Figure 4 on the right) characterized by cool pavements most of points are characterized by an average temperature below 26.91°C. This significant reduction in temperature by adopting a cool pavement redevelopment strategy occurs also for Milan (~ 1.2°C). For Palermo it is less noticeable, as specified before (~0.4°C).

It is important to highlight that the vertical greenery on façade (50%) does not significantly affect the value of external air temperature at the height of 1.5 m. Consequently, to evaluate the benefit of these buildings' redevelopment intervention, the surface temperature and other parameters deal with the buildings are considered.

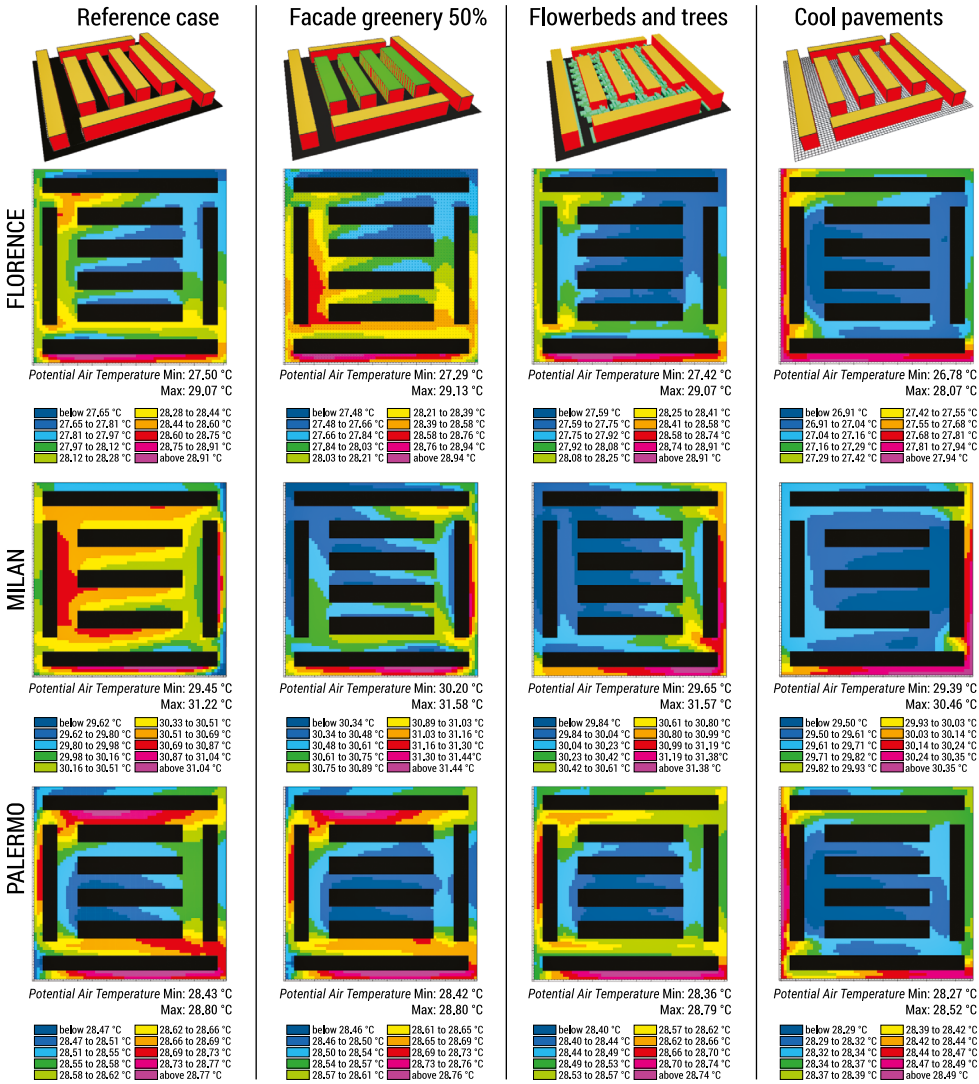

FIG. 4. Variation of external air temperature in the considered urban grid with the different cooling strategies and different locations

SOURCE: Own elaboration

Figure 5 illustrates the results related to the variation of the buildings' surface temperature (southern wall), the energy balance [W/m^2] with respect to incoming longwave radiation (LW_{in}) and outcoming (LW_{out}) by the southern wall and the external air temperature outside the wall, considering different possible locations.

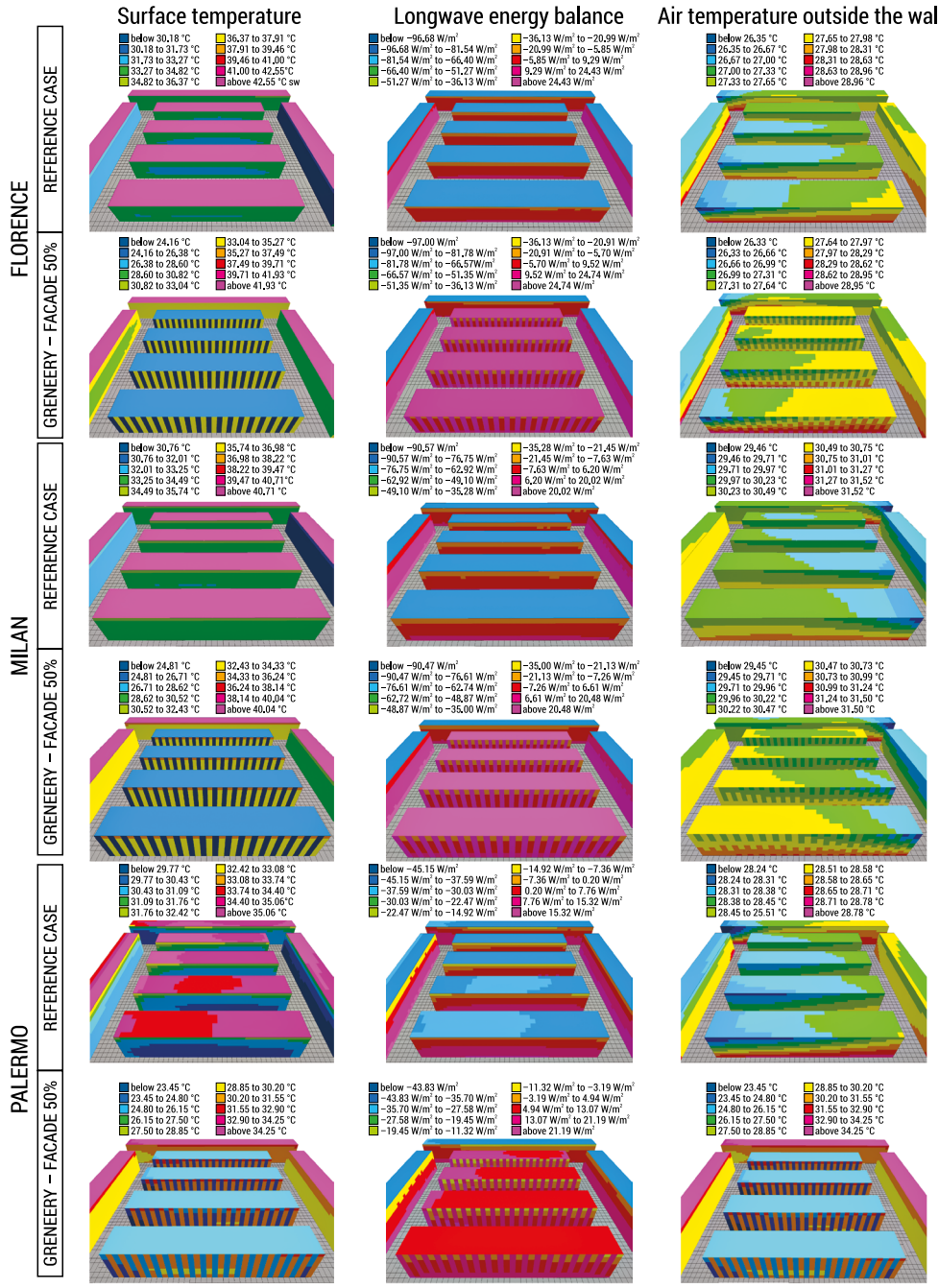

FIG. 5. Distribution of surface temperature [°C], longwave energy balance [W/m2] and air temperature outside the wall [°C] (southern) for both reference and vertical greenery at 50% cases in all cities considering multistorey buildings

SOURCE: own elaboration

For the city of Florence, regarding the southern wall surface temperature, green portions are characterized by a temperature of 22.26°C while for traditional façades it amounts to 34.31°C. At the same time, an observation related to the roof surface temperature is needed. In the central buildings, where the green roof technology is applied, the roof surface temperature varied between 26.53°C and 28.47°C. While for the other buildings, with traditional roof stratigraphy, the temperature significantly increases above 42°C. Both green façades and roofs inevitably affect the users' indoor thermal comfort and the buildings energy performance, especially considering cooling energy needs during the summer season.

As for energy balance, a significant decrease (~40 W/m^2) in the LW_{in} parameter occurs between green and traditional façades. The results show that the difference between LW_{in} (~414 W/m^2) and LW_{out} (~390 W/m^2) for a green façade is equal to about 24 W/m^2. It is worth to notice that if the southern wall total surface is considered (1152 m^2) a reduction in energy balance of about 14 kW occurs for 50% of green surface while for southern walls with 20% or 30% green surface, a slight decrease of around 5.5 kW and 8 kW happens respectively. Furthermore, if the variation of LW_{out} is considered along the wall height, the solution with green façade is less affected by variation of emitted radiation (~1 W/m^2). Finally with respect to the external air temperature outside the wall it is worth to notice that they are lower for a larger area considering vertical greenery at 50%.

As in Florence, as far as Milan is concerned, a significant decrease in wall surface temperature occurs, equal to 10°C. For the roof surface temperature, the same effect as in Florence occurs, and the value of roof surface temperature of both cities are comparable. With the green façade at 50% coverage, the incoming longwave radiation reduces to 22 W/m^2. This avoids 12672 W of incoming radiation when considering the whole southern façade surface. Another interesting result related to Milan deals with the energy balance, because with the introduction of a green façade at 50% there is a noticeable increase in building performance and the energy balance changes from –5 W/m^2 in the reference case, to 30.70 W/m^2 in the improved version. Compared to the reference case, Milan is the worst case compared to Florence and Palermo. Obviously, this result is affected by the choice of materials and the stratigraphy of the wall.

For Palermo, the most significant result is related to the value of the roof surface temperature. Even if the external air temperature is slightly higher than the same value related to Florence, the external roof surface temperature is lower by about 7°C and equal to 35°C. This is probably due to the wind velocity that significantly influences the micro-climate parameters as reported also in the literature. In fact, the wind speed (sea breeze) in Palermo is equal to 5 m/s at 18 m height while in Florence it is 0.83 m/s, and this inevitably affects the value of the surface temperature on the roof. To validate this result, another simulation is performed considering the building located in Lecce (HDD = 1153). In this case the wind speed is lower than in Palermo (3 m/s) and the distance from the sea is higher. In this case, the roof

surface temperature is above 43°C, as it should be expected. As for the energy balance, the LW_{in} is 438.63 W/m^2 and the LW_{out} is 434 W/m^2. So, also in this case, the previous results are confirmed: the introduction of the green façade at 50% increases the energy performance of the buildings and positively affects the internal thermal condition and occupants' comfort.

As for multistorey buildings, for tower buildings the substitution of dark asphalt with light asphalt is the most advantageous retrofitted measure for the urban external layout, considering buildings located in Florence. This improvement results in a decrease in average external air temperature of about 1.5°C (cool pavements average external air temperature equal to 27.04°C). In this case it is worth to highlight that the introduction of trees combined with flowerbeds leads to a reduction in external air temperature by about 0.6°C (average temperature equal to 27.77°C), unlike in the case of multistorey buildings. With respect to the vertical greenery on façade at 50% coverage, the solution with the highest value of RH is the one with a height equal to 30 m. A value equal to 67.73% is registered with an increase of 5% compared to the reference case. In an urban grid characterized by both higher buildings and higher density value, the cooling strategies have a greater effect on microclimate parameters.

For tower buildings, due to the computational time required by the calculation of micro-climate parameters related to the building's height, only the simulation considering the grid located in Florence was performed. All the different cooling redevelopment measures were considered.

Finally, in regard to courtyard buildings, the most significant results are illustrated below (Figure 6). They refer to the city of Florence. In this case, the microclimate parameters are measured at 1 m of height because of the ENVI-MET mesh construction. The average external air temperature for the reference configuration is comparable to the other ones. This occurs in all climate zones considered for the analysis. For the city of Florence, the average external air temperature is equal to about 28.12°C in the case of courtyard buildings. The most noticeable result in this case is related to the introduction of both flowerbeds and trees as redevelopment strategies. It results in a reduction of about 1.5°C in average external air temperature, comparable to other layout configurations. A simultaneous increase in RH occurs with the combination of flowerbeds and trees equal to 2%.

Compared to other studied cases in this configuration it is interesting to analyze the microclimate parameters inside the courtyard.

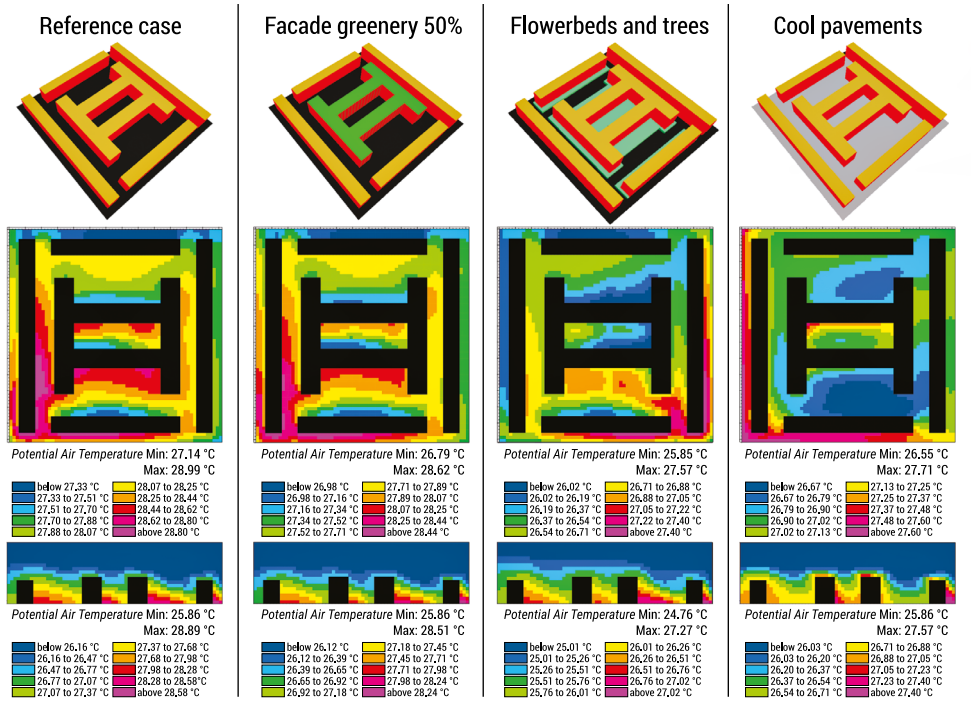

FIG. 6. Variation of external air temperature for courtyard buildings located in Florence in both plant and vertical section visualization

SOURCE: own elaboration

As for the reference case as well, the value of the external air temperature is different when comparing the inside and outside of the courtyard (Figure 9), while also considering building height. The southern houses facing the courtyard, from the first floor of the building, certainly have better energy performance with respect to the same height apartments facing the street. This is because the value of the external air temperature inside the courtyard is lower than on the outside. Moreover, compared to other building types, it is worth to notice that the use of cool pavements in the courtyard is not so advantageous because there is not as much air recirculation due to the lack of wind, being that the courtyard is laterally closed.

The most effective way to reduce external air temperature within the courtyard occurs with the use of flowerbeds combined with trees. In this case the reduction of average external air temperature is equal to about 1.9°C. This is obviously due to the shadow provided by the trees and the lack of wind inside the courtyard.

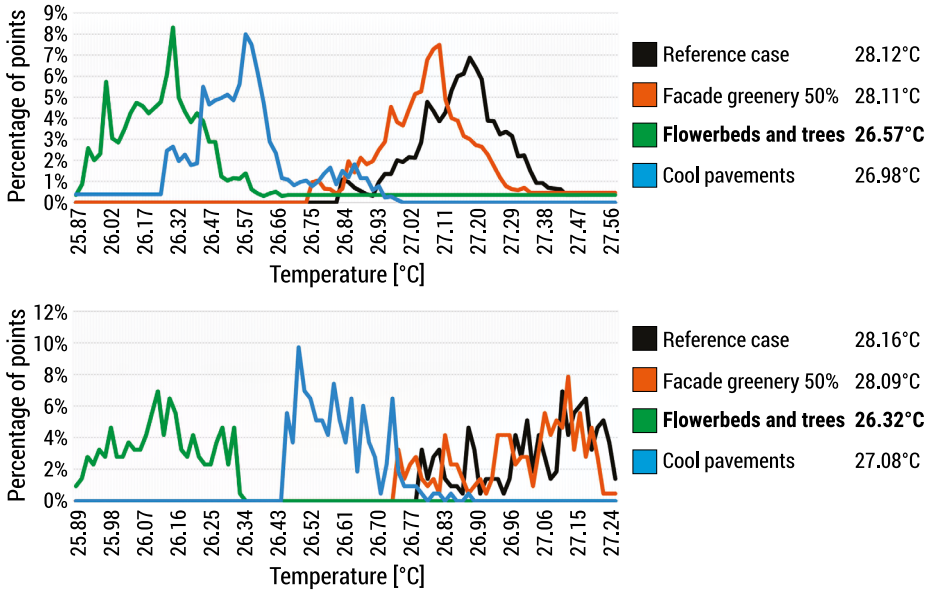

FIG. 7. Comparison of external air temperature for courtyard buildings outside (on the top) and inside (on the bottom) the courtyard with the indication of related average external air temperature (on the right column)

SOURCE: own elaboration

Conclusions

In conclusion, different building types on a typical Italian urban grid were analyzed with respect to some sustainable and cooling improvement strategies for both buildings and urban layouts considering different micro-climate parameters. The most advantageous and effective redevelopment measure proves to be the substitution of dark asphalt with a lighter one. This occurs for all cities and for multistorey and tower building types. This results in a significant decrease in average external air temperature of about 1°C for multistorey buildings and 1.5°C for towers. The only exception is for courtyard buildings where the most effective redevelopment measure is the introduction of flowerbeds and trees for both inside and outside the courtyard. This is inevitably affected by the higher number of trees that can be included in the urban grid due to the buildings' layout. In regards to Palermo it is worth to notice that the cool redevelopment measure has less impact on external micro-climate parameters (for instance on external air temperature).

If a low-density configuration is considered, for instance in a multistorey buildings urban grid, the results show that the increase in distance between buildings and the resulting reduction in covered area significantly influences the value of relative humidity rather than the average external temperature.

Furthermore, the application of greenery on southern façades mostly affects the surface temperature and the energy balance of buildings rather than external air temperature. For multistorey buildings located in Florence the vertical greenery at 50% coverage leads to a reduction in LW_{in} equal to about 14 kW, due to the difference of external surface temperature equal to 34.31°C and 22.26°C for green and traditional façade respectively. This certainly influences the cooling demand of the building. Considering the other 2 cities, for the reference case condition Milan is the worst case compared to others. In fact, the energy balance for the reference case is equal to –5 W/m^2. This result is obviously related also to the materials chosen for the external envelope stratigraphy.

In conclusion, for future developments, a real Italian district should be considered, also taking into account different kinds of cooling redevelopment measures and several building types. The parameters related to pedestrian comfort (such as the PMV – Predicted Mean Vote) should be considered when comparing different cooling strategies.

Literature

[1] WEB-1: Enerdata, *Evolution of households energy consumption patterns across the EU*, 2021. [online] Available from: https://www.enerdata.net/publications/executive-briefing/households-energy-efficiency.html [Accessed on 20th Aprile 2022]

[2] REN21 Secretariat REN21 *Renewables* 2021 *Global Status Report*, 2021. Paris, France; p. 42–45.

[3] Istat (Istituto nazionale di Statistica), *Report ISTAT* 18 *Costruzioni*, 2015, Rome, Italy, p. 582–583.

[4] ENEA, *Energy Efficiency trends and policies in Italy*. [online] Available from: https://www.odyssee-mure.eu/publications/national-reports/energy-efficiency-italy.pdf [Accessed on 20th April 2022].

[5] Governo Italiano, *Decreto Ministeriale* 26 *Giugno* 2015. *Applicazione delle Metodologie di calcolo delle prestazioni energetiche e definizione delle prescrizioni e dei requisiti minimi degli edifici*, 2015, Rome, Italy.

[6] Carpino C., Fajilla G., Gaudio A., et al., *Application of survey on energy consumption and occupancy in residential buildings. An experience in Southern Italy*, Energy Procedia 2018, 148, p. 1082–1089.

[7] Tootkaboni M.P., Ballarini I., Corrado V., *Analysing the future energy performance of residential buildings in the most populated Italian climatic zone: A study of climate change impacts*, Energy Reports 2021, 7, p. 8548–8560.

[8] Zinzi M., Carnielo E., *Impact of urban temperatures on energy performance and thermal comfort in residential buildings. The case of Rome, Italy*, Energy and Buildings 2017, 157, p. 20–29.

[9] Yıldız S., Kıvrak S., Gültekin A.B., Arslan G., *Built environment design – social sustainability relation in urban renewal*, Sustainable Cities and Society, 2020, 60, p. 102173.

[10] Abdallah A.S.H., Mahmoud R.M.A., *Urban morphology as an adaptation strategy to improve outdoor thermal comfort in urban residential community of new assiut city, Egypt*, Sustainable Cities and Society 2022, 78, p. 103648.

[11] ENVI-met 5.2, 2022.

[12] Ouyang W., Sinsel T., Simon H., et al., *Evaluating the thermal-radiative performance of ENVI-met model for green infrastructure typologies: Experience from a subtropical climate*, Building and Environment 2022, 207, p. 108427.

[13] Crank P.J., Sailor D.J., Ban-Weiss G., Taleghani M. *Evaluating the ENVI-met microscale model for suitability in analysis of targeted urban heat mitigation strategies*, Urban Climate 2018, 26, p. 188–197.

[14] Tsoka S., Tsikaloudaki A., Theodosiou T., *Analyzing the ENVI-met microclimate model's performance and assessing cool materials and urban vegetation applications – A review*, Sustainable Cities and Society 2018, 43, p. 55–76.

[15] Perini K., Chokhachian A., Dong S., Auer T., *Modeling and simulating urban outdoor comfort: Coupling ENVI-Met and TRNSYS by grasshopper*, Energy and Buildings 2017, 152, p. 373–384.

[16] Liu Z., Cheng W., Jim C.Y., et al., *Heat mitigation benefits of urban green and blue infrastructures: A systematic review of modeling techniques, validation and scenario simulation in ENVI-met V*4, Building and Environment 2021, 200, p. 107939.

[17] Faragallah R.N., Ragheb R.A., *Evaluation of thermal comfort and urban heat island through cool paving materials using ENVI-Met*, Ain Shams Engineering Journal 2022, 13, p. 101609.

[18] Cortes A., Rejuso A.J., Santos J.A., Blanco A., *Evaluating mitigation strategies for urban heat island in Mandaue City using ENVI-met*, Journal of Urban Management 2022, 11, p. 97–106.

[19] Karimimoshaver M., Shahrak M.S., *The effect of height and orientation of buildings on thermal comfort*, Sustainable Cities and Society 2022, 79, p. 103720.

[20] Wai K.M., Yuan C., Lai A., Yu P.K.N., *Relationship between pedestrian-level outdoor thermal comfort and building morphology in a high-density city*, Science of the Total Environment 2020, 708, p. 134516.

[21] Vassiliades C., Savvides A., Buonomano A., *Building integration of active solar energy systems for façades renovation in the urban fabric: Effects on the thermal comfort in outdoor public spaces in Naples and Thessaloniki,* Renewable Energy 2022, 190, p. 30–47.

[22] Sedaghat A., Sharif M., *Mitigation of the impacts of heat islands on energy consumption in buildings: A case study of the city of Tehran, Iran*. Sustainable Cities and Society 2022, 76, p. 103435.

A short review of metal-phenolic networks: synthesis methods and bio-applications

Keywords: metal-phenolic networks (MPNs), self-assembly, plant phenolic compounds, drug delivery, nanotechnology

Abstract: Metal-phenolic networks (MPNs) consist of metal ions, e.g. Al^{3+}, Mn^{2+}, or Fe^{3+} and monomeric building blocks of phenolic ligands containing galloyl and/or catechol groups (e.g. gallic acid, quercetin, or tannic acid). These bio-materials can be applied as thin bifunctional films on various materials, e.g. polymers, microorganisms, enzymes, mammal cells, etc. The data in available literature indicate the promising potential of MPNs film for applications in the biopharmaceutical and medical industries. The article reviews the latest knowledge on MPNs, which are of great interest to the pharmaceutical and biotechnology industries.

Introduction

Phenolic compounds (PCs) are plant secondary metabolites widely distributed in the plant kingdom. Most of these are derived from L-phenylalanine and shikimate pathways. Naturally, PCs play an important role in protecting plants against biotic (pathogens, herbivores) and abiotic (e.g., salinity, extreme temperatures, sun's ultraviolet (UV) radiation, heavy metals) stresses. PCs are characterized by the presence of one or more hydroxyl (–OH) groups attached to the aromatic ring. Based on chemical structure, PCs can be categorized into four main groups: flavonoids (accounting for about 60% of all PCs), phenolic acids (about 30% of all PCs), stilbenes, and lignans [1,2]. PCs are known to possess different biological properties, including antioxidant, antitumor, anti-aging, anti-atherogenic, cardioprotective, antibacterial, antifungal, antiviral, and anti-inflammatory [3–5]. All these properties make PCs interesting

substances for applications in many fields, such as biotechnology, cosmetology, food technology, medicine, and pharmaceuticals. The applications of PCs are often limited due to their low bioavailability, and poor water solubility. However, this problem can be solved with the development of self-assembly technology. Most of the PCs containing trihydroxyphenyl (galloyl) and/or dihydroxyphenyl (catechol) groups in their structures, such as gallic acid, tannic acid, or ellagic acid (Figure 1) can be engaged in multivalent coordination interactions with various *metal* ions (e.g. Al^{3+}, Mn^{2+}, Fe^{2+}, Fe^{3+}, Cu^{2+}, Zn^{2+}) to form metal-phenolic networks (MPNs) [6,7].

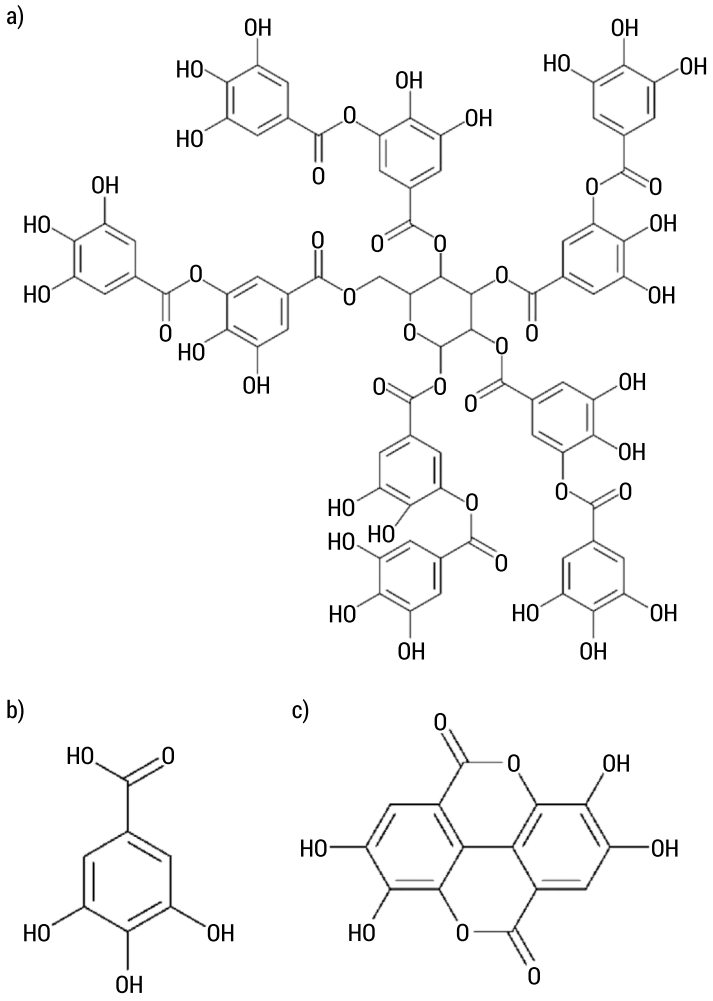

FIG. 1. The chemical structures of (a) tannic acid, (b) gallic acid, and (c) ellagic acid
SOURCE: own elaboration

Metal-phenolic networks are supramolecular coordination structures that consist of metal ions coordinated with phenolic ligands. This kind of coordination can be observed as new absorbance bands in the UV/Vis spectra and acid-responsive disassembly of MPNs. MPNs can be applied as thin films on diverse templates, such as porous substrates, colloidal particles (e.g. hollow capsules, nanogels, core-shell structures), or microorganisms [8,9]. MPNs-based coatings exhibit a wide range of valuable properties, including: (i) high biocompatibility and bioavailability, (ii) low toxicity, (iii) adhesive nature enabling the application to various nanomaterials, (iv) high drug loading capability, (v) antioxidant activity inherent to PCs, and (vi) stimuli-responsive drug release [9,10]. Moreover, MPNs exhibit tunable lipo/hydrophilic properties. For example, in a study conducted by Li et al. [11], MPNs consisting of tannic acid and Fe(III) ions increased the hydrophobicity of Zeolitic Imidazolate Framework-8 (ZIF-8) [11].

Assembly routes of MPNs

The "one-step" and "multistep" assembly via coordination interactions are the most commonly used methods for obtaining MPNs. The "one-step" system is based on mixing the organic phenolic ligand and the inorganic cross-linker (metal ions) in the presence of a substrate on which MPNs coating will be formed (Figure 2). Due to the universal adhesive properties of PCs, various materials can be used as a substrate (template), e.g. calcium carbonate ($CaCO_3$), or polystyrene [2,12]. For instance, the "one-step" assembly of MPNs consisting of commercially available tannic acid and Fe(III) ions was reported in the study of Ejima et al. [13]. The scientists mixed the mentioned ingredients with the template (polystyrene) in an aqueous solution for 20 seconds and 1 hour. The results showed that the stirring times did not affect the resulting film thickness (~2nm), suggesting that the film formation process was completed immediately. In this study, polystyrene was finally dissolved to obtain three-dimensional free-standing films known as hollow capsules [13]. Infrared spectroscopy FT-IR, Raman spectroscopy, UV/Vis spectroscopy, and X-ray photoelectron spectroscopy (XPS) can be used to confirm the formation of MPNs coatings [14]. The "one-step" method is easy and scalable. Moreover, it does not require the use of special and expensive equipment, and the material components are inexpensive and readily available [12,13].

In the case of "multistep" assembly, substrates are sequentially incubated in separate solutions of excess metal ions or phenolic ligands. The unabsorbed metal ions of phenolic ligands are removed between the incubation steps with multiple washing steps. In this way, the precise and dense layering of MPNs is possible. The "multistep" build-up of the MPNs process can be monitored by using quartz crystal microbalance (QCM) and via UV/Vis absorption spectroscopy. Moreover, the growth rate of the "multistep" technique can be controlled by pH values. MPNs synthesis using

the "multistep" method takes much more time (hours) than the "one-step" method (seconds), but it is not more expensive [2,8].

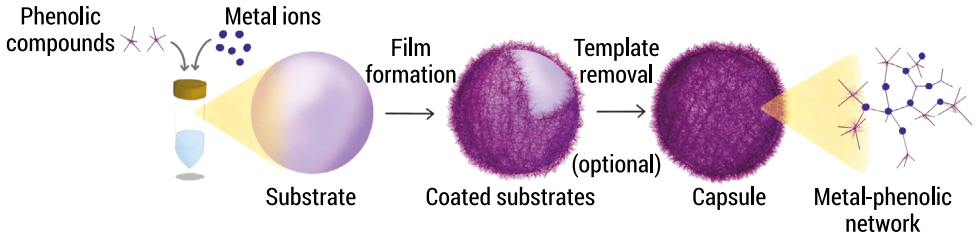

FIG. 2. Schematic illustration of the formation of MPNs
SOURCE: own elaboration based on [14]

Numerous studies have indicated that the physicochemical properties and formation kinetics of MPNs on substrates are dependent on (i) the metal-ligand molar ratio (M:L), (ii) the pH value, (iii) the concentration of the precursor, and (iv) the order of introduction of metal ions and phenolic ligands into the aqueous environment [15]. What is more, the molar ratio of galloyl and catechol units in the PC structure influences their binding strength to metal ions, metal oxides, or even template surfaces [6].

Bio-applications of phenolic compounds based MPNs

Phenolic compounds-based MPNs have been extensively used in the biopharmaceutical and medical fields because of their multiple functions, such as biocompatibility, long-term stability, biodegradability, and biosafety [12]. For example, in a study conducted by Lee et al. [16], mammalian cells were successfully coated with cytoprotective and biodegradable MPNs composed of tannic acid and Fe(III) metal ions. The results showed that the formed film not only protects the cells against UV-C radiation and toxic chemical – polyethyleneimine (PEI), but also its stimuli-responsive degradation led to programmed cell proliferation (Table 1) [16]. In another study, tannic acid was coordinated with 18 different metal ions (in the presence of a polystyrene template) to investigate the effect of metal types, and to obtain robust MPNs hollow capsules. It was found that tannic acid/Cu(II) capsules formed the thinnest (9.7 ± 1.0 nm) film, while tannic acid/Zr(IV) capsules were the thickest (14.2 ± 1.5 nm). Moreover, the pH-disassembly kinetics (in the pH range from 7.4 to 5.0) of the chosen MPNs capsules (with Cu(II), Zr(IV), and Al(III) ions) were examined. At pH = 5.0, the longest disintegration time was obtained for tannic acid/Al(III) MPNs (25% of the capsules disassembled after 6 hours), which is consistent with a profile desired for drug delivery. In comparison, at the same pH value, more than 25% of the tannic acid/Cu(II) capsules disassembled within 1 hour [14]. Park et al. [17] reported that encapsulation

of baker's yeast in a shell composed of tannic acid and Fe(III) ions provides cytoprotection of encapsulated cells against external factors [17]. In the study of Kim et al. [18], coating of curcumin-loaded nanoparticles using a tannic acid/Fe(III) complex resulted in a multi-responsive carrier for drug delivery. It was further found that the sustainability of drug release increased with the number of MPNs deposition layers. The cytotoxicity assay showed that the resulting formulations did not affect the viability of MRC-5 (human lung fibroblasts) cells [18]. Rahim et al. [19], described the simple and rapid MPNs film formation on the substrate surface by coordination of gallic acid, pyrogallol, and pyrocatechol with Fe(III) metal ions [19]. In a study by Bertleff-Zieschang et al. [20], the properties of MPNs films obtained by "one-step" assembly of four other flavonoids (quercetin, myricetin, luteolin, and fisetin) upon coordination with Fe(III) ions were reported. The results showed that quercetin/Fe(III) film exhibited about 10% higher $DPPH^{\bullet}$ (2,2-diphenyl-1-picrylhydrazyl) radical scavenging activity than free phenolic ligand [20]. Epigallocatechin gallate coordinated with Fe(III) [21], and Pt(II) [22] metal ions were reported to have cytoprotective properties [21,22]. In the work of Wang et al. [21], DOX (doxorubicin – antitumor antibiotic) doped ZIF-8 nanoparticles coated with a thin layer of epigallocatechin gallate/Fe(III) complexes showed good tumor growth inhibition of B16 cancer cells (84.2%) without affecting other cells [21]. In an acidic environment, which is characteristic for cancer sites, the coordination between metal ions and phenols networks in the capsule shell is weakened (due to the protonation of phenolic hydroxyl groups), and the encapsulated substances are released. The pH-dependent release of MPNs enables creation of efficient anticancer drug delivery systems [9,23]. The pH-responsive DOX-loaded capsules were also studied in the work of Ping et al. [24]. The authors found that more than 80% of tannic acid/Al(III) capsules degraded after 48 h of incubation at pH = 5.0, while at pH = 7.4 degradation was negligible [24]. These and other examples of MPNs bio-applications are summarized in Table 1.

TAB. 1. Bio-pharmaceutical applications of MPNs based on data from the literature

Phenolic ligands	Metal ions	Types of coated objects	Applications	Ref.
Tannic acid	Fe(III)	Mammalian cells (HeLa, NIH 3T3, and Jurkat cells)	Cytoprotective nanocoating	[16]
Tannic acid	Al(III), V(III), Cr(III), Mn(II), Fe(III), Co(II), Ni(II), Cu(II), Zn(II), Zr(IV), Mo(II), Ru(III), Rh(III), Cd(II), Ce(III), Eu(III), Gd(II), Tb(III)	Polystyrene particles	Hollow capsules, positron emission tomography (PET), and magnetic resonance imaging (MRI)	[14]

Phenolic ligands	Metal ions	Types of coated objects	Applications	Ref.
Tannic acid	Fe(III)	Colony of *Saccharomyces cerevisiae* (Baker's yeast)	Cytoprotective coating; the enhanced protection against UV-C radiation, *E.coli*, lyticase*, and silver nanoparticles	[17]
Tannic acid	Fe(III)	Gold nanoparticles	Catalysis	[25]
Tannic acid	Fe(III)	Curcumin loaded mesoporous silica nanoparticles (MCM-41)	pH- and glutathione-responsive release of curcumin	[18]
Tannic acid	Fe(III)	*Saccharomyces cerevisiae*, *Escherichia coli,* and PC12 mammalian cells (rat pheochromocytoma)	Protective coating; the enhanced protection against UV radiation and reactive oxygen damage	[26]
Tannic acid	Fe(III)	Nanodiamonds	Enhanced photoluminescence	[27]
Tannic acid	Fe(III)	Polystyrene particles	Hollow capsules, drug delivery	[28]
Tannic acid	Al(III)	DOX loaded $CaCO_3$ particles	Chemotherapy; promising candidate for cancer treatment	[24]
Gallic acid, pyrogallol, pyrocatechol	Fe(III)	Polystyrene particles	Hollow capsules, drug delivery	[19]
Quercetin, myricetin, luteolin, fisetin	Fe(III)	Polystyrene particles	Hollow capsules	[20]
Epigallocatechin gallate	Fe(III)	DOX-doped ZIF-8 nanoparticles	Chemotherapy; promising candidate for B16 melanoma therapy	[21]
Epigallocatechin gallate	Pt(II)	Polyethylene glycol (PEG) nanoparticles	Chemodynamic therapy (CDT) utilizing Fenton chemistry to destroy cancer cells by converting endogenous H_2O_2 into highly toxic reactive oxygen species (ROS)	[22]
(–)Epicatechin	Sm(III)	None	Hollow capsules; chemotherapy; promising candidate for colon cancer treatment	[29]

*lyticase – a mixture of enzymes used to degrade the cell wall of yeast

SOURCE: own elaboration

Summary

In recent years, phenolic compounds and metal-phenolic networks have attracted much attention because of their valuable physicochemical properties, and potential bio-applications in various fields of life. The simplicity, versality, and low cost of the formation of MPNs surface coatings and capsules make them attractive candidates for potential pharmaceutical and biomedical applications. However, there are still some deficiencies and challenges to overcome in the use of MPNs (e.g. premature drug release under biological conditions, low drug delivery efficiency, adverse interactions between MPNs and encapsulated substances) that need to be investigated and improved in the future.

Acknowledgments: The source of funding for the study was the Polish Ministry of Higher Education and Science Project No. WI/WB-IIS/3/2021.

Literature

[1] Hano C., Tungmunnithum D., *Plant Polyphenols, More than Just Simple Natural Antioxidants: Oxidative Stress, Aging and Age-Related Diseases*. Medicines 2020, 7(5), p. 26.

[2] Xie W., Guo Z., Zhao L., Wei Y., *Metal-phenolic networks: facile assembled complexes for cancer theranostics*. Theranostics 2021, 11(13), p. 6407–6426.

[3] Kalinowska M., Gołębiewska E., Świderski G., Męczyńska-Wielgosz S., Lewandowska H., Pietryczuk A., Cudowski A., Astel A., Świsłocka R., Samsonowicz M., Złowodzka A.B., Priebe W., Lewandowski W., *Plant-Derived and Dietary Hydroxybenzoic Acids—A Comprehensive Study of Structural, Anti-/Pro-Oxidant, Lipophilic, Antimicrobial, and Cytotoxic Activity in MDA-MB-231 and MCF-7 Cell Lines*. Nutrients 2021, 13(9), p. 3107.

[4] Kalinowska M., Gołębiewska E., Mazur L., Lewandowska H., Pruszyński M., Świderski G., Wyrwas M., Pawluczuk N., Lewandowski W., *Crystal Structure, Spectroscopic Characterization, Antioxidant and Cytotoxic Activity of New Mg(II) and Mn(II)/Na(I) Complexes of Isoferulic Acid*. Materials 2021, 14(12), p. 3236.

[5] Scalbert A., Manach C., Morand C., Rémésy C., Jiménez L., *Dietary Polyphenols and the Prevention of Diseases*. Crit. Rev. Food Sci. Nutr. 2007, 45(4), p. 287–306.

[6] Zhang X., Parekh G., Guo B., Huang X., Dong Y., Han W., Chen,X., Xiao G., *Polyphenol and self-assembly: metal polyphenol nanonetwork for drug delivery and pharmaceutical applications*. Future Drug Discovery 2019, 1(1), p. 1.

[7] Dai Q., Geng H., Yu Q., Hao J., Cui J., *Polyphenol-based particles for theranostics*. Theranostics 2019, 9(11), p. 3170–3190.

[8] Ejima H., Richardson J.J., Caruso F., *Metal-phenolic networks as a versatile platform to engineer nanomaterials and biointerfaces*. Nano Today 2017, 12(2), p. 136–148.

[9] Liu P., Shi X., Zhong,S., Peng Y., Qi Y., Ding J., Zhou W., *Metal-phenolic networks for cancer theranostics*. Biomater. Sci. 2021, 9(8), p. 2825–2849.

[10] Santoso S.P., Bundjaja V., Angkawijaya A.E., Gunarto C., Go A.W., Yuliana M., Tran-Nguyen P.L., Hsieh C.W., Ju Y.H., *One-step synthesis of nitrogen-grafted copper-gallic acid for enhanced methylene blue removal*. Sci. Reports 2021, 11(1), p. 1–14.

[11] Li W., Shi J., Zhao Y., Huo Q., Sun Y., Wu Y., Tian Y., Jiang Z., *Superhydrophobic Metal-Organic Framework Nanocoating Induced by Metal-Phenolic Networks for Oily Water Treatment*. ACS Sustain. Chem. Eng. 2020, 8(4), p. 1831–1839.

[12] Guo Y., Sun Q., Wu F.G., Dai Y., Chen X., *Polyphenol-Containing Nanoparticles: Synthesis, Properties, and Therapeutic Delivery*. Adv. Mater. 2021, 33(22), p. 2007356.

[13] Ejima H., Richardson J.J., Liang K., Best J.P., Van Koeverden M.P., Such G.K., Cui J., Caruso F., *One-step assembly of coordination complexes for versatile film and particle engineering*. Science 2013, 341(6142), p. 154–157.

[14] Guo J., Ping Y., Ejima H., Alt K., Meissner M., Richardson J.J., Yan Y., Peter K., Von Elverfeldt D., Hagemeyer C.E., et al., *Engineering Multifunctional Capsules through the Assembly of Metal–Phenolic Networks*. Angew. Chemie Int. Ed. 2014, 53(22), p. 5546–5551.

[15] Mazaheri O., Alivand M.S., Zavabeti A., Spoljaric S., Pan S., Chen D., Caruso F., Suter H.C., Mumford K.A., *Assembly of Metal–Phenolic Networks on Water-Soluble Substrates in Nonaqueous Media*. Adv. Funct. Mater. 2022, 32(24), p. 2111942.

[16] Lee J., Cho H., Choi J., Kim D., Hong D., Park J.H., Yang S.H., Choi I.S., *Chemical sporulation and germination: cytoprotective nanocoating of individual mammalian cells with a degradable tannic acid–FeIII complex*. Nanoscale 2015, 7(45), p. 18918–18922.

[17] Park J.H., Kim K., Lee J., Choi J.Y., Hong D., Yang S.H., Caruso F., Lee Y., Choi I.S., *A cytoprotective and degradable metal-polyphenol nanoshell for single-cell encapsulation*. Angew. Chem. Int. Ed. Engl. 2014, 53(46), p. 12420–12425.

[18] Kim S., Philippot S., Fontanay S., Duval R.E., Lamouroux E., Canilho N., Pasc A., *pH- and glutathione-responsive release of curcumin from mesoporous silica nanoparticles coated using tannic acid–Fe(III) complex*. RSC Adv. 2015, 5(110), p. 90550–90558.

[19] Rahim M.A., Kempe K., Müllner M., Ejima H., Ju Y., Van Koeverden M.P., Suma T., Braunger J.A., Leeming M.G., Abrahams B.F., et al., *Surface-Confined Amorphous Films from Metal-Coordinated Simple Phenolic Ligands*. Chem. Mater. 2015, 27(16), p. 5825–5832.

[20] Bertleff-Zieschang N., Rahim M.A., Ju Y., Braunger J.A., Suma T., Dai Y.; Pan S., Cavalieri F., Caruso F., *Biofunctional metal–phenolic films from dietary flavonoids*. Chem. Commun. 2017, 53(6), p. 1068–1071.

[21] Wang X., Li X., Liang X., Liang J., Zhang C., Yang J., Wang C., Kong D., Sun H., *ROS-responsive capsules engineered from green tea polyphenol–metal networks for anticancer drug delivery*. J. Mater. Chem. B 2018, 6(7), p. 1000–1010.

[22] Ren Z., Sun S., Sun R., Cui G., Hong L., Rao B., Li A., Yu Z., Kan Q., Mao Z., A *Metal-Polyphenol-Coordinated Nanomedicine for Synergistic Cascade Cancer Chemotherapy and Chemodynamic Therapy*. Adv. Mater. 2020, 32(6), p. 1906024.

[23] Yan Y., Ding H., *pH-Responsive Nanoparticles for Cancer Immunotherapy: A Brief Review*. Nanomaterials 2020, 10(8), p. 1–15.

[24] Ping Y., Guo J., Ejima H., Chen X., Richardson J.J., Sun H., Caruso F., *pH-Responsive Capsules Engineered from Metal-Phenolic Networks for Anticancer Drug Delivery*. Small 2015, 11(17), p. 2032–2036.

[25] Zeng T., Zhang X., Guo Y., Niu H., Cai Y., *Enhanced catalytic application of Au@ polyphenol-metal nanocomposites synthesized by a facile and green method*. J. Mater. Chem. A 2014, 2(36), p. 14807–14811.

[26] Li W., Bing W., Huang S., Ren J., Qu X., *Mussel Byssus-Like Reversible Metal-Chelated Supramolecular Complex Used for Dynamic Cellular Surface Engineering and Imaging*. Adv. Funct. Mater. 2015, 25(24), p. 3775–3784.

[27] Bray K., Previdi R., Gibson B.C. Shimoni, O. Aharonovich I., *Enhanced photoluminescence from single nitrogen-vacancy defects in nanodiamonds coated with phenol-ionic complexes*. Nanoscale 2015, 7(11), p. 4869–4874.

[28] Cherepanov P.V., Rahim M.A., Bertleff-Zieschang N., Sayeed M.A., O'Mullane A.P., Moulton S.E., Caruso F., *Electrochemical Behavior and Redox-Dependent Disassembly of Gallic Acid/FeIII Metal-Phenolic Networks*. ACS Appl. Mater. Interfaces 2018, 10(6), p. 5828–5834.

[29] Li K., Dai Y., Chen W., Yu K., Xiao G., Richardson J.J., Huang W., Guo J., Liao X., Shi B., *Self-Assembled Metal-Phenolic Nanoparticles for Enhanced Synergistic Combination Therapy against Colon Cancer*. Adv. Biosyst. 2019, 3(2), p. 1800241.

A methodology for interdisciplinary education of engineers, adapted to the needs of contemporary cities (Glocal Project, Erasmus+)

Keywords: Glocal, interdisciplinary training, blended learning

Abstract: The Glocal project (Erasmus+, 2019-1-PL01-KA203-065654) is part of European Strategic Partnerships Actions of the Erasmus+ program. It has been developed by a consortium of three European universities: Białystok University of Technology, from Poland (its leader), and two partners: Universidad Politécnica de Madrid, from Spain, and Klaipedos Valstybine Kolegija, from Lithuania. An important task of the project was the organization of summer schools. A methodology for international and interdisciplinary education was developed by the Glocal project team to conduct such summer schools, as will be explained by the authors, who are two of the six Glocal project coordinators involved in the development of this methodology. This is not related with individual work, as it is the result of the collaborative work of a team of more than 30 university teachers and professional experts, with important participation of students, who are also learning to work in international and interdisciplinary teams. Students worked in teams of three students, one from each country, to design a green bus stop. To be able to do so, students need knowledge that has been organized around four blocks or modules: Architecture and theory of design; Structures and building materials; 3D mapping and modelling; and Systems related to sustainable development. There is also a general module related to the project (coordination design criteria, related to the other four blocks but specifically to the first). The developed syllabus and methodology will be used by the project partner universities, but it will also be offered to all interested universities, to be freely downloaded from the Erasmus+ platform.

Introduction

The rapid development of technical sciences in engineering disciplines generates the need for education in more specialized fields. This is a response to the expectations of the modern labour market [1]. The activity of the university is therefore focused on adjusting the educational offer to the current conditions and needs. This process, however, is associated with a certain inertia resulting from the formal conditions for introducing new fields of study. At the same time, it is known that in real professional practice, the international cooperation of engineers from various industries is necessary [2]. This observation reveals a certain deficiency in the educational process. Graduates of technical universities in many cases show shortcomings in terms of cooperation in multi-disciplinary teams [3], especially when these teams deal with complex interdisciplinary projects [1, 4,5].

Hence there is a need for higher education institutions to react faster to the corrections of the education process [6]. This was possible thanks to participation in the European Erasmus + program, in the competition for applications 2019, Round 1 KA2 – Cooperation for innovation and exchange of good practices, in the activity category KA203 – Strategic Partnerships for Higher Education, that gave us the opportunity to carry out the Glocal project.

The aim of this study is to present the methodology of interdisciplinary education of future engineers, prepared as part of the Glocal Erasmus + project, by the Glocal team of more than 30 university teachers and professional experts, with important participation from students of the project.

Glocal Erasmus+ project: materials and methods

The project "Glocal – innovative education of future engineers responding to the problems of modern cities" (Erasmus +, 2019-1-PL01-KA203-065654) was carried out from 1.09.2019 to 31.12.2022, by a consortium of three European universities:

- Bialystok University of Technology (Poland) – leader,
- Universidad Politécnica de Madrid (Spain) – partner
- Kalaipedos Valstybine Kolegija (Lithuania) – partner.

As part of its activities, as well as one of its main goals, these universities developed a training program for the Glocal project, focusing on its Summer Schools [7]. The basis for the development of the training program was to be the experience of running two summer schools planned for the summers of the years 2020 and 2021;

due to Covid-19, both meetings occurred in 2022. The curriculum, teaching materials developed by the consortium teachers [8, 9] and the evaluated learning outcomes will be used to develop the final form of the syllabus.

The innovative GLOCAL module will be included in the educational offer for students at partner universities. It will be implemented as an optional subject (6 ECTS). We hope it will increase the attractiveness of technical studies, as well as complement the program with modern ICT technology achievements. It has been designed to contribute to the creation of a closer link between teaching and hands-on experience, thus responding to the needs of the European labour market.

Structure of the teaching program and Glocal training program

The Glocal project has been developing a methodology for the interdisciplinary education of young engineers.

The leading assumptions of the methodology were to achieve learning outcomes in the following areas:

- knowledge and skills in the field of multi-industry cooperation in the broadly understood architectural and construction area (including architecture, urban planning, landscape architecture, construction, environmental engineering, architectural and building structures, spatial management, geodesy, interior design, BIM)
- knowledge and skills in the field of implementing:
  - multi-sector projects corresponding to the needs of modern cities,
  - multi-sector projects with complex conditions (location, technical, social, legal, ecological, protection of cultural heritage, shaping the image and brand, improving the quality of life in the city),
  - creative work and cooperation in interdisciplinary, international teams of designers and contractors
- soft skills in terms of cooperation in an international team (including understanding the value of non-technical engineering activities)
- improving language skills

The adopted framework of learning outcomes, available resources in the form of laboratories and university equipment, as well as the scientific and didactic achievements of the consortium's lecturers were the basis for establishing the four basic education blocks (Fig. 1).

Structure of Glocal			
Architecture and theory of design	**Structures and building materials**	**3d mapping and modelling**	**Systems related to sustainable development**
Lectures Seminary Case study Studial trip Project	Lectures Laboratories Studial trip Project	Lectures Laboratories Studial trip Project	Lectures Laboratories Studial trip Project

FIG. 1. Structure of Glocal module
SOURCE: Glocal team own elaboration

Theoretical knowledge and skills transferred to students during the implementation of the four modules will be used in an interdisciplinary design of a small architecture facility located in the public space of a modern city (Project general module). A green public transport bus stop was selected as the theme of the project. It requires the analysis of numerous conditions in the field of geodesy, architecture, construction, installation, the selection of modern technologies and materials, of smart city solutions, and the establishment of criteria and conditions for sustainable urban development.

Architecture and theory of design

The thematic block "Architecture and theory of design" contains theoretical and practical topics in order to meet the needs of the Glocal project.

They concern thematic issues in the field of:

- theory and design of contemporary architecture, with particular emphasis on architecture located in public space. Analysis of good design practices regarding small architecture objects in the public space of cities,
- architectural design that meets the conditions of sustainable city development,
- universal design responding to the needs of people with disabilities, including principles of designing architectural models for people with disabilities,
- cultural values of the urban landscape of the cities of the Glocal project: Białystok, Klaipeda and Madrid,
- cultural heritage of European cities, with particular emphasis on the value of their public spaces. Protection of historical values of European cities,
- the theory of shaping the image and brand of the city.

The module "Architecture and theory of design" includes lectures, seminars and project classes. The analysis of selected case studies in the form of lectures and thematic excursions is foreseen (Fig. 2).


FIG. 2. Study trip to Warsaw
SOURCE: D. Gawryluk, 04.2022

This is one of the more extended academic content modules, as it provides the basic knowledge for the project work, and can be considered as general criteria to integrate the different, specialized elements of the construction system that are included in the four basic education blocks or modules. Project work related to this module consists in the design of a small architecture facility (green bus stop), been carried out by the students' teams.

Structures and building materials

The thematic block "Structures and building materials " was devoted to issues in the field of theory and practice of construction corresponding to the needs of the Glocal project. They concern thematic issues in the field of:

- basic design solutions of various types of structures used in small architecture facilities
- basic design schemes of the above-mentioned structure. Basic use of selected software for designing structures
- structure safety - issues related to ensuring the safety of structures and the use of structures ensuring safety in public space
- innovative technologies and materials in construction
- sustainable development in revitalization of public areas
- structures and new technologies in revitalization or building new small architecture objects in a heritage context
- basics of circular economy

The module "Structures and building materials " includes lectures, seminars, laboratories and design classes (Fig. 3).

a) b)

FIG.3A AND 3B. Structure Laboratory, Bialystok University of Technology
SOURCE: 3a. D. Gawryluk, 3b. M.A. Florez de la Colina, 04.2022

3D mapping and modelling

The thematic block "3D mapping and modelling" concerns the depiction of space in the field of geodesy, architecture, and landscape architecture through the use of various drawing techniques and selected databases and graphic programs. They concern thematic issues in the field of:

- principles of GIS, BIM, Lidar
- theory of digitalisation of heritage objects
- principles of a smart city (including smart public transport)
- 3D modelling (hand drawing, 3D printing, use of graphics programs)

The module "3D mapping and modelling" includes lectures, laboratory and design classes.

a) b)

FIG. 4A AND 4B. Drone workshop in Bialystok, teacher: Indrius Kuklys
SOURCE: 4a. M.A. Florez de la Colina, 4b D. Gawryluk, 04.2022

Systems related to sustainable development

The thematic block "Systems related to sustainable development" concerns broadly understood modern systems and services that are used in buildings and public spaces in cities. In the Glocal offer, they are thematically related to:

- greenery in public space
- small retention systems
- water installations (Fig. 5)
- renewable sources of energy, pv panels
- heating, cooling and ventilation systems

The module "Systems related to sustainable development" includes lectures, laboratory and design classes (Fig. 5).

a) b)

FIG. 5A AND 5B. "Instalaciones" Laboratory in Universidad Politécnica de Madrid
SOURCE: 5a. M.A. Florez de la Colina, 5b D. Gawryluk, 2021

Results of first testing experience: Glocal Summer School in Bialystok, Poland (Project work)

A pragmatic test of the explained methodology, applied to a specific design problem, was done during the First part of Glocal 1 Summer School, at Bialystok University of Technology, in Poland. Some of its first results are presented here, through the preliminary projects of a green public transport bus stop developed by students, as well as some of the activities focused on the integration of the students' teams.

Glocal project programmed activities included the opportunity to travel to Poland for students and teaching staff from the other two partner universities, Universidad Politécnica de Madrid, UPM, from Spain, and Klaipedos Valstybine Kolegija, Klaipeda State University of Applied Sciences, KVK, from Lithuania. Problems due to the Covid-19 pandemic delayed the course, planned for summer 2020 to the spring of 2022. Participants attended the First part of Glocal 1 Summer School in Bialystok,

in April 2022. This included 8 students from each of the 3 partner universities, 4 incoming teachers from each Spanish and Lithuanian partner, and 14 Polish lecturers from academia and from participating companies or local administrations.

During two intensive weeks, 8 teams of students were given a specific location, different for each team, in Poland, Spain or Lithuania. Each of the 3 team members came from a different country (Poland, Spain or Lithuania), making it international, but also each team member had a different course of study (Landscape architecture, Building construction engineering or Geodesy), making it interdisciplinary. They had to attend lectures, as well as laboratory and design classes, working with their team to create a bus stop shelter, as detailed in the agenda of the Summer Course (Glocal – innovative training of future engineers (pb.edu.pl) [7].

Student project work in Bialystok was supervised by an international and interdisciplinary group of teachers, helping students to collaborate in the design. As quite often occurs in multidisciplinary professional teams, the tendency was that each student was doing his or her "part", related with their specific studies. In the first days of the program, students created sketches of their ideas and shared them with other teams (Fig. 6).

FIG. 6. A,B,C,D. First part of Glocal 1 Summer School, in Bialystok: students and teachers sharing first ideas

SOURCE: M.A. Flórez de la Colina, D. Gawryluk

We wanted them to be interested in and to learn the basic knowledge included in each of our modules, to allow them to really and actively collaborate in the whole design, even if they gave more ideas related to their specific studies (Fig. 7).

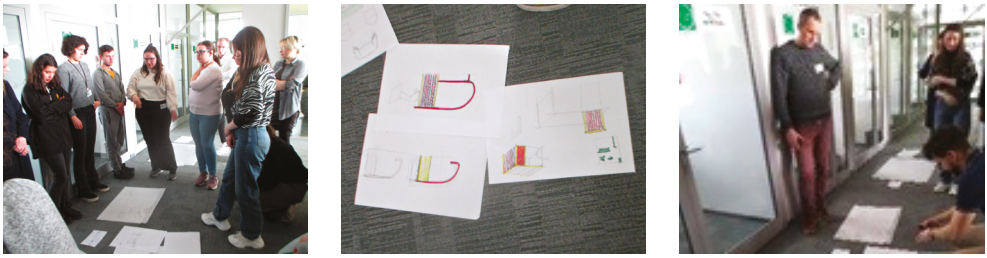

FIG. 7. First part of Glocal 1 Summer School, in Bialystok: students and teachers sharing first ideas
SOURCE: M.A. Flórez de la Colina, D. Gawryluk

As seen in those images, most of the student teams got accustomed in those two weeks to actively participate in sharing their ideas. We found that sometimes "unconventional places" to share ideas (a common space for instance, instead of a classroom, in the beautiful building of the library of the Bialystok University of Technology), could help those more reluctant or shy to express themselves in the English language.

The proposed educational criteria allow for the local government administration, producers and the professional environment of engineers to have an impact on the education process and at the same time expand their own knowledge. We have already found a positive effect on local and global economic development, through the interest of all participants related to Glocal 1 Summer School in Bialystok, Poland, to collaborate in this project.

The work of those teams and their teachers was not finished in April 2022. As already mentioned, this was only the first part of the Glocal Summer Courses and their work will continue with a second blended part, with three weeks of e-learning and two weeks face-to-face in Madrid, in September 2022. This will let us know if those good preliminary results could be improved.

Summary

A methodology of interdisciplinary education of future engineers has been developed using the teaching and research potential of three European universities: Bialystok University of Technology, Universidad Politécnica de Madrid and Klaipedos Valstybine Kolegija. The reason why participation in projects such as strategic partnerships of the Erasmus + program is interesting, is that it gives universities the opportunity to prepare a more attractive educational offer.

We consider that the Glocal course, prepared as part of the Glocal Erasmus + project, by the Glocal team of more than 30 university teachers and professional experts, with the important participation of students, has adequately prepared the 8 teams of 3 members of Glocal 1 for the changing needs of the labour market. Students have achieved a high level of adaptability related to the new knowledge transmitted to them through the four academic modules designed for this course (Architecture and theory of design, Structures and building materials, 3D mapping and modelling, Systems related to sustainable development). Collaboration between the members of each team is a key issue related with the best integration of technical elements in their projects, as well as in adapting new technical knowledge to the requirements of small objects in the public spaces of cities. The preliminary student project results of a green public transport bus stop, as the first pragmatic test of the explained methodology, allow us to think so.

We hope that the transfer of information, experience and skills between lecturers and students that have occurred in Glocal 1 Summer School in April 2022, in Bialystok, Poland, will have a positive impact on improving the quality of education, extending the offer and updating the content of education at other universities, as has already been the case with our universities.

Acknowledgements

This project would not have been possible if our universities had not received the financial support of an Erasmus project (2019-1-PL01-KA203-065654).

We would like to acknowledge the participation and advice of our colleagues, team coordinators of the Glocal project, Dorota Anna Krawczyk, from Bialystok University of Technology, Pilar Cristina Izquierdo Gracia, from Universidad Politécnica de Madrid, Dainora Jankauskienė and Egle Brezgytė, from Klaipedos Valstybine Kolegija. We consider them an essential part of the Glocal project team.

We would like to acknowledge the participation of the teachers and experts that have collaborated in classes, laboratories, as well as other activities including technical and cultural visits, in Glocal 1 Summer School in April 2022, in Bialystok, Poland, as well as the 24 students from Bialystok University of Technology, Universidad Politécnica de Madrid and Klaipedos Valstybine Kolegija. We consider them an important part of the Glocal project team.

Part of this study was based on previous scientific research done at Bialystok University of Technology WZ/WA-IA/6/2020. We would like to acknowledge as a preliminary part of the inspiration of carried out research of the Glocal project, the cooperation with the nationwide Polish Association of Landscape Architects (SPAK) and its Podlasie branch. The experience and advice of some of their members, who represent many Polish universities, has been of great help to us.

Literature

[1] Gawryluk D., Flórez de la Colina M.A., Krawczyk D., Izquierdo Gracia C.P., Jankauskienė D., Brezgyté E., *Understanding the problems of teaching future engineers to think globally and act locally: Glocal project*. In: Gómez Chova L, López Martínez A, Torres CI, editors. 13th International Conference of Education, Research and Innovation: ICERI 2020: conference proceedings. IATED; 2020. p. 7249–7257.

[2] Lucena J., Downey G., Jesiek B., Elber s., *Competencies Beyond Countries: The Re-Organization of Engineering Education in the United Dtates, Europe, and Latin America*, Journal of Engineering Education 2013, Volume 97, Issue 4, p. 433–447.

[3] Crawley E.F., Malmqvist J., Ostlund S., Brodeur D.R., Edstrom K., Integrated Curriculum Design. Inn: Rethinking Engineering Education, Springer, Cham 2014, p. 85–115.

[4] Lattuca L.R., Knight D.B., Bergom I.M., *Developing a Measure of Interdisciplinary Competence for Engineers* ASEE Annual Conference & Exposition 2012, San Antonio, Texas. 10.18260/1–2–21173.

[5] Kucinskiene J., Flórez de la Colina M.A., Gawryluk D., Krawczyk D., Izquierdo Gracia C.P., Jankauskienė D., *Small glossary of technical terms for english-polish-spanish-lithuanian languages*. In: Gómez Chova L, López Martínez A, Torres CI, eds. 13th International Conference of Education, Research and Innovation: ICERI 2020: Conference Proceedings. 13th International Conference of Education, Research and Innovation: ICERI 2020: conference proceedings. IATED; 2020:7307-7314.

[6] van Hattum-Janssen N., et al., *Team Teaching in PBL: A Literature Review in Engineering Education*. In: Carvalho Alves A. and van Hattum-Jansse N., eds *Training Engineering Students for Modern Technological Advancement,* IGI Global, 2022, p. 250–270.

[7] "Glocal-Innovative training of future engineers responding to problems of contemporary cities" (2019-1-PL01-KA203-065654); https://glocal.pb.edu.pl/en/ www.glocal.pb.edu.pl

[8] Gawryluk D., Kucinskiene J., eds. *Small Glossary of Technical Terms for English–Polish–Spanish–Lithuanian Languages*. Kaunas: Sausdino UAB „Vitae Litera"; 2020.

[9] Gawryluk D., Krawczyk D.A., eds. *Future of the City*, Oficyna Wydawnicza Politechniki Białostockiej, 2021.

Investigation of the effect of waste polypropylene originated metal contaminants on the pyrolysis of polypropylene

Keywords: chemical recycling, pyrolysis, plastic waste, polypropylene, ICP-MS.

Abstract: This study aims to characterize the waste PP that was found to have the highest share in the Household Plastic Waste (HPW) collected in Izmir, Turkey. PP's physicochemical properties were evaluated by using different characterization techniques, such as proximate and ultimate analysis, Fourier Transform Infrared Spectroscopy (FTIR), Thermogravimetric Analysis (TGA), and Differential Scanning Calorimetry (DSC). The metal content of the plastics is sourced from additives used to improve the stability and mechanical properties of plastics. These metals can have a catalytic role during the pyrolysis process. The quantities of metals in the PP-originated ash were investigated by an Inductively Coupled Plasma-Mass Spectrometry (ICP-MS) and Scanning Electron Microscopy – Energy Dispersive X-Ray Spectroscopy (SEM-EDX). Moreover, to evaluate the influence of the metal fraction of PP on the product yield and product distribution, pyrolysis experiments were conducted as thermal and catalytic with different PP to ash ratios (10:1, 50:1, and 100:1) at 450°C. The hydrocarbon distribution of liquid products was investigated by Gas Chromatography-Mass Spectrometry (GC-MS). It was found that the presence of PP-originated ash in pyrolysis conditions had no remarkable effect on liquid product yield but had an impact on fuel range (C_5–C_{15}) hydrocarbon distribution.

Introduction

Plastics are among the most utilized materials in various industries such as construction, packaging, automotive, etc. The variety of plastic products has a wide range, including various types of plastics listed according to the Standard Practice for Coding Plastic-Manufactured Articles for Resin Identification [1]. These are polyethylene terephthalate (PET, code: 1), high-density polyethylene (HDPE, code: 2), polyvinyl chloride (PVC, code: 3), low-density polyethylene (LDPE, code: 4), polypropylene (PP, code: 5), polystyrene (PS, code: 6), and OTHER (code: 7) [2]. OTHER is defined as the mixture of miscellaneous plastics, including polyethylene (PE), polycarbonate (PC), polylactide acid (PLA), acrylic, acrylonitrile butadiene styrene (ABS), polyamide (PA), polybutylene terephthalate (PBT), fiberglass, and nylon[3]. Each plastic type demonstrates different features, e.g., PET is lightweight and resistant to pressure, thus used in water and beverage bottles. In contrast, HDPE has long polymer chains and is highly crystalline, so the application area consists of detergent, shampoo, and oil containers [4]. PS is usually used in toys, medical devices, and electronics due to its light and heat resilience. PP has high resistance to heat and chemicals, and high rigidity, thus used in furniture production, carpets, and food packaging [4,5]. PVC also has high resistance to temperature and it is versatile so that it can be used in the production of credit cards, medical devices, food foil, and packaging. However, PVC produces hazardous chlorine gas in thermochemical treatment which is undesirable.

In Turkey, the production of raw plastic material is speculatively determined as higher than 1 thousand million tons for 2021. Turkish Plastics Industrialists Research, Development, and Education Foundation (PAGEV) reported the composition percentages of produced plastic raw materials for PET, HDPE, PVC, LDPE, PP, PS, and PVC are 23%, 9%, 15%, 31%, 12%, 10%, respectively for 2021[7]. Since there is no segregation step for plastic types in municipal waste, the composition of plastic waste is unknown. Table 1 shows the plastic-type distribution in municipal and household waste determined in different regions. Specific to this study, the related distribution for Izmir (Turkey) region is provided in the table as well.

TAB. 1. The plastic-type distribution in municipal and household waste

Plastic Type Distribution, (wt. %)	This study	India [7]	Spain [8]	Thailand [4]	Europe [2]*	Czech Republic [5]	Qatar [9]
PET	30.0	9	18.6	5.9	26	2.3	14
PE	37.5	66	49.9	77.8	37	49.3	43
HDPE	26.4	N/A	N/A	57.4	7	26.5	21
LDPE	11.1	N/A	N/A	17.4	30	22.8	22
PVC	N/A	4	N/A	2.2	N/A	N/A	16

Plastic Type Distribution, (wt. %)	This study	India [7]	Spain [8]	Thailand [4]	Europe [2]*	Czech Republic [5]	Qatar [9]
PP	27.6	10	10	7.3	7	30.4	19
PS	0.95	5	5.7	4.8	1	18	5
OTHER	3.4	6	15.8	5.0	25	N/A	N/A
LABEL	0.6	N/A	N/A	N/A	N/A	N/A	N/A

*Household waste

N/A: No data available

SOURCE: own elaboration

Pyrolysis is a thermochemical conversion technology that could be considered for waste plastics to produce intermediate energy carriers at reaction temperatures ca. 500°C in the absence of oxygen. Since the liquid product of plastic pyrolysis has a high calorific value, plastic waste is a promising feedstock for producing alternative fuels. The metal content of the plastics is sourced from additives used to improve the stability and mechanical properties of plastics. Moreover, these metals can have a catalytic role during the pyrolysis process. It has been reported in the literature that potassium, calcium and magnesium lower the decomposition temperature and increase the char yield during the co-pyrolysis of LDPE and wood sawdust [11]. Lin et al., have reported that alkali/alkaline earth metals in cellulose-derived char improved the cracking of HDPE to produce alkenes and potassium content, but decreased hydrocarbon formation [12]. To evaluate the effects of ash derived from PP on product yield and hydrocarbon distribution of the liquid product, pyrolysis processes were carried out as thermal and catalytic processes. Three different ratios of PP to ash (10:1, 50:1, and 100:1) were used for the catalytic pyrolysis of PP.

Materials and methods

For this study, 78 kg of HPW was collected between May and September 2021. The collected materials were classified according to Resin Identification Codes (RIC) [1]. Moreover, unidentified plastic labels were segregated into a stand-alone category (i.e., label). Figure 1 shows the plastic-type distribution of collected HPW. PET has the highest share with 30 wt.% while HDPE, LDPE, PP, PS, OTHER, and LABEL were 26.4 wt.%, 11.1 wt.%, 27.6 wt.%, 0.95 wt.%, 3.4 wt.%, and 0.6 wt.%, respectively. Because of the utilization area of PVC, PVC (code: 3) was not observed in the collected HPW.

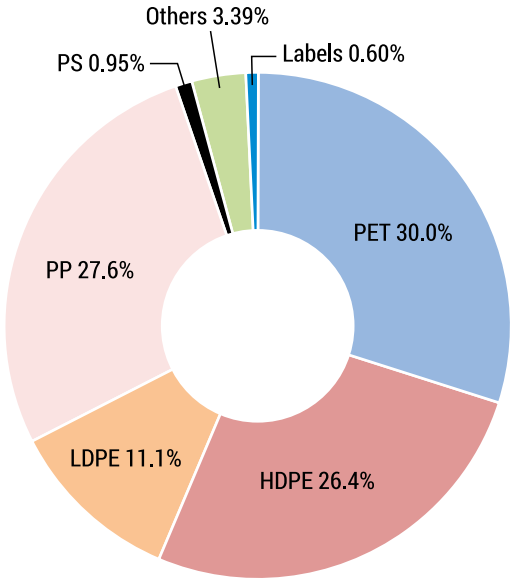

FIG. 1. Plastic-type distribution in collected HPW
SOURCE: own elaboration

Since PP had the highest share in collected HPW and would result in a liquid product with a high calorific value by pyrolysis process, the physicochemical properties of waste PP samples were characterized via different characterization techniques. The ultimate and proximate analyses, FTIR, ICP-MS, TGA, DSC, and SEM-EDX were conducted for this study. The equipment used for the physicochemical characterization of waste PP samples were summarized in Table 2. Proximate analyses were conducted according to related ASTM standards to determine moisture, ash, and volatile matter contents of waste PP samples [13]. Fixed carbon was determined by the mass balance after analysing the content of moisture, ash, and volatile content. Ultimate analysis was used to determine the CHN/S contents of PP samples. Oxygen content was also calculated by difference.

TAB. 2. Equipment used for the physicochemical characterization of waste PP samples

Analysis	Equipment and Standards
Proximate Analyses	
Moisture content	ASTM D3173
Ash content	ASTM D3174
Volatile matter content	ASTM D3175
CHN/S	Leco TruSpec CHN Analyzer

Analysis	Equipment and Standards
Heating Value	Parr 6300 Oxygen Bomb Calorimeter
Metal Content	Agilent 7500c Octopole Reaction (ICP-MS), CEM Mars 6 (Microwave Digestion System)
TGA	Perkin Elmer Diamond TG/DTA
DSC	Perkin Elmer Diamond TG/DTA
SEM-EDX	FEI QUANTA 250 FEG
FTIR	Perkin Elmer Fourier Transform Infrared Spectrometer System Spectrum BX

SOURCE: own elaboration

FTIR analysis was performed to obtain information concerning the functional compositional groups in the samples. The scanning wavenumber range was 4000 cm^{-1} to 600 cm^{-1} with a data interval of 1 cm^{-1}. Another characterization technique applied to waste PP is SEM-EDX, used to determine any trace elements that ICP-MS did not detect since their quantity is below the limit.

Obtained TGA and derivative thermogravimetric (DTG) curves were used to evaluate the thermal stability of the waste PP sample and its behaviour under a specific temperature regime. For the TGA tests, the sample temperature was increased from 25°C to 800°C by applying a heating rate of 10°C/min with an N_2 flow rate of 40 mL/min. DSC was performed to determine the melting temperature commonly used for the characterization of polymer mixtures. During the DSC analysis, the sample was heated from 25°C to 350°C with a heating rate of 10°C/min with an N_2 flow rate of 40 mL/min. The metal content of PP was investigated by ICP-MS. As a pre-treatment, microwave digestion was performed at 210°C with the addition of 10 mL HNO_3 to the 0.25 g of sample for transferring metal content from the solid phase into the liquid phase.

While physicochemical characterization techniques were applied to waste PP, pure PP was used for the pyrolysis process. The virgin PP was purchased from PETKIM. Since the maximum mass loss of PP occurred at 446°C according to the DTG curve, pyrolysis experiments were carried out as a thermal and catalytic at 450°C in a bench-scale continuous reactor. For catalytic pyrolysis, the solid residue that remained after ASTM D3174 analysis of waste PP which is the ASTM standard for the determination of the ash content was collected to obtain the metal fraction. Pure PP and ash fraction of waste PP were mixed homogeneously at different plastic-to-ash ratios (10:1, 50:1, and 100:1) and fed to a pyrolysis reactor. The continuous feeding rate was 60 g/h, and the nitrogen flow rate was 1 L/min for the continuous pyrolysis process. GC-MS analysis was performed by AGILENT 6890N GC/ 5973N Ei Network MSD to evaluate the fuel range hydrocarbon distribution.

Results and discussions

Table 3 shows the proximate, ultimate analysis results and higher heating values of waste PP. Waste PP has a calorific value of 43.0 MJ/kg, and the carbon and hydrogen contents are 80.9 wt.% and 13.5 wt.%, respectively. The ultimate and proximate analysis results of waste PP are in line with other studies in the literature [11,12].

TAB. 3. Results of ultimate analysis (wt.%), proximate analysis (wt.%), and heating values (cal/g and MJ/kg) of waste PP

	PP
Ultimate analysis	
C	80.9
H	13.5
O*	5.6
N	0
S	0
Proximate analysis	
Ash	2.30
Moisture content	0.4
Volatile matter	94.8
Fixed carbon*	2.6
Heating Values	
HHV (cal/g)	10279
HHV (MJ/kg)	43.0

SOURCE: own elaboration

Figure 2 shows the FTIR spectra of waste PP utilized in this work. Polypropylene is formed by the polymerization of propylene and contains methylene, methane, and a methyl group. Symmetric and asymmetric stretch bands of methyl appear at 2954 cm^{-1} and 2862 cm^{-1}, while the umbrella mode of methyl appears at 1376 cm^{-1}. Moreover, symmetric and asymmetric stretch bands of methylene appear at 2916 cm^{-1} and 2850 cm^{-1}.

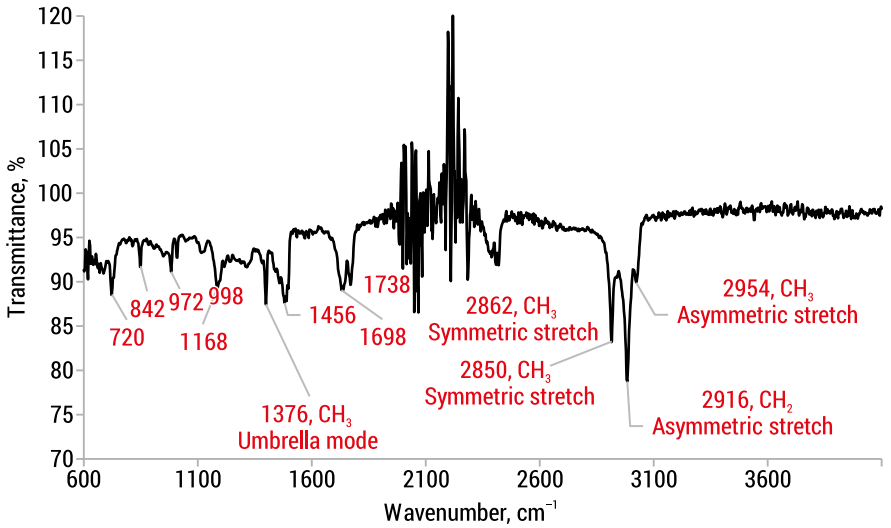

FIG. 2. FTIR spectra of waste PP

SOURCE: own elaboration

Figure 3 shows the TGA and DTG curves of waste PP utilized in this work. It can be seen from the graph that the thermal degradation starts at 250°C, and the maximum mass loss occurs at 443°C. Sharuddin et al., have studied TGA analyses for plastic types, and the result for PP was in the same line as the result of this study [11,13].

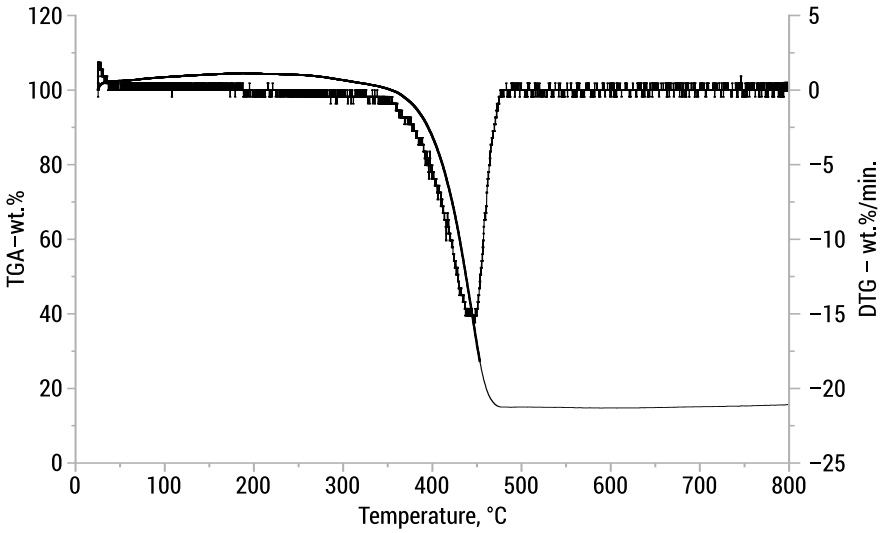

FIG. 3. TGA and DTG curves of waste PP

SOURCE: own elaboration

In this study, the melting point of PP was observed as 165°C by a DSC. The research of Majewsky et al. indicated the melting temperature of PP was observed as 165°C [17]. Moreover, Calero et al. studied the melting temperature of HDPE, LDPE, and PP samples, and the results showed that PE samples melted at 120–130°C whereas PP samples melted at 160°C [18]. While TGA and DSC analyses were conducted to assess thermal stabilization, ICP-MS and SEM-EDX analyses were conducted to evaluate the metal content of waste PP. Table 4 shows the element content of waste PP that ICP-MS determined.

TAB. 4. Results of metal content (µg/g) in waste PP

	Elements, µg/g												
	Pb	***Ba***	***Sr***	***Zn***	***Cu***	***Fe***	***Mn***	***Cr***	***Ca***	***K***	***Al***	***Mg***	***Na***
PP	0.18	28.6	5	28	81.7	72.8	1	1	174	70.9	2135	842.6	261.7

SOURCE: own elaboration

Aluminium has the highest concentration with 2135 µg/g, followed by magnesium, sodium, and calcium. The high concentrations of calcium, aluminium, magnesium, and sodium can be explained by the utilization of these metals as additives in the plastic production industry. Aluminium, calcium, and sodium are generally used as antioxidants in plastic production to reduce oxidation [19]. Calcium is used primarily as a filler and a photo-stabilizer in the form of $CaCO_3$ [21]. Aluminium and magnesium compounds are widely used as flame retardants to slow down or inhibit ignition or oxidation reactions of plastics [20, 22].

TAB. 5. SEM-EDX result of waste PP

Elements, wt.%									
C	***O***	***Na***	***Si***	***Ti***	***Cl***	***N***	***Cu***	***Al***	***Ca***
75.2	16.2	0	0.95	2.90	1.73	2.60	0.30	0.06	0

SOURCE: own elaboration

Table 5 shows the elemental composition of scanned areas of waste PP samples by weight percentages that SEM-EDX obtained. SEM-EDX results prove the presence of some elements in the sample, which ICP-MS did not detect since their quantity is below the limit. Titanium, silicon, and chlorine were the main elements seen by SEM-EDX. In general, titanium is used as a pigment, while calcium and silicon oxides may be used as reinforcing filler that provides tensile strength [18, 19].

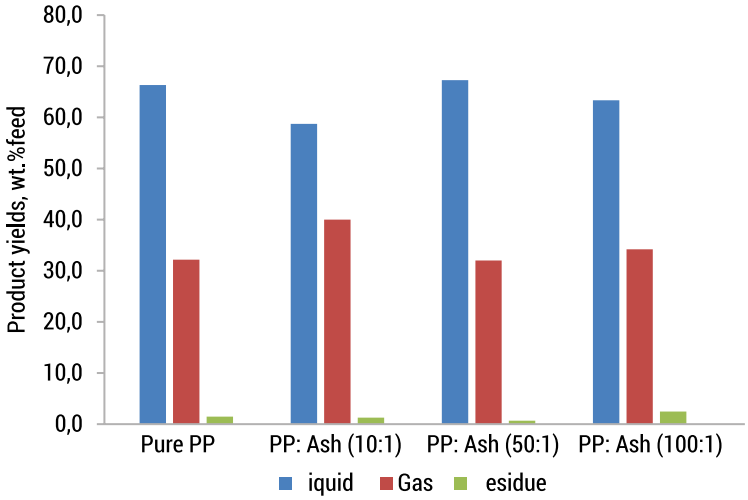

FIG. 4. Product yields for thermal and catalytic pyrolysis of PP
SOURCE: own elaboration

Pyrolysis experiments were carried out as thermal and catalytic to evaluate the effect of the metal fraction on the liquid product yield and quality. The product yields for the thermal pyrolysis of pure PP and the catalytic pyrolysis of PP with different PP-to-ash ratios (10:1, 50:1, and 100:1) are represented in Figure 4. The liquid yield for pyrolysis of pure PP is 66 wt.%, while liquid yields are 59 wt.% feed, 67 wt.% feed, and 63 wt.% feed for PP: Ash (10:1), PP: Ash (50:1), and PP: Ash (100:1), respectively. It can be seen from the graph that there is no remarkable effect of the metal fraction on liquid product yields since the liquid product yield has decreased in the presence of ash content with a PP-to-ash ratio of 10:1. The hydrocarbon composition of the liquid products of pure PP and the PP: Ash (10:1) were determined by the GC-MS analysis. Fuel range (C_5–C_{15}) hydrocarbon distribution increased from 72.5 wt.% to 81.6 wt.% in the presence of ash with a PP: Ash ratio of 10:1.

Conclusions

The detailed characterization of PP collected in Izmir provided information to evaluate their suitability as raw feedstock to achieve high conversion to the liquid product by pyrolysis process. This study concluded that the elemental composition of plastic waste could vary since several additives are used in the plastic production industry to improve the plastic properties for utilization in different sectors. According to TGA-DSC curves, PP completes its thermal degradation at 500°C, and the melting temperature is 165°C. The determined melting temperature can be used for process

optimization if pre-treatment is used for the pyrolysis system. The temperatures obtained with the DTG curves can be evaluated in optimizing the pyrolysis process to achieve maximum mass conversion. Aluminium, magnesium, sodium, and calcium were indicated as dominant elements by ICP-MS. The high concentrations of these metals can be explained by the utilization of these metals as antioxidants in plastic production to reduce oxidation. Titanium, silicon, and chlorine were the main elements seen by SEM-EDX. Primarily, these elements are used as a reinforcing filler that provides tensile strength. The yield of liquid products in thermal pyrolysis of pure PP and catalytic pyrolysis of PP with different ratios of PP to ash (10:1, 50:1, and 100:1) are 66 wt.%, 59 wt.%, 67 wt.%, and 63 wt.%, respectively. Moreover, the distribution of hydrocarbons in the fuel range (C_5–C_{15}) increased from 72.5 wt.% to 81.6 wt.% in the presence of 10:1 ash.

Acknowledgments: This work is supported and funded by the UK Department for Business, Energy and Industrial Strategy together with the Scientific and Technological Research Council of Turkey (TÜBİTAK; Project No. 119N302) and delivered by the British Council.

Literature

[1] ASTM International, *Standard Practice for Coding Plastic Manufactured Articles for Resin Identification*, https://www.astm.org/d7611_d7611m-21.html

[2] Elliott T., Gillie H., Thomson A., *European Union ' s plastic strategy and an impact assessment of the proposed directive on tackling single-use plastics items*. Elsevier Inc., 2020.

[3] Eriksen M.K., Damgaard A., Boldrin A., Astrup T.F., *Quality Assessment and Circularity Potential of Recovery Systems for Household Plastic Waste*, Journal of Industrial Ecology 2019, 23(1), p. 156–168.

[4] Anuar Sharuddin S.D., Abnisa F., Wan Daud W.M.A., Aroua M.K., *A review on pyrolysis of plastic wastes*, Energy Conversion and Management 2016, 115, p. 308–326.

[5] Areeprasert C. *et al*., *Municipal Plastic Waste Composition Study at Transfer Station of Bangkok and Possibility of its Energy Recovery by Pyrolysis*, Energy Procedia 2017, p. 222–226.

[6] Fortelný I., Michálková D., Kruliš Z., *An efficient method of material recycling of municipal plastic waste*, Polymer Degradation and Stability 2004, 85(3), p. 975–979.

[7] Demirci B., *Türkiye Plastik Sektörü* 2021 *Gerçekleşmeleri ve* 2022 *Beklentileri*. 2022.

[8] Aryan Y., Yadav P., Samadder S.R., *Life Cycle Assessment of the existing and proposed plastic waste management options in India: A case study*, Journal of Cleaner Production 2019, 211, p. 1268–1283.

[9] Soto J.M., Blázquez G., Calero M., Quesada L., Godoy V., Martín-Lara M.Á., *A real case study of mechanical recycling as an alternative for managing of polyethylene plastic film presented in mixed municipal solid waste*, Journal of Cleaner Production 2018, 203, p. 777–787.

[10] Hahladakis J.N., Aljabri H.M.S.J., *Delineating the plastic waste status in the State of Qatar: Potential opportunities, recovery and recycling routes*, Science of the Total Environment 2019, 653, p. 294–299.

[11] Zhou L., Zou H., Wang Y., Le Z., Liu Z., Adesina A.A., *Effect of potassium on thermogravimetric behavior and co-pyrolytic kinetics of wood biomass and low density polyethylene*, Renewable Energy 2017, 102, p. 134–141.

[12] Lin X., Kong L., Cai H., Zhang Q., Bi D., Yi W., *Effects of alkali and alkaline earth metals on the co-pyrolysis of cellulose and high density polyethylene using TGA and Py-GC/MS*, Fuel Processing Technology 2019, 191, p. 71–78.

[13] Annual Book of ASTM Standards, Section 5, American Society of Testing Materials, Philadelphia, 1993, p. D3172-D3189.

[14] Anuar Sharuddin S.D., Abnisa F., Wan Daud W.M.A., Aroua M.K., *Energy recovery from pyrolysis of plastic waste: Study on non-recycled plastics* (*NRP*) *data as the real measure of plastic waste*, Energy Conversion and Management 2017, 148, p. 925–934.

[15] Chhabra V., Bhattacharya S., Shastri Y., *Pyrolysis of mixed municipal solid waste: Characterisation, interaction effect and kinetic modelling using the thermogravimetric approach*, Waste Management 2019, 90, p. 152–167.

[16] Manivannan A., Seehra M.S., *Identification and quantification of polymers in waste plastics using differential scanning calorimetry*, ACS Division of Fuel Chemistry, Preprints 1997, 42(4), p. 1028–1030.

[17] Majewsky M., Bitter H., Eiche E., Horn H., *Determination of microplastic polyethylene* (*PE*) *and polypropylene* (*PP*) *in environmental samples using thermal analysis* (*TGA-DSC*), Science of the Total Environment 2016, 568, p. 507–511.

[18] Calero M. *et al.*, *Characterization of plastic materials present in municipal solid waste: Preliminary study for their mechanical recycling*, Detritus 2018, p. 104–112.

[19] Patchaiyappan A., Dowarah K., Zaki S., Prabakaran M., Jayakumar S., *Chemosphere Prevalence and characteristics of microplastics present in the street dust collected from Chennai metropolitan city, India* *, Chemosphere 2021, 269, p. 128757.

[20] Tolinski M., *Trends in Polyolefin and Additive Use*, Additives for Polyolefins 2009, p. 9–21.

[21] Ügdüler S., Van Geem K.M., Roosen M., Delbeke E.I.P., De Meester S., *Challenges and opportunities of solvent-based additive extraction methods for plastic recycling,* Waste Management 2020, 104, p. 148–182.

[22] Turku I., Kärki T., Rinne K., Puurtinen A., *Characterization of plastic blends made from mixed plastics waste of different sources*, Waste Management & Research 2017, 35(2), p. 200–206.

Environmental and water-use impact for indirect evaporative coolers in the mediterranean climate area

Keywords: indirect evaporative cooling technology, experimental tests, air-cooling system, water-use efficiency, CO_2 emissions

Abstract: The energy consumption of the heating, ventilation, and air-conditioning systems (HVAC) represents around 40% of energy consumption in Europe. According to several studies, evaporative cooling technology presents an interesting solution to conventional air-cooling systems in terms of energy efficiency. However, few research works analysed water-related indexes in indirect evaporative coolers (IEC). So, the main objective of this research study was to evaluate the environmental and the water-use impact on IEC systems in the Mediterranean climate area. Several experimental tests were carried out to fit the empirical models of cooling capacity, power consumption and water consumption of an IEC. These models were used for annual energy simulations. Several key performance indices (KPI) were obtained with the results of these annual simulations. These KPIs for the IEC system were evaluated for four different climate zones. Based on energy simulations, the IEC system reached the highest values of annual seasonal energy efficiency ratio (*SEER*), 3.8, and cooling capacity per unit of water consumed ($KPI_{C\text{-}W}$), 0.23 kWh/l, for the Athens weather conditions, but also the highest value of annual CO_2 emissions ($\dot{E}_{CO2}$), 3378.4 kgCO_2/year. The results showed that the IEC systems reached the highest values of environmental impact and water-use efficiency for hot climate zones.

Introduction

The energy consumption of the heating, ventilation, and air-conditioning systems (HVAC) represents a high percentage of the total energy consumption in the world, around 50% [1]. According to several studies in the last decade, the final energy consumption in buildings accounts for 40% of the total energy consumption and 36% of the total CO_2 emissions in Europe [2]. The Energy Performance of Buildings Directive established sustainable development and the achievement of competitive HVAC systems as main objectives [3]. The main types of HVAC systems are divided in the literature as: conventional HVAC systems based on direct expansion units, air-cooling systems based on evaporative cooling technology and hybrid HVAC systems, see Fig. 1.

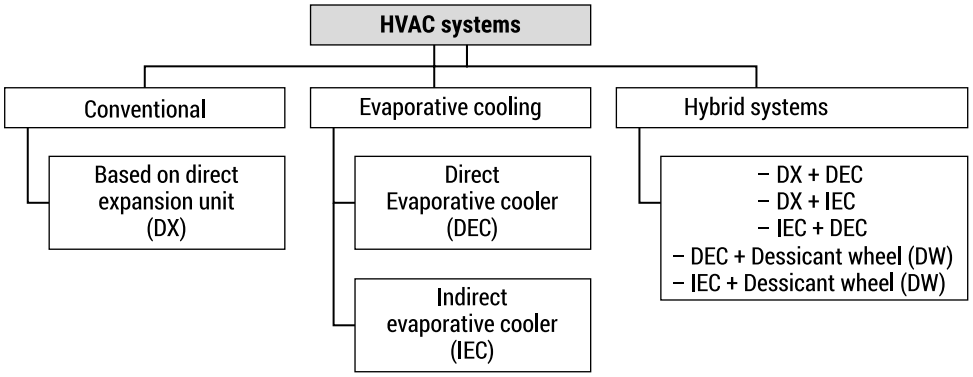

FIG. 1. Main types of air-cooling systems

SOURCE: own elaboration

Evaporative cooling technology presents an interesting solution to conventional cooling technologies based on direct expansion units. Most of the experimental studies of indirect evaporative coolers (IEC) focused on the analysis of energy performance. A recently published article performed the energy consumption comparison between three different air-cooling systems in Mediterranean climates [4]. The main finding was that the IEC system and the hybrid system, composed of an IEC system and a desiccant wheel (DW) consumed three, four, ten and fifteen times less than the conventional DX system depending on the climate zone. However, few research works have analysed water-related indexes in indirect evaporative coolers. A methodology to determine the water-use efficiency in evaporative coolers was developed [5]. Another study showed high values of water-use efficiency for the IEC technology and combined systems with IEC [6].

Based on the lack of research studies on environmental and water indexes of indirect evaporative coolers, the main objective of the present work was to evaluate the environmental impact and the water-use efficiency for indirect evaporative coolers in different climate zones of the Mediterranean area.

Experimental setup of the IEC system

An innovative air-cooling system based on an indirect evaporative cooler (IEC) was experimentally studied in this work. The evaluated IEC system was mainly composed of the following elements, see Fig. 2:

- An efficient counterflow heat exchanger.
- A process fan.
- A gross 60% filter (gross filter).
- An ePM_1 65% filter (fine filter).
- Several sensors of air temperature (T), air relative humidity (RH), pressure drop (P), volumetric air flow (V), electrical power consumption (W) and water consumption (W_W).

The sensors of air temperature, air relative humidity and pressure drop were used to evaluate the IEC performance. The accuracy of the sensors of air temperature, air relative humidity ratio, pressure dop in the outlet gate of the IEC system, volumetric air flow, electrical power consumption and water consumption are shown in Table 1.

TAB. 1. Accuracy of the sensors in experimental setup

Variable	Sensor	Accuracy
Temperature (T)	PT100	±0.2 °C (0–50°C)
Relative humidity (RH)	Capacitive	±3.0% (0–90%)
Pressure drop (P)	Piezo-resistive	±0.05 hPa (–150–150 hPa)
Volumetric air flow (V)	Differential	±5% reading (< 500 Pa)
Electrical power consumption (W)	3-phase	±1.0% reading (0–10 kW)
Water consumption (W_W)	3-paths valve	±2.0% reading (0–3 l/s)

SOURCE: own elaboration

The inlet air conditions were adjusted with an air handling unit (AHU) composed of a cooling coil, a heating coil, a steam humidifier and a centrifugal fan, as shown in Fig. 2. With this experimental setup, the IEC system was evaluated under different working conditions.

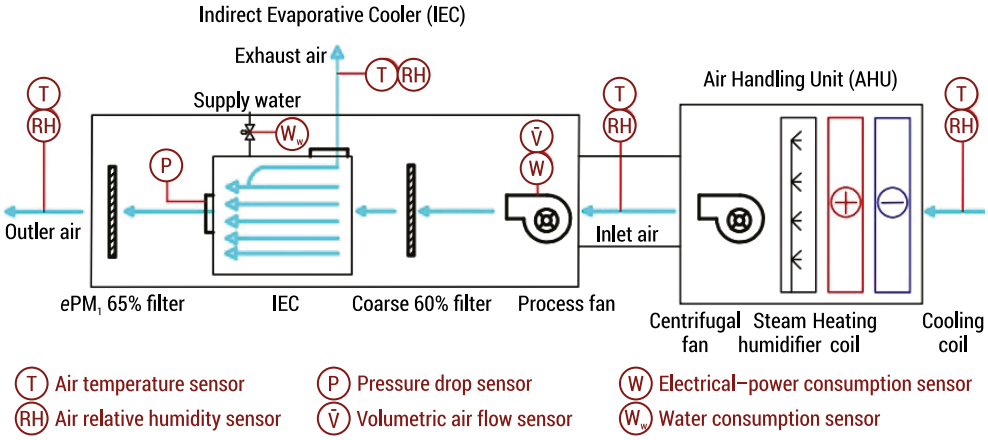

FIG. 2. Experimental setup of the evaluated IEC system

SOURCE: own elaboration

The IEC system worked with a single inlet air stream. This air flow was 100% inlet air (IA) which was divided into two air streams: exhaust air (EA) and outlet air (OA). This efficient air-cooling system consisted of alternative wet and dry channels separated by thin plates. The inlet air flow was cooled without increasing its air humidity ratio and the exhaust air flow was humidified and then exhausted outside. The most important characteristics of this indirect evaporative cooler are shown in Table 2. It should be noted that the value of the exhaust air ratio (R_{EX}) was the value of the relation between the exhaust air flow rate ($\dot{V}_{EA}$) and the inlet air flow rate ($\dot{V}_{IA}$). The nominal values of the cooling capacity, inlet air flow rate and exhaust air ratio for the evaluated IEC system were 18 kW, 5000 $m^3\ h^{-1}$ and 0.45, respectively.

TAB. 2. Main characteristics of evaluated IEC system

Parameter	Value	Unit
Nominal cooling capacity	18	kW
Nominal inlet air flow rate	5000	$m^3\ h^{-1}$
Exhaust air ratio ($R_{EX} = \dot{V}_{EA}/\dot{V}_{IA}$)	0.45	–
Nominal power consumption	1.5	kW
Maximum water consumption	44	$l\ h^{-1}$

SOURCE: own elaboration

The IEC system evaluation

Experimental tests were used to obtain the models of the different established output parameters: cooling capacity ($\dot{Q}_{cooling}$), power consumption ($\dot{W}_{cons}$), and water consumption ($\dot{V}_W$). Each experimental test was carried out under different working conditions during a steady-state period of thirty minutes. During these experimental tests in the IEC system, different values of inlet air temperature (T_{IA}), inlet air humidity ratio (ω_{IA}), inlet volumetric air flow ($\dot{V}_{IA}$), and exhaust air ratio (R_{EX}) were considered to develop the respective mathematical models, see Table 3.

TAB. 3. Summary of experimental tests in IEC system

Test	T_{IA} [°C]	$\dot{V}_{IA}$ [g/kg]	$\dot{V}_{IA}$ [m^3/h]	R_{EX} [–]	Test	T_{IA} [°C]	ω_{IA} [g/kg]	$\dot{V}_{IA}$ [m^3/h]	R_{EX} [–]
N1	32	11	3000	0.3	N6	40	11	3700	0.7
N2	32	8	3000	0.5	N7	32	11	4500	0.3
N3	32	11	3000	0.7	N8	32	14	4500	0.5
N4	40	11	3700	0.3	N9	32	11	4500	0.7
N5	40	8	3700	0.5					

SOURCE: own elaboration

Second order polynomial equations were used to obtain the relationship between the input parameters (inlet air temperature, inlet air humidity ratio, inlet volumetric air flow and exhaust air ratio) and the output parameters (cooling capacity, power consumption and water consumption), see Eq. 1.

$$\hat{Y} = b_0 + \sum_{i=1}^{k} b_i \cdot X_i + \sum_{i=1}^{k} b_{ii} \cdot X_i^2 + \sum_{i=1}^{k=1} \sum_{i=2;j>i}^{k} b_{ij} \cdot X_i \cdot X_j \quad (1)$$

Where $\hat{Y}$ was the estimated output value, X were the input parameters; b_0 was the average response in each model, and b_i, b_{ii} and b_{ij} were the estimated parameters of linear, quadratic and the second-order terms, respectively.

On the other hand, several energy simulations were carried out to compare the environmental impact of the IEC system under different climate zones in Mediterranean area climate. The Transient System Simulation Tool (TRNSYS) was the software used to carry out annual energy simulations [7]. The Köppen-Geiger climate classification was the climate criterion selected in this work [8]. It should be noted that the typical climate zones in the Mediterranean area were represented by the Almeria weather conditions, the Zagreb weather conditions, the Athens weather conditions, and the Genoa weather conditions, (see Table 4). The first letter of the nomenclatures of the four selected climate zones indicated the main climate,

the second letter of the nomenclatures of these climate zones indicated the characteristic precipitation and the third letter of these nomenclatures represented the characteristic temperature in summer:

- Almeria – BSk. (B: arid; S: steppe; k: cold arid).
- Athens – Csa. (C: warm temperate; s: summer dry; a: hot summer).
- Genoa – Csb. (C: warm temperate; s: summer dry; b: warm summer).
- Zagreb – Cfc. (C: warm temperate; f: fully humid; c: cool summer).

The IEC system was evaluated during the cooling period. The value of the annual cooling period for each climate zone was the number of hours in which the outdoor air temperature (T_{IA}) was above 18°C. These annual cooling periods and the CO_2 emission factors considered (F_{CO2}) for each city are also shown in Table 4. The values of the inlet volumetric air flow rate ($\dot{V}_{IA}$) and the exhaust air rate (R_{EX}) considered during the energy simulations were constant. These values were the respective nominal values, see Table 2.

TAB. 4. Selected climate zones of Mediterranean area

Climate zone	City	Country	F_{CO2} [kgCO_2/kWh]	Cooling period [h]
BSk	Almeria	Spain	0.331	4337.52
Csa	Athens	Greece	0.577	4072.08
Csb	Genoa	Italy	0.466	3343.36
Cfc	Zagreb	Croatia	0.273	2222.44

SOURCE: own elaboration

The IEC system studied in this work was evaluated in terms of the output parameters shown in Eq. 2 to Eq. 4, for the experimental tests N1-N9, see Table 2. In addition, several environmental impact indexes were established to analyse the energy behaviour of the IEC system, see Eq. 5 to Eq. 9. The values of environmental impact and water-use efficiency indexes were obtained for the respective annual cooling period of each selected climate zone:

$$\text{Cooling capacity [kW]: } \dot{Q}_{cooling} = \rho_{air} \cdot \dot{V}_{OA} \cdot (h_{IA} - h_{OA}) \tag{2}$$

$$\text{Power consumption [kW]: } \dot{W}_{cons} = \dot{W}_{Process\,fan} + \dot{W}_{Pump} \tag{3}$$

$$\text{Water consumption [l/h]: } \dot{V}_{W} = \text{Measurement of IEC water consumption} \tag{4}$$

$$\text{Seasonal energy efficiency ratio [–]: } SEER = \frac{\Sigma \dot{Q}_{cooling}}{\Sigma \dot{W}_{cons}} \tag{5}$$

$$\text{Annual } CO_2 \text{ emissions [kg}CO_2\text{/year]: } \dot{E}_{CO2} = F_{CO2} \cdot \Sigma \dot{W}_{cons} \tag{6}$$

$$\text{Cooling capacity per } CO_2 \text{ emission [kWh/kg}CO_2\text{]: } KPI_{C-CO2} = \frac{\sum \dot{Q}_{cooling}}{\sum \dot{E}CO2} \quad (7)$$

$$\text{Cooling capacity per unit of water consumed [kWh/l]: } KPI_{C-W} = \frac{\sum \dot{Q}_{cooling}}{\sum \dot{V}_W} \quad (8)$$

$$\text{Water consumption per } CO_2 \text{ emission [l/kg}CO_2\text{]: } KPI_{W-CO2} = \frac{\sum \dot{V}_W}{\sum \dot{E}CO2} \quad (9)$$

Experimental results of the output parameters

The results of cooling capacity, power consumption and water consumption of the IEC system for each experimental test are shown in Table 5. It can be observed that the highest values of $\dot{Q}_{cooling}$ were achieved under working conditions of tests N4 and N7. In both cases, the values of the inlet air humidity ratio and the exhaust air ratio were 11 g/kg and 0.3, respectively. However, the value of the cooling capacity in test N7 was higher than the value of the cooling capacity in test N4 due to the higher inlet air flow rate and so, a higher outlet air flow rate value. The lowest values of power consumption ($\dot{W}_{cons}$) were achieved when the value of the exhaust air ratio (R_{EX}) was 0.7, see tests N3, N6 and N9 in Table 5. This was due to the lower outlet air flow rate values for these three experimental tests. However, the highest values of water consumption ($\dot{V}_W$) were also reached for tests N3, N6 and N9 with a R_{EX} value of 0.7. This was due to the higher values of the humidified air flow ($\dot{V}_{EA}$).

From the experimental results shown in Table 5, mathematical models of the output parameters were developed. The coefficients of determination (R^2) for the cooling capacity ($\dot{Q}_{cooling}$) model, the power consumption ($\dot{W}_{cons}$) model and the water consumption ($\dot{V}_W$) model of the evaluated IEC system were greater than 0.987 for all output parameters. Therefore, these models adequately predicted the experimental behaviour of the IEC system.

TAB. 5. Experimental results of the output parameters for the studied IEC

Test	$\dot{Q}_{cooling}$ [kW]	$\dot{W}_{cons}$ [kW]	$\dot{V}_W$ [l/h]	Test	$\dot{Q}_{cooling}$ [kW]	$\dot{W}_{cons}$ [kW]	$\dot{V}_W$ [l/h]
N1	17.5	0.377	14.6	N6	22.2	0.669	43.7
N2	16.7	0.399	21.3	N7	33.5	1.130	17.2
N3	13.3	0.376	37.8	N8	26.8	1.126	40.8
N4	30.0	0.692	17.3	N9	24.3	1.079	42.5
N5	28.3	0.703	23.2				

SOURCE: own elaboration

Annual results of environmental and water-use impact

The annual values of several indexes related to environmental impact and water-use efficiency were obtained according to Eq. 5 to Eq. 9. The cooling period considered for each climate zone (Almeria, Athens, Genoa and Zagreb) was defined as the number of hours in which T_{IA} exceeded 18°C, see Table 4.

The results of the seasonal energy efficiency ratio and the cooling capacity per unit of water consumed indexes for the evaluated IEC system can be observed in Fig. 3. Both performance indexes were related to the cooling capacity of the IEC system. It should be noted that both indexes showed the same trend: the seasonal energy efficiency ratio (*SEER*) value increased when the cooling capacity per unit of water consumed (KPI_{C-W}) increased and vice versa. The highest *SEER* value was obtained for the climate conditions of Athens, being the only climate zone characterised by having a hot summer (Csa). The order of the cities shown in Fig. 3 and Fig. 4 was selected according to the descending order of the respective cooling periods, see Table 4. It can be observed that the order of the cities according to their *SEER* values did not coincide with this descending order. This direct relationship was not established since the cooling period was counted as the period in which the outdoor air temperature exceeded 18°C during a year. However, the climate severity in the different cooling periods was different for each climate zone or city. The results of the KPI_{C-W} index showed that the KPI_{C-W} value for the Athens weather conditions was 2.0, 3.8 and 7.6 times higher than the KPI_{C-W} values for the Zagreb, Almeria and Genoa weather conditions.

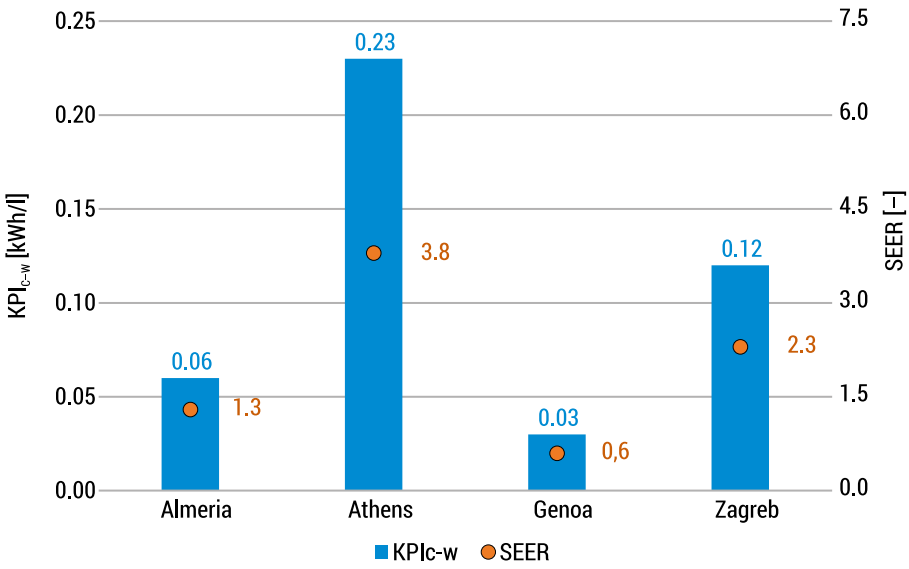

FIG. 3. Results of IEC annual environmental impact: KPI_{C-W} and SEER

SOURCE: own elaboration

Fig. 4 shows the results of CO_2 emissions ($\dot{E}_{CO2}$), the cooling capacity per CO_2 emission (KPI_{C-CO2}), and the water consumption per CO_2 emission (KPI_{W-CO2}) indexes for the evaluated IEC system. All these environmental impact indexes were related to the CO_2 emissions. According to Eq. 9, the value of this CO_2 emissions index was directly related to the value of annual power consumption and the CO_2 emissions factor (F_{CO2}) for each country. The value of this factor can be observed in Table 4. In fact, the order of the climate zones according to the value of F_{CO2} coincided with the order of the climate zones according to the results of annual CO_2 emissions ($\dot{E}_{CO2}$), see Fig. 4. However, it should be noted that the KPI_{W-CO2} value decreased and increased when the value of annual $\dot{E}_{CO2}$ increased and decreased, respectively, see Fig.4. The lowest annual $\dot{E}_{CO2}$ value and the highest KPI_{W-CO2} value were reached for the Zagreb weather conditions, 870.7 $kgCO_2$/year and 71.4 l/$kgCO_2$, respectively.

Another important environmental index was the cooling capacity per CO_2 emission (KPI_{C-CO2}). The results of this index can also be seen in Fig. 4. The highest values of the KPI_{C-CO2} index were reached for the Zagreb and Athens weather conditions, 8.3 kWh/$kgCO_2$ and 6.7 kWh/$kgCO_2$, respectively. The results of the KPI_{C-CO2} index showed that the KPI_{C-CO2} value for the Zagreb weather conditions was 1.2, 2.0 and 6.4 times higher than the KPI_{C-CO2} values for the Athens, Almeria and Genoa weather conditions, respectively. It should be noted that Zagreb was the climate zone with the lowest number of cooling hours.

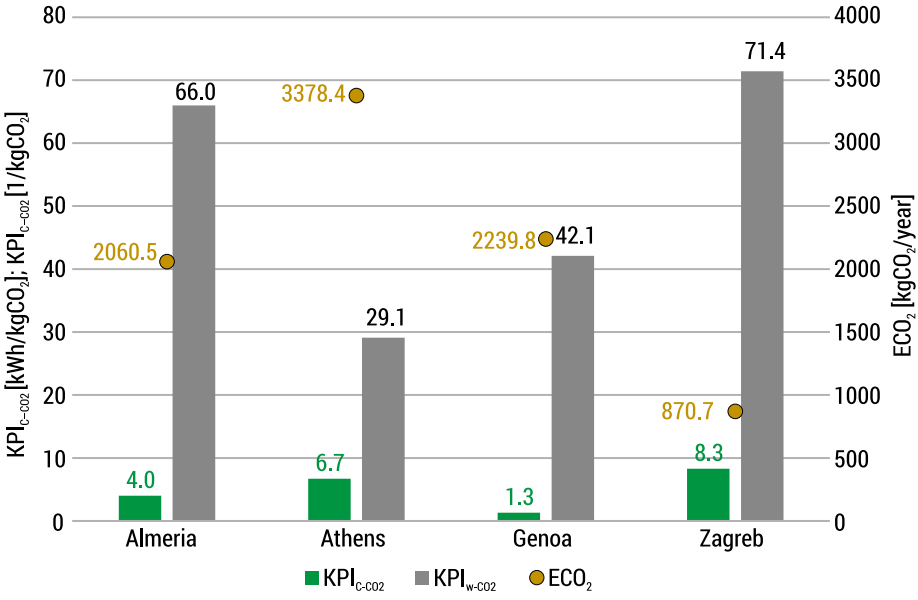

FIG. 4. Results of IEC annual environmental impact: KPI_{C-CO2}, KPI_{W-CO2} and $\dot{E}_{CO2}$

SOURCE: own elaboration

According to the results of the five indexes of environmental impact and water-use efficiency for the evaluated IEC system in the four climate zones representative of the Mediterranean climate area, the following points should be highlighted:

- The values of the seasonal energy efficiency ratio (*SEER*) ranged from 0.6 to 3.8 for the four climate zones. The IEC system for Athens weather conditions achieved the highest *SEER* value, 3.8. However, the IEC system for the weather conditions of Genoa obtained the lowest *SEER* value, 0.6, due to less severe climate conditions.
- The values of CO_2 emissions ($\dot{E}_{CO2}$) ranged from 870.7 to 3378.4 $kgCO_2$/year for the four climate zones. The IEC system for weather conditions of Zagreb, with a *SEER* value of 2.3, achieved the lowest value of CO_2 emissions, 870.7 $kgCO_2$/year. However, the IEC system for the weather conditions of Athens, despite having the highest *SEER* value, obtained the highest value of CO_2 emissions, 3378.4 $kgCO_2$/year. This was due to the fact that the values of the F_{CO2} factor and cooling period for the Athens climate zone were higher than those for the Zagreb climate zone.
- The values of the cooling capacity per CO_2 emission (KPI_{C-CO2}) ranged from 1.3 to 8.3 kWh/$kgCO_2$ for the four climate zones. The IEC system for the weather conditions of Zagreb, with the lowest value of annual CO_2 emissions, achieved the highest value of cooling capacity per CO_2 emission, 8.3 kWh/$kgCO_2$. However, the IEC system for the temperate weather conditions of Genoa obtained the lowest value of cooling capacity per CO_2 emission, 1.3 kWh/$kgCO_2$.
- The values of the cooling capacity per unit of water consumed (KPI_{W-CO2}) ranged from 0.03 to 0.23 kWh/l for the four climate zones. The IEC system for Athens weather conditions achieved the highest value of this important index, 0.23 kWh/l. However, the IEC system for the less severe climate conditions of Genoa showed the lowest value of this water-use efficiency index, 0.03 kWh/l.
- The values of the water consumption per CO_2 emission (KPI_{W-CO2}) ranged from 29.1 to 71.4 l/$kgCO_2$ for the four climate zones. The IEC system for the weather conditions of Athens, with the highest value of cooling capacity per unit of water consumed, achieved the lowest value of water consumption per CO_2 emission, 29.1 l/$kgCO_2$. However, the IEC system for weather conditions in Zagreb, with the lowest value of CO_2 emissions, obtained the highest value of water consumption per CO_2 emission, 71.4 l/$kgCO_2$.

Conclusions

In the present work, the environmental and water-use impact for indirect evaporative coolers (IEC) in the Mediterranean climate area were analysed. Experimental tests were carried out to develop several IEC models. These empirical models were used to simulate IEC annual operative conditions under four different European

climates. Then, key performance indices (KPI) such us *SEER*, KPI_{C-W}, KPI_{C-CO2} and $\dot{E}_{CO2}$ were calculated on an annual basis. Based on the annual results obtained, the IEC system for the weather conditions of Athens, the only climate zone characterised by having a hot summer (Csa), reached the highest values of *SEER* and KPI_{C-W}. Then, the IEC for Zagreb weather conditions showed the lowest value of $\dot{E}_{CO2}$ and the highest value of KPI_{C-CO2} due to the lowest number of cooling hours and, so, the lowest number of IEC operation hours. These results show that the IEC system for hot climate zones reaches the highest environmental impact and water-use efficiency values.

Literature

[1] Duan Z. et al. *Indirect evaporative cooling: Past, present and future potentials*. Renewable and Sustainable Energy Reviews 2012, 16(9), p. 6823–6850.

[2] Congedo P.M., Baglivo C., D'Agostino D., Zacà, I., *Cost-optimal design for nearly zero energy office buildings located in warm climates*. Energy 2015, 91, p. 967–982.

[3] Directive 2010/31/EU. European Parliament and of the Council of 19 May 2010 on the Energy Performance of Buildings (Recast); OJ L 153, 18.6.2010, p. 13–35 (BG, ES, CS, DA, DE, ET, EL, EN, FR, IT, LV, HU, MT, NL, PL, PT, RO, SK, SL, FI, SV) Special edition in Croatian; EUR-Lex: Brussels, Belgium, 2010; Chapter 12; Volume 003, p. 124–146.

[4] Romero-Lara M.J., Comino F., Ruiz de Adana M., *Seasonal analysis comparison of three air-cooling systems in terms of thermal comfort, air quality and energy consumption for school buildings in Mediterranean climates*. Energies 2021, 14, p. 4436.

[5] Sahai R., Shah N., Phadke A., *Addressing water consumption of evaporative coolers with greywather*. Environmental Energy Technologies Division. International Energy Studies Group 2012.

[6] Pistochini T., Modera M., *Water-use efficiency for alternative cooling technologies in arid climates*. Energy and Buildings 2011, 43, p. 631–638.

[7] Klein, S.A. TRNSYS 17: A Transient System Simulation Program. 2006. Not available online.

[8] Kottek M., Grieser J., Beck C., Rudolf B., Rubel F., *World map of the Köppen-Geiger climate classification updated*, Meteorol. Zeitschrift 2006, 15(3), p. 259–263.

Study of antioxidant properties of zinc and manganese complexes with phenolic acids

Keywords: antioxidants, phenolic acids, superoxide dismutase, IR spectroscopy, Raman spectroscopy

Abstract: Superoxide dismutase is the strongest antioxidant found in cells. It is an enzyme that is part of the antioxidant defence system developed by organisms to protect themselves from hazardous activity of free radicals [1]. These atoms or molecules both naturally occur in the body and may be formed as a result of external factors. In addition to a number of important functions they perform, their excess can contribute to the formation of many disorders in the normal functioning of the body [2]. Unfortunately, due to its relatively large size, superoxide dismutase cannot be used to treat the mentioned disorders, so for years the search for compounds with similar activity has continued [3]. One group of the compounds known for their antiradical properties are phenolic acids. They have both the ability to scavenge free radicals by donating a hydrogen atom and exhibit indirect antioxidant activity [4]. Their properties point to their potential use as SOD mimetics – low molecular weight compounds that act similarly to superoxide dismutase. In many of the SOD mimetics known to date, there is a metal ion that is the acceptor of the unpaired electron from the free radical, thereby inactivating it [3]. This paper reviews the literature on the subject and presents the synthesis of Mn and Zn metal complexes with p-coumaric and cinnamic acids. Spectroscopic studies, i.e. IR and Raman spectroscopy, were carried out, which showed that the studied metals attach to the carboxyl group of selected phenolic acids. The antioxidant properties of the complexes were determined through investigating OH radical inhibition and SOD activity. All the complexes showed antioxidant properties. Theoretical values of HOMO and LUMO molecular orbitals for the studied complexes were also determined as a parameter of their antioxidant capacity.

Introduction

Free radicals, including reactive oxygen species (ROS), are constantly produced by living organisms during their metabolism. Free radicals are atoms or molecule that have one or more unpaired electrons on its valence shell [2]. They have many functions in the body. For example, ROS are produced by phagocytes to fight pathogenic microorganisms, which make them an important part of body's immune system [5]. Free radicals also act as signalling molecules in the cerebral circulation and are essential in relay processes. They influence neuroplasticity, memory formation and the regulated production, release and reuptake of neurotransmitters. Furthermore, it is less well known that catecholamines and serotonin have significant free radical scavenging and neuroprotective capacities, indicating that redox regulation may also play a key role in neurotransmission [6].

Other beneficial effects of free radicals are related to their physiological roles in the functioning of many cellular signalling systems [5]. As secondary messengers, they are involved in cell growth and death; they can also be an inducer of apoptosis. Reactive oxygen species are also involved in: oxidation and reduction reactions in the respiratory chain; detoxification and purification of the body by, among other things, participating in the metabolism of xenobiotics; restoration of energy sources in the form of high-energy phosphate compounds; synthesis of prostaglandins and leukotrienes [7].

Free radicals are characterised by their high reactivity and lack of stability. In order to "find a pair" for their unpaired electron, free radicals tend to attack other molecules, and due to their high reactivity, can take electrons from them. Therefore, if due to overproduction or exogenous causes there are too many free radicals in the body, undesirable effects may occur. Excessive amounts of reactive oxygen species can lead to a chain reaction, and as a result, to cell damage [2]. ROS cause a number of dysfunctions in the body. The spectrum of these disorders is really wide, from irregularities in the functioning of neurotransmitters, to damage to cell membranes, to carcinogenesis. The action of free radicals has been linked to the aging process, as well as to many diseases, including autoimmune disorders, neurodegenerative diseases and cancer [2, 8, 9]. Selected diseases and disorders with which the effects of reactive oxygen species have so far been linked include Alzheimer's disease, insulin resistance, autism, malaria, multiple sclerosis, muscular dystrophy, cancer, Parkinson's disease, chronic granulomatous disease, depression, rheumatoid arthritis, schizophrenia, diabetes, and anaemia [8].

Phenolic acids are significant compounds of the human diet. Examples of compounds from the phenolic acid group include cinnamic acid and its derivative: p-coumaric acid, both shown in figure 1 [10].

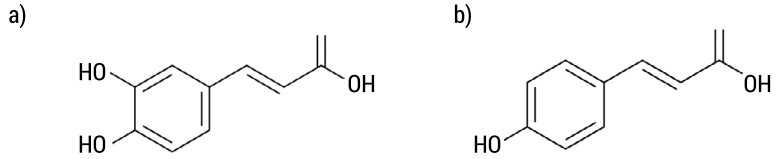

FIG. 1. a) Cinnamic acid and b) p-coumaric acid
SOURCE: [11]

Phenolic acids are characterised by their great antioxidant activity. They can scavenge various oxidants [12, 4], such as reactive oxygen species, even those as toxic as the hydroxyl radical [12]. They play a crucial role in scavenging superoxide radicals in the human organism. Their activity helps protect lipids and proteins present in the human body from oxidation [13]. The main method of neutralizing the action of free radicals is considered to be the donation of hydrogen from the OH group to the radical which leads to its neutralization. However, these compounds also exhibit indirect antioxidant activity by enhancing the body's endogenous protection against free radicals [14]. For example they can form complexes with metal ions, causing these metals to lose their oxidative properties. This effect is called chelation and can have application in treatment and prevention of many diseases [15]. Phenolic acids can also act as inducers of endogenous protective enzymes such as catalase and extracellular superoxide dismutase. In addition, phenolic acids show positive regulatory effects on signalling pathways [14], they can be inducers of apoptosis which improve cellular antioxidant defence mechanisms [16]. Phenolic acids also show ability to protect DNA from harmful effects of free radicals including H_2O_2 [4].

While phenolic acids belong to the non-enzymatic defence against free radicals, the body also has antioxidant enzymes, among them superoxide dismutase (SOD). This enzyme is considered to be the most effective antioxidant in the cell. It catalyses the dismutation of two molecules of superoxide anion radical to hydrogen peroxide and molecular oxygen [1]. This reaction occurs in two stages. In the first stage, the metal ion is reduced with the simultaneous release of an oxygen molecule, while in the second stage the metal ion is oxidised with the participation of a superoxide anion radical and hydrogen with the simultaneous generation of hydrogen peroxide [17]. There are three types of superoxide dismutase in mammal organisms:

- cytosolic – containing copper and zinc – CuZnSOD,
- mitochondrial – with manganese in the active centre – MnSOD,
- extracellular dismutase ECSOD [18,19].

Superoxide dismutase was proven to help to protect the body against many diseases, such as Parkinson's disease and cancer [20]. However, in many cases the use of natural superoxide dismutase does is not effective. This is because these enzymes are characterised by a relatively large size which causes a number of limitations in their application

[3, 20, 21]. These limitations include: lack of activity when administered orally; inability to gain access to the intracellular space where superoxide is produced; immunogenicity when obtained from non-human sources; short half-lives and high cost [20, 21]. To overcome these barriers, research has been conducted for years to develop low molecular weight compounds that are superoxide dismutase mimetics [3, 20, 21] that potentially could improve treatment of several diseases [21].

Experimental part

The syntheses of all of the complexes were carried out in the same way: a 0,001 mole of phenolic acid was weighed and then dissolved in a stoichiometric amount (10 cm^3) of 0,1M aqueous sodium hydroxide solution. The solution was stirred and heated to 50°C until the acid dissolved entirely. A clear solution of sodium salt of p-coumaric acid was obtained. At the next stage, 5 cm^3 of copper (II) chloride solution (0,0005 mole) was slowly added (dropwise) to the previously prepared solution of sodium salt of p-coumaric acid, stirring all the time. The stoichiometric ratio in the ligand mixture (p-coumarate ion: copper ion) was 2:1. The mixture was shaken on a shaker for 2h at 50°C. Then the whole mixture was left for 3 days for the precipitation of p-coumaric acid-copper complex. The precipitated complex was filtered off on a funnel with a filter paper and washed to remove residual chloride. The precipitate was allowed to dry at room temperature and then dried at 50°C for two days and transferred to a desiccator.

FTIR spectra of the obtained complexes were recorded on KBr matrix in the range of 4000–400 cm^{-1} using OPUS software. Raman spectra of the obtained complexes were also recorded using OPUS software in the range of 4000–400 cm^{-1}. All spectra were analysed using Specwiever software.

The antioxidant properties were investigated by OH radical inhibition assay. In its assay, the hydroxyl radical formed in the Fenton reaction is trapped by salicylic acid, and 2,3-dihydroxybenzoic acid is formed. The antioxidant competes with salicylic acid in trapping the hydroxyl radical and reduces the generation of 2,3-dihydroxybenzoic acid, which has an absorbance maximum at $\lambda = 510$ nm. The more effective the antioxidant, the lower the absorbance at $\lambda = 510$ nm [21]. Solutions of the studied complexes in dimethyl sulfoxide were prepared. Test sample (At) was as follows: 1 ml solution of the tested compound in dimethyl sulfoxide, 0,3 ml of 8 mM $FeSO_4$ solution, 1 ml of 3 mM ethanolic salicylic acid solution and 0,25 ml of 20 mM H_2O_2 solution were added to a test tube and mixed. The sample was then incubated at 37°C. After 30 minutes, 0,5 ml deionized water was added and the absorbance was measured at $\lambda = 510$ nm in reference to deionized water. Control sample (A_c) contained H_2O instead of H_2O_2 and blank sample (A_b) contained dimethyl sulfoxide instead of a solution of the tested compound in dimethyl sulfoxide. Percentage of OH radical inhibition was calculated using the following formula (1):

$$I\% = \left(1 - \left(\frac{A_t - A_c}{A_b}\right)\right) \times 100\% \quad (1)$$

where: A_t – absorbance of the tested sample, A_c – absorbance of the control sample, A_b – absorbance of blank sample.

SOD activity was determined by an indirect method based on the competitive reaction of the tested compounds and XTT dye (2,3-bis(2-methoxy-4-nitro5-sulfophenyl)-2h-tetrazolium-5-carboxanilide natrium salt) with a saturated solution of potassium peroxide in dimethyl sulfoxide. The studied complexes, acting as scavengers of superoxide anion radical, decreased the absorbance at 480 nm [23]. Solutions of the studied complexes in dimethyl sulfoxide were prepared. Test sample (At) was as follows: 100 µl of a solution of the tested compound in dimethyl sulfoxide, 2 ml of 0,01 M phosphate buffer and 150 µl of XTT dye solution in dimethyl sulfoxide were added to a test tube. Then the sample was mixed, 100 µl of saturated KO_2 solution was added and the sample was mixed again. Then the sample was incubated in the dark. After 30 minutes, the absorbance at $\lambda = 480$ nm was measured in reference to the phosphate buffer used for sample preparation. Control sample (A_c) contained dimethyl sulfoxide instead of a solution of the tested compound in dimethyl sulfoxide. Percentage of radical inhibition was calculated using the following formula (2):

$$I\% = \frac{A_c - A_t}{A_c} \times 100\% \quad (2)$$

where: A_t – absorbance of the tested sample, A_c – absorbance of the control sample.

The electron affinity (EA), which is a parameter that determines the radical inactivation capacity, was determined [24]. For model systems of zinc and manganese complexes, the energies of Zn (II) and Mn (II) complexes were calculated, as well as the energies of complexes with reduced charge of the central ion (which is the effect of electron transfer during the reaction). Which can be represented as (3)–(4):

$$E - Zn(II) + O_2^{\bullet -} \rightarrow E - Zn(II)^{(-1)} + O_2 \quad (3)$$

$$E - Mn(II) + O_2^{\bullet -} \rightarrow E - Mn(II)^{(-1)} + O_2 \quad (4)$$

According to literature the compounds with the lowest EA value are characterized by increased SOD activity [24].

The energy values of HOMO (Highest Occupied Molecular Orbital) and LUMO (Lowest Unoccupied Molecular Orbital) orbitals of the optimized chemical structures were calculated. Molecules with higher HOMO energies exhibit lower SOD activity [24] and those having low LUMO energy value are characterized by high SOD activity [25].

Results

Examples of IR and Raman spectra are presented in figure 2. The values of wave numbers and intensities as well as band assignments present in the spectra of the studied compounds are summarised in tables 1 and 2. They were compared to literature values of studied phenolic acids.

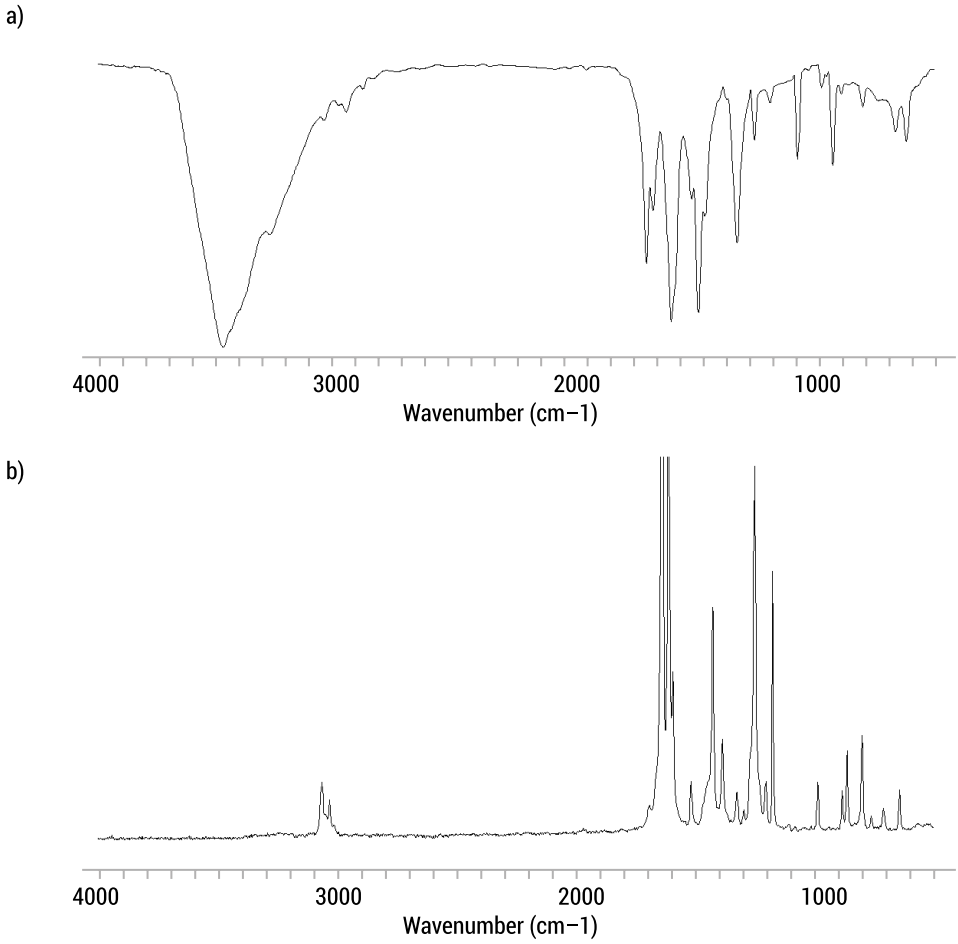

FIG. 2. a) IR and b) Raman spectra of manganese p-coumarate
SOURCE: own elaboration

TAB. 1. Wave numbers and intensities of the bands of the IR_{KBr} and Raman spectra of p-coumaric acid and its complex with manganese and zinc

P-coumaric acid [26]		Manganese p-coumarate		Zinc p-coumarate		Assignment [27]
IR_{KBr}	Raman	IR_{KBr}	Raman	IR_{KBr}	Raman	
3383 VS	–	3456 VS	–	3425 VS	–	$\upsilon (OH)_{aro.}$
3080 W	3069 VW	–	3062 W	–	3060 W	$\upsilon (CH)_{aro.} + \upsilon(CH)_{C=C}$
3026 W	2025 VW	3023W	3030 VW	3027 M	3036 VW	$\upsilon (CH)_{aro.} + \upsilon(CH)_{C=C}$
2839 M–2513 M	–	2959 W–2813 VW	–	2974 W–2819 W	2985 VW	$\upsilon (OH)_{aro.}$
1672 VS	–	–	–	–	–	υ (C=O)
1628 S	1636 M	1636 S	1638 VS	1636 S	1647 VS	$\upsilon (CC)_{C=C}$
1601 VS	1606 VS	1609 M	1609 M	1606 S	1624 M	$\upsilon (CC)_{aro}$
1591 S	1593 M	–	–	–	1601 W	$\upsilon (CC)_{aro}$
–	–	1528 VS	–	1541 S	–	$\upsilon_{as}(COO^{-})$
1512 S	1519 VW	–	1515 VW	1512 VS	1538 VW	$\upsilon (CC)_{aro}$
1449 VS	1448 W	1442 M	–	1445 M	1450 VW	$\upsilon (CC)_{aro}$
–	–	1412 S	1425 W	–	1409 W	$\upsilon_{s}(COO^{-})$
1379 M	–	1384 M	1384 VW	1398 M	–	$\beta (CH)_{C=C} + \beta (OH)_{aro.}$
1327 S	–	–	1324 VW	–	1330 VW	$\beta (CH)_{C=C}$
1314 S	1306 VW	1290 W	1294 VW	1285 W	1304 VW	$\beta (CH)_{C=C} + \beta (CH)_{aro.}$
1283 M	1282 W	1245 M	1250 M	–	1263 M	υ (C–OH)
1244 VS	1260 M	–	–	1244 S	–	$\beta (OH)_{aro.}$
1215 VS	1213 M	–	1204 VW	–	1208 W	β (CH)
1173 S	1172 S	1171W	1174 W	1171 M	1157 VW	$\beta (CH)_{aro.}$
1105 M	–	1105 W	–	1106 W	–	β (CH)
1013 W	–	–	–	–	1033 VW	β (CH)
978 S	977 W	984 M	986 VW	986 W	982 VW	υ (CCO)
941 M	952 VW	–	–	939 VW	–	$\gamma(CH)_{aro.}$
920 M	–	881 VW	882 VW	–	876 VW	γ(CO)
860 W	864 W	–	862 VW	870 W	853 VW	γ(CH)
833 S	837 VW	834 M	–	833 M	–	γ
799 M	800 W	797 W	800 VW	810 W	–	α (CCC)
–	–	–	760 VW	741 W	764 VW	$\gamma_{s}(COO^{-})$
692 M	680 VW	705 W	710 VW	–	–	β (CO)
646 W	645 VW	–	643 VW	642 W	619VW	Φ (CC)
557 W	552 VW	565 W	–	–	–	γ(OH)

P-coumaric acid [26]		Manganese p-coumarate		Zinc p-coumarate		Assignment [27]
IR_{KBr}	Raman	IR_{KBr}	Raman	IR_{KBr}	Raman	
525 M	534 VW	–	–	535 W	–	α (C=C–C)
–	–	–	–	520 W	–	$\beta_s(COO^-)$
517 M	516 VW	517 W	–	–	–	Φ (CC)
453 W		–	–	–	–	Φ (CC)
430 VW	421 VW					β (CH)

s – strong, vs – very strong, m – medium, sh – shoulder, w – weak, vw – very weak

SOURCE: own elaboration

TAB. 2. Wave numbers and intensities of the bands of the IR_{KBr} and Raman spectra of cinnamic acid and its complex with manganese and zinc

Cinnamic acid [28]		Manganese cinnamate		Zinc cinnamate		Assignment [27]
IR_{KBr}	Raman	IR_{KBr}	Raman	IR_{KBr}	Raman	
3495 W	–	3456 S	–	3416 S	–	υ (OH)
3066 M	3068 W	3058 S	3061 M	3061 S	3060 M	υ (CH)
3027 M	3031 VW	3025 S	3029 VW	3030 S	3036 W	υ (CH)
2982 M–2542 M	–	–	–	–	2985 VW	υ (OH)
1685 VS	–	–	–	–	–	υ (C=O)
1629 S	1638 VS	1638 M	1640 VS	1646 M	1647 VS	$\upsilon (C=C)_{.}$
–	1600 S	–	1599 M	–	1601 M	$\upsilon (CC)_{aro.}$ + β (CH)
1577 M	–	1574 M	–	1578 M	–	$\upsilon (CC)_{aro.}$ + β (CH) +α (CCC)
–	–	1537 S	–	1538 S	1538 VW	$\upsilon_{as}(COO^-)$
1495 M	1496 VW	1473 M	1497 VW	1504 M	1498 VW	$\beta (CH)_{aro.}$
1449 S	1444 VW	1450 M	1453 W	1449 M	1450 W	$\upsilon (CC)_{aro}$+ $\beta (CH)_{aro.}$
1421 S	–	–	1427 VW	–	–	$\upsilon (CC)_{aro}$+ β (CH) +β (OH)
–	–	1418 S	1396 VW	1408 VS	1409 VW	$\upsilon_s(COO^-)$
1334 M	1329 VW	–	–	–	1330 VW	$\upsilon (CC)_{aro.}$+ β (OH) + $\beta (CH)_{aro.}$ + β (CH)
1313 S	1308 VW	–	1325 VW	1302 W	–	$\upsilon (CC)_{aro}$+ $\beta(CH)_{aro.}$ +β (CH)

Cinnamic acid [28]		Manganese cinnamate		Zinc cinnamate		Assignment [27]
IR_{KBr}	Raman	IR_{KBr}	Raman	IR_{KBr}	Raman	
1286 S	1293 M	–	1299 VW	–	1304 VW	υ C–(OH)+ $υ(CC)_{aro.}$ +β (OH)
–	–	1252 W	1254 W	1258 W	1263 W	υ (CC) + β (CH)
1222 S	1211 W	1204 W	1204 W	1207 W	1208 W	$υ (CC)_{aro.}$ + β (CH)
1176 M	1179 M	–	1180 W	1157 VW	1157 W	$υ (CC)_{aro}$+ $β (CH)_{aro.}$
–	–	–	–	–	–	$β (CH)_{aro.}$
1073 W	–	1071 W	–	1069 VW	–	$υ (CC)_{aro}$+ $β (CH)_{aro.}$
1027 W	1027 W	1028 W	1029 VW	1029 W	1033 VW	$υ (CC)_{aro}$+ $β (CH)_{aro.}$
–	1002 M	–	1001 W	–	1003 W	$υ (CC)_{aro}$+ α (CCC)
980 S	977 VW	983 W	–	915 VW	982 VW	υ (C–O)+ γ(C–C)
914 M	–	–	–	–	–	γ(CCH)
875 W	876 VW	881 W	878 VW	877 W	878 VW	$γ(CH)_{aro.}$
–	–	–	849 VW	–	853 VW	$β_s (COO^-)$
847 W	849 VW	–	–	850 W	–	$γ(CH)_{aro.}$+ γ(OCOC) + γ (CCC)
769 S	771 VW	779 W	–	771 M	763 VW	$γ(CH)_{aro.}$+ γ (HCCO) + γ(OCOC)
–	–	717 W	–	717 W	–	$γ_s (COO^-)$
711 S	714 VW	–	–		–	$γ(CH)_{aro.}$+Φ(CCC)
–	688 VW	687 M	–	683 M	–	β (C=O) + α (CCC)
683 M	681 VW	–	–	–	–	α (CCC)
620 W	619 VW	696 W	620 VW	637 W	619 VW	β (C=O) + α (CCC)
590 M	–	–	–	–	–	γ(C=O)
542 M	–	537 W	–	538 VW	–	γ(OCC) + α(C=C–C)
483 M	–	491 W	–	484 W	–	Φ(CCC)

s – strong, vs – very strong, m – medium, sh – shoulder, w – weak, vw – very weak

SOURCE: own elaboration

In the spectra of complexes of p-coumaric and cinnamic acids with manganese, and zinc, bands indicating the presence of C=O carboxylic group, such as very strong stretching vibration υ(C=O) in the range 1672–1685 cm^{-1}, disappeared. In the case of IR_{KBr} spectra of cinnamates, asymmetric stretching vibrations $υ_{as}(COO^-)$ appear in the range 1537–1538 cm^{-1}, symmetric stretching vibrations $υ_s(COO^-)$ in the range 1408–1414 cm^{-1} and bending vibrations $γ_s(COO^-)$ appear in the range 717 cm^{-1}. When it comes to p-coumarates, asymmetric stretching vibrations $υ_{as}(COO^-)$ appear in the range 1528–1541 cm^{-1}, $υ_s(COO^-)$ in the range 1412 cm^{-1} and bending vibrations $γ_s(COO^-)$ appear in the range 741 cm^{-1}. Raman spectra show symmetric bending

oscillations β_s(COO–) in the range 849–853 cm^{-1} (cinnamates), asymmetric stretching vibrations υ_{as}(COO^-) 1538 cm^{-1} (zinc cinnamate) and symmetric stretching vibrations υ_s(COO–) in the range 1396–1409 cm^{-1} (cinnamates) and 1409–1425 cm^{-1} (p-coumarates).

Figure 3 shows the results of investigating OH radical inhibition properties and SOD activity of the tested complexes. SOD activity of tested complexes was compared using IC50 parameter (concentration [mM] at which the tested compound shows scavenging of 50% of radical). When analysing OH radical inhibition activity it was not possible to determine IC50 parameter so activity of solutions of concentration 1 mM was compared instead.

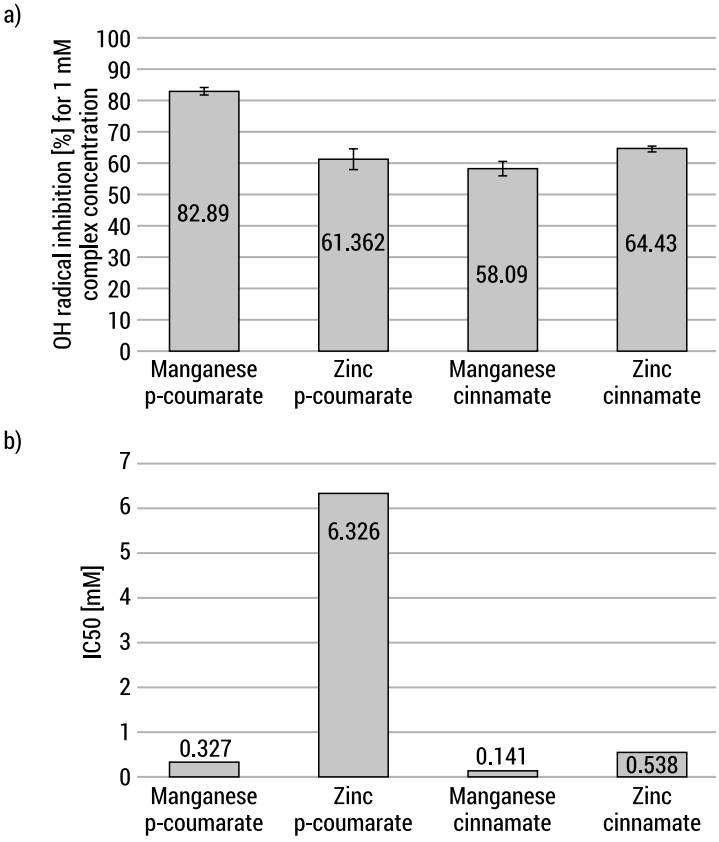

FIG. 3. Results of a) OH radical inhibition activity assay and b) SOD activity assay
SOURCE: own elaboration

As shown in figure 3, manganese p-coumarate in concentration 1 mM shows the best OH radical scavenging activity (82,89%±1,194). All of the other investigated complexes show similar activity in that area with manganese cinnamate being least

active (58,09%±2,143). Considering all of the above it is not possible to find an unambiguous relationship between which of investigated metals have the greatest impact on increasing OH scavenging activity of phenolic acids.

As a parameter of antioxidant capacity of the studied compounds, the values of the energy of molecular orbitals HOMO and LUMO were determined (theoretically) for optimised structures of complexes of zinc and manganese with the studied acids. Geometric optimization was performed using the density functional B3LYP method using the LAN2LDZ database.

TAB. 3. Theoretical energy parameters for molecules of manganese and zinc complexes with p-coumaric and cinnamic acids

Parameter	Manganese pcoumarate	Zinc pcoumarate	Manganese cinnamate	Zinc cinnamate
HOMO [eV]	−6,3867	−8,9892	−6,1614	−9,5671
LUMO [eV]	−6,3189	−6,07948	−5,4321	−6,2887
ΔHOMO/LUMO [eV]	0,0678	2,90972	0,7293	3,2784
EA [kcal/mol]	−43,2470	−27,4433	−22,5740	−30,0279

SOURCE: own elaboration

Molecules with higher HOMO energies show lower SOD activity [24]. On the other hand, according to Schepetkin et al. [25], molecules that have low LUMO energies have high SOD activity. Schepetkin also found by comparing theoretical data of calculated HOMO and LUMO energies that they correlate well with experimentally determined SOD activity, which was represented as log (1 / IC50) [25]. According to the calculated HOMO and LUMO energy values, manganese cinnamate have the highest SOD activity, among the studied complexes. This is consistent with the results of the SOD activity assay. Figures 4 and 5 show shapes of theoretical HOMO and LUMO orbitals of studied complexes.

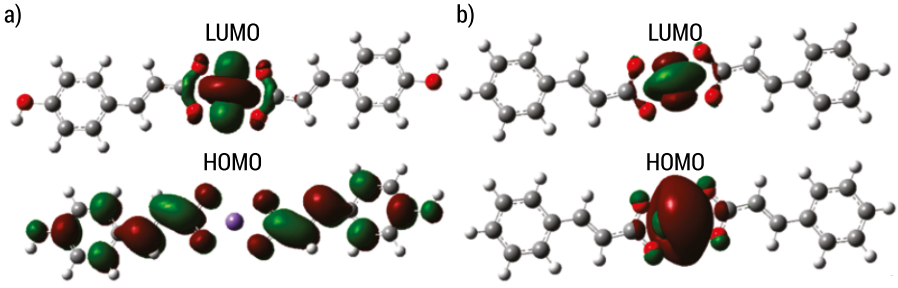

FIG. 4. Shapes of theoretical HOMO and LUMO orbitals of a) manganese p-coumarate and b) manganese cinnamate

SOURCE: own elaboration

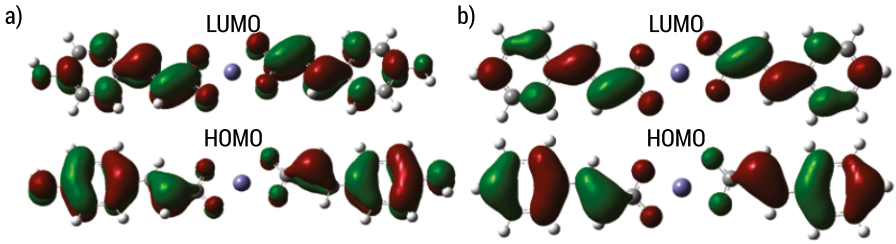

FIG. 5. Shapes of theoretical HOMO and LUMO orbitals of a) zinc p-coumarate and b) zinc cinnamate

SOURCE: own elaboration

Based on the calculated values of the electron affinity EA, it can be concluded that the studied complexes exhibit a rather good capacity to scavenge the superoxide radical, a result consistent with those obtained in the performed tests for OH radical inhibition and SOD activity. The EA energy for superoxide dismutase is –195,79 kcal/mol [24]. With respect to this value, the highest SOD activity among manganese complexes is shown by manganese p-coumarate. Manganese complex with cinnamic acid show lower activity. Considering the influence of the ligand on the antioxidant properties of SOD, it can be observed that complexes with cinnamic acid are characterised by the lowest potential to inactivate the superoxide radical, which, however, was not unambiguously confirmed by antioxidant studies.

Conclusions

Manganese and zinc complexes with p-coumaric and cinnamic acid exhibit good antioxidant properties and high SOD activity. It was proven both by OH radical inhibition and SOD activity assays. Manganese p-coumarate showed the highest level of OH radical inhibition, and the complex with the best SOD activity was manganese cinnamate. When it comes to SOD activity determined by theoretical parameters such as electron affinity and HOMO and LUMO energies, manganese p-coumarate showed the best results. FTIR and Raman spectra showed that the synthesis of said complexes is possible and that the metals attach to the carboxyl group of investigated acids. The studied metal complexes with phenolic acids are good antioxidants and can be considered as potential mimetics of superoxide dismutase, which could help in treatment of various diseases. Further research is needed to confirm the properties of the tested compounds and the possibility and safety of their application.

Acknowledgement: Research funded by the NCN grant OPUS 15 UMO-2018/29/B/NZ9/01997.

Literature

[1] Ighodaro O.M., Akinloye O.A., *First line defence antioxidants-superoxide dismutase* (*SOD*)*, catalase* (*CAT*) *and glutathione peroxidase* (*GPX*)*: Their fundamental role in the entire antioxidant defence grid*, Alexandria Journal of Medicine 2017, 54(4), p. 287–293.

[2] Phaniendra A., Jestadi D.B., Periyasamy L., *Free Radicals: Properties, Sources, Targets, and Their Implication in Various Diseases*, Indian Journal of Clinical Biochemistry 2014, 30(1), p. 11–26.

[3] Woźniak M., Czyż M., *Mimetyki dysmutazy ponadtlenkowej – potencjalne zastosowania kliniczne*, Postepy Hig Med Dosw.(online) 2008, 62, p. 613–624.

[4] Sevgi K., Tepe B., Sarikurkcu C., *Antioxidant and DNA damage protection potentials of selected phenolic acids*, Food and Chemical Toxicology 2015, 77, p. 12–21.

[5] Pham-Huy L.A., He H., Pham-Huy C., *Free radicals, antioxidants in disease and health*, International journal of biomedical science: IJBS 2008, 4(2), p. 89–96.

[6] Bókkon I., *Recognition of functional roles of free radicals*, Current neuropharmacology 2012, 10(4), p. 287–288.

[7] Wójcik A., Czerniak J., *Reaktywne formy tlenu*, Śląski Uniwersytet Medyczny w Katowicach 2014

[8] Di Meo S., Venditti P., *Evolution of the Knowledge of Free Radicals and Other Oxidants,* Oxidative Medicine and Cellular Longevity 2020, vol. 2020, Article ID 9829176, 32.

[9] Petzke E., *Ocena właściwości antyoksydacyjnych* 3,4,5,4'*-tetrametoksystylbenu w modelu kancerogenezy chemicznej u szczura*, Doctoral thesis 2017 Poznań.

[10] Vuolo M.M., Lima V.S., Maróstica Junior M.R., *Phenolic Compounds: Structure, Classification, and Antioxidant Power*, Bioactive Compounds 2019, p. 33–50.

[11] Sigmaaldrich.com.

[12] Sroka Z., Cisowski W., *Hydrogen peroxide scavenging, antioxidant and anti-radical activity of some phenolic acids,* Food and Chemical Toxicology 2003, 41(6), p. 753–758.

[13] Nikolic K.M., *Theoretical study of phenolic antioxidants properties in reaction with oxygen-centered radicals*, Journal of molecular structure: THEOCHEM 2006, 774(1–3), p. 95–105.

[14] Kumar N., Goel N., *Phenolic acids: Natural versatile molecules with promising therapeutic applications*, Biotechnology Reports 2019, e00370.

[15] Craft B.D., Kerrihard A.L., Amarowicz R., Pegg R.B., *Phenol-Based Antioxidants and the In Vitro Methods Used for Their Assessment,* Comprehensive Reviews in Food Science and Food Safety 2012, 11(2), 148–173.

[16] Saibabu V., Fatima Z., Khan L.A., Hameed S., *Therapeutic Potential of Dietary Phenolic Acids,* Advances in Pharmacological Sciences 2015, p. 1–10.

[17] Gałecka E., Jacewicz R., Mrowicka M., Florkowski A., Gałecki P., *Antioxidative enzymes-structure, properties, functions*, Polski Merkuriusz Lekarski: Organ Polskiego Towarzystwa Lekarskieg 2008, 25(147), p. 266–268.

[18] Kulbacka J., Saczko J., Chwiłkowska A., *Stres oksydacyjny w procesach uszkodzenia komórek,* Pol. Merk. Lek. 2009, XXVII, 157, p. 44–47.

[19] Skrzycki M., Czeczot H., *Zewnątrzkomórkowa dysmutaza ponadtlenkowa* (*EC-SOD*) *– budowa, właściwości i funkcje*, Postepy Hig Med Dosw.(online) 2004, 58, p. 301–311.

[20] Salvemini D., Riley D.P., Cuzzocrea S., *Sod mimetics are coming of age,* Nature Reviews Drug Discovery 2002, 1(5), p. 367–374.

[21] Riley D.P., Schall, O.F., *Structure – Activity Studies and the Design of Synthetic Superoxide Dismutase* (*SOD*) *Mimetics as Therapeutics*, Advances in Inorganic Chemistry 2006, 59, p. 233–263.

[22] Xiong S., Li A., Huang N., Lu F., Hou D., *Antioxidant and immunoregulatory activity of different polysaccharide fractions from tuber of Ophiopogon japonicus*, Carbohydrate Polymers 2011, 86(3), p. 1273–1280.

[23] Štarha P., Trávníček Z., Herchel R., Popa I., Suchý P., Vančo J., *Dinuclear copper*(*II*) *complexes containing* 6-(*benzylamino*)*purines as bridging ligands: Synthesis, characterization, and in vitro and in vivo antioxidant activities,* Journal of Inorganic Biochemistry 2009, 103(3), p. 432–440.

[24] Ji H.-F., Zhang H.-Y., *A Theoretical Study on Cu*(*II*) *Binding Modes and Antioxidant Activity of Mammalian Normal Prion Protein,* Chemical Research in Toxicology 2004, 17(4), p. 471–475.

[25] Schepetkin I., Potapov A., Khlebnikov A., Korotkova E., Lukina A., Malovichko G., Kirpotina L., Quinn M.T., *Decomposition of reactive oxygen species by copper*(*II*) *bis*(1-*pyrazolyl*)*methane complexes*, JBIC Journal of Biological Inorganic Chemistry 2006, 11(4), p. 499–513.

[26] Świsłocka R., Kowczyk-Sadowy M., Kalinowska M., Lewandowski W., *Spectroscopic* (*FT-IR, FT-Raman,* 1*H and* 13*C NMR*) *and theoretical studies of p-coumaric acid and alkali metal p-coumarates,* Spectroscopy 2012 27(1), p. 35–48.

[27] Varsanyi G., *Assignment for Vibrational Spectra of Seven Hundered Benzene Derivatives;* Adam Hilger 1974: London.

[28] Kalinowska M., Świsłocka R., Lewandowski W., *The spectroscopic* (*FT-IR, FT-Raman and* 1*H,* 13*C NMR*) *and theoretical studies of cinnamic acid and alkali metal cinnamates,* Journal of Molecular Structure 2007, 834–836, p. 572–580.

The application of nanoadsorbents in wastewater treatment

Keywords: adsorption, heavy metals, nanomaterials, water treatment, biosorption

Abstract: The aim of this review was to describe the recent achievements in the application of nanoparticles as biosorbent nanocomposites in heavy metal removal from water and wastewater. Treatment of water and wastewater contaminated with heavy metal ions is one of the main tasks of environmental engineering. This is due to the increasing industrialization of society. In addition, heavy metals getting into the environment result in serious disturbances in the metabolism of fauna and flora. One of the sustainable approaches proposed by science is the use of low-harmful biosorbents, produced on the basis of waste from the agri-food industry, including fruit pomace. Due to the relatively low specificity and, consequently, insufficient sorption efficiency, attempts are made to modify such wastes, which will still be economically viable. In this review, four heavy metal ions, often found in industrial wastewater, were taken into account: copper(II), lead(II), cadmium(II) and zinc(II). Data on their sorption on different nanoscale particles has been collected and discussed.

Introduction

Adsorption is one of the most described methods used to remove non-biodegradable pollution such as heavy metals, dyes, and drugs. There are several techniques for removing heavy metals from wastewater, i.e. precipitation, ion exchange, membrane filtration or adsorption. In this decade, the last one is more and more widely described as the most effective and at the same time profitable [1]. During the last decade, nanoadsorbents were noted to be promising materials in heavy metal removal

in water and wastewater treatment [2]. Among many nanoadsorbents, some materials stand out, for example CuO, MgO, ZnO or hydroxyapatite nanoparticles [3, 4]. According to the literature data, they have low toxicity and are easily accessible sorbents. It was already proven that some nanoparticles linked with biomass show fast adsorption rates and good sorption efficiency towards a broad range of heavy metal ions in wastewater. Their application in water treatment results in significantly improved performance due to bigger surface area, stability in operating conditions and no secondary pollution [5]. The use of advanced nanoengineering technologies, such as an innovative combination of the basics of chemical engineering and nanotechnology, expands the horizons on the treatment of waters contaminated with heavy metals [6].

Nanomaterials as heavy metal sorbents

Different metal oxides, being known for their applications as sorbents, now are widely prepared in the nanoscale with the sudden development of nanotechnology. Their biggest advantages are better selectivity and affinity against heavy metals. Nanoadsorbents have high surface area, short diffusion paths, catalytic properties and high porosity, which makes them effective sorption materials [7].

Many nanomaterials have been studied for their potential in heavy metal sorption. They can be divided into categories, such as carbon based, silica based, metal and metal oxide nanoparticles and nanocomposites [8]. The most described heavy metal sorbents are magnetic (iron oxide) nanoparticles, which are easy to separate from the wastewater with a magnetic field, which is non-toxic and inexpensive [9]. Nevertheless, under certain circumstances, the separation requires large magnetic fields, causing an increase in cost. Other metal oxides (e.g. ZnO, MgO, CuO) nanoparticles are cheaper. Their disadvantage is an agglomeration tendency, which can decrease their sorption efficiency [2]. Activated carbon has proven high sorption activity towards many pollutants, including heavy metals. In recent years, innovative carbon nanotubes, fullerenes or graphene oxides are being widely developed and used as nanosorbents. However, there is a problem with their potential toxicity in the environment [10, 11]. Between various sorption factors, the one that stands out as the most important is the concentration of nanoadsorbent. Table 1 brings together information about the removal of four different heavy metal ions from water solutions, using the most effective nanoadsorbents [12–24].

According to the information collected in Table 1, for copper(II) ions, ZnO nanoplates were definitely the most effective sorbents, with the sorption capacity equal to 1600 mg of Cu(II) ions in 1 g of the sorbent. It is the highest found sorption capacity in current review. The use of MgO nanoparticles, which are easier and less expensive to prepare, allowed the obtaining of the second highest value of q, equal to 593 mg/g.

As for Pb(II) and Cd(II) ions, the most effective sorbents were manganese oxide nanoparticles and nano zerovalent iron, respectively, 352.55 and 769.00 mg/g. There is much less data about zinc(II) ion removal on nanosorbents. The highest found sorption capacity was 44.248 mg/g for CuO nanopowder. Activated carbon was the weakest sorbent for all heavy metal ions in this review, however it is hard to compare with other sorbents due to the lack of information on adsorption parameters, such as pH or time of sorption.

TAB. 1. Nanoadsorbents for the removal of Cu(II), Pb(II), Cd(II) and Zn(II) ions from water

Metal ion	Adsorbent	Sorption factors	Maximum adsorption capacity (q) [mg/g]	Isotherm	Ref.
Cu(II)	Magnetic nanoparticles	5 min pH 6 298K	25.77	n.d.*	[12]
	Chitosan coated magnetic nanoparticles	30 min pH 6 303K	236.7	Langmuir	[13]
	ZnO nanoplates	n.d.	1600	Freundlich	[14]
	Magnesium oxide nanoparticles	120 min pH 3–4 343K	593	Freundlich	[15]
	Zinc oxide nanoparticles	120 min pH 3–4 343K	226	Freundlich	[15]
	Chitosan/multiwall carbon nanotubes composite	n.d.	454.5	n.d.	[16]
Pb(II)	Iron oxide nanoparticles	120 min pH 2–3 298K	36	Langmuir, Freundlich	[17]
	Manganese oxide nanoparticles	298K	352.55	Langmuir	[18]
	Nano-alumina	90 min pH 5 RT	100	Langmuir, Freundlich	[19]
	CuO nanoparticles	120 min pH 6	14.859	Langmuir	[20]
	Activated carbon	n.d.	6.68	n.d.	[21]

Metal ion	Adsorbent	Sorption factors	Maximum adsorption capacity (q) [mg/g]	Isotherm	Ref.
Cd(II)	Magnetic nanoparticles	60 min	18.8	Langmuir, Freundlich	[22]
	Nano-alumina	90 min pH 5 RT	83.33	Langmuir, Freundlich	[19]
	Multi-walled carbon nanotubes	30 min pH 8 298K	25.7	Langmuir	[23]
	Nano zerovalent iron	297K	769	Langmuir	[24]
Zn(II)	CuO nanopowder	120 min pH 7	44.248	Langmuir	[20]
	Activated carbon	n.d.	11.24	n.d.	[21]

* n.d. – no data.

SOURCE: own elaboration

The potential of nano-biosorbents

Conventional nanomaterials have some disadvantages, such as difficulties in separating or instability. The solution to this problem is the immobilization of nanoparticles in various matrices, e.g. biomass. There are many materials suitable for this purpose, e.g. biomass char, easily obtained from the biological waste or fruit/vegetable pomace from the agri-food industry. Obtained nano-biosorbents composites are likely to be more effective in comparison to non-modified biosorbents or nanoparticles alone. For example, the addition of iron nanoparticles caused the increase of the surface area of rice husk biochar and thus improved its sorption activity [25]. Moreover, these nano-composites have better thermal stability. Data on the sorption activity of nano-biosorbents are summarized in Table 2 [26–34].

TAB. 2. Nanoadsorbents combined with biomass for the removal of Cu(II), Pb(II), Cd(II) and Zn(II) ions from water

Metal ion	Adsorbent	Sorption factors	Maximum adsorption capacity [mg/g]	Isotherm	Ref.
Cu(II)	MgO nanopartices/ olive pomace composite	pH 5	186.219	Langmuir	[26]
	Dactyloctenium aegyptium biomass/ montmorillonite clay nanocomposite	n.d.	98.8 (% removal)	Langmuir/ Freundlich/ Temkin/Dubinin-Radushkevich	[27]
	Nanoscale zero-valent iron/ *Posidonia oceanica* marine biomass	30 min	227.2	Langmuir/ Freundlich	[28]
Pb(II)	Hydroxyapatite nanoparticles/ apple pomace composite	0.02 g HANP@AP pH 5 C = 100 mg/l Pb^{2+}	303	Langmuir	[29]
	Dactyloctenium aegyptium biomass/ montmorillonite clay nanocomposite	n.d.	81.54 (% removal)	Langmuir/ Freundlich/ Temkin/ Dubinin-Radushkevich	[27]
	Nano-zero valent iron/undulating venus shell composite	pH 6	29.91	Langmuir	[30]
	Nanoscale zero-valent iron/ *Posidonia oceanica* marine biomass	30 min	108	Langmuir/ Freundlich	[28]
	Fish bone hydroxyapatite nanopowder	n.d.	576.495	n.d.	[31]

Metal ion	Adsorbent	Sorption factors	Maximum adsorption capacity [mg/g]	Isotherm	Ref.
Cd(II)	Hydroxyapatite nanoparticles/ apple pomace composite	0.02 grams of sorbent/L pH 5 C = 100 mg/l Cd^{2+}	250	Langmuir	[29]
	Nano-zero valent iron/undulating venus shell composite	pH 6	38.99	Langmuir	[30]
	Dactyloctenium aegyptium biomass/ montmorillonite clay nanocomposite	n.d.	76.32 (% removal)	n.d.	[27]
	Magnetic biochar	295K	41.33	Langmuir	[32]
	Iron nanoparticles/ chitin nanoparticles composite	30 min	94.2 (% removal)	n.d.	[33]
	Nanoscale zero-valent iron/ *Posidonia oceanica* marine biomass	30 min	72	Langmuir/ Freundlich	[28]
	Fish bone hydroxyapatite nanopowder	n.d.	75.877	n.d.	[31]
Zn(II)	Magnetic biochar	295K	35.40	Langmuir	[32]
	Magnetite nanoparticles/ laurel sawdust composite	3h 7 grams of sorbent/L	98.9 (% removal)	Freundlich	[34]
	Magnetite nanoparticles/ canelo sawdust composite		98.8 (% removal)		
	Magnetite nanoparticles/ eucalyptus sawdust composite		97.6 (% removal)		

SOURCE: own elaboration

Referring to Table 2, it can be noted that some of the collected data was hard to compare due to the lack of information on sorption parameters (e.g. [34]). Nano-biomass powder can be produced by ball milling, the most common physical modification method. Magnetic nano-modified biomass is easily separated from pollutants with a magnetic field, preventing the contamination of groundwater and making the sorption process less expensive [34, 35]. The nano-biosorbent pointed out in Cu(II) ion removal is nanoscale zero-valent iron impregnated in *Posidonia oceanica* marine biomass [28]. High copper(II) removal (98.8%) was also obtained in the case of *Dactyloctenium aegyptium* biomass/montmorillonite clay nanocomposite [26]. The greatest adsorption capacity for lead(II) ions was gained using hydroxyapatite nanopowder made from fish bones [31]. In another work, the most active nano-biosorbent for Cd(II) sorption, which was the hydroxyapatite/apple pomace nanocomposite, was produced [29]. As for the information on % removal of these ions, iron nanoparticles immobilized on chitin was more active (94.20%) compared to *Dactyloctenium aegyptium* bio-mass/montmorillonite clay nanocomposite (76.32%). In the case of zinc(II), magnetic biochar had an adsorption capacity equal to 35.40 mg/g, which was a higher value in comparison to the activated carbon, but lower than CuO nanopowder alone (Table 1). Between different sawdust/magnetite nanoparticle composites, the highest Zn(II) removal was obtained with the use of laurel sawdust. The production of nano-sorbents and their modification by various methods should be assessed in terms of costs, being eco-friendly by using e.g. wastes from the agri-food industry as a raw material matrix [37].

Summary

As discussed above, nanomaterials and naturally derived sorbents in the nanoscale can be used as effective sorbents to remove heavy metal ions from contaminated water and wastewater. In this review, the use of nanomaterials and their different combinations with biomass to remove the divalent ions of four heavy metals (copper, lead, cadmium and zinc) was described. As a result of this review, it was observed that due to the physical and chemical modifications of their sorption surfaces, nano-biocomposites showed an increased sorption capacity towards heavy metal ions compared to the nanomaterials or biosorbents of natural origin. Easy synthesis, economic availability and easily modified sorption surfaces are some of the major features that led to the development of this innovative technology. In addition, properly modified nano-biosorbents are recyclable thanks to easier separation of pollutants from them. Further research is needed to develop ecological methods for the synthesis of nano-biocomposites for the sorption of heavy metals using waste biomass. There is a need

to develop the possibility of the scale-up by improving the environmental friendliness of nanoparticles and circular economy production, making the entire process of using nano-biosorbents in heavy metal removal as cost-effective as possible.

Funding: This research was carried out as part of the work no. WI/WB-IIŚ/4/2021 and financed from funds from the Ministry of Science and Higher Education.

Literature

[1] Kolluru S.S., Agarwal S., et al., *Heavy metal removal from wastewater using nanomaterials-process and engineering aspects,* Process Safety and Environmental Protection 2021, 150, p. 323–355.

[2] Thekkudan V.N., Vaidyanathan V.K. et al, *Review on nanoadsorbents: a solution for heavy metal removal from wastewater,* IET Nanobiotechnology 2017, 11(3), p. 213–224.

[3] Dhiman V., Kondal N., ZnO *Nanoadsorbents: A potent material for removal of heavy metal ions from wastewater,* Colloid and Interface Science Communications 2021, 41, 100380.

[4] Chand P., Pakade Y.B., *Removal of Pb from Water by Adsorption on Apple Pomace: Equilibrium, Kinetics and Thermodynamics Studies*, Journal of Chemistry 2013, 164575.

[5] El-Nagar D.A., Massoud S.A., Ismail S.H., *Removal of some heavy metals and fungicides from aqueous solutions using nano-hydroxyapatite, nano-bentonite and nanocomposite*, Arabian Journal od Chemistry 2020, 13(11), p. 7695–7706.

[6] Dutta M.M., Charingia A., *Nanotechnology-Based Nano-Biosorbents*, in: Handbook of Research on Emerging Developments and Environmental Impacts of Ecological Chemistry 2020, IGI Global.

[7] Mensah M.B., Lewis D.J. et al, *Heavy metal pollution and the role of inorganic nanomaterials in environmental remediation,* Royal Society Open Science 2021, 8, 201485.

[8] Kumar R., Rauwel P., Rauwel E., *Nanoadsorbants for the Removal of Heavy Metals from Contaminated Water: Current Scenario and Future Directions,* Processes 2021, 9(8), 1379.

[9] El-Dib F.I., Mohamed D.E., et l., *Study the adsorption properties of magnetite nanoparticles in the presence of different synthesized surfactants for heavy metal ions removal,* Egyptian Journal of Petroleum 2020, 29(1), p.1–7.

[10] Tian Y., Gao B., et al, *Methods of using carbon nanotubes as filter media to remove aqueous heavy metals,* Chemical Engineering Journal 2012, 210, p. 557–563.

[11] Gangupomu H.R., Sattler M.L, et al, *Carbon nanotubes for air pollutant control via adsorption: A review,* Reviews in Nanoscience and Nanotechnology 2014, 3(2), p. 149–160.

[12] Hao Y.M., Man C., Hu Z.B., *Effective removal of Cu(II) ions from aqueous solution by amino-functionalized magnetic nanoparticles,* Journal of Hazardous Materials 2010, 184(1), p. 392–399.

[13] Neeraj G., Krishnan S., et al, *Performance study on sequestration of copper ions from water using synthesized high effective chitosan coated magnetic nanoparticles,* Journal of Molecular Liquids 2016, 214, p. 335–346.

[14] Wang X., Cai W., et al, *Mass production od micro/nanostructured porous ZnO plates and their strong structurally enhanced and selective adsorption performance for environmental remediation,* Journal of Materials Chemistry 2010, 20(39), p. 8582–8590.

[15] Rafiq Z., Nazir R., et al, *Utilization of magnesium and zinc oxide nano-adsorbents as potential materials for treatment of copper electroplating industry wastewater,* Journal of Environmental Chemical Engineering 2014, 2(1), p. 642–651.

[16] Salam M.A., Makki M.S.I., et al, *Preparation and characterization of multi-walled carbon nanotubes/chitosan nanocomposite and its application for the removal of heavy metals from aqueous solution,* Journal of Alloys and Compounds 2011, 509(5), p. 2582–2587.

[17] Nassar N.N., *Rapid removal and recovery of Pb(II) from wastewater by magnetic nanoadsorbents,* Journal of Hazardous Materials 2010, 184(1–3), p. 538–546.

[18] Xu M., Wang H., et al., *Removal of Pb(II) from aqueous solution by hydrous manganese dioxide: Adsorption behavior and mechanism,* Journal of Environmental Sciences, 25(3), p. 479–486.

[19] Afkhami A., Saber-Tehrani M., Bagheri H., *Simultaneous removal of heavy-metal ions in wastewater samples using nano-alumina modified with 2,4-dinitrophenylhydrazine,* Journal of Hazardous Materials 2010, 181(1–3), p. 839–844.

[20] Ossman M.E., Abdelfattah M., *CuO nanopowder for removel of Pb(II) and Zn(II),* Journal of Environmental Engineering and Science 2015, 10(1), p. 10–18.

[21] Mishra P.C., Pater R.K., *Use of agricultural waste for the removal of nitrate-nitrogen from aqueous medium,* Journal of Environmental Management 2009, 90(1), p. 519–522.

[22] Gong J., Chen L., et al, *Shellac-coated iron oxide nanoparticles for removal of cadmium(II) ions from aqueous solution,* Journal of Environmental Sciences 2012, 24(7), p. 1165–1173.

[23] Vuković G.D., Marinković A.D., et al. *Removal of cadmium from aqueous solutions by oxidized and ethylenediamine-functionalized multi-walled carbon nanotubes,* Chemical Engineering Journal 2010, 157(1), p. 238–248.

[24] Boparai H.K., Joseph M., O'Carroll D.M., *Kinetics and thermodynamics of cadmkum ion removal by adsorption onto nano zerovalent iron particles,* Journal of Hazardous Materials 2011, 186(1), p. 458–465.

[25] Islam T., Li Y., Cheng H., *Biochar and Engineered Biochars for Water and Soil Remediation: A Review*, Sustainability 2021, 13, 9932.

[26] Dakroury G.A., Abo-Zahra Sh.F., Hassan H.S., *Utilization of olive pomace in nano MgO modification for sorption of Ni(II) and Cu(II) metal ions from aqueous solutions*, Arabian Journal of Chemistry 2020, 13(8), p. 6510–6522.

[27] Khan U., Khan Rao R.A., *Dactyloctenium aegyptium biomass (DAB)-MMT nano-composite: Synthesis and its application for the bio-sorption of Cu(II) ions from aqueous solution*, Process Safety and Environmental Protection 2017, 111, p. 409–419.

[28] Boubakri S., Djebbi M.A., et al, *Nanoscale zero-valent iron functionalized Posidonia oceanica marine biomass for heavy metal removal from water*, Environmental Science and Pollution Research 2017, 24, p. 27879–27896.

[29] Chand P., Pakade Y.B., *Synthesis and characterization of hydroxyapatite nano-particles impregnated on apple pomace to enhanced adsorption of Pb(II), Cd(II) and Ni(II) ions from aqueous solution*, Environmental Science and Pollution Research 2015, 22(14), p. 10919–29.

[30] Wang Z., Wu X., et al., *Shell biomass material supported nano-zero valent iron to remove Pb^{2+} and Cd^{2+} in water,* Royal Society Open Science 2020, 7(10), 201192.

[31] Shreadah M.A., Osama E.M.R., et al., *Removal of Some Toxic Ions from Seawater and Wastewater by sorption onto Natural, Synthetic Hydroxyapatite and Alignate-Hydroxyapatite Composite Nanoparticles: A Comparative Study,* Journal of Environmental Protection 2019, 10(9), p. 1155–1173.

[32] Kołodyńska D., Bąk J., et al., *Investigations of Heavy Metal Ion Sorption Using Nanocomposites of Iron-Modified Biochar,* Nano Express 2017, 12, 433.

[33] Gomaa E.Z., *Iron Nanoparticles alpha-Chitin Nanocomposite for Enhances Antimicrobial, Dyes Degradation and Heavy Metals Removal Activities,* Journal of Polymers and the Environment 2018, 26(9), p. 3638–3654.

[34] Asimbaya C., Rosas-Laverde N.M., et al., *Magnetite Impregnated Lignocellulosic Biomass for Zn(II) Removal,* Materials 2022, 15(3), 728.

[35] Wang B., Jiang Y.S., Li F.Y., *Preparation of biochar by simultaneous carbonization, magnetization and activation for norfloxacin removal in water.* Bioresource Technology 2017, 233, p. 159–165.

[36] Bhushan B., Gupta V., Kotnala S., *Development of magnetic–biochar nano–composite: Assessment of its physico-chemical properties*. Materials Today: Proceedings 2020, 26, p. 3271–3274.

[37] Basheer A.A., *New generation nano-sorbents for the removal of emerging contaminants in water*, Journal of Molecular Liquids 2018, 261, p. 583–593.

[38] Zhang J., Lin S., et al., *Adsorption Properties of Magnetic Magnetite Nanoparticles for Coexistent Cr(VI) and Cu(II) in Mixed Solution,* MDPI Water 2020, 12, 446, p. 1–12.

[39] Nasirimoghaddam S., Zeinali S., et al., *Chitosan coated magnetic nanoparticles as nano-adsorbent for efficient removal of mercury contents from industrial aqueous and oily samples,* Journal of Industrial and Engineering Chemistry 2014, 27, p. 79–87.

Antioxidant studies of rosmarinic acid and its complexes with zinc and copper in experimental and theoretical approach

Keywords: rosmarinic acid, FRAP, DPPH, DFT studies, metal complexation

Abstract: In this article, DFT studies on the antioxidant properties of rosmarinic acid and its zinc and copper complexes were conducted to indicate which of the functional groups of the tested compounds is the most involved in radical scavenging activity. For this purpose the BDE, PA and PDE parameters were calculated. The results of the theoretical calculations proved, that the hydroxyl group attached to the aromatic ring of caffeic acid, which is a component of rosmarinic acid, has the greatest activity in radical scavenging reaction. The antioxidant activity of acid and its copper and zinc complexes were compared in DPPH and FRAP assays. In DPPH assay, zinc and copper complexes exhibited greater antioxidant activity than rosmarinic acid, while in FRAP assay only zinc improved the antioxidant properties, while copper exhibited similar ferric reduction activity as rosmarinic acid.

Introduction

Rosmarinic acid is an ester of 3,4-dihydroxyphenylacetic acid and caffeic acid linked by an ester bond. It occurs in many plants, but for the first time as a pure compound, it was isolated from *Rosmarinus officinalis*, to which it owes its name. Due to the common presence among both highest plant families like *Lamiacae* and *Blechnaceae* and lowest plant families like hornworts, *Potamogetonaceae* and *Cannaceae,* rosmarinic acid cannot be used as a chemo taxonomical marker to differentiate plant families.

Rosmarinic acid plays an important role in plant cells as a defense compound against herbivores and pathogens [1]. In the human body, rosmarinic acid and its derivatives exhibit biological activities – they improve cognitive performance, prevent the development of Alzheimer's disease, show cardioprotective effects and are applied in cancer chemoprevention [2]. High antioxidant activity of rosmarinic acid contributes to strong antitumor properties. Studies performed on rats proved that rosmarinic acid at the concentration of 5 mg/kg body weight reduces lipid peroxidation. Anticancer activity is also a result of its ability to increase apoptotic proteins expression [3]. In the body of a rat, rosmarinic acid is metabolized into coumaric and caffeic acid. These metabolites have a great impact on reducing the cholesterol concentrations in rat cells by increasing fatty acid β-oxidation activity [4,5]. Rosmarinic acid also exhibits anti-inflammatory and antiviral antibacterial properties. It is used in the cosmetic industry as a fragrant additive. In the food industry, rosmarinic acid is an important food additive, that prevents food spoilage. In the pharmaceutical industry, rosmarinic acid is used as a medicinal substance and dietary supplement [6]. Pharmacological application of rosmarinic acid is based on its capacity to prevent the oxidation of low density lipoprotein, inhibition of cyclooxygenase and the prevention of murine cell proliferation [7]. Studies of rosmarinic acid showed that it exhibits anti-HIV activity [8]. Due to the molecular structure of rosmarinic acid, which contains four phenolic hydrogens and two catechol moieties, this compound has great antioxidant properties. The phenolic hydrogens are responsible for radical scavenging capacity, while the presence of two catechol moieties provide the polarity of the molecule, that facilitate the penetration of the lipid bilayers in cells, protecting them against oxidation [9]. Studies conducted by Gao et al. [10] show that rosmarinic acid harms the H_2O_2 induced apoptosis in astrocytes and reduces the level of reactive oxygen species and malondialdehyde. Experimental antioxidant scavenging activity tests shows that rosmarinic acid has greater radical scavenging activity in comparison with Trolox and ascorbic acid [11]. The aim of this study is to investigate the influence of metal complexation on the antioxidant properties of rosmarinic acid. Metal complexation of ligands leads to the perturbation of electronic charge distribution within the moiety. Alkali metals and heavy metals like Hg(II), Hg(I), Ag(I) and Pb(II) perturb the electronic system, whereas transition metals stabilize it. It occurs, that metal complexation of ligands contributes to its biological properties and reactivity [12]. Studies over antioxidant properties shows, that metal chelates are more efficient in the free radicals scavenging in comparison with pure ligands [13]. In the framework of this paper, the DFT calculations were performed, in order to indicate the most probable placement of a reactive functional group that is responsible for the antioxidant capacity of the rosmarinic acid molecule. For this purpose, the bond dissociation energy was calculated. Bond dissociation enthalpy (BDE) is given with the following formula (1) [14]:

$$BDE = H_{\textit{molecule radical}} + H_{\textit{hydrogen radical}} - H_{\textit{parent molecule}} \quad (1)$$

The cited formula describes the mechanism of the radical scavenging of the compound, that rely on the hydrogen transfer between the antioxidant and free radical, thus BDE is the parameter that determines the strength of the OH bond [15]. Copper and zinc were selected for the complexation of rosmarinic acid, due to their potent influence on the human body. Since 1930, copper is considered as the essential trace metal in living organisms. Cu(II) cation constitutes a coordination center both in mononuclear and multinuclear coordination compounds, especially in case of polymer ligands [16].

In organisms, copper plays a major role as an enzyme cofactor and a structural element of proteins involved in the charge transfer processes. Copper deficiency reduces the activity of certain enzymes e.g., zinc-copper superoxide dismutase Cu / ZnSOD, ceruloplasmin and enzymes independent from copper, e.g. catalase or glutathione peroxidase, and also affects the proper functioning of free radical scavengers, i.e. metallothionein or glutathione [17,18].

Copper deficiency in the body can cause: hernias, aneurysms, rupture of blood vessels, nosebleeds, osteoporosis, brain disorders, disorders in glucose and cholesterol metabolism, in the functioning of the thyroid gland, general weakness and fatigue [19]. Zinc is a necessary trace element, supporting the proper functioning of metalloenzymes such as oxidoreductases, ligase or hydrolases, in which zinc plays the main structural or catalytic role. Zinc has antioxidant properties. It prevents the formation of a dangerous hydroxyl radical $OH^{\bullet}$ and the oxide radical anion $O_2^{\bullet -}$ [20]. Zinc also plays a significant role in maintaining redox balance in cells [21].

Material and methods

Zinc and copper rosmarinates were obtained in a two step reaction. The first step consisted in obtaining the sodium salt of rosmarinic acid, by adding in a stechiometric ratio (1:1) the powder of rosmarinic acid to the sodium hydroxide water solution (0,1M). The obtained suspension was placed in an ultrasonic bath and heated up to 60°C until the complete dissolution of the rosmarinic acid took place.

In the second step, the water solution of zinc and copper chloride were added in order to obtain zinc and copper rosmarinates respectively. The chloride salts were added to the sodium rosmarinate solution in a molar ratio like 1:2 (2,5 ml of 0,1M zinc/copper chloride). The complexes were placed in a shaker for two hours at room temperature. The precipitate was washed with acetone to rinse the remaining chlorides under the control of an $AgNO_3$ solution. The obtained solution was dried at 70°C. The compounds obtained this way were subjected to an antioxidant test. The FRAP and DPPH antioxidant assays were performed with initial concentration of rosmarinic acids and its complexes of $5 \cdot 10^{-5}$M water solutions. Theoretical studies were performed using the Gauss 08 computational program. All theoretical calculations

were made in the B3LYP database using the LAN2DLZ density functional. All calculations of the thermodynamical parameters were performed for optimized rosmarinic acid isomer with the lowest energy value.

Results

I. Theoretical approach – DFT results

The optimized structure of rosmarinic acid with atom numeration and designated positions for possible nucleophilic acid is presented in Fig.1 All calculations were carried out for isomers with the lowest energy values.

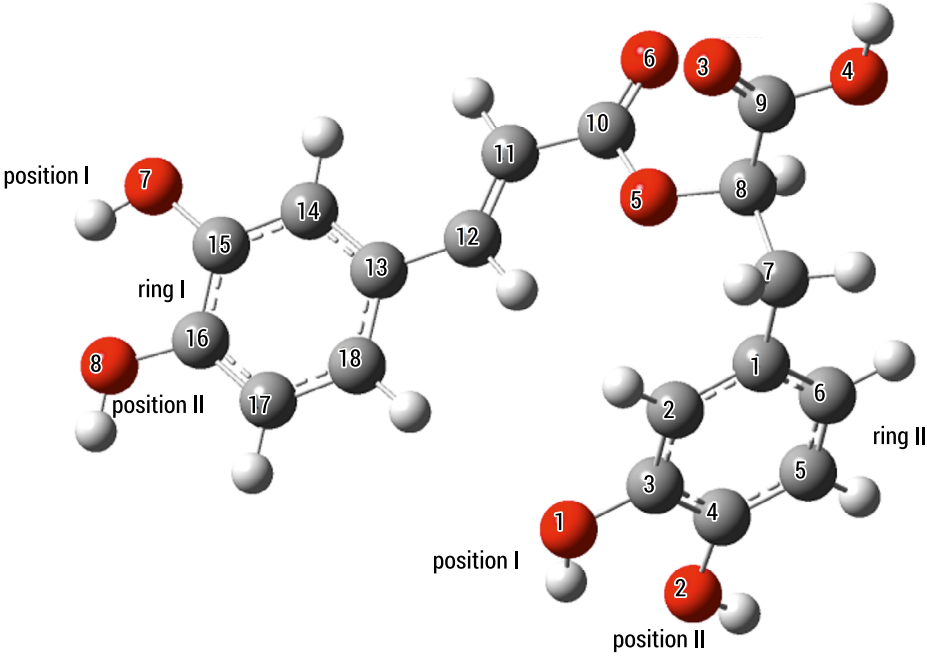

FIG. 1. Optimized rosmarinic acid molecule with atom numeration and positions prone to the nucleophilic attack

SOURCE: own elaboration

In Table 1 the results of calculated BDE parameters for hydroxyl and carboxylic radicals, marked with positions as shown in Fig. 1 are given.

TAB. 1. BDE values for individual radicals within the rosmarinic acid molecule

The radicals of hydroxyl groups within the aromatic ring of rosmarinic acid molecule				Radical of carboxylic group
Ring I Position I	Ring I Position II	Ring II Position I	Ring II Position II	–
BDE [kJ/mol]				
45,11	50,78	85,57	66,74	410,15

SOURCE: own elaboration

The antioxidant properties are determined by the functional group of the compound in which the value of the BDE parameter, i.e. the dissociation energy of the O-H bond, is the lowest [22]. Based on the results of experimental studies, it can be concluded that the hydroxyl group attached to the first aromatic ring in position I has the greatest share in increasing the antioxidant properties of the compound. The BDE parameter determines the probability of the HAT mechanism in which the reaction between the antioxidant and the radical proceeds according to the equation (2) [23]:

$$ArOH + H^{\bullet} \rightarrow ArO^{\bullet} + XH \quad (2)$$

For the specified positions of the hydroxyl groups and for the carboxyl group of rosmarinic acid, the values of the PA (proton affinity) parameter were calculated. This parameter describes the first of two stages of the SPLET (Sequential Proton-Loss Electron Transfer) antioxidant mechanism, which proceeds according to the following reaction equation: $ArOH \rightarrow ArO^{-} + H^{+}$. The numerical value of this parameter was calculated according to the equation: $PA = H_{ArO\bullet} + H_{(H^{+})} - H_{ArOH..}$. According to the above-mentioned reaction equation, PA shows a tendency to donate a proton with the simultaneous formation of an anion in the antioxidant molecule [24]. Table 2 shows the PA values.

TAB. 2. Proton affinity values calculated for individual hydroxyl positions and carboxyl group in rosmarinic acid. Position numeration according to Figure 1

Anions of the hydroxyl groups of the aromatic ring				The anion of the carboxyl group
Ring I Position I	Ring I Position II	Ring II Position I	Ring II Position II	–
PA [kJ/mol]				
251,69	336,51	336,51	312,90	323,64

SOURCE: own elaboration

The comparison of the numerical values of the PA parameter shows that the hydroxyl group attached to the I aromatic ring in the first position shows the greatest tendency to lose a proton and form an anion. Therefore, this position can be indicated as the most reactive in relation to the other analyzed ones in the rosmarinic acid molecule. The IP (Ionisation Potential) and PDE (Proton Dissociation Enthalpies) parameters were also calculated. They describe the first and second steps of the ET-PT (Electron Transfer – Proton Transer) mechanism, respectively. The first step can be described by the reaction equation: $ArOH+X^{\bullet} \rightarrow ArOH^{\bullet+}+XH$. The equation that allows us to calculate the enthalpy of the above reaction is as follows: $IP = H_{ArOH^{\bullet+}} + H_{H^+} - H_{ArOH}$. The second step of the ET-PT mechanism is described by the following chemical reaction equation: $ArOH^{\bullet+} \rightarrow ArO^{\bullet} + H^+$. The PDE parameter was calculated based on the equation: $PDE = H_{ArO^{\bullet}}+H_{H^+}-H_{ArOH^{\bullet+}}$ [25]. The IP parameter for the rosmarinic acid molecule is 116.50 kJ / mol. The Table 3 presents the numerical values of the PDE parameter:

TAB. 3. PDE values calculated for individual hydroxyl positions and carboxyl group in rosmarinic acid. Position numeration according to Figure 1

The radicals of hydroxyl groups within the aromatic ring of rosmarinic acid molecule				Radical of carboxylic group
Ring I Position I	Ring I Position II	Ring II Position I	Ring II Position II	–
PDE [kJ/mol]				
242,77	248,44	283,23	264,41	607,81

SOURCE: own elaboration

The lowest value of the PDE parameter is characteristic for the radical of the hydroxyl group of ring I in position I, which means that it is the radical cation of this hydroxyl group that most readily decomposes into the radical and proton. Based on theoretical calculations of the electron parameters discussed above, it can be concluded that the hydroxyl group attached to the first ring in the first position has the greatest influence on the antioxidant properties of rosmarinic acid. The high chemical activity of this group indicates that zinc and copper cations will attach to it, forming zinc rosemary and copper rosemary complexes, respectively. The diagram of the aforementioned complexes with the numbering of atoms in the molecule is presented below.

The numbering of the hydrogen atoms has not been included in the Fig. 2 for the sake of clarity. It has been assumed that the numbering of hydrogen atoms corresponds to the number of the carbon or oxygen atom to which it is attached. The letter M symbolically denotes a metal atom (zinc or copper).

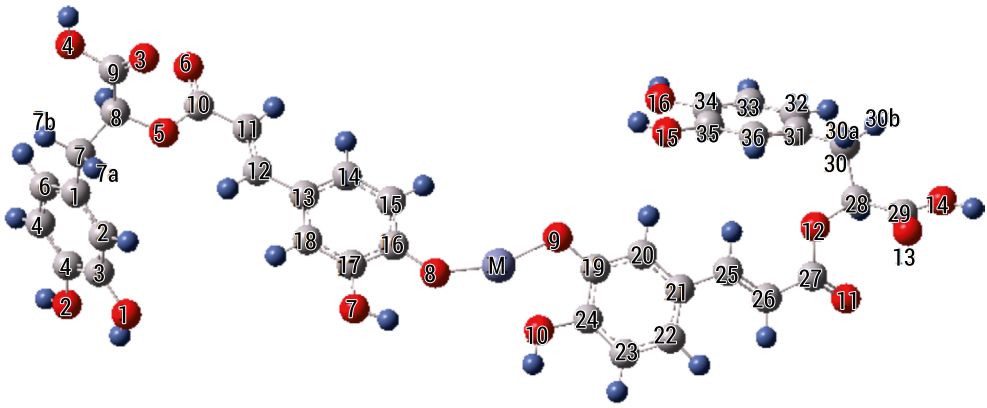

FIG. 2. Scheme of the optimized structure of the rosmarinic acid complex, where the letter M denotes a zinc or copper atom

SOURCE: own elaboration

HOMA aromaticity indices were calculated for the molecule of rosmarinic acid and its zinc and copper complexes. Table 3 shows the HOMA values.

TAB. 4. HOMA aromaticity index values of rosmarinic acid and its complexes

Rosmarinic acid		Copper rosmarinate		Zinc rosmarinate	
Ring I	Ring II	Ring I	Ring II	Ring I	Ring II
0,874	0,901	0,874	0,901	0,843	0,901

SOURCE: own elaboration

II. Experimental approach – Antioxidant assays results

FRAP and DPPH antioxidant tests were performed, which compared the activity of rosmarinic acid and its complexes with copper and zinc. The obtained results are presented as IC50 in the case of the DPPH method and as mM Fe^{2+} in the case of the FRAP method. Fig. 3 presents the results of antioxidant tests in graphical form for the DPPH test. In DPPH antioxidant assay the highest radical scavenging activity shows zinc rosmarinate (0,015 mM). Slightly worse antioxidant activity towards DPPH radical shows copper rosmarinate (0,0024 mM). Rosmarinic acid exhibits the worst free radical scavenging activity (0,0029 mM).

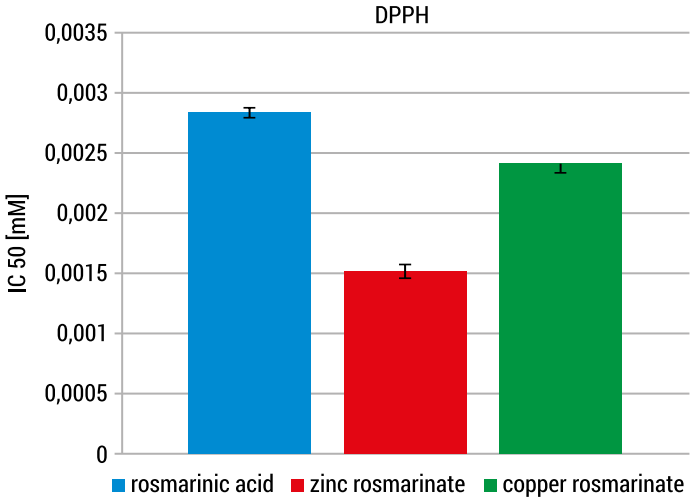

FIG. 3. Comparison of antioxidant activity of rosmarinic acid and its complexes with copper and zinc by DPPH method

SOURCE: own elaboration

In Fig. 4 the results of FRAP antioxidant activity is presented. In the FRAP test, the antioxidant activity increases according to the following order: copper rosmarinate → rosmarinic acid → zinc rosmarinate.

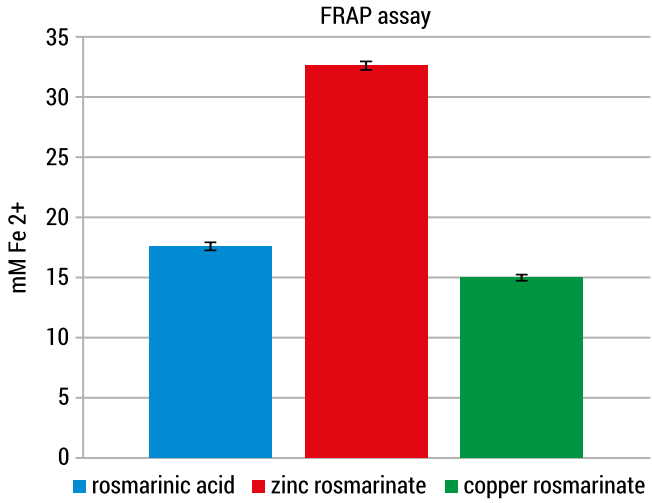

FIG. 4. Comparison of antioxidant activity of rosmarinic acid and its complexes with copper and zinc by FRAP method

SOURCE: own elaboration

Summary

As part of the work, theoretical calculations of the structure of rosmarinic acid and its complexes with copper and zinc were performed using the DFT method, with the B3LYP function, using the LANL2DZ database. For the optimized structure of rosmarinic acid, the following thermodynamic parameters were calculated: BDE, PA, PDE and IP in order to establish the position and functional group responsible for the antioxidant properties of this compound. Rosmarinic acid is an ester of caffeic acid and 3,4-dihydroxyphenyl lactic acid. The most active is the hydroxyl group derived from caffeic acid located in the aromatic ring. Metals, i.e. zinc and copper, do not affect the electron charge distribution of the aromatic ring, as evidenced by the calculated values of the HOMA index. The only slight difference occurs for the aromatic ring I of zinc rosmarinate, for which the value of HOMA index is 0,843, while for rosmarinic acid the value of this parameter is 0,840. Rosmarinic acid and the discussed complexes were subjected to antioxidant tests using DPPH and FRAP methods. In the case of determining the antioxidant capacity in the DPPH free radical quenching test, the antioxidant activity increases in the series: zinc rosemary, cupric rosemary, rosmarinic acid. The FRAP method allows direct determination of the reduction abilities of a compound. In FRAP assay the greatest reduction activity showed zinc rosmarinate, while the smallest reduction activity exhibited copper rosmarinate. Thus, complexation of rosmarinic acid with transition metals (Zn, Cu (II)) resulted in an increase in antioxidant properties in DPPH assay, while in FRAP assay, zinc exhibited better antioxidant properties than copper.

Acknowledgement: This work was financially supported by National Science Centre, Poland, under the research project number 2018/29/B/NZ9/01997

Literature

[1] Petersen M.S.J., Simomnds M., Molecules of interests. *Rosmarinic acid*, Phytochemistry 2003, 62, p. 121–125.

[2] Bulgakov V.B., Inyushkina Y.V., Fedoreyev S.A., *Rosmarinic acid and its derivatives: biotechnology and applications*, Critical Reviews in Biotechnology 2012, 32, p. 203–217.

[3] Venkatachalam K., Gunasekaran S., Namasivayam N., *Biochemical and molecular mechanisms underlying the chemopreventive efficacy of rosmarinic acid in a rat colon cancer*, European Journal of Pharmacology 2016, 791, p. 37–50.

[4] Cho A., Jeon S., Kim M., Yeo J., Seo K., Choi M., Lee M., *Chlorogenic acid exhibits anti-obesity property and improves lipid metabolism in high-fat diet-induced-obese mice*, Food and Chemical Toxicology 2010, 48, p. 937–943.

[5] Fadel F., El Kirat K., Morandat S., *The natural antioxidant rosmarinic acid spontaneously penetrates membrane to inhibit lipid peroxidation in situ*, Biochemica et Biophysica Acta 2011 1808, p. 2973–2980.

[6] Peng X., Wang X., Wei Q., Su R., He Z., *Affinity of rosmarinic acid to human serum albumin and its effect on protein conformation stability*, Food Chemistry 2016, 192, p. 178–187.

[7] Park S.U., Uddin M. R., Xu H., Kim Y.K., Lee S.Y., *Biotechnological applications for rosmarinic acid production in plant*, African Journal of Biotechnology 2008, 7, p. 4959–4965.

[8] Chen H., Chen F., Zhang Y.L., Song J.Y., *Production of lithospermic acid B and rosmarinic acid in hairy root cultures of Salvia miltiorrhiza*, Journal of Industrial Microbiology and Biotechnology 1999, 22, p. 133–138.

[9] Amoah K.S., Sandjo P.L., Kratz J.M., Biavatii M.W., *Rosmarinic Acid – Pharmaceutical and Clinical Aspects*, Planta Medica 2015, 82, p. 388–406.

[10] Gao L.P, Wei H.L., Zhao X.S., Xiao X.Y., Zheng R.L., *Antiapoptotic and antioxidant effects of rosmarinic acid in astrocytes*, Pharmazie 2005, 60, p. 62–65.

[11] Popov A.M., Osipov A.N., Korepanova E.A., Krivoshapko O.N., Atryukov A.A., *Study of antioxidant and membrane activity of rosmarinic acid using different model system*, Biophysics 2013, 58, p. 775–785.

[12] Świderski G., Łaźny R., Sienkiewicz M., Kalinowska M., Świsłocka R., Ackar A.O., Golonko A., Matejczyk M., Lewandowski W., *Synthesis, Spectroscopic and Theoretical Study of Copper and Cobalt Complexes with Dacarbazine*, Materials 2021, 14, p. 1–21.

[13] Świderski G., Jabłońska-Trypuć A., Kalinowska M., Świsłocka R., Karpowicz D., Magnuszewska M., Lewandowski W., *Spectroscopic, Theoretical and Antioxidant Study of 3d-Transition Metals* (*Co*(*II*), *Ni*(*II*), *Cu*(*II*), *Zn*(*II*)) *Complexes with Cichoric Acid*, Materials 2020, 13, p. 1–21.

[14] Marković Z., Tošović J., Milenković D., Marković S., *Revisiting the solvatation enthalpies and free energies of proton and electron in various solvents*, Computational and Theoretical Chemistry 2015, 1077, p. 11–17.

[15] Lespade L., Bercion S., *Theoretical investigation of the effect of sugar substitution to the antioxidant properties of flavonoids*, Free Radical Research 2012, 43, p. 346–358.

[16] Piotrowska A., Drzeżdżon J., Jacewicz D., Chmurzyński L., *Właściwości antyoksydacyjne, antybakteryjne i przeciwgrzybicze związków kompleksowych miedzi*(*II*), Wiadomości chemiczne 2017, 7, p. 219–240.

[17] Ciba J., Trojanowska J., Zołotajkin M., Mała encyklopedia pierwiastków. Wyd. Naukowo-Techniczne, Warszawa 1996.

[18] Kolditz L. Chemia nieorganiczna, cz. 2. Wyd. PWN, Warszawa 1994.

[19] Osredkar J., Sustar N., *Copper and zinc, biological role and significance of copper/zinc imbalance*, Journal of Clinical Toxicology 2011, 3, p. 2–18.

[20] Faa G., Nurchi V.M., Ravarino A., Fanni D., Nemolato S., Gerosa C., Van Eyken P., Geboes K., *Zinc in gastrointestinal and liver disease*, Coordination Chemistry Reviews 2008, 252, p. 1257–1269.

[21] Puzanowska-Tarasiewicz H., Kuźmicka L., Tarasiewicz M., *Funkcje biologiczne wybranych pierwiastków. III. Cynk – składnik i aktywator enzymów*, Polski Tygodnik Lekarski 2009, 27, p. 419–422.

[22] Wright J.S., *Predicting the antioxidant activity of curcumin and curcuminoids*, Journal of Molecular Structure 2002, 591, p. 201–217.

[23] Mohajeri A., Asemani S.S., *Theoretical investigation on antioxidant activity of vitamins and phenolic acids for designing a novel antioxidant*, Journal of Molecular Structure 2009, 930, p. 15–20.

[24] Pandithavidana D.R., Jayawardana S.B., *Comparative Study of Antioxidant Potential of Selected Dietary Vitamins; Computational Insights*, Molecules 2019, 24, p. 1646–1655.

[25] Urbaniak A., Szeląg M., Molski M., *Theoretical investigation of stereochemistry and solvent influence on antioxidant activity of ferulic acid*, Computational and Theoretical Chemistry 2013, 1012, p. 33–40.

Heat pump market in Poland in recent years

Keywords: heat pumps, renewable energy, heating, cooling, heat pump market

Abstract: The purpose of this study is to show current trends in the heat pump market in Poland, Europe, and the world and to characterize the factors shaping this market. The analysis focuses mainly on the years 2020–2021, but in order to illustrate the trends in a broader time perspective, it also takes into account the sales and stock of heat pumps even since 2005. Moreover, the study identifies, based on the example of Poland, what actions should be taken to overcome the barriers that hinder the growth of the heat pump market in Central and Eastern Europe (CEE). For this analysis, a detailed review of reports, data, and articles on the heat pump market in Poland over the past years was conducted. The number of units sold was determined, and the results were compared to the achievements of other European and global markets. The study also described two scenarios (baseline and optimistic) for the heat pump market development until 2030. Based on the available data, factors shaping the heat pump market, including European and national policies and financial support programs, were presented and characterized, and barriers impeding the dynamic growth of heat pump technology were identified.

Introduction

In current times, some of the major challenges of the modern world are climate change and excessive energy consumption. Global demand for heat and power is growing rapidly, driven by economic growth. As a result, greenhouse gas and volatile pollutants emissions into the atmosphere are also increasing at an equally rapid rate [10]. One of the technological solutions to reduce these risks are heat pumps. They are an energy-efficient, economical and environmentally friendly alternative to gas boilers

or air-conditioners in all climate zones [3]. These devices convert work into heat, whereby the ratio of the effect of the work to the expenditure of driving energy is, according to the law of conservation of energy, greater than or equal to one. Heat pumps work on the same principle as refrigerators, but the heat flow is in the opposite direction – the heat pump takes heat from the environment and transfers it to the heating system. The heat transformed by the heat pump usually comes from renewable sources such as air, water, or ground, making it an extremely future-proof solution [8]. In this paper, on the basis of a literature review, we analyzed the Polish heat pump market with respect to the global and European markets, and identified opportunities and threats for this technology. It also allowed, among others, to estimate the situation on the Polish heat pump market in the future years, as well as to determine what actions should be taken for further and more dynamic growth of this market.

Global heat pump market

In 2020, nearly 180 million heat pumps were used worldwide to heat buildings. Over the past years, the global stock has grown by approximately 10% per year, and this growth is particularly evident in the three major global heating markets – North America, Europe and North Asia [1, 16].

Despite the upward trend, heat pumps still meet a small amount of the world's residential heating demand (about 7% in 2020) and most heat pumps are installed in new buildings. Progress is still needed worldwide to increase the use of heat pumps, especially in existing buildings [1].

Considering the type of heat pumps, air-to-air heat pumps dominate global sales. The development of energy policy and increasing demand for air-conditioning have undoubtedly contributed to their growing popularity. Less popular in the world are ground source heat pumps with annual sales of about 400,000 units, more than half of which are installed in the United States [1]. The reasons for that may be due to the higher costs of the installation with a Ground Source Heat Pump (GSHP) (in comparison with an Air Source Heat Pump (ASHP)) and the necessity to possess a plot of land on which the boreholes could be made.

To better illustrate the situation on the global heat pump market, Figure 1 shows the size of the global heat pump stock by region, compared to the assumptions to be met according to the Net Zero Scenario [1].

It can be noticed that the global heat pump resource is growing steadily with China and North America accounting for the largest market share. However, it seems that this growth is not dynamic enough to meet the NZE scenario targets predicted for 2025 and 2030, as confirmed by [16]. Therefore, actions and activities must be taken to improve and disseminate heat pump technology worldwide.

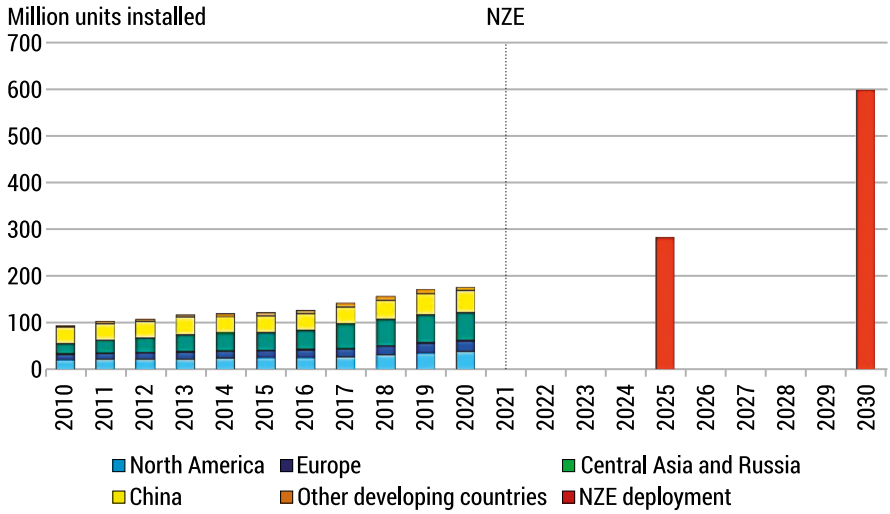

FIG. 1. Development of heat pump market by region compared to NZE assumptions
SOURCE: IEA (2021) Heat Pumps. All rights reserved

Global growth in the heat pump market can be seen not only in terms of sales volumes, but also in the development of heat pump technology itself. The typical seasonal performance factor for heat pumps (an indicator of average annual energy efficiency) has increased steadily since 2010 and now stands at almost 4 for space heating. The increase in heat pump efficiency in recent years has been primarily influenced by the shift from inverter-less to inverter technology. This means that not only regulations, standards, and labeling, but also technological advances themselves are contributing to improvement worldwide [1].

European heat pump market

As estimated in [14], despite challenging conditions in the heating device market, heat pump sales in Europe increased by 7.4% in 2020, with 1.62 million units sold across Europe. Under the assumption that the lifetime of heat pumps is about 20 years, the current stock of heat pumps in Europe is about 14.86 million units, of which as many as 13.2 million are used for heating. Taking into account 115–120 million residential buildings in Europe, the share of heat pumps in the building market was determined to be around 11%. The following table (Tab. 1) compares the volume of heat pumps sold and the market size for these devices in Europe from 2005 to 2020.

TAB. 1. Development of heat pump sales and stock in Europe

Year	Sales	Stock
2005	446 037	1 150 000
2006	509 794	1 660 000
2007	589 118	2 240 000
2008	804 457	3 050 000
2009	734 282	3 770 000
2010	800 388	4 570 000
2011	808 591	5 370 000
2012	750 436	6 110 000
2013	769 879	6 870 000
2014	792 621	7 640 000
2015	892 809	8 520 000
2016	999 682	9 490 000
2017	1 120 000	10 580 000
2018	1 270 000	11 810 000
2019	1 510 000	13 290 000
2020	1 620 000	14 860 000

SOURCE: [14]

According to [14], three main factors influence the growth of the heat pump market in recent years:

1) Modern technological solutions of heat pumps, which currently allow them to operate in a wide range of temperatures (with outdoor temperatures as low as –25°C) and to provide domestic hot water even at 65°C. This, in turn, makes it possible to use heat pumps in many more buildings than even a decade earlier.
2) The need for an accelerated energy transformation, including the heating and cooling sector, has put heat pumps in the spotlight of policy makers. Legislation passed in recent years is being implemented in all European Union (EU) member states, with building standards limiting maximum heat demand per m^2, mandating the integration of renewable energy and favoring smart buildings. These measures are beginning to bear fruit, and moreover are often supported by institutional and financial subsides.
3) Steadily increasing sales, which result in reduced purchase costs for heat pumps and increased availability of these devices and their components. Thanks to the parallel reduction in purchase costs of the photovoltaic (PV) system, the self-generated electricity can be used to power the heat pumps, making the entire system very economical.

In 2021, the strongest relative growth in the heat pump market compared to 2020 was achieved in Poland (43.8%), Germany (37.2%) and the Netherlands (30.5%), while only Norway saw a decline, with 12.6% fewer heat pumps sold in 2020 [14].

The sales development, especially in the context of the COVID-19 pandemic, indicates the ongoing strong market expansion of the heat pump industry in Europe [14].

In terms of units sold, the largest heat pump markets in Europe are France (394,129 units), Italy (232,834 units), Germany (140,390 units), Spain (127,856 units) and Sweden (107,723 units) [14, 6]. France, Italy and Germany, as the three largest heat pump markets, together account for 48% of total sales. With Spain, Sweden, Finland, Norway, Denmark, the Netherlands, and most importantly Poland, the top 10 heat pump markets account for a total of 87% of annual sales [6].

In 2020, a total of 14.24 GW of heat pumps were installed in Europe, generating approximately 27.11 TWh of useful energy and using 16.92 TWh of renewable energy for heating and cooling, while avoiding 4.31 Mt of equivalent CO_2 emissions. This has also generated a total employment need of 89,784 FTEs. In total, nearly 14.86 million heat pumps have been installed since 1996, representing an installed thermal capacity of 128.7 GW. All heat pumps in operation have produced 252.6 TWh of usable energy, including 160.2 TWh from renewable sources, and have saved 204.8 TWh of final energy and 93.11 TWh of primary energy [14].

Heat pumps sold in the last 20 years have contributed 41.07 Mt of greenhouse gas (GHG) emissions savings. The distribution of this savings across countries is directly proportional to the distribution of renewable energy. Both of these are directly related to the reduction of fossil energy demand. However, the current rate of growth of heat pumps in Europe is still insufficient to decarbonize heating and cooling by 2050. A distorted pricing mechanism that favors the use of fossil fuels and technologies based on them is identified as one of the problems to be solved [14].

Today, more and more countries are undertaking significant energy transition activities in the district heating sector. To this end, the European Union (EU) has presented its strategy for the integration of this sector. This document predicts that by 2030, 40% of all residential buildings and 65% of all commercial buildings will be heated by electricity. Furthermore, according to the European Green Deal [5] and the Paris Agreement [17], the EU's goal is to achieve climate neutrality by 2050 (i.e. an economy with zero net GHG emissions) [4]. Considering that and bearing in mind that at the same time the principle of preserving energy efficiency still applies, it can be estimated that most new buildings in Europe will be heated and cooled precisely by means of heat pump systems [6].

Polish heat pump market

In recent years, the Polish heat pump market has been developing at a very fast pace. In 2020, the number of heat pumps sold exceeded the number of coal boilers sold

for the first time and heat pumps became the first choice technology. In terms of sales growth, it was ranked 5th, which was considered an excellent result, while predicting that in 2021 it will be ranked 3rd in this respect [7].

According to [13], in 2021 Poland experienced the fastest growth rate for heat pump technology in Europe, with market expansion by 66% with over 90,000 units installed, reaching a total of more than 330,000 units. The Polish Heat Pump Technology Development Organization (PORT PC) also found that the number of heat pumps sold for central heating increased by 80% in 2021 compared to 2020. What is more, their analysis shows that the largest increase in heat pump sales in Poland in 2021 was in the air-to-water heat pump market, where 79,000 units were sold, which in turn means an 88% increase over sales in 2020. Per capita, more heat pumps were installed last year than in other key emerging heat pump markets such as Germany and the UK [9]. This is particularly important because for years Poland has been considered one of the most energy independent countries in Europe. Its coal mining sector and coal-fired power plants have provided carbon-intensive but domestic energy – both for heating and cooling. Even now, with the recent development of renewable energy sources that helps reduce the dependence of Poland on conventional sources, the share of coal in electricity and heat generation is approximately 70% [13].

Given the above, it can be presumed that the heat pump market achieved such growth, mainly due to the implementation of the ten-year "Clean-Air" program, which began in 2018. Under this project, Poland is to allocate nearly 25 billion euros to improve energy efficiency and replace old coal-fired heating systems with cleaner alternatives. As early as March 2020, it was estimated that over 32% of grant applications were for heat pumps [11]. In addition to subsides, many regions in Poland have also begun phasing out coal-fired heating systems through the introduction of appropriate regulations and standards. Prior to this, the number of heat pump installations was moderate and has increased modestly over the years, which shows that national policy is really important in market transformation towards green heating without fossil fuel-based heating systems [13]. In addition, the PORT PC association in its report pointed out that in the case of air-source heat pumps, the key element behind such a significant increase in their sales are: growing attractiveness of the solutions, favorable heating costs, growing trust in this technology among users and installers, investors' interest in emission-free heating systems, comfort of use and growing ecological awareness of the society [9]. Systemic support is also envisaged to facilitate transformation of Polish companies from the heating sector towards innovative, "green" technologies. An example of such activities is, among others, launching a competition at the National Centre for Research and Development (NCBiR) under the "Fast Track" addressed to such entities [11].

It is worth mentioning that an important role in the implementation of heat pump technology in Poland was also played by the activity of PORT PC itself, which is responsible for developing and implementing industry guidelines, quality standards, and certification, as well as conducting training programs for installers.

Figure 2 shows the number of heat pumps sold in Poland in 2015–2021 by type of heat source: air source heat pump (ASHP) or ground source heat pump (GSHP) and their purpose: heating or domestic hot water preparation (dhw).

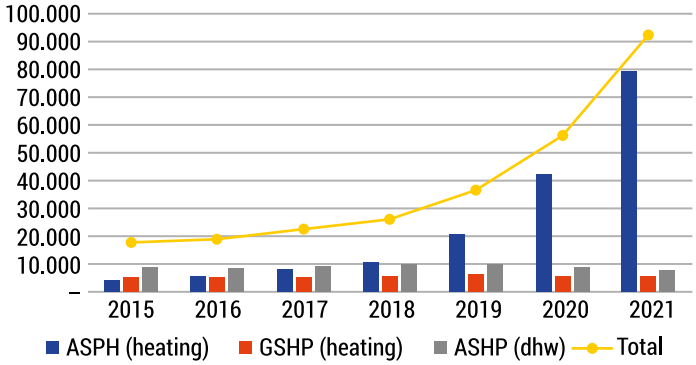

FIG. 2. Sales of different types of heat pumps in Poland during 2015–2021
SOURCE: Own study based on [9, 7]

When analyzing the chart, it can be seen that as of 2018, air-source heat pumps, used primarily for heating purposes – ASHP (heating), are the most popular solution, due to the availability of air as a lower heat source and lower capital costs than in the case of ground-source heat pumps – GSHP (heating). Moreover, also since 2018, a dynamic growth in the total number of heat pumps sold can be observed, compared to previous years, when the growth occurred, but was very slow.

Currently, to maintain such dynamic growth of heat pump sales in Poland, a new program called "My Heat" has been announced. It provides subsidies for the installation of air, water and ground source heat pumps, used either for heating the home alone or in combination with simultaneous provision of domestic hot water. The beneficiaries of the program are the owners or co-owners of newly built single-family houses [12].

According to the PORT PC analysis [11] and [7], sales growth will continue in 2022, mainly for air-to-water heat pumps and to some extent for ground source heat pumps. Stagnation or even a slight decrease is expected in sales of heat pumps for preparation of domestic hot water. It has been estimated that in new buildings with surface heating the costs of heating with heat pumps are even less than 50% of the costs of heating with wood pellets, natural gas or fuel oil. In existing single-family homes, heating cost savings can be up to 30% by using heat pumps.

PORT PC in its report [11, 15] also presented forecasts for the development of the heat pump market in single family buildings in Poland until 2030, assuming two scenarios – the baseline and the optimistic.

The first scenario predicts that in 2030 there will be approximately 1.09 million heat pumps operating in Polish households, providing approximately 29.81 PJ/year of RES energy (average share in all buildings at 10%).

In the second scenario, the number of heat pumps is expected to reach approximately 2.08 million and the value of the RES energy produced by them will be approximately 60.36 PJ/year (share – 22.8%). The values presented depended on, among others, the adopted intensity of support for this technology in various areas.

Figure 3 shows the forecast for the development of heat pump energy production in 2020–2030 divided into the baseline and optimistic scenarios [11].

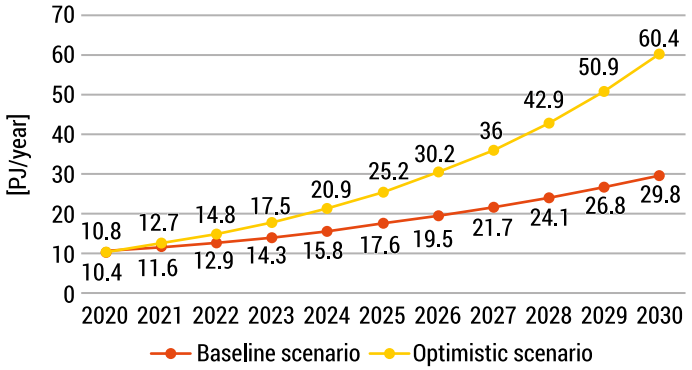

FIG. 3. Forecast of the development of RES energy production from heat pumps in Poland in 2020–2030

SOURCE: Own study based on [11]

In addition to environmental benefits, the dynamic growth of the heat pump market will also contribute to the development of Polish companies manufacturing heat pump components and service companies. According to estimates by PORT PC and EHPA, in 2030 in Poland, with a projected number of 1.09 to 2.08 million heat pumps in operation (depending on the scenario), the heat pump manufacturing, installation and servicing sector will employ 11,000 to 20,000 people [11, 2].

Opportunities and threats

It is estimated that with continued improvements in heat pump energy efficiency and cleaner energy production (rapid reduction of emissions associated with electricity supply), heat pumps could meet 90% of global heating needs with a lower carbon footprint than condensing gas boilers, and by 2025, 100% of heat pumps will be lower carbon than natural gas boilers. The potential of air-source heat pumps to reduce CO_2 emissions compared to condensing gas boilers is presented in the figure below (Fig. 4) [1].

Unfortunately, it can be observed that Poland has a slightly lower potential for CO_2 reduction by air-source heat pumps than its eastern, western and southern

neighbors, which may be due to the national energy mix. This is particularly worrying, as the main goal of the European Green Deal is precisely to decarbonize the entire EU economy by as much as 95% by 2050 [11].

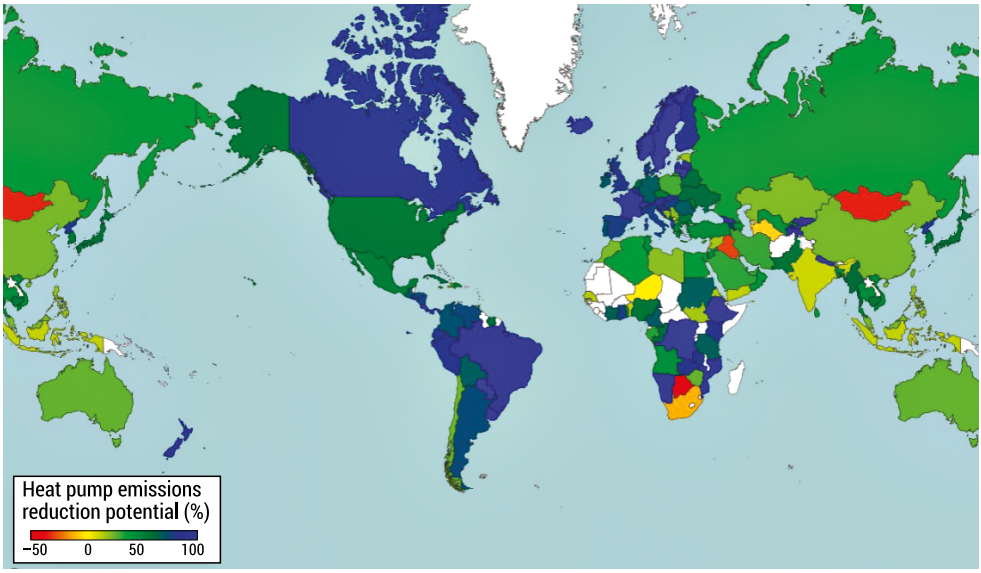

FIG. 4. Potential of ASHPs to reduce CO_2 emissions compared to condensing gas boilers
SOURCE: IEA (2021) Heat Pumps. All rights reserved

Regardless of whether the global, European or Polish market is analyzed, the main barrier against the development of heat pump technology is the high price of equipment purchase and installation. On many world markets the ratio of the size of investment outlay for a heat pump installation compared to the potential savings in energy costs (e.g. when replacing a gas boiler with an electric heat pump) is often not so attractive and beneficial as to encourage the potential user to purchase it, especially in case of renovation of the existing heating system [1, 2].

Another inconvenience when using a heat pump system is high electricity prices. Worldwide, they are about twice or even three times higher than natural gas prices. Closing the gap between electricity and natural gas prices while eliminating electricity taxes in 'power-to-heat' applications would definitely influence the uptake of heat pump technology [1]. The authors in [13] indicate that for Poland, the most effective way to completely eliminate coal from individual heating, as well as to meet policy goals (including increasing energy security, reducing CO_2 emissions, and lowering heating costs), would be to massively introduce heat pumps and energy efficiency programs while increasing the use of RES for electricity generation. According to a PORT PC report [11, 15] and [2], 2022 will be another year of challenges and opportunities for the heat pump industry in Poland. The lack of qualified installers dealing

with the installation of heat pumps has been singled out as a significant barrier to the development of the market for these devices. Other challenges facing the Polish heat pump market include the need to manufacture low-cost Polish equipment, simplify the assembly and commissioning of heat pumps, shorten the supply chain, and manufacture components and accessories for heat pumps. It is estimated that common systems for training of installers, implementation of intelligent R&D programs for manufacturers and monitoring studies of working pumps in residential buildings would undoubtedly bring beneficial results. Attention was also drawn to the need for an information campaign on heat pumps [9]. As the use of heat pumps is closely related to the domestic electricity market, it would also be an important step forward to introduce dedicated electricity tariffs for heat pumps in Poland in parallel with the launch of the Demand Side Response (DSR) service aggregation project [11].

With the exception of domestic politics, all of the above opportunities and threats can to some extent be applied to the rest of the Central and Eastern Europe markets.

Summary

Analyzing the heat pump market in Poland and reviewing the characteristics of the global and European market, it can be concluded that heat pumps are one of the leading technologies, ready to implement the new energy policy strategy of decarbonization in Poland. It seems to be true, that they act as a kind of pioneer among energy systems, combining features of current solutions and modern, fully digitalized solutions of the future. Unfortunately, the development of this technology faces many barriers and threats, mainly related to economic aspects and lack of education and information, as well as execution of installations with these devices itself. Importantly, numerous R&D gaps in this technology are also pointed out. Currently, due to the favorable growth trend of the heat pump market, measures such as raising energy and emission standards, harmonizing definitions related to heat pump efficiency, increasing requirements for thermal performance of buildings, and energy efficiency of the heating devices and their components would contribute to wider use of heat pumps and make heat pumps and other renewable energy sources the primary heat providers.

Acknowledgement: This study was carried out as a part of the work no. WI/WB-IIŚ/9/2022 at the Bialystok University of Technology and was financed from the research subvention provided by the Minister responsible for science.

Literature

[1] Abergel T., *Heat Pumps. More efforts needed*, IEA 2021, online: https://www.iea.org/reports/heat-pumps (accessed on 08.05.2022). All rights reserved.

[2] Crowdway, *Perspektywy rozwoju rynku pomp ciepła w Polsce i UE do* 2030 *roku*, 2021, online: https://www.crowdway.pl/raport-rynek-pomp-ciepla/ (accessed on 08.05.2022).

[3] Energy Saver, *Heat Pump Systems*, online: https://www.energy.gov/energysaver/heat-pump-systems (accessed on 08.05.2022).

[4] European Commission, 2050 *long-term strategy*, online: https://ec.europa.eu/clima/eu-action/climate-strategies-targets/2050-long-term-strategy_en (accessed on 08.05.2022).

[5] European Commission, *Communication from the Commission to the European Parliament, the European Council, the Council, the European Economic and Social Committee and the Committee the Regions: The European Green Deal*, 2019, COM(2019) 640 final

[6] European Heat Pump Association, *Market data*, 2021, online: https://www.ehpa.org/market-data/ (accessed on 08.05.2022).

[7] Fodrowska K., *Pompy ciepła w Polsce – Podsumowanie* 2021 *[Raport]*, Enerad 2022, online: https://enerad.pl/aktualnosci/pompy-ciepla-podsumowanie-2021-raport-enerad-pl/ (accessed on 08.05.2022).

[8] Foit H., *Zastosowanie odnawialnych źródeł ciepła w ogrzewnictwie i wentylacji*, Wydawnictwo Politechniki Śląskiej 2013, ISBN: 978-83-7335-572-9.

[9] IEA HPT, *Can Heat Pumps free Poland from Russian Gas Dependency? Yes, they can says Poland: A Significant Heat Pump Market Growth Recorded In* 2021, online: https://heatpumpingtechnologies.org/news/1/57291 (accessed on 08.05.2022).

[10] Jung Y., Oh J., Han U., Lee H, *A comprehensive review of thermal potential and heat utilization for water source heat pump system*, Energy and Buildings 2022, 266, 112124.

[11] Lechman P., Rączka J., Schnell C., Wróbel P., *Scenariusze elektryfikacji ogrzewania w budynkach jednorodzinnych w Polsce do* 2030 *roku*, PORT PC 2020.

[12] Ministerstwo Klimatu i Środowiska, *Szansa na uzyskanie z NFOŚiGW dotacji do pomp ciepła w nowo budowanych domach. Program „Moje Ciepło" wystartował*, 2022, online: https://www.gov.pl/web/klimat (accessed on 08.05.2022).

[13] Morawiecka M., Rosenow J., *From laggard do leader: How Poland became Europe's fastest-growing heat pump market*, 2022, Foresight Climate & Energy, online: https://foresightdk.com/from-laggard-to-leader-how-poland-became-europes-fastest-growing-heat-pump-market/ (accessed on 08.05.2022).

[14] Nowak T., *European heat pump market*, REHVA Journal 2021, 4.

[15] PORT PC. O 80% większa sprzedaż pomp ciepła do ogrzewania budynków w 2021 r., Rynek Instalacyjny 2022, online: https://www.rynekinstalacyjny.pl/artykul/aktualnosci/133227,o-80-wieksza-sprzedaz-pomp-ciepla-do-ogrzewania-budynkow-w-2021-r (accessed on 08.05.2022).

[16] Rosenow J., Gibb D., Nowak T., Lowes R., *Heating up the global heat pump market*, Nature Energy 2022, 7, p. 901–904.

[17] United Nations, *Paris Agreement*, 2015.

Pesticide industry wastewater treatment with photo-Fenton process

Keywords: raw pesticide wastewater, photo-Fenton process, Box-Behnken design

Abstract: Pesticide manufacturing industry wastewater causes pollution problems due to the toxic components, high chemical oxygen demand (COD), biochemical oxygen demand (BOD), high total dissolved solids (TDS) and intensive color, disgusting odor and generally low pH values. Since sufficient treatment efficiency cannot be obtained with biological treatment in these wastewaters, chemical processes based on advanced oxidation methods are needed for the removal of toxicity and organic load caused by pesticide wastewater. Advanced oxidation methods are based on the formation of hydroxyl radicals ($OH^{\bullet}$) and provide the conversion of toxic organic substances into harmless products. The major objective of this study is to investigate the oxidation of raw pesticide wastewater by the photo-Fenton process by using a Box-Behnken statistical experimental design and surface response methodology. In the photo-Fenton experiments, the effects of different oxidant and catalyst concentrations for COD removal at different reaction times were investigated by using Box-Behnken statistical design. As a result of the studies, the most appropriate reaction conditions according to COD removal; H_2O_2 concentration was 1000 mg/L, Fe^{+2} concentration was 325 mg/L, reaction time was 35 minutes and COD yield was 70%.

Introduction

Pesticides are agricultural drugs used to combat weeds, plants and insects that are harmful to crops and affect the efficiency during the cultivation of plants. They are often used in modern agriculture to meet the nutrition needs of the growing

population and to obtain increased yields. However, pesticides are highly toxic, carcinogenic and mutagenic in nature, and persist in nature at low concentrations for a long period of time after use.

Pesticide manufacturing industry wastewater causes pollution problems due to the toxic components, high chemical oxygen demand (COD), biochemical oxygen demand (BOD), high Total dissolved solids (TDS) and intensive color, disgusting odor, and generally low pH values [1]. Chemical oxidation demand of pesticide wastewater is higher than biological oxidation demand of it. Therefore, microorganisms cannot easily degrade wastewater originating from the pesticide industry. Despite the low economic cost aspect of biological treatment, conventional biological methods have not been an effective method to treat or degrade refractory and toxic organics in pesticides in wastewater. In addition, the pH value of pesticide wastewater is very low and this pH value is not suitable for the biological treatment processes. So, pesticide wastewater cannot be treated by biological processes directly, it is not feasible to use single conventional biological methods or conventional chemical-precipitation methods in the treatment of pesticide wastewater.

New technologies are to be developed for effective treatment of wastewater containing pesticides. An advanced oxidation process that depends on highly concentrated and refractory compounds in pesticide wastewater should be preferred as a pretreatment process before biological treatment methods to treat or degrade non-biodegradable pesticides in wastewater. In recent years, advanced oxidation processes (AOPs) have been used as potentially powerful methods capable of transforming non-biodegradable pollutants into harmless substances. Almost all AOPs rely on the generation of reactive free radicals, such as hydroxyl ($OH^{\bullet}$), with a redox potential of 2.8 V. The free radicals react rapidly with most of the organic compounds, either by addition to a double bond or by abstraction of a hydrogen atom from aliphatic organic molecules. The resulting organic radicals then react with oxygen to initiate a series of oxidation reactions leading to mineralization of the organics to produce CO_2 and H_2O. Therefore, advanced oxidation is a promising alternative for mineralization and reducing recalcitrant organic compounds in wastewater. The Photo-Fenton process as an advanced oxidation process is a very effective method to degrade pesticides in wastewater. It changes the form of compounds, converting them into an easily degradable form for microorganisms in biological treatment methods [2]. In addition, the photo-Fenton process has many advantages, it requires a short reaction time and low amounts of oxidant and catalyst doses compared to other advanced oxidation methods.

The major objective of this study is to investigate the advanced oxidation of pesticide wastewaters by the Photo-Fenton process as a pretreatment process. The effect of hydrogen peroxide (H_2O_2) and ferrous ion (Fe^{+2}) concentrations and reaction times on the oxidation of pesticide wastewater was investigated with chemical oxidation demand (COD) removal by using a Box-Behnken statistical experimental design and surface response methodology.

Material and methods

The pesticide wastewater used in these experiments was obtained from a pesticide factory in İzmir, Turkey. This factory produced many kinds of pesticides, such as azoxytrubin, imidaclobrid, epoxinazole and methoxy fenozide etc. The wastewater from the pesticide production industry contained a lot of precursor chemicals and pesticides. The COD concentration of the wastewater was around 150,000 mg/L. The pH value of the wastewater was around 5. In addition, suspended solids were very high. The Photo-Fenton experiments were carried out at room temperature (23±2°C) using different hydrogen peroxide and ferrous ions. Hydrogen peroxide solution (35% w/w) and ferrous sulfate was obtained from Merck, and was used as an oxidant and catalyst, respectively.

Design of experiments

The effects of variables on the response are complicated and observed by means of the mostly known approach, which is altering one factor at a time for multivariable systems. However, this technique is not practical for estimation of responses. So, some experimental statically design should be used for optimization of the reaction conditions. For this purpose, several significant parameters are determined by response surface methodology (RSM). Between all RSM designs, Box-Behnken design needs fewer experimental runs and shows to be efficient at intermediate levels not experimentally studied [3–4].

The main objective of the study was to statistically determine the most favorable levels of the parameters for the treatment of pesticide wastewater. Oxidation of pesticide wastewater was investigated by the Photo-Fenton process in terms of COD removal efficiency. The effects of H_2O_2 and ferrous ion concentrations and reaction time on the oxidation of real pesticide wastewater, which is produced by the pesticide industry, were investigated by using a Box-Behnken statistical experiment design method. As the dependent variable, the most important parameter was considered as COD and the COD removal efficiencies were examined. In the statistical method, Fe^{+2} and H_2O_2 concentrations and reaction time were selected as independent variables. Operating range for the independent variable; H_2O_2 concentration was 1000–5000 mg/L (X_1), Fe^{+2} concentration was 100–500 mg/L (X_2), reaction time was determined as 5–60 minutes (X_3).

Experimental procedure

All batch photo-oxidation experiments were performed in the completely mixed, batch, cylindrical photochemical reactor containing a 16 W low-pressure mercury vapor lamp with a total volume of 2.2 L. Figure 1 shows a schematic diagram of the laboratory-

-scale photochemical reactor which was used for oxidation experiments in previous studies [5].

After the addition of raw pesticide wastewater into the reactor, ferrous ion as a catalyst was added and mixed well with the wastewater before the addition of hydrogen peroxide as an oxidant. The UV lamp was immediately turned on after the addition of hydrogen peroxide to the reactor. The time at which the ultraviolet lamp was turned on was considered as time zero, or the beginning of the experiment. Samples withdrawn from the reactor at certain time intervals were analyzed immediately to avoid further reactions. Raw and treated wastewater samples were withdrawn from the reactor in order to execute chemical oxygen demand and pH analysis. In addition, total organic carbon and suspended solids analyses were also done.

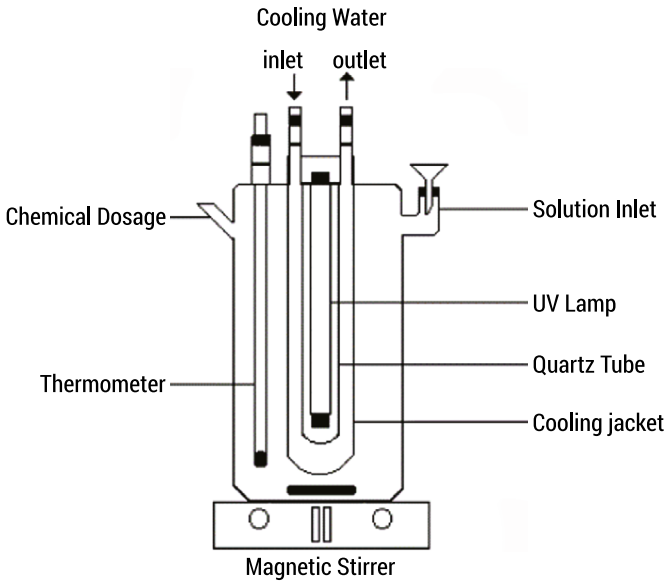

FIG. 1. A schematic diagram of the laboratory-scale photochemical reactor
SOURCE: own study based on [5]

In the experiments, the effects of hydrogen peroxide (H_2O_2) and ferrous ion (Fe^{+2}) concentrations and reaction times as independent variables on the oxidation of raw pesticide wastewater were evaluated in terms of chemical oxidation demand (COD) removal as dependent variables in the Box-Behnken design.

Results and discussion

The Box-Behnken design approach is mentioned as an effective and useful way for optimization of the three variable response functions, predicting the response of the fitted

model by the ANOVA tests. Hydrogen peroxide (X_1), ferrous ion (X_2) and reaction time (X_3) as the independent variables were selected in design. In addition, percent COD removal (Y_1) as the dependent variable was selected in statically design for this purpose. The low, center and high levels of each variable organized by statically approach as –1, 0, and +1 respectively as shown in Table 1.

TAB. 1. Levels of variables in Box-Behnken design

Parameter/Codes	H_2O_2 (mg/L)	Fe^{+2} (mg/L)	Reaction Time (min)
	X_1	X_2	X_3
Low (–1)	1000	100	5
Center (0)	3000	300	32,5
High (+1)	5000	500	60

SOURCE: own elaboration

Reaction conditions for independent variable; H_2O_2 concentration was 1000–5000 mg/L (X_1), Fe^{+2} concentration was 100–500 mg/L (X_2), reaction time was determined as 5–60 minutes (X_3). The effects of independent variables (hydrogen peroxide, ferrous ion and reaction time) on dependent variable (percent COD removal) were evaluated. The experimental conditions of the Box-Behnken experiment design and results of for Photo-Fenton processes presented in Table 2.

TAB. 2. The experimental conditions in photo-Fenton oxidation and COD Removal efficiencies as dependent variables in Box-Behnken design

Run	H_2O_2 (mg/L); X_1	Fe^{+2} (mg/L); X_2	Reaction Time (min); X_3	COD Rem. Eff. (%);Y_1
1	1000	100	32,5	61,6
2	5000	100	32,5	42,4
3	1000	500	32,5	55,2
4	5000	500	32,5	52
5	1000	300	5	70
6	5000	300	5	48,8
7	1000	300	60	68
8	5000	300	60	68
9	3000	100	5	42,2
10	3000	500	5	27
11	3000	100	60	30
12	3000	500	60	45,6
13	3000	300	32,5	52

Run	H_2O_2 (mg/L); X_1	Fe^{+2} (mg/L); X_2	Reaction Time (min); X_3	COD Rem. Eff. (%);Y_1
14	3000	300	32,5	52
15	3000	300	32,5	52

SOURCE: own elaboration

This statically design was preferred due to fewer combinations of the independent variables to estimate the second-order polynomial regression model. Coefficients in the regression model were determined by means of 15 runs. Nine coefficients were calculated such as one block term, three linear terms, three quadratic terms and three interaction terms. The application of RSM offers an empirical relationship between the response function and the independent variables. The mathematical relationship between the response function (Y) and the independent variables (X) can be approximated by a quadratic (second-order) polynomial equation as follows:

$$Y = b_0 + b_1X_1 + b_2X_2 + b_3X_3 + b_{12}X_1X_2 + b_{13}X_1X_3 + b_{23}X_2X_3 + b_{11}X_1^2 + b_{22}X_2^2 + b_{33}X_3^2 \quad (1)$$

The coefficients of the response functions for different dependent variables were determined by correlating the experimental results with the relevant functions used in a Stat-Ease regression program. Different response functions with the determined coefficients are presented by Eq. (2). Evaluations of experimental results and designated of all Figures were done by means of Eqs. (2) and Stat-Ease regression program. The objective function for COD removal efficiency with the determined coefficient is presented by Eq. (2).

$$Y_1 = 86{,}44 - 0{,}03X_1 + 0{,}13X_2 - 0{,}39X_3 + 1{,}0E^{-05}X_1X_2 + 1{,}0E^{-04}X_1X_3 + \\ + 0{,}0014X_2X_3 - 3{,}54E^{-06}X_1^2 - 0{,}0003X_2^2 - 0{,}003X_3^2 \text{ (R-Squared = 0.9931)} \quad (2)$$

The results of analysis of variance (ANOVA) are also presented in Tables 3 indicating the fact that that the predictability of the model is at a 99% confidence interval.

TAB. 3. ANOVA test for response function Y_1 (COD removal, %)

Source	Sum of squares	D.F.	Mean square	F Value	p-value
Model	2259,44	9	251,05	79,75	< 0,0001
X_1-H_2O_2	237,62	1	237,62	75,48	0,0003
X_2-Fe^{+2}	1,62	1	1,62	0,5146	0,5053
X_3-Reaction time	69,62	1	69,62	22,12	0,0053
X_1X_2	64,00	1	64,00	20,33	0,0063
X_1X_3	112,36	1	112,36	35,69	0,0019
X_2X_3	237,16	1	237,16	75,34	0,0003
X_1^2	739,28	1	739,28	234,84	< 0,0001

Source	Sum of squares	D.F.	Mean square	F Value	p-value
X_2^2	658,05	1	658,05	209,04	< 0,0001
X_3^2	22,16	1	22,16	7,04	0,0452
Residual	15,74	5	3,15		
Lack of Fit	15,74	3	5,25		
Pure Error	0,0000	2	0,0000		
Cor Total	2275,18	14			

SOURCE: own elaboration

Response function predictions are in good agreement with the experimental data with a coefficient of determination (R^2) of higher than 0.993. Furthermore, the computed F value (79.75) is much greater than that of the tabular $F_{0.01\ (14,\ 14)}$ value of 3.70 suggesting that the treatment is highly significant. P values of less than 0.05 for any factor in the analysis of variance (ANOVA) indicated a significant effect of the corresponding variable on the response.

From the analysis of the ANOVA test presented in Tables 3, it can be said that hydrogen peroxide dose and reaction time (X_1, X_3, X_1X_2, X_1X_3, X_2X_3, X_1^2, X_2^2, X_3^2) were the two major factors affecting the COD removal due to high 'F' ratios and low 'p' values. Response functions with determined coefficients were used to estimate variations of response functions with the independent variables under different conditions.

Figure 2 shows the effect of different Fe^{+2} concentrations and different reaction times ion on percent COD removal when the initial concentration of H_2O_2 was 1000 mg/L.

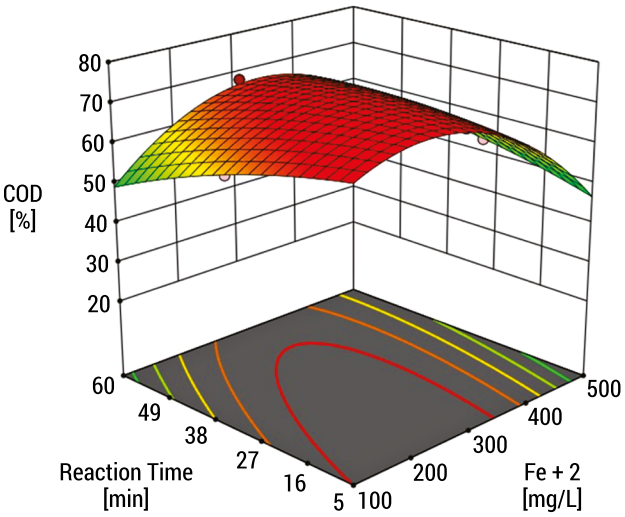

FIG. 2. COD removal efficiencies achieved with different Fe^{+2} concentrations and reaction times (H_2O_2: 1000 mg/L, pH:5)

SOURCE: own elaboration

The addition of ferrous ion to the oxidation process increased the COD removal efficiencies due to the acceleration of hydroxyl radical formation by means of ferrous ion. When ferrous ion increased to 350 mg/L from 100 mg/L, COD removals were increased to 70% from 50% at H_2O_2 concentration of 1000 mg/L and reaction time of 5 min. As shown in Figure 2, percent COD removals were 58, 65 and 48% when Fe^{+2} concentrations of 100, 300 and 500 mg/L, respectively at a H_2O_2 concentration of 1000 mg/L and reaction time of 5 min. Excess amounts of ferrous ion caused to decrease COD removal efficiencies due to the inhibition effect of ferrous ion on production of hydroxyl radical. When reaction time was increased to 60 min from 5 min, COD removals were not significantly increased at H_2O_2 concentration of 1000 mg/L and reaction time of 5 min. Long reaction times as independent variables are not preferable, because oxidation reactions occur rapidly and low reaction times are sufficient to produce hydroxyl radicals to react with refractory organics.

Figure 3 shows the effect of different Fe^{+2} concentrations and different reaction times ion on percent COD removal when the initial concentration of H_2O_2 was 1000 mg/L. As shown in Figure 3, percent COD removals were 40, 68 and 65% when Fe^{+2} concentrations were 100, 300 and 500 mg/L, respectively at a H_2O_2 concentration of 3000 mg/L and a reaction time of 60 min. When reaction time decreased to 5 min from 60 min, only 20% COD removal efficiencies were ascended at H_2O_2 concentration of 3000 mg/L and ferrous ion concentration of 300 mg/L. At these results, it can be said that a high amount of hydrogen peroxide needs long reaction times to be efficient at COD removal.

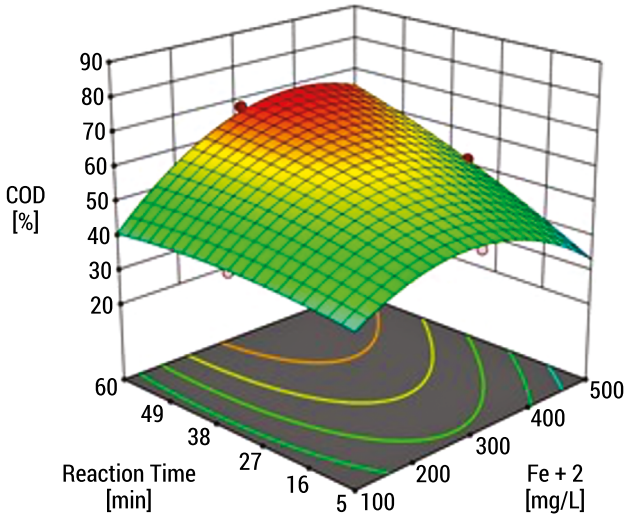

FIG. 3. COD removal efficiencies achieved with different Fe^{+2} concentrations and reaction times (H_2O_2: 3000 mg/L, pH:5)

SOURCE: own elaboration

Figure 4 shows the effect of different Fe^{+2} concentrations and different reaction times ion on percent COD removal at when initial concentration of H_2O_2 was 5000 mg/L. As shown in Figure 4, percent COD removals were 30, 52 and 42% when Fe^{+2} concentrations of 100, 300 and 500 mg/L, respectively at a H_2O_2 concentration of 5000 mg/L and reaction time of 60 min.

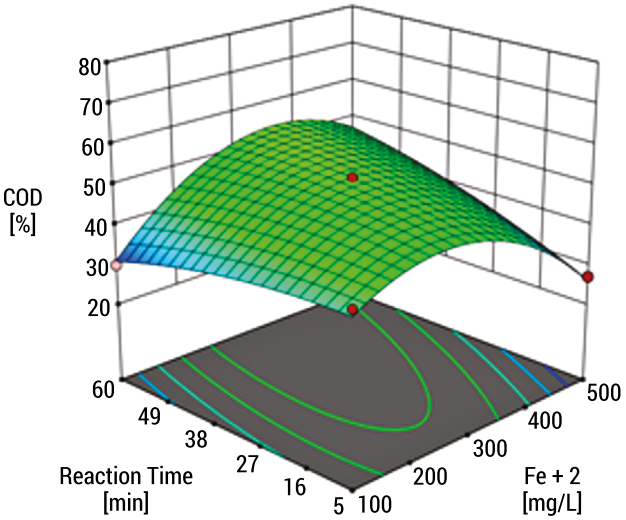

FIG. 4. COD removal efficiencies achieved with different Fe^{+2} concentrations and reaction times (H_2O_2: 5000 mg/L, pH:5)

SOURCE: own elaboration

As shown in Figure 2-3-4, percent COD removals were 65, 42 and 32% when H_2O_2 concentrations of 1000, 3000 and 5000 mg/L, respectively, at a ferrous ion concentration of 300 mg/L and reaction time of 5 min. It can be said that the requirement of a hydrogen peroxide concentration to degrade real pesticide wastewater was small at a medium ferric ion concentration. At this situation, high oxidant usage resulted in a low COD removal efficiency due to excess H_2O_2/Fe (II) molar ratio. At high H_2O_2 concentrations, it is probable that H_2O_2 served as a free-radical scavenger for itself, reducing the [$OH^{\bullet}$].

$$OH^{\bullet} + H_2O_2 \rightarrow H_2O + HO_2^{\bullet} \quad (3)$$

$$OH^{\bullet} + HO_2^{\bullet} \rightarrow H_2O + O_2 \quad (4)$$

An excess of H_2O_2 favors reactions consuming such radicals, which is an adverse effect. In agreement with Tokumura et al. [6] a reduction in process performance was observed at high H_2O_2 concentrations indicating the adverse effects of excess H_2O_2.

The optimal H_2O_2/Fe^{+2}/reaction time ratio resulting in the maximum COD (70%) removal was found to be 1000/325/35. Optimal values of the operating parameters maximizing COD removal were determined. In addition, at these operating parameters, TOC and suspended solids removals were also observed as 20% and 32.5%, respectively. After the photo-Fenton process as a pretreatment method, treated pesticide wastewater was then to be treated with the biological treatment method. Biological treatment methods can be applied to effluent from the Photo-Fenton process and discharge standards to surface water can be reached.

Summary

Real pesticide wastewater treatment with the Photo-Fenton process as a pretreatment process was investigated. The Box-Behnken statistical experiment design and the response surface methodology (RSM) were used for this purpose. The effects of hydrogen peroxide (H_2O_2) and ferrous ion (Fe^{+2}) concentrations and reaction times as independent variables on the oxidation of raw pesticide wastewater were evaluated in terms of chemical oxidation demand (COD) removal as dependent variables in the Box-Behnken design.

In the statistical method, Fe^{+2} and H_2O_2 concentrations and reaction time were selected as independent variables. The operating range for independent variable; H_2O_2 concentration was 1000–5000 mg/L (X_1), Fe^{+2} concentration was 100–500 mg/L (X_2), reaction time was determined as 5–60 minutes (X_3). Experimental data was used to determine the coefficients of the response functions. Predictions obtained from the response functions were in good agreement with the experimental results, indicating the reliability of the method used.

The optimal H_2O_2/Fe^{+2}/reaction time ratio resulting in the maximum COD (70%) removal was found to be 1000/325/35. Optimal values of the operating parameters maximizing COD removal were determined. In addition, at these operating parameters, TOC and suspended solids removals were also observed as 20% and 32.5%, respectively. After the photo-Fenton process was utilized as a pretreatment process, treated pesticide wastewater was converted to be treated with a biological treatment method. Therefore, the aim of the research was successful.

Literature

[1] Singare P., Dhabarde S., *Pollution Scenario due to Discharge of Effluent from Agrochemicals and Pesticides Manufacturing Industries of Dombivali Industrial Belt of Mumbai, India,* International Letters of Chemistry, Physics and Astronomy 2016, 22, p. 8–15.

[2] Catalkaya E., Kargi F., *Advanced oxidation treatment of pulp mill effluent for TOC and toxicity removals,* Journal of Environmental Management 2008, 87 (3), p. 396–404.

[3] Sastry S., Khan M.A., *Aqueous based polymeric dispersion: Plackett – Burman design for screening of formulation variables of atenolol gastrointestinal therapeutic system,* Pharmaceutica Acta Helvetiae 1998, 73, p. 105–112.

[4] Hamed E., Sakr A., *Application of multiple response optimization technique to extended release formulations design,* Journal of Control Release 2001, 73, p. 329–338.

[5] Çokay E., *Effects of the heterogeneous photo-Fenton oxidation and sulfate radical-based oxidation on atrazine degradation,* Desalination and Wastewater 2022, 252, p. 233–242.

[6] Tokumura M., Morito R., Hatayama R., Kawase Y., *Iron redox cycling in hydroxyl radical generation during the photo-Fenton oxidative degradation: dynamic change of hydroxyl radical concentration,* Applied Catalysis B: Environmental 2011, 106, p. 565–576.

Determination of optimal pyrolysis process parameters to maximize gasoline-like renewable fuel production from polypropylene: a review

Keywords: PP, plastic pyrolysis, process optimization, renewable fuels, plastic waste

Abstract: Polypropylene (PP) is the most common type of plastic found in municipal plastic waste. Its physicochemical properties (e.g., volatiles, calorific value) make PP suitable for pyrolysis to produce alternative fuels. In this study, a literature review was conducted to determine the optimal parameters (e.g., temperature and vapor residence time) and units (e.g., reactor type) of a pyrolysis process for maximum production of hydrocarbons in the gasoline range (C5–C12). To be consistent with industrial processes and to understand the behavior of thermal pyrolysis, the scientific articles on continuously operated and non-catalytic pyrolysis of PP were studied in terms of product yield and pyrolysis oil composition. The yield of pyrolysis oil decreased at a temperature higher than 550°C. The maximum yield of gasoline (54 wt.%) was obtained in continuously stirred tank reactors (CSTRs), which proved to be the reactor with the best performance. The main product was mainly wax in continuously spouted bed reactors (CSBRs) because the vapor residence time (i.e. less than a second) was too short for the formation of lighter products. Gas production was the target for bubbling fluidized bed reactors (BFBRs), falling-film reactors (FFRs), and rotating cone reactors (RCRs).

Introduction

Due to their durability, low price, and ease of processing, demand for the production of plastics has increased since the mid-20th century [1]. This demand, driven mainly by the packaging, construction, automotive, and electrical appliance industries, has resulted in the production of 55 million tons of plastics in the EU27+3 countries or 367 million tons worldwide [2]. There is no doubt that the generation of plastic waste, which is directly related to the production rate of plastics, is a threat to the environment. One of the approaches to address this problem is the Waste-to-Energy (WtE) approach, which aims to recover energy, monomer and fuel from plastic waste through incineration, mechanical recycling and chemical recycling, respectively. Incineration is used to generate heat and power, while mechanical recycling mainly involves the extrusion and reforming of used plastics. Pyrolysis, on the other hand, is a thermochemical conversion technology that leads to the production of fuel-like products from plastics.

Polypropylene (PP) is the most abundant type of plastic in the documented amount of plastic waste and has suitable physicochemical properties for the production of gasoline-like fuels (i.e., C5–C13 hydrocarbons) [2] by pyrolysis. Pure PP consists mainly of volatiles (about 99.2 wt.%) and traces of ash and moisture [3]. In addition, the high C/H ratio (about ca. 6.6) of PP indicates a high calorific value of ca. 47.3 MJ/kg [3]. The amount of energy that could be generated by burning PP equal to 10 wt.% of the amount fed to the process can meet the energy demand of the pyrolysis process [4]. Due to these characteristics, the pyrolysis of PP – as an energetically self-sufficient process – can simultaneously provide a renewable fuel and contribute to the reduction of non-recycled plastic waste. However, the high viscosity and low thermal conductivity of PP limit heat transfer during pyrolysis. Therefore, the type of pyrolysis reactor, in addition to other process parameters (e.g. reaction temperature, residence time) directly affects the quantity and quality of the products of PP pyrolysis [5]. The main product of thermal pyrolysis PP is wax. Limiting wax formation and increasing lighter fuel production are possible by establishing optimal operating parameters and units for non-catalytic pyrolysis. In the pyrolysis of PP, increasing the pyrolysis temperature favors the cracking of waxes into smaller hydrocarbons (e.g., gasoline-like fuels, non-condensable gases) [6]. Another option is to increase the vapor residence time; many studies find that longer vapor residence times result in hydrocarbons with lower molecular weights [7, 8]. To set an optimal pyrolysis temperature and a vapor residence time, the pyrolysis reactor should be adjustable. Batch and/or semi-batch reactors are often preferred for laboratory scale because of their ease of operation but are difficult to scale up. In contrast, continuously operated reactors such as continuously spouted bed reactors (CSBRs), rotating cone reactors (RCRs) and continuously stirred tank reactors (CSTRs) overcome mass and heat transfer limitations [9] and are therefore well suited for scaling and use in large-scale processes.

In this work, published scientific articles focusing on continuous and non-catalytic pyrolysis of PP are reviewed. The ultimate goal is to find optimal conditions for process parameters and the most suitable reactor type for the production of gasoline-like liquid fuels. At the same time, the other focus is on NC pyrolysis of PP, to find optimal conditions for the production of C5–C13 hydrocarbons without promoters such as catalysts or other upgrades. To understand the relationship between temperature, reactor type, and liquid yield, the maximum allowable pyrolysis temperature, and lowest yield were set to be 550°C and 70 wt.%, respectively. The data matching the highest liquid production range were further analyzed to determine the residence time of the vapor in different types of reactors. In this study, the literature reports addressing the results of PP pyrolysis obtained from non-catalytic and continuously operated pyrolysis systems are reviewed. The report summarizes the status and achievements of research and technology development based on scientific literature, available reports of commercial/industrial trials, and scientific expertise acquired in our research group in the field of plastic pyrolysis. The objective is to develop some recommendations and suggestions regarding the design of a plastic pyrolysis process on a commercial/industrial scale.

Materials and methods

The data used for this work was collected from Web of Science, Scopus, and Wiley databases for the period 1984 to 2021. The articles were searched with the keywords "Polypropylene" and "Pyrolysis". The collected data were split into three sets according to an operation mode used for pyrolysis: Batch, Semi-batch, and Continuous. Only the articles in the "Continuous" set were selected for this study to be in line with the industrial processes. The articles in this set were further categorized into two sets depending on the catalyst usage: Non-catalytic and Catalytic. The articles in the "Non-catalytic" set were used to explain the characteristics of the products of pyrolysis changing with process parameters (e.g. temperature, vapor residence time) and units (e.g. reactor types) without using any promoters such as catalyst and steam. In total, 14 articles [6,7,17–20,8,10–16] concerning non-catalytic and continuous pyrolysis of PP were collected and analyzed in detail to explain optimum pyrolysis conditions for gasoline-like fuel production.

Thermal gravimetric analysis (TGA) shows that pyrolysis of PP occurs at temperatures between 415°C and 540°C under an inert gas (e.g. N_2) flow rate [10]. The maximum cracking takes place for PP at 470°C determined by differential thermal derivative thermogravimetry (DTG) [11]. Also, many studies reported that almost a complete conversion of the initial mass of PP is measured by TGA [10, 12]. In light of the kinetic data of PP, the maximum allowable temperature for pyrolysis was

selected at 550°C (vertical dashed lines in Figure 1), while the lowest liquid yield was 70 wt.% (horizontal dashed lines in Figure 1) and was selected by considering possible experimental errors and the average yield data of the collected articles.

The data fulfilling the yield and temperature boundaries (upper-left section of Figure 1) were examined in terms of the detailed composition of liquid products varying with process parameters (i.e. temperature and vapor residence time). Studies [13–15] did not report any data about wax, gasoline, and diesel range hydrocarbons being excluded in this part even though the data was located between the temperature and the yield boundaries.

Results

Figure 1. shows the correlation between liquid yield and pyrolysis temperature. At a temperature higher than 550°C, liquid production decreases with increasing temperature, while gas production accelerates due to secondary reactions, regardless of reactor type [6, 15, 16]. The compositions of the liquid products are listed in Table 1, except for the studies by Jin et al. (2018), Fraczack et al. (2021), Kaminsky (1991), and Walendziewski (2005), for which no data are available. In the temperature range of liquid production (T≤ 550°C), the main product of pyrolysis oil is wax [17]. The trend is consistent with the collected data from the literature, except for the continuous and non-catalytic pyrolysis data in CSTRs. Leaving the hot pyrolysis vapors for more than one second improves the cracking of the wax and the production of light hydrocarbons, especially at temperatures above 500°C [7].

CSTRs were operated below the temperature (i.e. 470°C) where maximum degradation occurs, according to DTG data mentioned above. Although the pyrolysis temperatures were significantly lower for CSTRs, the liquid yields were not lower than 90 wt.% [14, 18, 19]. All studies used an extruder to preheat PP before delivering CSTRs to it. The use of a pretreatment reactor boosted liquid yield by shortening the time to reach pyrolysis temperature, which prevented the production of by-products (e.g., char) generated by slow pyrolysis [20]. Gasoline range hydrocarbons were the product in CSTRs (see Table 1). The formation of lighter hydrocarbons is unusual for the non-catalytic pyrolysis of plastics at very low temperatures (~400°C). This trend can be explained in two ways:

1) PP is a branched polymer and has a lower C–C bond-breaking energy compared to other plastics (e.g., low density polyethylene, high density polyethylene), which allows for greater cracking even at lower temperatures [21].
2) Elevated vapor residence time can also lead to the formation of C5–C12 hydrocarbons, but the authors have not provided data on vapor residence time [14, 18, 19].

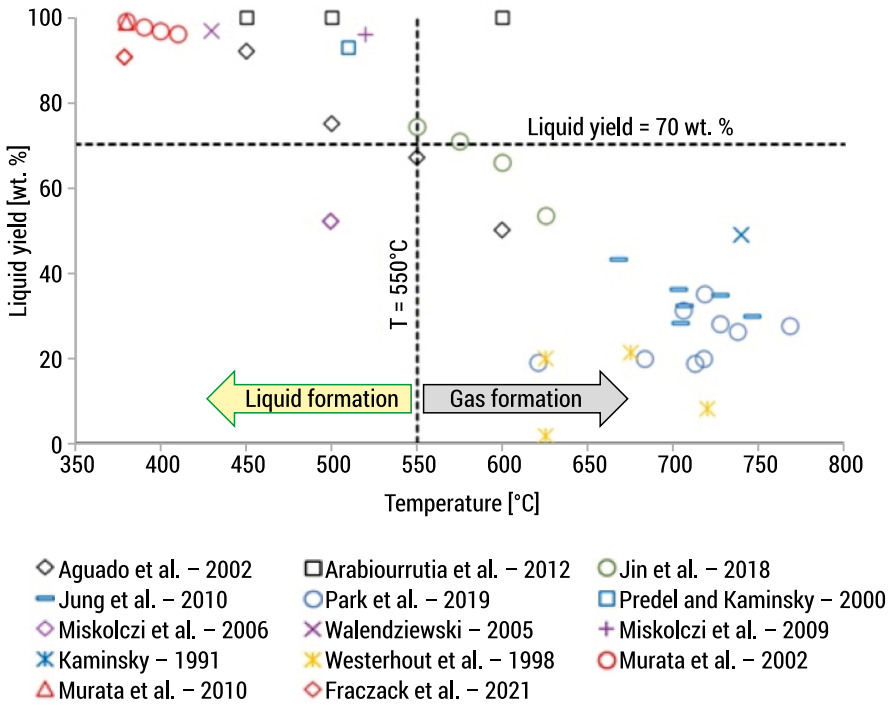

FIG. 1. The correlation between liquid yield and pyrolysis temperature for PP (**Black:** CSBR, **Red:** CSTR, **Blue:** BFBR, **Green:** FFR, **Orange:** RCR, **Purple:** CFR)

SOURCE: own elaboration

Vapor residence time was less than one second for CSBRs suppressing both gas and light oil (i.e., C5–C20 hydrocarbons) yields. Arabiourrutia et al. (2012) reported that the gasoline and diesel range hydrocarbon yields were increased when the pyrolysis temperature was increased from 450 to 500°C [6]. In contrast to the study by Arabiourrutia et al. (2012), Aguado et al. (2002) did not observe any change in the yield of hydrocarbons in the gasoline and diesel range at the same temperatures [16]. As can be seen in Table 1, a slight increase in vapor residence time leads to the production of C5–C12 hydrocarbons.

Continuous flow reactors (CFRs) were continuously operated tubular reactors. The data obtained for CFRs were in the range of liquid formation in Figure 1. In all studies, an extruder operated at a temperature between 250 and 280°C was used as the pretreatment reactor [13, 22, 23]. Miskolczi et al. (2009) and Walendziewski (2005) reported a liquid yield of 96 wt%. The almost complete liquid production would be triggered by the above-mentioned pretreatment process. In contrast to other studies, Miskolczi et al. (2006) reported 52 wt.%, 3 wt.%, and 45 wt.% as liquid, gas, and solid yields, respectively [23]. Although no process time was mentioned

in the study, the pyrolysis time would not have been sufficient for this study, which resulted in a high amount of solid product.

TAB. 1. The composition of liquid products of the data point falling in temperature and yield boundaries

Temperature (°C)	Vapor residence time (s)	Wax (C21+) yield (wt.%)	Gasoline (C5–C12) yield (wt.%)	Diesel (C5–C13) yield (wt.%)	Total liquid yield (wt.%)	Reference
450	0.020	92.0	0.00	0.00	92.0	[16]
500	0.020	75.0	0.00	0.00	75.0	[16]
550	0.020	67.0	0.00	0.00	67.0	[16]
450	0.054	92.0	1.10	6.90	100	[6]
500	0.054	75.0	3.30	21.7	100	[6]
510	5.60	56.2	28.8	6.40	91.4	[7]
510	4.20	57.5	31.1	6.48	95.1	[7]
520	N/A	48.9	28.9	18.0	95.8	[22]
380	N/A	13.4	54.3	32.4	100	[19]
380	N/A	13.2	54.2	32.5	100	[18]

N/A: Not available

SOURCE: own elaboration

Bubbling fluidized bed reactors (BFBRs) [8, 24, 25], falling-film reactors (FFRs) [15], and RCRs [26] were operated at higher temperatures compared to other reactor types. Therefore, the data obtained for these reactors were placed in the gas formation section of Figure 1. Since these reactors, especially BFBRs and RCRs, overcome heat transfer limitations due to the use of heat transfer media (e.g. sand), keeping the pyrolysis temperature in the liquid formation range and increasing the vapor residence time lead to an improvement in gasoline-like oil production. For example, Predel and Kaminsky (2000) studied the non-catalytic pyrolysis of PP in a BFBR at 510°C, where the vapor residence time was about 5 s [7]. In this study, 92 wt.% liquid and 30 wt.% C5–C12 hydrocarbons were produced.

CSTRs were found to be the most efficient reactors for the production of gasoline range (C5–C12) hydrocarbons at lower temperatures (~400°C). It should be mentioned that the use of a pretreatment reactor for the hot plastic melt helps to obtain the highest yield of gasoline-like oil (54 wt.%). Although more than 90 wt.% liquid yield was obtained in CSBRs, the liquid product was almost all wax due to the immediate removal of vapors from the reactors. BFBRs, FFRs and RCRs were operated at gas production temperatures (T > 550°C). These studies were good examples of gas production rather than gasoline production.

Conclusions

This study reviews the literature reports dealing with the results of PP pyrolysis from non-catalytic and continuously operated pyrolysis systems. The main conclusions are presented below:

- At temperature higher than 550°C, the yield of liquid product decreases.
- Using a heat carrier such as hot sand or pretreatment reactor to feed hot plastic to the main reactor enhances lightweight fuel production.
- CSTRs are found to be the best performing reactors to produce gasoline-like fuel at temperatures below 450°C.
- The maximum C5–C12 hydrocarbons yield was 54 wt.% obtained in CSTRs at 380°C.
- The main product in the pyrolysis oil was wax for CSBRs due to very short vapor residence time.
- In general, BFBRs, FFRs, and RCRs were operated at gas formation range (T > 550°C).

Acknowledgements: This work is supported and funded by the UK Department for Business, Energy and Industrial Strategy together with the Scientific and Technological Research Council of Turkey (TÜBİTAK; Project No. 119N302) and delivered by the British Council.

Literature

[1] Armenise S., SyieLuing W., Ramírez-Velásquez J. M., Launay F., Wuebben D., Ngadi N., Muñoz M., *Plastic waste recycling via pyrolysis: A bibliometric survey and literature review,* Journal of Analytical and Applied Pyrolysis 2021, 158.

[2] PlasticEurope., Plastics – the Facts. Brussels 2021. Retrieved from https://plasticseurope.org/knowledge-hub/plastics-the-facts-2021/.

[3] Phyllis2., ECN Phyllis classification-Plastics 2022. Retrieved April 26, 2022, from https://phyllis.nl/Browse/Standard/ECN-Phyllis#plastic.

[4] Dispons J., *Continuous Thermal Process for Cracking Polyolefin Wastes to Produce Hydrocarbons*, In S. John & W. Kaminsky (Eds.), Feedstock Recycling and Pyrolysis of Waste Plastics: Converting Waste Plastics into Diesel and Other Fuels 2006 (1st ed., pp. 595–604). Wiley.

[5] Czajczyńska D., Anguilano L., Ghazal H., Krzyżyńska R., Reynolds A.J., Spencer N., Jouhara H., *Potential of pyrolysis processes in the waste management sector,* Thermal Science and Engineering Progress 2017, 3, p. 171–197.

[6] Arabiourrutia M., Elordi G., Lopez G., Borsella E., Bilbao J., Olazar M., *Characterization of the waxes obtained by the pyrolysis of polyolefin plastics in a conical spouted bed reactor*, Journal of Analytical and Applied Pyrolysis 2012, 94, p. 230–237.

[7] Predel M., Kaminsky W., *Pyrolysis of mixed polyolefins in a fluidized-bed reactor and on a pyro-GC/MS to yield aliphatic waxes*, Polymer Degradation and Stability 2000, 70(3), p. 373–385.

[8] Park K.B., Jeong Y.S., Kim J.S., *Activator-assisted pyrolysis of polypropylene*, Applied Energy2019, 253(May), 113558.

[9] Miandad R., Barakat M.A., Aburiazaiza A.S., Rehan M., Nizami A.S., *Catalytic pyrolysis of plastic waste: A review,* Process Safety and Environmental Protection 2016, 102, p. 822–838.

[10] Diaz Silvarrey L.S., Phan A.N., *Kinetic study of municipal plastic waste*, International Journal of Hydrogen Energy 2016, 41(37), p. 16352–16364.

[11] Saad J.M., Williams P.T., Zhang Y.S., Yao D., Yang H., Zhou H., *Comparison of waste plastics pyrolysis under nitrogen and carbon dioxide atmospheres: A thermogravimetric and kinetic study,* Journal of Analytical and Applied Pyrolysis 2021, 156(May), 105135.

[12] Xu F., Wang B., Yang D., Hao J., Qiao Y., Tian Y., *Thermal degradation of typical plastics under high heating rate conditions by TG-FTIR: Pyrolysis behaviors and kinetic analysis*, Energy Conversion and Management 2018, 171(April), p. 1106–1115.

[13] Walendziewski J., *Continuous flow cracking of waste plastics*, Fuel Processing Technology 2005, 86(12–13), p.1265–1278.

[14] Frączak D., Fabiś G., Orlińska B., *Influence of the Feedstock on the Process Parameters, Product Composition and Pilot-Scale Cracking of Plastics*, Materials 2021, 14(11), 3094.

[15] Jin Z., Chen D., Yin L., Hu Y., Zhu H., Hong L., *Molten waste plastic pyrolysis in a vertical falling film reactor and the influence of temperature on the pyrolysis products*, Chinese Journal of Chemical Engineering 2018, 26(2), p. 400–406.

[16] Aguado R., Olazar M., San José M.J., Gaisán B., Bilbao J., *Wax formation in the pyrolysis of polyolefins in a conical spouted bed reactor*, Energy and Fuels 2002, 16(6), p. 1429–1437.

[17] Qureshi M.S., Oasmaa A., Pihkola H., Deviatkin I., Tenhunen A., Mannila J., Laineylijoki J., *Pyrolysis of plastic waste: Opportunities and challenges*, Journal of Analytical and Applied Pyrolysis 2020, 148(February).

[18] Murata K., Hirano Y., Sakata Y., Uddin M.A., *Basic study on a continuous flow reactor for thermal degradation of polymers*, Journal of Analytical and Applied Pyrolysis 2002, 65(1), p. 71–90.

[19] Murata K., Brebu M., Sakata Y., *The effect of silica-alumina catalysts on degradation of polyolefins by a continuous flow reactor*, Journal of Analytical and Applied Pyrolysis 2010, 89(1), p. 30–38.

[20] Papari S., Bamdad H., Berruti F., *Pyrolytic conversion of plastic waste to value-added products and fuels: A review*, Materials 2021, 14(10).

[21] Peng Y., Wang Y., Ke L., Dai L., Wu Q., Cobb K., Ruan R., *A review on catalytic pyrolysis of plastic wastes to high-value products*, Energy Conversion and Management 2022, 254(January), 115243.

[22] Miskolczi N., Angyal A., Bartha L., Valkai I., *Fuels by pyrolysis of waste plastics from agricultural and packaging sectors in a pilot scale reactor,* Fuel Processing Technology 2009, 90(7–8), p. 1032–1040.

[23] Miskolczi N., Bartha L., Angyal A., *High energy containing fractions from plastic wastes by their chemical recycling*, Macromolecular Symposia 2006, 245–246, p. 599–606.

[24] Jung S.H., Cho M.H., Kang B.S., Kim J.S., *Pyrolysis of a fraction of waste polypropylene and polyethylene for the recovery of BTX aromatics using a fluidized bed reactor,* Fuel Processing Technology 2010, 91(3), p. 277–284.

[25] Kaminsky W., *Recycling of polymeric materials by pyrolysis,* Makromolekulare Chemie 1991. Macromolecular Symposia, 48–49(1), p. 381–393.

[26] Westerhout R.W.J., Waanders J., Kuipers J.A.M., Van Swaaij, W. P. M., *Recycling of polyethene and polypropene in a novel bench-scale rotating cone reactor by high--temperature pyrolysis*, Industrial and Engineering Chemistry Research 1998, 37(6), p. 2293–2300.

Acid leaching for the recovery of lithium and cobalt from spent lithium-ion batteries

Keywords: Li-ion batteries, leaching, recovery of metals, waste management, environmental engineering

Abstract: Spent batteries are one of the most problematic in the waste management sector. The number of batteries grows annually, where only a few percent of materials are successfully recovered. Battery waste recovery is challenging for its complex composition including porous electrodes and toxic electrolytes. In this work, we refer to the acid leaching of spent battery waste for the recovery of Li and Co. Spent batteries were discharged, mechanically disassembled, and electrode powder was treated chemically. The leaching agents were mild organic acids like glutaric, lactic, and formic acids, and/or sulphuric acid. The morphology of spent electrode carbon-based powder was determined with SEM. The post-leaching solutions were studied within the ICP-OES to estimate the % of the recovery rate of certain metals. The recovery rate reaches even 59% and 82% of Co and Li, respectively, when the acid-leaching bath contained sulphuric acid, hydrogen peroxide, and glutaric acid.

Introduction

Portable electronic equipment has become an indispensable element of work and everyday life, and the demand for new devices of this type is constantly growing. It is associated with a significant increase in production, among others polymetallic batteries and accumulators, the proper recycling of which has been a challenge for the functioning waste management systems for years. Currently, metallic raw materials contained in waste electronic equipment can be efficiently recovered, but the methods of their recycling and preparation for re-use must be constantly improved and adapted

to the changing material composition of polymetallic components depending on the technologies used for their production [1].

The lack of effective regulations, collection systems and battery waste recycling technologies poses a challenge, especially in solving two global problems related to the management of this type of waste [2]. One of them is a potential risk of contamination with transition metal compounds from battery waste, which is toxic to the water and soil environment, as well as to living organisms. The second problem, especially related to battery management, is the overexploitation of natural resources of metals, which are the basic raw material used in the production of all types of used batteries and accumulators. Therefore, in order to develop comprehensive solutions in the management of the battery waste stream, it is necessary not only to introduce new regulations regarding the improvement of waste battery collection systems but above all to modernize the method of their recycling, from mechanical treatment, through the recovery of individual components of used batteries, to their recycling and use, e.g. for the production of new cells [3, 4].

Lithium-ion batteries (LiBs) are currently the most common type of cells used to power electronic equipment as well as modern hybrid and electric vehicles. LiBs are made of many different components, and their raw material composition may vary depending on the type of battery (especially the chemical composition of the cathode material used) and its manufacturer [5].

The largest part that builds Li-ion batteries is the so-called battery black mass (also known as battery powder) i.e., powdered anode and cathode materials obtained from the paramagnetic fraction, which is released as a result of separation and fragmentation operations carried out during the mechanical processing of used batteries and accumulators. Battery mass is rich in compounds of various metals, incl. lithium, cobalt, nickel, manganese, iron, copper and aluminum. The chemical composition of a typical lithium-ion battery is described in Shin et al. According to the authors, it contains 5–20% cobalt, 5–10% nickel, and 5–7% lithium [6]. In addition, the battery powder is on average 40–50% of the weight of the entire battery.

Li-ion battery waste is a source of many valuable materials, in particular metallic raw materials, incl. lithium, aluminum, cobalt, copper, zinc, nickel, and manganese, which are permanent components of this type of battery [7–9] numerous literature reports also indicate that apart from the most frequently mentioned metals occurring in the cathode of Li-ion batteries, the cells also contain other elements that require recovery in order to protect the environment. These are in particular: As, Ba, Cd, Cr, Pb, Hg, Se, Ag, As, Ba, Cd, Cr, Fe, Hg, Mo, Pb, Sb, Se, Tl and V [10–14]. Most of them are adversely affected by living organisms, causing numerous health problems, including cancer [15, 16].

The recovery of metals from used batteries can be carried out by many techniques, including hydrometallurgical methods based on the use of chemical compounds to dissolve the individual components of the battery and, subsequently, precipitate them from the solution and separate them. The use of hydrometallurgical processes allows

for achieving a higher purity of the recovered products compared to other methods while reducing energy consumption and reducing gas emissions. Nevertheless, they require pre-treatment of the batteries (e.g. crushing, magnetic separation, immersion in water or solutions), and then the use of strong chemical compounds, especially inorganic acids, generating secondary pollution difficult to neutralize [17–19].

Typically, inorganic and/or organic acids are used to leach electrode powder from spent batteries in which metals from the electrodes are dissolved and then recovered from the solution. The most commonly used leaching agents are inorganic acids (mainly sulphuric acid [20, 21], hydrochloric acid [22, 23], nitric acid [24], phosphoric acid [25, 26]) and organic acids – citric acid [27, 28], acetic acid [29], ascorbic acid [30], glutaric acid [31,32], succinic acid [33] as well as mixtures of various acids [34, 35]. Additionally, organic acids used together with inorganic acids act as a reducing agent. Leaching is most often carried out by combining acids with hydrogen peroxide (H_2O_2) [36, 37]. In addition, literature sources also indicate the use of other reducing compounds, such as e.g. sodium bisulfate ($NaHSO_3$)[38, 39], sodium thiosulfate (Na_2S2O_3) [40], ammonium chloride (NH_4Cl) [41], glucose [42], sucrose [42] and cellulose [43].

In the literature, the most frequently studied are spent lithium-ion batteries with a cathode in the form of $LiCoO_2$, which were previously used in laptops or mobile phones. In this work, for comparative purposes, similar studies were conducted to determine the quantitative and qualitative composition of spent LiBs from laptops. The material was subjected to initial, manual mechanical treatment in order to separate the anode-cathode powder. The battery mass was leached with mixtures of chemical compounds to recover the lithium and cobalt contained therein.

Materials and methods

The material taken for metal recovery investigation after the acid leaching was the electrode powder separated from spent Li-ion batteries previously contained in the older types of laptops (flat cells, similar to those currently used in mobile phones). Before the mechanical disassembling, spent batteries were discharged with the use of DC electronic load (Figure 1) to avoid hazards during mechanical processing (sudden changes in temperature, current conduction, explosion).

The next stage of the research was mechanical treatment in order to separate the individual components of the battery as much as possible and to separate the electrode powder containing metals, including lithium and cobalt. The anode-cathode material tested was mineralized, and the metal content in the obtained solution was determined using the ICP-OES method.

a) b)

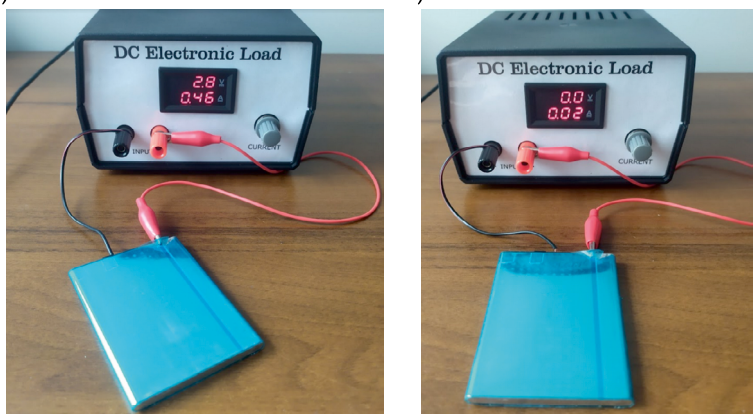

FIG. 1. Discharging an exemplary tested waste LiB: a) the charging state of the waste LiB just after connecting to the device, b) the state of the waste LiB after discharge

SOURCE: own elaboration

Metal leaching experiments from the tested battery powder were carried out with the use of sulphuric, lactic or formic acids as the leaching agents. The process was supported by a reducing agent in the form of hydrogen peroxide or hydrogen peroxide and glutaric acid in order to demonstrate their synergistic effect in a given, acidic reaction environment. The exact parameters of the performed leaching experiments are presented in Table 1.

TAB. 1. Determined parameters of the leaching process

Sample	Leaching agent	Reducing agent	Temperature	Solid/liquid ratio	Time
1	1.5 M sulphuric acid	3 mL H_2O_2	90°C	1/10	120 min
2	1.5 M sulphuric acid	3 mL H_2O_2 + 5 g glutaric acid			
3	5 M lactic acid	3 mL H_2O_2			
4	5 M lactic acid	3 mL H_2O_2 + 5 g glutaric acid			
5	5 M formic acid	3 mL H_2O_2			
6	5 M formic acid	3 mL H_2O_2 + 5 g glutaric acid			

SOURCE: own elaboration

After the leaching experiments were completed, the samples were vacuum filtered. The content of lithium and cobalt in the obtained polymetallic solutions was determined using the Inductively Coupled Plasma Optical Emission Spectroscopy

(ICP-OES) method (Agilent 720). The powder residues were dried at 105°C overnight and then subjected to Scanning Electron Microscopy (SEM) analysis – FE-SEM Merlin (Zeiss) equipped with a Gemini II column was used, operating in low kV value range (0.5–1.5 kV) and probe current 10–20 μA.

Results and discussion

As a result of the mechanical treatment of spent li-ion batteries, various material fractions were obtained, which can be classified into three basic groups i.e., ferromagnets – steel parts (mainly the outer casing), diamagnets – plastic outer protection and separators, and paramagnets – mainly anode and cathode powders deposited on copper and aluminum foil, respectively (material for further research on chemical leaching). The individual components of the battery obtained as a result of mechanical processing are shown in Figure 2.

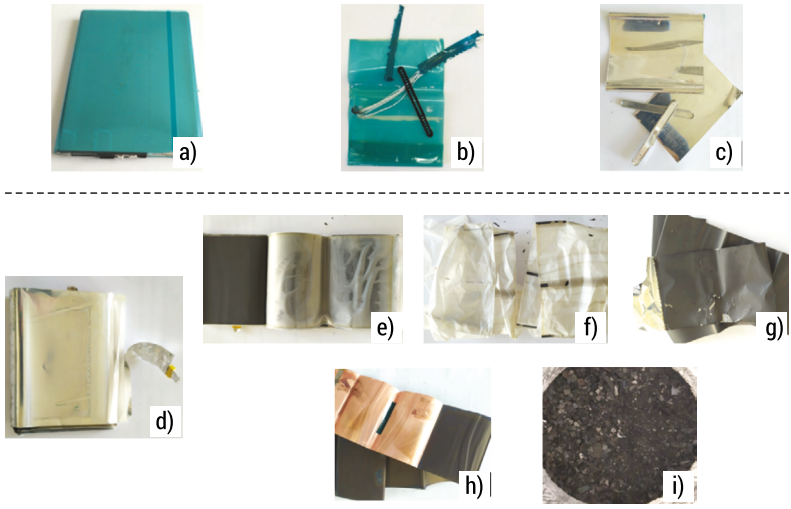

FIG. 2. Spent Li-ion battery – before and after the mechanical treatment: a) spent battery before mechanical treatment, b) protective foil, c) steel casing, d) the cell after removing the outer casings, e) internal structure of the cell (a coil of anode and cathode materials and separators), f) separator, g) aluminum foil with embedded cathode material, h) copper foil with deposited anode material, i) electrode powder saturated with electrolyte

SOURCE: own elaboration

Based on the fragmentation and separation operations as well as measurements of the masses of individual components, it was determined that the largest part of the battery (over 40 wt.%) is the electrode powder containing both electrolyte and metals, including Al, Co, Cu, Li, Mn, Ni and Zn (Table 2).

TAB. 2. Metal content in the powdery initial material

Metal	Al	Co	Cu	Li	Mn	Ni	Zn
Concentration, mg/kg	875	198000	3782	40100	756	12550	87

SOURCE: own elaboration

Next, the anode and cathode powders were mixed and washed within the distilled water several times to remove the electrolyte. As the spent battery electrode powder contains several valuable metals, it was treated with acids to recover them. Post-leaching powder was separated from the solution within the filtration, and the solution containing acids and metal ions was studied with ICP-OES. So far, depending on the composition of the leaching agents, different lithium and cobalt recovery rates were recorded. At first, bare sulphuric acid was used, as the most commonly used leaching acid, with hydrogen peroxide and/or glutaric acid acting as reducing agents. Then, the sulphuric acid was changed with a mild acid, like formic acid. Other conditions, such as glutaric acid or hydrogen peroxide contents, were the same as for sulphuric acid. Next, formic acid was used as the main leaching agent, while the other experimental conditions were analogical to the previous ones.

The results of the Co and Li recovery rates indicate that the highest leaching of these two metals was simultaneously obtained in sample 2, where the sulphuric acid was used as the leaching agent and the reducing agents were H_2O_2, and glutaric acid (59% and 82%, respectively). In turn, the lowest rate of cobalt recovery was obtained in sample 1 (1.5 M H_2SO_4 + H_2O_2), despite using hydrogen peroxide as a reducing agent, often indicated in the literature as a compound that significantly improves the leaching of this metal [44]. The low cobalt recovery rate in the present experiments, despite the use of H_2O_2, can probably be explained by a too-small dose of this factor. The preparation of the powder material for testing may also have an impact – the entire electrode powder was used i.e., anodic and cathodic mass, without additional thermal or chemical treatment, which is often practiced in literature sources to eliminate potential contamination, at the same time affecting a more complicated material preparation process than the one presented in this paper. The use of organic acids as leaching agents affected the Li recovery rates. These results were much lower than for the sulphuric acid leach tests, while higher rates of this metal recovery were obtained for samples 5 and 6 leached with formic acid (47 and 45%, respectively). In the case of cobalt recovery, for samples 3–6, the rates were higher than for sample 1, but also lower than for sample 2. Among the experiments with organic acids, the best results for both

tested metals were received for sample 6 (5 M CH_2O_2 + H_2O_2 + $C_5H_8O_4$) – Co: 26%, Li: 45%. Nevertheless, they are significantly lower than for a similar blend of reducing agents but combined with an inorganic leaching agent in the form of H_2SO_4 (sample 2).

Next, the morphology of the post-leaching battery powder was investigated with the Scanning Electron Microscopy (SEM), (see Figure 4). Sample 1 was treated with H_2SO_4 + H_2O_2 and has quite a uniform morphology, where the carbon-based layers are visible. Additionally, some granules are present that appear randomly on the surface, see Fig. 4a. Next, the leaching within the bath also containing glutaric acid delivers a completely different morphology.

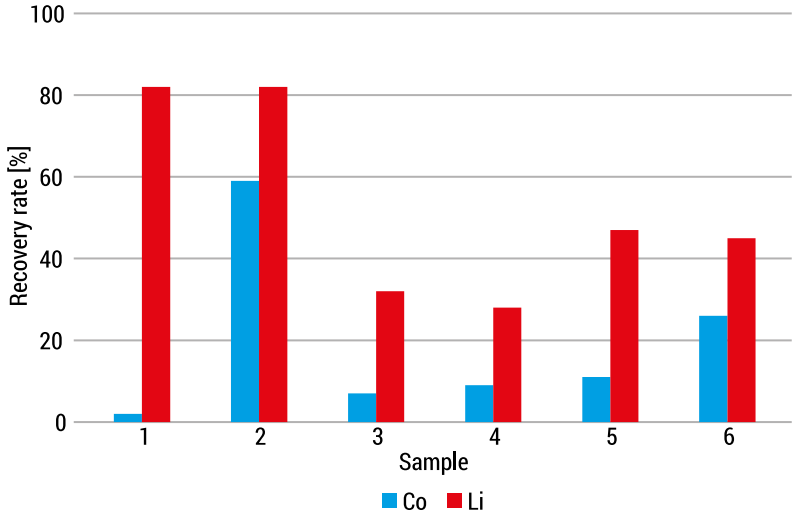

FIG. 3. Recovery rates of Li and Co obtained as a result of acid leaching of electrode powder from spent Li-ion batteries

SOURCE: own elaboration

The structure of carbon-based electrodes is highly porous, where the non-regular flake-like and grain-like structures can be distinguished. These structures having a size of 2–5 μm are coated with small spherical objects having a size of about a few hundred nanometers, see Fig. 4b. So far, the leaching with the acid bath containing mild organic acid as a reducing agent etches the electrode surface more effectively than the bath without the glutaric acid.

The following Fig. 4c corresponds to the sample treated with lactic acid and hydrogen peroxide. The morphology of sample 3 is similar to the morphology of sample 1, while more tiny grains and flake-like structures on the surface are visible.

Addition of glutaric acid to the bath for sample 4 leads to a similar effect as for sample 2. The surface has a completely different morphology when the mild acid is added, where both bulk structures and nanostructures can be observed. The whole sample is coated with tiny granules, see Fig. 4d.

When sample 5 is treated with the formic acid and hydrogen peroxide presented in Fig. 4e, the surface of the sample seems to be similar to sample 3 (Fig. 4c).

However, after the glutaric acid addition to the leaching bath, the morphology looks similar to sample 4, where the grain-like structures are observed, see Fig. 4f.

The surface is highly non-uniform, having cracks and granules. So far, it is clearly seen that depending on the application of the leaching agents the morphology of the samples changes, where the addition of the organic acid as a reducing agent improves the leaching and increases non-homogeneity of the surface which can be an advantage to the future applications of spent battery powder in catalysis or electrocatalysis [45].

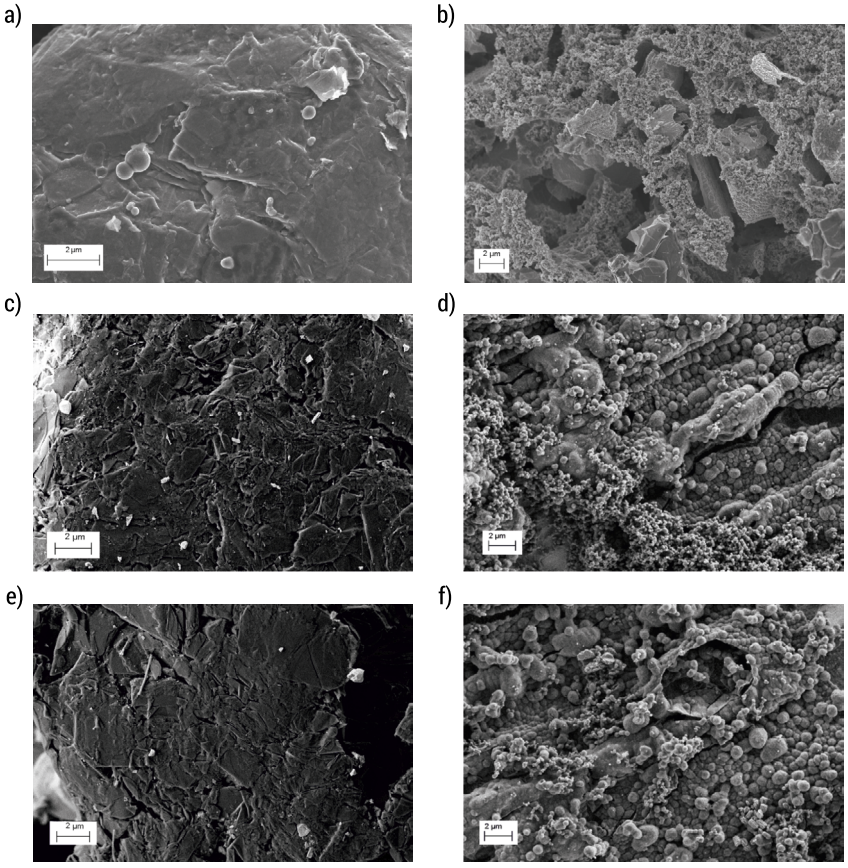

FIG. 4. Scanning Electron Microscopy images of the a) sample 1, b) sample 2, c) sample 3, d) sample 4, e) sample 5, and f) sample 6

SOURCE: own elaboration

Conclusions

One of the most common ways to recover valuable metals from the spent battery waste-based electrodes is the hydrometallurgical method. It is based on the application of strong inorganic acids that are used to treat the carbon-based powder full of valuable metals. In this work, we present the application of the acid leaching of the spent battery waste by use of mild organic acids including lactic, formic, and glutaric acids, and the mixture of these acids with one of the most commonly used acid leaching agents – sulphuric acid. The results of the recovery rate of valuable metals like Li and were investigated with the ICP-OES, where obtained results were compared to the reference solution containing sulphuric acid and hydrogen peroxide. Depending on the composition of the leaching solution, the recovery rate differs. Leaching of battery waste powder in H_2SO_4 and H_2O_2 leads to the high recovery rate of Li – about 82%, while the Co recovery is very low at ~ 2%. The addition of the glutaric acid to the leaching bath increases the Co recovery rate to 59% and the Li recovery remains stable. When the sulphuric acid is substituted with the mild organic acids like lactic or formic acid, the lithium recovery drops, but still, the values are higher than for the application of H_2SO_4 and H_2O_2.

Formic acid acts more efficiently as a leaching agent than the lactic acid and each time, the application of glutaric acid improves the cobalt recovery from the electrode powder leading to Co: 26%, Li: 45% recovery rates when the $CH_2O_2 + H_2O_2 + C_5H_8O_4$ were used. Since the most effective recovery rates from Li and Co were obtained for baths containing H_2SO_4, H_2O_2, and $C_5H_8O_4$, substitution of the sulphuric acid with eco-friendly mild organic acids also makes it possible to recover metals leading. Additionally, the morphology of post-leaching spent battery waste powder was investigated with SEM. It is seen that depending on the composition of the leaching bath, the morphology differs. The most developed surface is observed for the samples leached in the presence of glutaric acid leaching solutions. These studies require further investigation to determine the composition of the character, especially in photocatalytic studies, where traces of Co and its compounds are desired.

Literature

[1] Natarajan S., Aravindan V., *An Urgent Call to Spent LIB Recycling: Whys and Wherefores for Graphite Recovery*, Adv Energy Mater 2020, 10, p. 1–8.

[2] Velázquez-Martínez O., Valio J., Santasalo-Aarnio A., Reuter M, Serna-Guerrero R., *A critical review of lithium-ion battery recycling processes from a circular economy perspective,* Batteries 2019, 5, p. 5–7.

[3] Lai X., Huang Y., Gu H., Deng C., Han X., Feng X., *Turning waste into wealth: A systematic review on echelon utilization and material recycling of retired lithium-ion batteries,* Energy Storage Mater 2021, 40, p. 96–123.

[4] Matos C. T., Mathieux F., Ciacci L., Lundhaug M. C., León M. F. G., Müller D. B., *Material system analysis: A novel multilayer system approach to correlate EU flows and stocks of Li-ion batteries and their raw materials*, J Ind Ecol 2022, p. 1–16.

[5] Yoshino A., *Development of the Lithium-Ion Battery and Recent Technological Trends*, Elsevier 2014.

[6] Shin M. S., Kim N. H., Sohn J. S., Yang D. H., Kim Y. H. D*evelopment of metal recovery process from Li-ion battery wastes,* Hydrometallurgy, 2005, 79, p. 172–181.

[7] Siqi Z., Guangming L., Wenzhi H., Juwen H., Haochen Z., *Recovery methods and regulation status of waste lithium-ion batteries in China: A mini review,* Waste Manag Res 2019, 37, p. 1142–1152.

[8] Dutta T., Kim K. H., Deep A., Szulejko J. E., Vellingiri K., Kumar S., *Recovery of nanomaterials from battery and electronic wastes: A new paradigm of environmental waste management,* Renew Sustain Energy Rev 2018, 82, p. 3694–3704.

[9] Vanitha M., Balasubramanian N., *Waste minimization and recovery of valuable metals from spent lithium-ion batteries – a review,* Environ Technol Rev 2013, 2, p. 101–115.

[10] Lindqvist O., *Environmental impact of mercury and other heavy metals*, J Power Sources 1995, 57, p. 3–7.

[11] Karnchanawong S., Limpiteeprakan P., *Evaluation of heavy metal leaching from spent household batteries disposed in municipal solid waste,* Waste Manag 2009, 29, p. 550–558.

[12] Sayilgan E., Kukrer T., Civelekoglu G., Ferella F., Akcil A., Veglio F., *A review of technologies for the recovery of metals from spent alkaline and zinc-carbon batteries,* Hydrometallurgy 2009, 97, p. 158–66.

[13] Afolayan A. O., *Accumulation of Heavy Metals from Battery Waste in Topsoil, Surface Water, and Garden Grown Maize at Omilende Area, Olodo, Nigeria,* Glob Challenges 2018, 2, p. 1–12.

[14] Krishnan S., Zulkapli N. S., Kamyab H., Taib S. M., Din M., Majid Z. A., *Current technologies for recovery of metals from industrial wastes: An overview,* Environ Technol Innov 2021, 22, p. 1–19.

[15] Fasinu P. S., Orisakwe O. E., *Heavy metal pollution in sub-saharan africa and possible implications in cancer epidemiology,* Asian Pacific J Cancer Prev 2013, 14, p 3393–3402.

[16] Kim H. S., Kim Y. J., Seo Y. R., *An Overview of Carcinogenic Heavy Metal: Molecular Toxicity Mechanism and Prevention,* J Cancer Prev 2015, 20, p. 232–240.

[17] Zhang P., Yokoyama T., Itabashi O., Suzuki T. O., Inoue K., *Hydrometallurgical process for recovery of metal values from spent lithium-ion secondary batteries,* Hydrometallurgy 1998, 47, 259–271.

[18] Tanong K., Coudert L., Mercier G., Blais J. F., *Recovery of metals from a mixture of various spent batteries by a hydrometallurgical process,* J Environ Manage 2016, 181, p. 95–107.

[19] Asadi Dalini E., Karimi G., Zandevakili S., Goodarzi M., *A Review on Environmental, Economic and Hydrometallurgical Processes of Recycling Spent Lithium-ion Batteries,* Miner Process Extr Metall Rev 2020, p. 1–22.

[20] Li H., Xing S., Liu Y., Li F., Guo H., Kuang G., *Recovery of Lithium, Iron, and Phosphorus from Spent LiFePO*4 *Batteries Using Stoichiometric Sulfuric Acid Leaching System*, ACS Sustain Chem Eng 2017, 5, p. 8017–8024.

[21] Porvali A., Shukla S., Lundström M., *Low-acid leaching of lithium-ion battery active materials in Fe-catalyzed Cu-H2SO*4 *system,* Hydrometallurgy 2020, 195, p. 1–5.

[22] Guo Y., Li F., Zhu H., Li G., Huang J., He W., *Leaching lithium from the anode electrode materials of spent lithium-ion batteries by hydrochloric acid* (*HCl*), Waste Manage 2016, 51, p. 227–233.

[23] Fernandes A., Afonso J. C., Dutra A. J. B., *Separation of nickel*(*II*), *cobalt*(*II*) *and lanthanides from spent Ni-MH batteries by hydrochloric acid leaching, solvent extraction and precipitation,* Hydrometallurgy 2013,133, p. 37–43.

[24] Lee C. K., Rhee K. I., *Reductive leaching of cathodic active materials from lithium ion battery wastes,* Hydrometallurgy 2003, 68, p. 5–10.

[25] Chen X., Ma H., Luo C., Zhou T., *Recovery of valuable metals from waste cathode materials of spent lithium-ion batteries using mild phosphoric acid,* J Hazard Mater 2017, 326, p. 77–86.

[26] Pinna E. G., Ruiz M. C., Ojeda M. W., Rodriguez M. H., *Cathodes of spent Li-ion batteries: Dissolution with phosphoric acid and recovery of lithium and cobalt from leach liquors,* Hydrometallurgy 2017, 167, p. 66–71.

[27] Yang J., Fan E., Lin J., Arshad F., Zhang X., Wang H., *Recovery and Reuse of Anode Graphite from Spent Lithium-Ion Batteries via Citric Acid Leaching,* ACS Appl Energy Mater 2021, 4, p. 6261–6268.

[28] Li L., Ge J., Wu F., Chen R., Chen S., Wu B., *Recovery of cobalt and lithium from spent lithium ion batteries using organic citric acid as leachant*, J Hazard Mater 2010, 176, p. 288–293.

[29] Setiawan H., Petrus H., Perdana I., *Reaction kinetics modeling for lithium and cobalt recovery from spent lithium-ion batteries using acetic acid*, Int J Miner Metall Mater 2019, 26, p. 98–107.

[30] Li L., Lu J., Ren Y., Zhang X. X., Chen R. J., Wu F., *Ascorbic-acid-assisted recovery of cobalt and lithium from spent Li-ion batteries,* J Power Sources 2012, 218, p. 21–27.

[31] Urbańska W., *Recovery of Co, Li, and Ni from spent li-ion batteries by the inorganic and/or organic reducer assisted leaching method,* Minerals 2020, 10, p. 1–13.

[32] Urbanska W., Osial M., *Investigation of the physico-chemical properties of the products obtained after mixed organic-inorganic leaching of spent li-ion batteries,* Energies 2020, 13, p. 1–15.

[33] Li L., Qu W., Zhang X., Lu J., Chen R., Wu F., *Succinic acid-based leaching system: A sustainable process for recovery of valuable metals from spent Li-ion batteries,* J Power Sources 2015, 282, p. 544–551.

[34] Nayaka G. P., Manjanna J., Pai K. V., Vadavi R., Keny S. J., Tripathi V. S., *Recovery of valuable metal ions from the spent lithium-ion battery using aqueous mixture of mild organic acids as alternative to mineral acids,* Hydrometallurgy 2015, 151, p. 73–77.

[35] Golmohammadzadeh R., Faraji F., Rashchi F., *Recovery of lithium and cobalt from spent lithium ion batteries* (*LIBs*) *using organic acids as leaching reagents: A review,* Resour Conserv Recycl 2018, 136, p. 418–35.

[36] Li L., Dunn J. B., Zhang X. X., Gaines L., Chen R. J., Wu F., *Recovery of metals from spent lithium-ion batteries with organic acids as leaching reagents and environmental assessment,* J Power Sources 2013, 233, p. 180–189.

[37] Cheng X., Guo G., Cheng Y., Liu M., Ji J., *Effect of Hydrogen Peroxide on the Recovery of Valuable Metals from Spent LiNi*0.6*Co*0.2*Mn*0.2*O*2 *Batteries,* Energy Technol 2022, 10, p. 1–12.

[38] Wang D., Zhang X., Chen H., Sun J., *Separation of Li and Co from the active mass of spent Li-ion batteries by selective sulfating roasting with sodium bisulfate and water leaching*, Miner Eng 2018, 126, p. 28–35.

[39] Meshram P., Abhilash Pandey B. D., Mankhand T. R., Deveci H., *Comparision of Different Reductants in Leaching of Spent Lithium Ion Batteries*, Miner Met Mater Soc Comp 2016, 68, p. 2613–2623.

[40] Aaltonen M., Peng C., Wilson B. P., Lundström M., *Leaching of metals from spent lithium-ion batteries*, Recycling 2017, 2, p. 1–9.

[41] Lv W., Wang Z., Cao H., Zheng X., Jin W., Zhang Y., *A sustainable process for metal recycling from spent lithium-ion batteries using ammonium chloride*, Waste Manag 2018, 79, p. 545–553.

[42] Chen X., Guo C., Ma H., Li J., Zhou T., Cao L., *Organic reductants based leaching: A sustainable process for the recovery of valuable metals from spent lithium ion batteries,* Waste Manag 2018, 75, p. 459–468.

[43] Meng Q., Zhang Y., Dong P., *Use of glucose as reductant to recover Co from spent lithium ions batteries,* Waste Manage 2017, 64, p. 214–218.

[44] Li L., Chen R., Wu F., Chen S., Zhang X., Environmental friendly leaching reagent for cobalt and lithium recovery from spent lithium-ion batteries, Waste Manage 2010, 30, p. 2615–2621.

[45] Warczak M., Osial M., Urbańska W., Pisarek M., Nogala W., Opallo M., *Hydrogen peroxide generation catalyzed by battery waste material*, Electrochem Commun 2022, 136, p. 1–6.

Politechnika Białostocka